

Clemson University

TigerPrints

All Dissertations

Dissertations

8-2022

Airborne Contaminant Dispersal in Critical Built Environments

Arup Bhattacharya
arupb@clemson.edu

Follow this and additional works at: https://tigerprints.clemson.edu/all_dissertations



Part of the [Construction Engineering and Management Commons](#)

Recommended Citation

Bhattacharya, Arup, "Airborne Contaminant Dispersal in Critical Built Environments" (2022). *All Dissertations*. 3081.

https://tigerprints.clemson.edu/all_dissertations/3081

This Dissertation is brought to you for free and open access by the Dissertations at TigerPrints. It has been accepted for inclusion in All Dissertations by an authorized administrator of TigerPrints. For more information, please contact kokeefe@clemson.edu.

AIRBORNE CONTAMINANT DISPERSAL IN CRITICAL BUILT ENVIRONMENTS

A Dissertation
Presented to
The Graduate School of
Clemson University

In Partial Fulfillment
of the Requirements for the Degree
Doctor of Philosophy
Planning, Design, and the Built Environment

by
Arup Bhattacharya
August 2022

Accepted by
Dr. Ehsan Mousavi, Committee Chair
Dr. Joseph M. Burgett
Dr. Andrew R. Metcalf
Dr. Vincent M. Blouin

Abstract

The Indoor Air Quality (IAQ), being one of the most significant exposures to human beings, encompasses the concepts of comfort and safety from unwanted contaminants. Whereas the thermal comfort is controlled through proper conditioning and distribution of ventilated air, controlling the airborne contaminants requires careful investigation of the flow characteristics. IAQ translates to different requirements, depending on the intended use of the indoor environment. In critical indoor spaces such as Operating Rooms and Cleanrooms, the principal focus of IAQ is to remove/contain/divert contaminants flowing with the airstream to maintain the required sterility, as contamination can lead to adverse patient/product outcomes.

The airborne contaminants, generally submicron-sized particles, are controlled by directional airflow through differential pressure, depending on whether the space needs to exfiltrate (e.g., Operating Room – positive pressure) or contain (e.g., Isolation Room – negative pressure) the airborne contaminants. The current design paradigm that determines such pressure differential assumes steady-state conditions. Theoretically, during the steady-state, the rate of flow velocity change is zero, resulting in a constant flow field in time, and the distribution of contaminants in the space can be modeled using ordinary differential equations. Therefore, the steady-state assumption must hold to explain the contamination dispersal. However, in practice, transient occupant interventions like a door opening and walking through the steady-state flow fields alter the flow characteristics.

In response, this dissertation examines how occupant-introduced transient events affect the steady-state flow. This study aims to quantify and identify patterns of the changes in the flow characteristics for different scenarios of realistic door openings and human walks under a range of ventilation rates through controlled experiments and numerical simulations. Through specifically designed experiments, the impacts of door operation and occupant walking were

characterized and quantified based on different levels of supply flow rates from the ventilation system. The results of the experiments suggested that special considerations were required to control for the transient phenomena and the pressure differential. The walking and door opening experiments also found distinguishable changes in the flow characteristics under each separate interaction between the indoor environment and the occupant. It was interesting to note that even though the magnitude of the effects was different for different levels of initial condition and intervention types, the changes in the flow properties exhibited identical patterns that were possible to model and make predictions.

Thus, this dissertation considers the sporadic transient interventions from the occupants (e.g., - door opening and walking) as events and discusses an approximation method called 'Event-Based Modeling' (EBM) using the collected data through these experiments. Two-dimensional numerical models were developed to obtain additional data on the changes in airflow characteristics and were used to model and test the accuracy of EBM's prediction capabilities. The results demonstrated that the predictions from EBM were accurate, and the computational efficiency is improved compared to the traditional numerical simulation approach. This method can eliminate parallel modeling of the same phenomena, providing alternatives to simulate complex and computationally intensive transient events repeatedly. As a potential application, the changes in flow velocities from human-environment interactions in a critical indoor environment like an operating room can be predicted using the EBM method. This way, the ventilation systems can be designed as occupant-centric and energy-efficient by considering the impacts of the transient events instead of only considering the steady-state events.

Dedication

To my parents, who have sacrificed their needs and dreams every day to let me understand what education means. I hope to keep growing as a human being while carrying their legacy of love and kindness forward.

To my mom, Dipali Bhattacharya, for all the patience, love, lessons, and sleepless nights just to see me thrive. To my dad, Asit Kumar Bhattacharya, for all the support and life lessons that hardships are just tests to make one stronger and better. To my brother, Debjyoti Bhattacharya, who showed me the passion and sacrifices required to follow and realize a dream. To my sister-in-law, Sangita Goswami, who inspired me every day with her encouragement and immense patience while juggling the hoops of multitasking.

Acknowledgments

I am fortunate to be a protégé of my advisor Dr. Ehsan Mousavi. I am beyond grateful to have learned so much from him. The opportunities he provided to work on provoked me to think critically and grow independently while being patient. I am also incredibly grateful to my committee members Dr. Joseph M. Burgett, Dr. Andrew R. Metcalf, and Dr. Vincent M. Bluoin, for their constant support, encouragement, and feedback. They made me not only a better researcher but also a better collaborator. I'll cherish the connections I made with these brilliant faculty members throughout my life.

This journey would not have been so rewarding without the support of the Nieri Family Department of Construction Science and Management faculty and staff. Dr. Mike Jackson has helped me grow as a teacher by providing the opportunities to teach independently which has been an incredible gift to interact with outstanding students. Dr. Shima Clarke was always there to provide valuable guidance when I could not see the path clearly. I can't thank Dr. Dennis Bausman enough for being a mentor in every situation – learning from him, in and outside the classroom, was definitely a highlight of my time at Clemson. Other faculty members, Dr. Dhaval Gajjar, Dr. Vivek Sharma, and Dr. Jason Lucas, have always been supportive in all my endeavors allowing me to learn on the task – I have immense respect for how they guided me. Ms. Deborah Anthony has been a pillar of support with kind words and candies, always supporting me from the background and ensuring I always had everything I needed to thrive. Every single individual associated with the department has been kind, respectful, and accepting; I am delighted to have worked with them for the past four years.

Finally, my friends back home and here in Clemson have supported me through thick and thin. Dhrubajyoti, Joy, Ankita, Partho, Tiyaishi, Anirban, Manash, Abhisek, Pratyay, and Bidisha have always made me comfortable and cared for my loved ones while I was busy pursuing my dreams

9000 miles away amidst a global pandemic. Shubhashrita, Blake, Lela, Tanin, Bob, Todd, Alastair, Ashish, and Ajay were constant support and guidance in both bad and better days. Mina, Colin, Ahmed, Laura, Ramses, Daniel, Aditya, Nico, Oksana, and Vishal made me feel at home here at Clemson with their love and affection, no matter how difficult. I am so thankful to have Vivian as a friend who made sure to listen to me, support me, and partner in the craziness. I met brothers and sisters from different mothers who cared for me genuinely and were by my side daily through ups and downs. I could not have been where I am today without their gracious presence in my life.

Contents

Abstract.....	i
Dedication.....	iii
Acknowledgments.....	iv
Chapter 1.....	1
Introduction.....	1
Chapter 2.....	8
Literature Review.....	8
Introduction:.....	8
Clean Spaces:.....	9
Ventilation Requirements in Clean Spaces.....	12
Contaminant Concentration Measurements and Suggestions for Removal.....	18
External Perturbations on Indoor Airflow:.....	26
Event-Based Modeling:.....	33
Theoretical Framework:.....	34
Conclusion:.....	36
Chapter 3.....	39
Research Design.....	39
General Research Strategy:.....	39
Operational Measures:.....	40
Experiment Design:.....	43
Numerical Simulation:.....	50
Chapter 4.....	53
Factors Affecting Airflow and Particle Dispersion in a Clean Space Under Occupant Movements.....	53
Methods:.....	53
Findings:.....	63
Limitations:.....	74
Conclusion:.....	74
Chapter 5.....	77
Effects of Indoor Human Movements on Indoor Airflow Patterns.....	77
Methods:.....	77
Findings:.....	83

Walking Once- Still Air:	83
Limitations:.....	95
Conclusions:	96
Chapter 6	99
Effects of Door Opening on Indoor Airflow Patterns.....	99
Methods:	99
Findings:	105
Limitations and Conclusions:.....	130
Chapter 7	133
Event-Based Approach for Modeling Airflow Patterns.....	133
Core Idea:	133
EBM Definition of Superposition using Dynamic Modal Decomposition.....	135
Validation Approach:	139
Assessment of EBM Using the Experimental data:	139
Assessment of EBM Using Numerical Simulation Data:	148
Conclusion:	156
Limitations, future outlook, and applications:.....	159
Chapter 8	161
An application and future outlook of EBM	161
Methods:	162
Evaluating the prediction:.....	170
Extending the EBM approach to approximate airborne particle movement:.....	172
Chapter 9	176
Research Validity and Limitations.....	176
Internal:.....	176
External:	177
Construct:	177
Reliability:	178
Limitations:.....	178
Chapter 10	180
Conclusion	180
Annexure 1 – List of the Sources of Limitations.....	185
Chapter 4:	185
Chapter 5:	186
Chapter 6:	186

Chapter 7:	187
Chapter 8:	187
References:	188

Schedule of Figures

Figure 1: Literature Review Map	9
Figure 2: Best practices to control contaminant in cleanrooms	25
Figure 3: DPSEEA Framework (Hasselaar, 2006).....	35
Figure 4: Research Design Map.....	39
Figure 5: Systematic Relations.....	41
Figure 6: Plan view of Cleanroom at Clemson University	46
Figure 7: Schematic of Controlled Environment Chamber at UC Berkeley	47
Figure 8: Velocity Measurement Devices: (a) Omnidirectional (b) Ultrasound	49
Figure 9: Layout of the cleanroom and experimental setup.	54
Figure 10: Pressure differential across the cleanroom door during 5-second door openings for the high-pressure experiments. The door was opened at time =5 s and closed at time = 10 s. The different colored markers indicate each individual event during the experiments.	64
Figure 11: Pressure differential across the cleanroom door under 'low ΔP '. The door was opened at time = 5 s. and closed at time = 10 s. The different colored markers indicate each individual event during the experiments.	65
Figure 12: Concentration heat map inside the CR for low ΔP (top figure) and high ΔP (bottom figure) for 0.3 μm particle measurements. Note the difference in colorbar concentration scale between the two images	70
Figure 13: Particle Counts inside CR with Respect to Cleanroom Door Opening	71
Figure 14: Exposure in CR with respect to traffic movement direction. Particles were released in GR	73
Figure 15: Chamber Geometry and Experimental Design	79
Figure 16: Air Speed due to walking once in still air by omnidirectional (–) and ultrasound (°)...	85
Figure 17: Patterns of air speed for Sensor L3 and the Cartesian components of air velocity ...	86
Figure 18: Effect of Human Walking on the Airflow Perpendicular to Walking Direction for Walking Once (bottom) and Walking Twice (Top)	88
Figure 19: Air Speed due to walking twice in still air by omnidirectional (–) and ultrasound (°) .	90
Figure 20: Velocity Magnitudes in Sensor L4 for Three Initial Conditions and Two Walking Schemes.....	92
Figure 21: Velocity Magnitudes in Sensor R4 for Three Initial Conditions and Two Walking Schemes.....	93
Figure 22: Total Kinetic Energy of Still Air for Two Walking Schemes and Two Measurement Techniques; Sum Over All Sensor Locations	95

Figure 23: (a) Chamber geometry – 3D (b) Peripheral Configuration of Sensors (c) Radial Configuration of Sensors (d) Actual Photograph from Test Chamber	101
Figure 24: Data Consistency	104
Figure 25: Temporal velocity trends for lower elevation sensors - door-opening once.....	106
Figure 26: Temporal velocity trends for higher elevation sensors - door-opening once	108
Figure 27: Temporal velocity trends at lower elevation sensors - door-opening twice.....	111
Figure 28: Temporal velocity trends at upper elevation sensors - door-opening twice	112
Figure 29: Placement of Sensors and Coordinate Definitions.....	116
Figure 30: Cartesian and Cylindrical Coordinates Conversion.....	117
Figure 31: Mass flow rates in kg/s during door opening for various test conditions.....	119
Figure 32: Transient Pattern of Air Speed from Door Opening Once (Test 1).....	121
Figure 33: Cartesian components of velocity at location P2 for (a) Test 1, (b) Test 3, and (c) Test 5.....	123
Figure 34: Transient pattern of Air Speed from Door Opening and Closing Twice (Test 4).....	125
Figure 35: Spatial Distribution of Velocity Fields.....	127
Figure 36: Total Kinetic Energy of Still Air for two door opening schemes; sum over all sensor locations.....	128
Figure 37: Error from Door Opening Events - Weighted Average Approach: [a] Comparison of Temporal Trend - Door Opening Once and Twice, [b] Error Distribution - Door Opening Once, and [c] Error Distribution - Door Opening Twice	142
Figure 38: CS approach - temporal trend of absolute error: The pointers show absolute error at all locations at every timestep; the line shows spatially averaged absolute error.....	143
Figure 39: Distribution of error - CS approach.....	144
Figure 40: Effect of Number of Close Cases Selected to Approximate α on Average Absolute Error - CS Approach.....	145
Figure 41: Comparison of DCS approach and CS approach for approximating a new case using two close cases ($N = 2$) from the training dataset.....	147
Figure 42: Comparison of Spatial Velocity Fields Obtained from Experiment and Approximated using DCS Approach.....	148
Figure 43: Simulation Geometry.....	149
Figure 44: Mesh Configuration	150
Figure 45: Initial Condition for the CFD Simulations	152
Figure 46: Temporal Trend of Average Absolute Error for the Simulated Walking Events	155
Figure 47: Distribution of Absolute Error for Simulated Walking Event	156

Figure 48: Comparison of Velocity Fields from CFD Simulation and EBM.....	157
Figure 49: Multiple Walk Geometry	163
Figure 50: The Area Considered to Obtain Velocity Data for the Training Set	165
Figure 51: Defining Prediction Subspace for the Multiple Walk Scenario.....	167
Figure 52: Spatially Averaged Absolute Error.....	170
Figure 53: Distribution of Temporally Averaged Error.....	171

Schedule of Tables

Table 1: Cleanroom Classification.....	10
Table 2: Conversion of Cleanroom Classes	11
Table 3: Indices used in literature.....	19
Table 4: Gravitational Settling Time of Particles with Different Size.....	55
Table 5: Test Procedure - background, injection and cycle 1	57
Table 6: Experimental Setups	58
Table 7: Airflow inside the cleanroom.....	60
Table 8: Mean temperature (°C) at the sampling location, and the corresponding standard deviation	61
Table 9: Exposures at different compartments from particle release in CH	66
Table 10: Exposures at different compartments from particle release in GR	69
Table 11: Experiment conditions	80
Table 12: Comparison between the measurements by ultrasound vs. omnidirectional sensors.	81
Table 13: Consistency of Data Measurements By Omnidirectional sensors for all Test Repetitions	83
Table 14: Three-dimensional velocities, lag, and range of non-zero data recorded by ultrasound sensor.....	84
Table 15 : Comparison between Time-Averaged Velocity Components of Walking Once and Twice	91
Table 16: Kinetic Energy of Human Walking vs. Initial Condition.....	94
Table 17: Experiment Conditions	103
Table 18: The maximum velocity associated to the sensing stations and the time it occurred .	110
Table 19: Change in velocity proportion from opening once to twice at all sensor locations	113
Table 20: Total amount of air exchange (kg) across the door for different pressure differentials and door openings	120
Table 21: Time-averages Kinetic Energy for two door opening schemes	129
Table 22: Transient Movements.....	151
Table 23: Multiple Walking Scheme	162

Chapter 1

Introduction

Overview of IAQ: The concept of ventilation is generally defined as the process of supply and exhaust of air (may or may not be conditioned) that removes dust and unwanted foreign particles, ensuring comfort and safety of the occupants of a variety of indoor environments (*The American Society of Heating and Ventilating Engineers Guide*, 1922). It is particularly significant given indoor air is the most influential exposure to humans (Sundell, 2004), as, on average, human beings spend nearly 90% of their total time indoors (Awbi, 2003). Indoor Air Quality (IAQ) is a concept that broadly encompasses thermal comfort and freedom from noxious substances (particles, odors, gases, etc.). The idea of thermal comfort in an indoor setting is a multifaceted subject that depends on factors like activity level, clothing requirement, occupant density, etc., in addition to the ventilation requirements (Fagner, 1970). On the other hand, the safety issue from particles (generically termed as contaminants) corresponds mostly to the space function (the specified indoor setting) and the associated ventilation requirements. Controlling the thermal comfort is implemented through the proper conditioning of the supplied air – the temperature and humidity in indoor environments are measured and administered to match the thermal comfort requirements. But, to assess the effects of contaminant transport through air movements, it is necessary to study the ventilation system that determines the flow characteristics.

IAQ in Critical Spaces: The indoor airflow patterns are derived from the ventilation system design, which depends on the IAQ requirements of the space it is being designed for. IAQ translates to different meanings depending on the intended use of individual indoor environments. Apart from general residential or commercial indoor environments, where the focus of IAQ is the health and wellbeing of the occupants (ASHRAE, 2019), there are controlled environments where IAQ is

implemented following the guidelines to control the dispersion of contaminants, along with the air quality parameters (Whyte, 2010). For example, a classroom and an operating room (OR), both having the approximate average size of 600 SF (for a medium-sized classroom for 20-30 students, source: [NYU's Space Planning Working Group](#), and for a typical OR, source: [Steris Healthcare](#)), are used for different purposes. Cleanliness requirement takes precedence over thermal comfort in an OR, whereas temperature and humidity control are emphasized more in a classroom. Similarly, Cleanrooms, other healthcare facilities, and laboratories are such controlled environments where the ventilation system is primarily responsible for removing/containing/diverting contaminants flowing with the airstream. The ventilation systems in such spaces must be designed to minimize exposure to unwanted substances in these spaces. Hence, these spaces are termed critical built environments in this research.

Health outcomes from airborne contamination: Healthcare facilities, such as operating rooms and isolation rooms, are among the most sensitive places as they host patients with open wounds and suppressed immune systems susceptible to infection from airborne contamination, where detrimental patient outcomes can result from system malfunctions (Meneguetti et al., 2013; E. Mousavi et al., 2019). The recent outbreak of the COVID-19 pandemic has presented an unprecedented challenge to the healthcare provider community (Heffernan et al., 2020), since they are at a disproportionately higher risk (29% higher than others) of contracting the SARS – CoV-2 (Bai, Yan; Yao, Lingsheng; Wei, tao; Tian, Fei; Jin, Dong-Yan; Chen, Lijuan; Wang, 2020). Although the mechanism behind the spread of COVID-19 is debated, researchers have provided evidence of significant airborne transmission (Mittal et al., 2020; Morawska & Cao, 2020; Setti et al., 2020). Thus, in terms of airborne contamination, IAQ is one of the seminal properties that must be adequately understood and established through careful study of the ventilation system in critical spaces like cleanrooms and healthcare facilities.

Nature in terms of sizes of Airborne particulate contaminants: Airborne pollutants are defined as part of the air mixture that is foreign to the normal state of the air, which can be harmful, irritating, or nuisance to the human occupants (Talty, 1998). Whether a particle is airborne is dependent on the size of the particle and the distance it can travel. It was shown that smaller particles are passive, meaning they follow the airstream (Garner & Hospital Infection Control Practices Advisory Committee, 1996; Thomas H. Kuehn, 1988). World Health Organization differentiates between airborne and droplet transmission using 5 μm as the cutoff particle size (WHO, 2007). The gravitation settling time of particles in the air, as determined from Stokes' Law, for size $\leq 10 \mu\text{m}$ is considerably high, indicating that submicron-sized particles can stay afloat in the air for a fairly long time, are capable of adopting the flow velocity and follow the airflow patterns (Hinds, 1999). Hence, in critical spaces, it is crucial to understand their dispersion patterns to ensure freedom from airborne contaminants and obtain prescribed IAQ (Hathway et al., 2015; Hu et al., 1996).

Engineering solutions to airborne contamination control: To navigate through the challenges related to the passive contamination spread, encountered in sensitive spaces, a number of different approaches are employed through the mechanical ventilation systems. The mechanically ventilated spaces control airstreams by employing directional airflow through (de)pressurization of the space for adjacent chambers and rooms with respect to the hallways/corridors, in addition to the locations of air inlets and outlets (Chung & Hsu, 2001; E. S. Mousavi & Grosskopf, 2016). This differential pressure between two adjacent spaces governs the flow direction. Indoor spaces that require contaminants to exfiltrate (e.g., cleanrooms, ORs, etc.) to maintain sterility free from particulate contamination are kept under positive pressure by supplying more air. On the contrary, spaces that need to contain the contaminants (e.g., isolation rooms) so that airborne contaminant are inhibited within the space are kept under negative pressure with respect to their adjacent chambers preventing the air outflow (ASHRAE Standard 170, 2013; B. Zhou et al., 2018a).

Despite these arrangements and proper control of cleanliness (e.g. clean equipment, proper personnel protective equipment, etc.), surgical site infections (SSI) are reported (Liu et al., 2016; Xie et al., 2010), proving the inadequacy of implementing only directional airflow to remove the contaminants, which in turn suggests that thorough understanding of air movement patterns and the factors that affect such movements are crucial for understanding the pathogen transport mechanisms.

The HVAC system design and its limitation – introduction of occupant-introduced perturbation:

The ventilation system design assumes a steady state condition, which asserts that the calculations related to ventilation can be done when the overall system has reached a stable condition, i.e., the prescribed balance between the inlet-exhaust airflow has been obtained. For an enclosed indoor space, after a certain time, the supplied air is well mixed with the existing air, and the net inflow or outflow of air reaches a near-constant value, depending on the differential pressure. Theoretically, during the steady state, the rate of flow velocity change is zero, resulting in a constant flow field in time. Therefore, the distribution of contaminants within the space, modeled via the Lagrangian frame of reference, can be explained by an ordinary differential equation. These equations are much less computationally expensive to solve than complex partial differential equations. Hence, to quantify the distribution of contaminants through the flow fields, it is important that the assumption of steady state holds.

But the occupants of the indoor environments often interact with the environment, and the steady state condition breaks down. During the design of a mechanical ventilation system, the flow patterns are comprehended when the chamber is sealed and no interaction with the occupants is present. With the introduction of occupant intervention, a transient system emerges. It is extremely difficult, if not entirely impossible, given the limitations of the computational resources to solve the governing equations to quantify the flow. There are several types of perturbations introduced by the occupants, that have been discussed in the literature (Beggs et al., 2008;

Eames et al., 2009; Gustafson et al., 1982; Josephson & Gombert, 1988; Li et al., 2007), including door opening and closing, human movement, furniture movement, and other similar ways of occupants interacting with the existing flow field. Door openings and human walks are the most common occurrences in indoor environments (Hang et al., 2014, 2015; Josephson & Gombert, 1988). Hence, it is imperative to understand the airflow characteristics during the transient events initiated by the occupants to comprehensively understand the airborne spread of contaminants in mechanically ventilated sensitive spaces.

The approach of this study: Several studies have probed into the factors affecting indoor air streams through different modes of investigation employing different methods (C. Chen et al., 2016; Luo et al., 2018; Mattsson, M.; Sandberg, 1996; Mazumdar et al., 2010; O. Rouaud et al., 2004). Most of the published research is concentrated on examining the near-body flow phenomena and temporal flow profiles. A significant proportion of the previous investigations have presented conclusions based on numerical simulations and observations that have been performed, considering a narrow focus on the number of factors involved. There is a shortage of studies that characterizes changes in the steady-state airflow patterns resulting from multiple external interactions under a range of ventilation performances.

In response, this study examines how the changes introduced by the transient events resulting from external disturbances affect the ventilated airflow. This study aims to quantify and identify patterns of the changes in the steady-state flow characteristics under different scenarios of realistic door openings and human walks under a range of ventilation rates through controlled experiments and numerical simulations. This study aimed to answer the following questions:

1. What are the factors, and how do they influence the airflow and particle dispersion in a clean space under occupant introduced perturbations?
2. How can the effects of occupant-introduced disturbances be measured quantitatively?

3. How to model and predict the changes in airflow patterns originating from human-built environment interactions?
4. What are the potential applications of predictive modeling?

The hypotheses considered for this study are:

- It is possible to measure flow velocity to assess and quantify the effects of discrete events on indoor airflow.
- Controlling extraneous variables (e.g., temperature, humidity, supply and exhaust location, ventilation system type, etc.), the trends of flow alterations under discrete events can be extended to mathematically model and make accurate predictions.

Based on the research questions developed and to test the hypotheses, specific experiments were designed to characterize and quantify the impacts of occupant movements, specifically walking and door operation in steady state indoor environments. At first, the combined effects of the door opening, walking in/out, and door closing were tested on the particle movements inside a cleanroom environment, depending on the pressure differentials and the source of particles. Next, in a controlled environment chamber, emulated as a positively pressurized healthcare environment, two constrained walking exercises were studied to understand how the airflow patterns changed for different levels of inlet airflow. In the same chamber, two different opening and closing cycles of a swing door were tested for different levels of steady state settings, identical to the walking experiments.

The findings of this research suggest that differential pressure is an effective method to control the flow of airborne particles. Still, with the emergence of the transient phenomena, special considerations are required to control airborne contamination in critical spaces. The location of the principal source of contamination and the direction of the steady state airflow significantly impacts how occupant movements affect the indoor flow patterns. The walking and door opening

experiments also found that there are distinguishable changes in the flow characteristics under each separate interaction between the indoor environment and the occupant. It was interesting to note that even though the magnitude of the effects was different for different levels of initial condition and intervention types, the changes in the flow properties exhibited identical patterns that were possible to model and make predictions.

Thus, this dissertation considers the sporadic transient interventions from the occupants (e.g., - door opening and walking) as events and discusses an approximation method called 'Event-Based Modeling' (EBM) using the collected data through these experiments. Two-dimensional numerical models were developed to obtain additional data on the changes in airflow characteristics and were used to model and test the accuracy of EBM's prediction capabilities. This approach can eliminate parallel modeling of the same phenomena, providing alternatives to repeatedly simulate complex and computationally intensive transient events. This way, the ventilation systems can be designed as occupant-centric and energy-efficient by taking into account the impacts of the transient events instead of only considering the steady-state events. As a potential application, the changes in flow velocities from human-environment interactions in a critical indoor environment like an operating room can be predicted using the EBM method. Although out of scope for this research, those predicted velocities can then be used as an input to model particle velocity using the Lagrangian framework of particle flow modeling, providing a way to have an understanding of how occupant movements in steady state fields impact the particle dispersion. Subsequently, the ventilation system can be designed to tackle the sporadic unintended dispersion of airborne particles.

Chapter 2

Literature Review

Introduction:

In this section, the existing body of research related to airborne contamination spread in clean spaces (including cleanrooms, operating rooms, and other contaminants free indoor environments) is revisited, presenting a comprehensive review of ventilation requirements and performance in sterile areas, contamination control methodologies related to ventilation requirements, and quantification of changes in flow parameters resulting from external perturbations. Specific emphasis is placed on studies examining the impacts of human traffic and door operations in understanding indoor air stream movements and delineating ways to quantify them. This section also informs the methods to answer the research questions. This detailed review will serve to derive/identify the variables that this research should consider for measurement and identify the gaps in the knowledge base where this study can fit in.

Figure 1 depicts the overall literature review process, which begins to scrutinize publications related to clean spaces and operating rooms, their ventilation requirements to achieve the prescribed level of cleanliness, and an understanding of the methods and measures used to quantify these parameters. Subsequently, a closer inspection is done on the papers that have studied two primary sources of occupant-introduced disturbances in the airflow, namely human movement and door operations, to understand the impacts these events have on the indoor flow field. The studies that introduced event-based modeling are examined further down, providing insights into the critical factors contributing to the predictive model building. The findings from this wide array of pertinent literature pieces are applied to narrow down the gaps in the existing knowledge and help formulate the research questions.

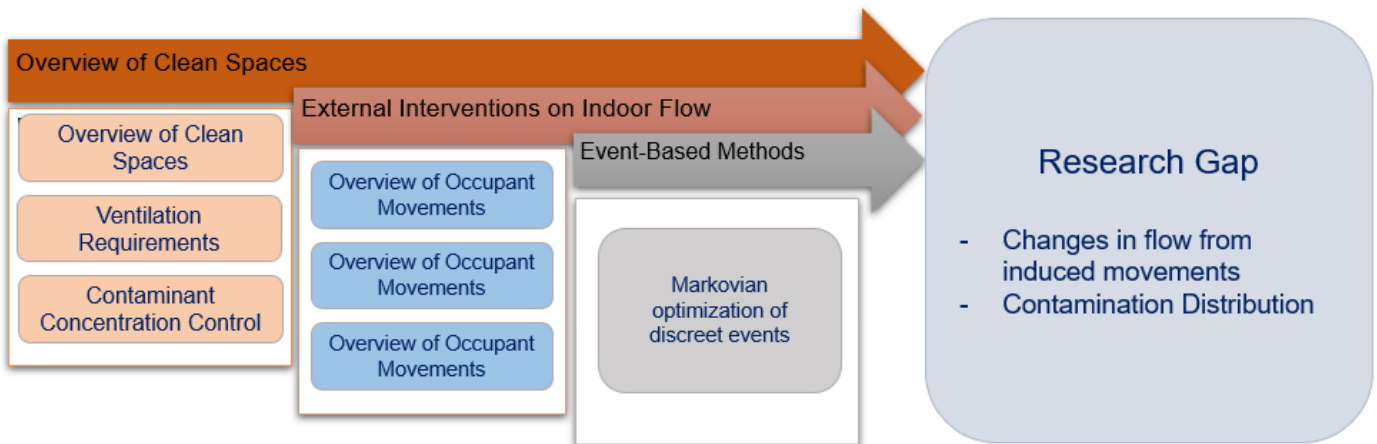


Figure 1: Literature Review Map

Clean Spaces:

Overview

Cleanrooms are specially constructed to control environmental factors such as temperature, humidity, air pressure, airflow patterns, air motion, vibration, noise, and lighting, emphasizing controlling particulate and microbial contamination concentration and dispersion. Cleanrooms are defined as a room where the concentration of airborne particles is controlled to specific limits ("Airborne Particulate Cleanliness Classes in Clean Rooms and Clean Zones," 1992). Going a step further, British Standard 5295 (Whyte, William; Johnston, 1990) defines cleanrooms as rooms with control of particulate concentration, constructed and used in such a way as to minimize the introduction, generation, and retention of particles inside the space where the temperature, humidity, airflow patterns, air motion, and pressure are also controlled. This definition is also adopted by the International Organization for Standardization (ISO) standard 14644-11 (International Organisation for Standardization, 2015).

Table 1: Cleanroom Classification

Clean Room Class	No. of particles not to exceed per ft ³ for particle sizes				
	0.1 μm	0.2 μm	0.3 μm	0.5 μm	> 0.5 μm
1	35	7.5	3	1	-
10	350	75	30	10	-
100	-	750	300	100	-
1000	-	-	-	1000	7
10000	-	-	-	10000	70
100000	-	-	-	100000	700

The utilization of clean spaces is dominated by sophisticated manufacturing industries, which require spaces that can control particulate and microbial contamination with reasonable expenses concerning construction and operation. One such example is the semiconductor industry. In the early 2000s, a cleanroom benchmarking study showed that 58% of cleanrooms in California were semiconductor cleanrooms (Tschudi et al., 2001). Additionally, pharmaceutical, aeronautics, and high infection risk zones in healthcare facilities also use cleanrooms to no small extent.

Cleanrooms are classified into classes depending on the cleanliness level, which is determined by particles' concentration in a unit volume of air. According to the count of specific-sized particles, Federal Standard 209E categorizes cleanrooms into six general classes. Table 1 describes the cleanroom classes in terms of allowable limits of particles of different sizes according to classes. Classes 1, 10, and 100 do not allow any particle size of more than 0.5 μm , while the other three do. Interpreting the table, in a cleanroom of class 1000, the maximum concentration of particles of size 0.5 μm or less is limited to 1000 per ft³ (Airborne Particulate Cleanliness Classes in Clean Rooms and Clean Zones, 1992). The ISO technical committee TC 209 classifies cleanrooms differently, and this standard is replacing the Federal Standard. ISO standard based on the metric

system of measurement where the classes are 3,4,5,6,7, and 8 (Harrison, 2011). A class 5 cleanroom allows 3520 particles of size $\leq 0.5 \mu\text{m}$ per cubic meter of air, which translates to 100 particles per cubic foot, as in cleanroom class 100, according to Federal Standard 209E (Y.Venkata Bharath, 2013). Table 2 shows the equivalence of cleanroom classes, rated according to both these standards.

Table 2: Conversion of Cleanroom Classes

Federal Standard 209E	ISO Standard
1	3
10	4
100	5
1000	6
10000	7
100000	8

Sources of Contamination in Clean Spaces

Internal: These are the contaminations that originate inside the cleanroom boundary. The largest contamination source is people, generating particles from respiratory emissions, skin flakes, and shedding particles from clothing and cosmetics (Y.Venkata Bharath, 2013). The shedding of surfaces and particles generated from the process is also considered the internal source. Contingent on the process, the generation of particles includes chemical vapors, fumes, cleaning agents, VOCs, and other manufacturing agents. These generated particles' sizes range from submicron levels to several hundred microns (ASHRAE, 2019). The predominant method of

controlling the passive internal contaminants is designing proper ventilation systems that minimize contaminants' retention and maximize their dispersion out of the cleanroom (International Organisation for Standardization, 2015).

External: Contaminant origins that are primarily situated outside the boundaries of a clean space are considered external sources. The primary method of external contaminant introduction to cleanrooms is the makeup air required for ventilation. In addition to the ventilation system, external contamination can migrate to clean spaces through doors, windows, gaps around frames, pipes, and ducts required for mechanical-electrical plumbing. Controlling the external contaminant migration to cleanrooms requires proper equipment selection, rigorous process employment, use of personnel protective equipment, timely maintenance of the facility, and pertinent facility design (ASHRAE, 2019). For this proposed study, the interest lies in investigating the migration pattern for external and internal contaminants under the influence of the ventilation system and occupant movement.

Ventilation Requirements in Clean Spaces

The ventilation requirement translates to the conditions that ensure the desired environment in a ventilated space. The requirements can vary according to the specified use for clean areas, but generally, ventilation requirements in cleanrooms concentrate on minimizing contamination concentration. In the early 1920s, ventilation requirements were aimed more at occupant comfort in terms of indoor temperature and humidity and less focused on contamination control. Moving air has been a method of providing quality healthcare environments since the late 19th century (Burch & Depasquale, 1959). Hospitals, due to their functions, are a natural harborage for infections. So, minimizing the incidence of infections was subject to study in the last century (Laforce, 1986). The initial intent of ventilating operating rooms was to avoid explosion hazards from the accumulation of anesthetic vapor indoors (Henderson, 1930). Several studies in the 1930s talked about removing anesthetic gases and odors (Tovell, Ralph M.; Friend, 1942; Yaglou

et al., 1930). A study by Crane (1963) showed that till the early 1960s, the healthcare facilities in the US had operable windows to in natural ventilation (Crane, 1963). As filters became more commercially available, mechanical ventilation started prevailing with filtration systems installed (English, 2016). A device called an isolator was developed in 1967 for patients needing additional protection from exogenous infection (Holý & Matoušková, 2012).

A controlled air distribution pattern, which is a crucial goal for cleanroom ventilation, can be controlled by room design, design of the ventilation system, and by optimizing the locations of supply and exhaust grilles. The airflow in cleanrooms is broadly divided into unidirectional (where air flows from the supply to the exhaust in streamlines), and turbulent (where a non-perfect mixing of airflow exists). The most popular air distribution systems used in cleanrooms are laminar flow, to prevent particle settling, and ceiling diffuser systems, to sweep particles on surfaces (Sandle, 2011; Sooter, 1964). Charnley et al. (1969) showed that laminar flow operating rooms reduced the infection rate from 8.9% to 1.3% (Charnley & Eftekhar, 1969). A study of different ventilation systems used for bone marrow transplant patients showed that a laminar airflow system controlled the most contamination particles (Kundsin et al., 1979). W J Whitfield and his colleague (1981) reviewed the evolution of airflow systems in cleanrooms from 1959 to 1973. In 1959, with no means of decontamination in the room, a partial solution was achieved by unidirectional airflow. Contemporary studies of this decade concluded that with unidirectional airflow, the mixing of contaminants was reduced, and the unidirectional airflow was able to expunge the contamination with the airstream. By 1961, an operational unidirectional airflow room was in place, and by 1962, the installation of clean benches and hoods were present. In 1963, cleanroom standards were developed, and laminar crossflow rooms were more common. By 1967, the usage of laminar flow rooms for different applications other than in industrial cleanrooms was increased (Whitfield & Whitfield, 1981). William Fung (2002) reviewed various international Cleanroom Standards and Guidelines for operating suite design and concluded that FS 209 D Class 100 (ISO Class 5) was

achieved when the air was supplied from the ceiling to obtain unidirectional laminar vertical downflow (Fung, 2002). To provide uniform airflow patterns and reduce the risk of re-entrainment, Wang et al. (2007) suggested installing multiple air diffusers in the room (H. Wang et al., 2007). Wan et al. used experiments and simulations to show that a unidirectional downward flow ventilation design is recommended for the most effective removal of particles (Wan et al., 2007). Eslami and colleagues (2016) tested many different design configurations of supply and exhaust inlets. It was suggested that the supply inlets should be placed vertically along with the ceiling by the short wall, and the exhaust inlets should be placed symmetrically along the long walls (Eslami et al., 2016). When summarizing their findings on the flow path of cough aerosols, Thatiparti et al. (2017) suggested placing the exhaust close to the contamination source and the supply vent farther from the source. With this design, clean air flows from uncontaminated to contaminated parts and is then exhausted (Sharan Thatiparti et al., 2017). Khankari (2017) demonstrated that as strong flows from mini environments may expose the workers to a higher risk, the location of air supply in the cleanroom was best when directly above the operator's head on the ceiling, as opposed to behind the operator or on the wall to adequately remove the particles (Khankari, 2017). In 2019, Vutla and colleagues compared the airflow from two different ventilation configurations, side vents and floor tile vents. Their study concluded that side vents cause some flow stagnation as well as nonuniform velocity distribution. The authors also provided the idea that a cleanroom's design and layout can affect airflow. If the airflow is not optimal, particles could travel around the room (Vutla et al., 2019).

The questions of the required airflow rate and directions to minimize the particle concentration remained debated. Airflow control through air supply velocity and quantity measured using Air Change per Hour. In contrast, the airflow direction is controlled using pressure differentials. In the healthcare facilities, the early studies showed a lot of debates in determining the appropriate quantity of air for proper ventilation. Watt (1936) claimed that 3 ACH offers suitable ventilation

(Watt, 1933). A research team led by Dr. Robertson (1940) observed that besides the thermal comfort and RH, controlling the level of contamination and preventing airborne pathogens from spreading indoors had remained a challenge in healthcare facilities. Airborne pathogens can travel into an operating room, or the source may be located right inside the room (Robertson, 1940). During the late 1960s, the spaces with isolators used 20 ACH for patient protection, which later developed hospital cleanrooms for hematopoietic stem cell patients (Holý & Matoušková, 2012). A 1963 study by Gaulin claimed that 12 ACH was required to maintain contamination level to an acceptable level (GAULIN, 1963), whereas Greenburg suggested a range of 18-30 ACH depending on the goal of ventilation, namely, asepsis, odor, and the level of contamination in operating rooms (Greenberg, 1963). An experimental study proposed a laminar flow ventilation system for operating rooms and suggested 10-20 ACH to remove the airborne contamination (Fox, 1969). Manjo (1977) conducted a literature review to suggest that 25 ACH was sufficient for operating room sterility (Manzo, 1977). Bringmann et al. (1985) suggested that 300-600 ACH was required for higher classes of clean spaces after reviewing standards for semiconductor manufacturing cleanrooms (Bringmann & Meuter, 1985). Chaddock (1986) referenced the Hill-Burton Act and suggested that 5 to 15 ACH is required if only outdoor air is supplied. However, it was stated that the air change rate should be increased to 25 air changes per hour if a mixture of indoor and outdoor air is used. The ventilation rate of 25 ACH must contain 5 ACH of fresh outside air and 20 ACH of recirculated indoor air. Chaddock emphasized that ASHRAE 62 required only 1.2 ACH based on an estimated occupancy of 20 people per 1000 square ft (Chaddock, 1986). Bugaj and Przydrozny (1986) suggested that for a supply grille width 1.9 m and height 0.8 m, lower edge at 1.5 m above floor and exhaust through floor level ports, supply air velocity and air change rate should be equal to 0.45 m/s and 20 ACH, respectively. For supply grille width of 1.9 m and height of 1.1 m, lower edge at 1.2 m above the floor level and exhaust same as before, satisfactory supply velocity should be 0.35 m/s with the corresponding ACH of 21.5 (Bugaj & Przydrozny, 1986). In Sadjadi and Liu's (1991) experimental tests, decreasing average velocity

from 46 cm /s to 41cm/s offered a 3% decrease in air velocity non-uniformity, reducing the probability of contaminant spread through air mixing (Sadjadi & Liu, 1991). Maxwell et al. (1994) conducted a study on optimizing cleanroom air velocity that found that supply airspeed close to 0.3 m/s can control particle contamination and airflow. This study tested many different configurations, so it was also recommended that airflow velocities be tested for all arrangements because of varying contamination source locations (Maxwell et al., 1994). Campbell (1996) recommended 4 to 5 air changes per minute (240 to 300 ACH) to mitigate the risk of gas leaks in semiconductor cleanrooms (Campbell, 1996). Tacutu et al. stated that 2-4 m/s in secondary branches and 5-8 m/s in main branches were standard supply velocities in hospital operating rooms where main supplies are above the operating zone and branches located outwards (Tacutu et al., 2016). Using simulations in hospital operating rooms, Rui et al. (2008) found that 0.25 m/s air supply velocity controls particles' spread (Rui et al., 2008). Yang et al. (2015) numerically simulated a unidirectional protection isolation room to determine the recommended supply airflow rate to achieve ISO – 5 cleanliness for standing, sitting or lying positions of a manikin. They suggested that a minimum supply velocity of 0.25 m/s can prove to be appropriate to control particles and achieve ISO 5 level cleanliness for standing and sitting body. For a lying body, to maintain cleanliness, the supply velocity had to be equal to or greater than 0.2 m/s to achieve ISO 5 level cleanliness. Hence, the authors suggest supplying air at 0.25 m/s during the day and 0.2 m/s during the night (C. Yang et al., 2015). Hakim and colleagues (2018) referenced ASHRAE Cleanroom standards to conclude that 15-20 ACH was required in operating rooms (Hakim et al., 2018). The review of existing literature by Kang et al. (2017) suggested that the airflow pattern in an operating cleanroom is significant in controlling pollutants. They observed the optimization of a unidirectional clean air conditioning system using three three-stage fans, which increased the indoor airflow and in turn, the ventilation coefficient, which aided in decreasing pollutant concentration (Kang et al., 2017). In a simulation study by Alhamid et al. (2018) in an operating room, higher velocity in the inlet air HEPA filter resulted in turbulent air movement, which

dispersed the contaminants throughout the operating room. Increasing the size of ducts and the HEPA filters, which slowed down the inlet air velocity, was recommended to achieve laminar flow and, as a result, the desired contaminant flow (Alhamid et al., 2018). In 2019, Loomans and colleagues investigated optimization in cleanroom ventilation. Their findings suggested that air change rates be lowered using demand-controlled filtration or finetuning, offering a minimum of 6 ACH (Loomans et al., 2019).

The airflow direction is controlled using pressurization – a ventilated space is kept at higher pressure with respect to adjacent chambers, creating a pressure gradient that facilitates directional airflow. Positive pressurization allows external sources of contaminants to be controlled (Y.Venkata Bharath, 2013) for sterile environments other than isolation rooms, where negative pressure is required to prevent the outflow of pollutants. Chien et al. (2009) demonstrated the ease of smoke exhaust when inside pressure was higher (Chien, 2009). Karimipناه (1998) used the pressure differential to describe airflow in the room and suggested that the use of pressure differential to predict airflow properties such as turbulence, deflection, and impingement (Karimipناه, 1998). Campbell (1996) recommended maintaining a -0.1 water gauge pipe pressure to be preemptive against gas leaks in cleanrooms (Campbell, 1996). Lakshmana Prabhu et al. (2016) discussed good manufacturing practices and provided the range of 0.67 to 2.7 KPa of positive pressure in pharmaceutical manufacturing rooms, depending on the cleanliness class (Lakshmana Prabhu et al., 2016). Maintaining such stringent requirements has its toll in terms of energy consumption. Clean spaces consume almost 30-65% of the total energy consumed by high-tech fabrication plants (Shan & Wang, 2017), which is 30-50 times more energy than the average commercial space in the U.S. (Kircher et al., 2010). These high energy demands make cleanroom operations very expensive - and a Class 10 environment typically costs around \$1 million per year to operate (L. Yang & Eng Gan, 2007).

The preceding discussion shows that there is no set base to determine ventilation requirements in clean environments. Instead, the literature review provides an overview that optimizing the ventilation system for airborne contamination control requires careful study of the space design and its intended use. It is to be noted that there is a lack of pertinent research that focuses on applications in sterile healthcare applications in the context of airborne contamination.

Contaminant Concentration Measurements and Suggestions for Removal

The ventilation requirements to achieve a prescribed level of cleanliness in cleanrooms were based on examining whether airborne particles' predefined concentration was exceeded. The previous section was inclined to establish proper air supply and exhaust criteria. In this section, the studies that quantified the pathogen concentration in sterile environments are discussed and examined to review the quantification indices, emphasizing the methods used to formulate the index. Besides establishing strategies to measure the concentration, mechanisms to reduce airborne particle pollution and manage unpredictable dispersion are also discussed. The idea of ventilation-driven pollutant removal is that the airflow should carry the contaminants towards the exit where the pollutants were assumed to be transported by convective transport, which is the transport of passive particles through air streamlines (Bengt Ljungqvist & Reinmuller, 1996). The transient behavior of turbulence was demonstrated by employing a numerical simulation method (Suesada et al., 2002) and the solution of the diffusion equation in a well-defined flow field considering constant diffusion coefficient and continuous point source, provided the contamination concentration model for both laminar and turbulent flow cleanrooms (B Ljungqvist, 1979). The results demonstrated that the contaminant dispersion from the source was uniform for the laminar flow cleanroom. In the presence of isotropic turbulent vortex, the concentration was accumulated in a nonlinear way. Hence, different airflow systems studied by researchers provided several bases of contamination control through ventilation. Table 3 summarizes a set of efficiency

indices defined to capture the role of the ventilation system in removing contaminants from the cleanroom. Methods utilized to arrive at these indices are discussed subsequently.

Table 3: Indices used in literature

Indices	Definition/Explanation
Clean Air Delivery Rate (CADR)	$CADR = V(k_e - k_n - k_c)$ Clean air delivery rate (CADR) in $\frac{m^3}{hr}$ (ft ³ /hr); V is the volume of the chamber in m^3 (ft ³); k_e is the total decay rate in h^{-1} , including both ventilation and cleaner; k_n is the natural decay rate, including only ventilation in h^{-1} ; k_c is the decay rate of the pollutant concentration, reflecting the loss of pollutants due to deposition or adsorption in h^{-1} (Ciuzas et al., 2016).
Mean age of air	The average time it takes for the inlet air to reach any point of the room. Calculated using the tracer decay method. $\tau = \frac{1}{C_{a0}} \int_{t_0}^{\infty} C_a(t) dt$. Uniform concentration at the time t_0 is C_{a0} , the tracer C_{a0} is decaying replacing the supply air. τ is the time to clean any point in the room (O. Rouaud & Havet, 2005).
SVE 3	Index carried out from Fourier series low-order-components for 3D concentration distribution, agreeing to normalized age of air and normalized pollutant concentration, when a uniform source of contamination is assumed (Kato, S.; Murakami, 1988; Kato et al., 1992).
Contamination removal effectiveness	$\varepsilon_c = \frac{C_e(t_{\infty})}{C_m(t_{\infty})}$ where, C_e = Contamination concentration at exhaust, C_m = mean concentration in the room and t_{∞} = time required to obtain a stationary concentration (Brouns, C.; Waters, 1991; O. Rouaud & Havet, 2005)
Air Change Rate	$ACH = \frac{3600q_0C_0}{C_mV}$, where q_0 = airflow rate injected at pollutant source, C_0 = contaminant concentration at the source, V is room volume (O. Rouaud & Havet, 2005).
Final efficiency	$FE = \frac{C_0}{C_m} \frac{L}{SR}$, where C_0 – concentration at the outlet, C_m – mean concentration in the room, SR – spreading radius, and L is the characteristic length making this index non-dimensional. SR = the first moment of the contaminant distribution function, calculated as $SR = \left[\frac{\int (X-X_0)^2 C dV}{\int C dV} \right]^{0.5}$, where X_0 is the mass center of the concentration distribution function and is defined by $X_0 = \frac{\int X C dV}{\int C dV}$ (Saidi et al., 2011).
Efficiency Factor	The ratio of particle concentration in return air and average particle concentration in the room (L. Zhou et al., 2017).

In 1979, Kundsins et al. measured microorganisms in a Laminar Air Flow Room (LAFR) with a ventilation rate of 240-360 ACH, a patient room where only recirculated air was provided, and an ICU room with minimal airflow of 34-43 ACH, with a single patient as the occupant in all these rooms. It was found that LAFR had the least fallout of viable particles resulting from the filtration used, and the patient room, which had recirculated air supply without filtration, had the most. These results indicated a laminar (unidirectional) flow of filtered air to influence particle reduction (Kundsins et al., 1979).

While two-dimensional simulation studies were cited to be insufficient to obtain meaningful insight, Kuehn and colleagues recommended three-dimensional models to understand airflow and contaminant concentration relations (T. H. Kuehn et al., 1992). The accuracy of cleanroom airflow simulation was higher using RNG $k-\epsilon$ than standard $k-\epsilon$, especially when turbulence was present (Olivier Rouaud & Havet, 2002). In their simulation study, E. Khalil (2011) used local air age to demonstrate ventilation effectiveness in terms of air distribution and scavenging passive contaminants and showed that local air age depends on supply characteristics and supply. The author compared recommendations in various international cleanroom standards and guidelines for operating suite design and suggested that for cleanrooms with nonlinear ceiling-mounted supply, the inlet velocity requirement was higher to achieve desired cleanliness (Khalil, 2011). In a first-of-its-kind study using numerical simulation, Kato et al. (1992) simulated conventional laminar flow-type cleanrooms for locally balanced supply and exhaust airflow rates. They utilized a method of analyzing ventilation effectiveness using the scale of ventilation efficiency, namely SVE 1-3 (Table 3), proposed by (Kato, S.; Murakami, 1988). It was demonstrated that a locally balanced airflow system removed contaminants more efficiently and allowed less extensive diffusion. Minor changes in exhaust inlets' location did not affect the ventilation when supply and exhaust were locally balanced in each flow unit. A massive imbalance between supply and exhaust due to excessive air supply or excessive air exhaust per flow unit might decrease the

ventilation efficiency (Kato et al., 1992). Numerical simulation of ISO class 5 and class 6 operating rooms to examine the airflow effects on the bacteria deposition patterns demonstrated that even though the depositions were different in two cleanliness classes, under static conditions, for the same ACH, concentrations reduced with improved airflow patterns (Rui et al., 2008). This study simulated different airspeeds and concluded that bacteria concentration would increase if the ACH was increased beyond a specific limit. Rui and colleagues recommended 0.25 m/s as the ideal supply speed. Rouaud et al. (2005) conducted a CFD simulation and compared the findings with previous experimental data to suggest an optimum ventilation rate. The investigators proposed an index 'Contamination Removal Efficiency' (Table 3) and applied it for analysis coupled with 'Air Change Rate' (Table 3) measurements. It was demonstrated that the relation between pathogen concentration and ACH in a cleanroom is nonlinear; hence arbitrarily increasing ACH cannot efficiently remove contaminants. They also claimed that the location of contamination sources needed to be optimized, and when optimized, lowering ACH increased the removal effectiveness. The 'mean age of air' (Table 3) was also increased with lower ACH values when pollution sources were optimized (O. Rouaud & Havet, 2005). Saidi et al. modeled a full-scale cleanroom to measure the effects of source movement on contaminant spread and introduced performance measurement indices called 'final efficiency' and 'spreading radius' (Table 3). It was shown that the pollution source motion and its direction impact the distribution, and the authors recommended shifting the source motion path to the ventilation airflow's dominant direction for improved contaminant distribution and final efficiency. The best overall performance was achieved with the lateral inlet/outlet configuration (Saidi et al., 2011). The studies by Zhou et al. (2017) observed that increasing ACH decreased concentration in a study that compared four-particle concentration models and proposed a time-based model to analyze particle concentration at any time in space inside cleanrooms using the 'efficiency factor' (Table 3). The conclusion from this study showed that particles' concentration is quantifiable using the efficiency factor; as the efficiency factor increases, particle concentration decreases (L. Zhou et al., 2017).

In discussions about factors affecting the intended airflow in cleanrooms, Zhao et al. (2004) demonstrated through a simulation study in a cleanroom that the airflow and the contaminant concentration varied based on occupant level and furniture inside a cleanroom because obstacles significantly influenced airflow. The occupants and furniture also acted as heat sources, creating eddies, reducing airflow, and aiding in accumulating contaminants. This study recommended evaluating cleanroom environments considering human occupants and other furniture, citing their environmental impact (Zhao et al., 2004). To understand the contaminant dispersion in cleanrooms, it is crucial to understand the generation trend depending on cleanrooms' intended use. In 2019, Ogunsola et al. ran experiments in Pharmaceutical and Biomedical cleanrooms. The sampled data showed that the generation of particles is process-specific, and biotechnological cleanrooms generate smaller-sized particles than pharmaceutical cleanrooms (Ogunsola et al., 2019). Numerical modeling of a ventilated industrial room had shown that as the distance between the pollutant source and the measuring location increased, a reduction in particle concentration was achieved (Plesu et al., 2018). It is vital to develop methods that can reduce the pollutants or manage the unpredictable dispersion by implementing a wide range of strategies. In the cleanroom related discussion in the ASHRAE Laboratory Design Guide of 2002, it was recommended that particle-free ambient air might be used as a makeup supply air to cleanrooms if the particles are filtered through roughing filter, pre-filter, and high-efficiency particle arrestance (HEPA) or ultra-low penetration arrestance (ULPA) filter (Dorgan et al., 2002). The cleanrooms' static pressure must be maintained positive to avoid infiltration of air that contains surplus airborne particles. A proper ventilation system is independent of the main HVAC system (Dorgan et al., 2002). A series of studies examined the effects of different ventilation schemes concerning contamination reduction and control in cleanrooms. Apart from HVAC systems, Joyce and the team reviewed past works and discussed the importance and selection of proper equipment to reduce gas phase contaminants (Joyce & Iliria, 1998). In contrast, Vlasenko et al.

(1998) discussed cleanroom garments with filtration to remove particles and contain moisture levels (Vlasenko et al., 1998).

Two novel ventilation ideas – upward displacement ventilation and exponential ultra-clean laminar airflow in an operating room were studied to compare ceiling supply with near-floor exhaust conventional ventilation and horizontal & vertical Laminar Air Flow (LAF) ventilation to examine the particle concentration in those cleanrooms by Friberg and his colleague (Friberg & Friberg, 2005). This study depicted that the turbulent ventilation systems yielded a significant interconnection between air and surface contamination when the turbulent ventilation system was in effect, which was not apparent for the LAF systems (Friberg & Friberg, 2005). Lin et al. (2010) studied the ventilation effectiveness of a proposed new ventilation scheme experimentally in a semiconductor manufacturing cleanroom with a high cooling load. They observed that process equipment possessed a smaller passage for airflow and generated a higher heat load. For conventional ceiling-supply wall-return-type non-unidirectional cleanrooms, there were upward streams of hot air with particles. The authors proposed a novel ventilation system where installing Fan Dry Coil Unit (FDCU) above the process tools that generated the same ACH as conventional wall return type ventilation consumes less power. It was evident from this study that the proposed FDCU system could remove 20-70% more sub-micron particles compared to the conventional cleanroom (T. Lin, Hu, et al., 2010). As the ceiling supply–wall return non-unidirectional industrial cleanroom airflow gets affected by the layout of equipment in the cleanroom, Lin et al. (2010) proposed a ceiling supply, ceiling return with an FDCU system to study the effectiveness of this system in removing 0.1-micron particles. The integration of the proposed air-dry coil unit enhanced the elimination of 0.1-micron particles by 50%. This paper also demonstrated the particle removal rate significantly depends on the air exchange rate (T. Lin, Tung, et al., 2010). Suwa et al. (2011) numerically examined the possibility of optimizing ventilation in semiconductor manufacturing cleanrooms with Front Opening Unified Pod (FOUP) systems. The authors

demonstrated, using the 'SVE-3' index (Table 3) and an SVE 3 value of 0.5 for unidirectional cleanroom as a baseline, that less ventilation was characterized by a higher mean age of air and increasing SVE 3. They also demonstrated that filter layout might have influenced the distribution of SVE3 – spread type filter with adjusted diffusion rate was able to enhance cleanliness even with a 40% lower filter coverage area, as SVE3 increased. It was also shown that a controlled increase in horizontal laminar flow contributed to contaminant decrease (Suwa et al., 2011). For chilled ceiling displacement ventilation type cleanrooms, Kanaan et al. (2014) developed a CFD model capable of predicting airborne bacteria dispersion and suggested utilizing upper-room ultraviolet germicidal irradiation, resulting in improved energy efficiency and acceptable air quality (Kanaan et al., 2014).

In other attempts to reduce contaminants from cleanrooms, Sadrizadeh and colleagues recommended using mobile laminar airflow units in sensitive operating rooms to reduce microbial concentration when sampling shows unacceptable concentration (Sadrizadeh & Holmberg, 2015). Ciuzas et al. (2016) tested ventilation efficiency as measured by the capability to remove aerosol and VOC particles for air cleaners combined with ventilation systems (Ciuzas et al., 2016). They considered the Clean Air Delivery Rate (CADR) as the measurement index, calculated using the method described in ANSI standard AC-1-2006 (ANSI, 2006). The cleaners could remove 97% of aerosol particles sized from 0.1 to 1.2 microns within 30 min when the generation source is inside the room. For VOCs, the cleaners could remove between a range of 21.4 to 45.7 (Ciuzas et al., 2016). To avoid manufactured semiconductors getting contaminated, the necessity of minute cleanliness resulted in the recommendation of using laminar flow workstations featuring self-contained units for cleanrooms (Dorgan et al., 2002).

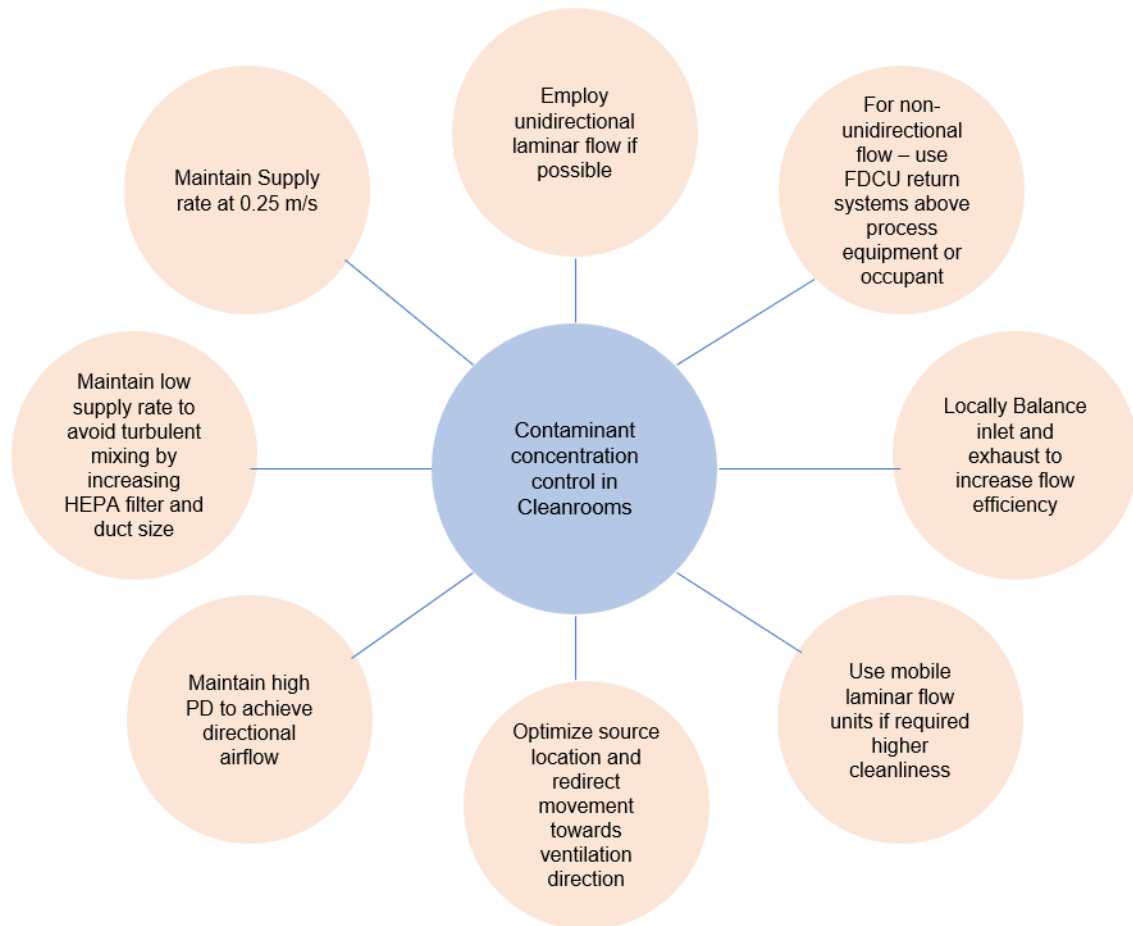


Figure 2: Best practices to control contaminants in cleanrooms

An experimental study conducted by Tengfang Xu (2007) characterized the operation of mini environments used to produce cleaner space in a semiconductor manufacturing cleanroom. The results showed that the average airspeed of 0.37 m/s inside open-loop mini environments is higher (range of 0.27 - 0.50 m/s) than the cleanroom airspeed, averaging at 0.22 m/s. It was also established a lower differential pressure between the mini-environment and the cleanroom (ranging from 0.025 to 0.175 Pa), which WAS lower than the recommended pressure differential (2.5 to 12.5 Pa) between a cleanroom and outside, but the desired cleanliness was still achieved inside the mini-environment (Xu, 2007). A numerical simulation study, using mean air-age and effective flow rate as measurement indices, studied the cleanliness level of a mini environment and illustrated that cleanliness and contaminant concentration were calculated using airflow

characteristics could qualitatively assess the performance of an environment. In contrast, it was possible to use mean air-age and effective flow rates to estimate particle concentration quantitatively in a mini-environment. The authors recommended modifying the inlet and exhaust to increase the effective flow rate reduces contamination concentration through enhanced air parallelization (Noh et al., 2008). The summary of these contaminant reduction practices, suggested by the authors, is presented in Figure 2.

The review in this section provides essential insights into the practices that can characterize airborne pollutant diffusion and its mitigation. This discussion has also brought multiple facets of studies to examine ventilation systems. For example, the flexibility of numerical simulation can be applied to a wide array of ventilation systems and space functions, the ability to conduct scaled experiments to supplement and validate numerical studies, and the possibility of assessing and employing findings in different space functions. Still, these reviews have illustrated that most of these studies did not look at the migration patterns; instead, these were mainly focused on concentration, revealing little insights about the flow characteristics that carry those contaminants. Moreover, there was inadequate focus on the external interactions with the ventilated flow. Hence, it is important to pin down the external factors obstructing the undisturbed flow and distinguish recognizable patterns to scrutinize the contingent conditions for pattern matching.

External Perturbations on Indoor Airflow:

The ventilation systems are designed to direct the supplied air towards the exhaust, sweeping through the enclosed environment, carrying the pollutants with the stream towards the outlets. The balance between the supply and exhaust air determines the pressure differential. The directional airflow, driven by the pressure differential, results in a steady-state flow. When these flow fields interact with the external moving objects, the steady-state condition breaks down, and turbulent vortices are generated. Door opening and human movements are the two most common perturbations that interact with indoor flow fields in any indoor environment. In addition to being

the most common interactions with the steady-state environments, the concepts of the effects of human walking and door movement can be expanded to other occupant-induced movements. These interactions result in the generation of secondary flow fields that alter the normal course of airstreams, aiding in the unplanned diffusion of contamination. That's why it is essential to understand the flow characteristics and affecting factors of the airflow (Hathway et al., 2015; Hu et al., 1996). A number of studies that date back almost 40 years have conducted research to identify occupant interactions such as door movement and individual walks as potent sources of pollutant dispersal (Beggs et al., 2008; Eames et al., 2009; Gustafson et al., 1982; Josephson & Gombert, 1988; Li et al., 2007). Leclair et al. (1980) studied particle transmission related to indoor pedestrian traffic (Leclair et al., 1980). Shih et al. (2007) described the distribution of velocity and pressure fields under the aerodynamic effects of a moving person and a door opening in an isolation room using mathematical simulation (Shih et al., 2007). Hang et al. (2015) corroborated the findings of airborne disease transmission through experimental studies (Hang et al., 2015). His results described the sweeping effects of door motion that aided in volumetric exchange on either side of the door, even in pressure differential – controlling the ventilated airflow. Various scientists have studied moving objects induced flow fields in several settings (Bjorn, E.; Mattsson, M.; Sandberg, M.; Nielson, 1997; Mattsson, M.; Sandberg, 1996; Nielsen, 1999). The present works of literature that have studied the effects of door operation and human walks on the flow fields are discussed in the following two sections.

Door Opening

The principal method of maximizing airborne pollutants' continuous removal is directional airflow by differential pressure (E. S. Mousavi & Grosskopf, 2016). Still, it was shown that door opening has adverse impacts on pressurized spaces as it disrupts the isolation condition and can reverse the differential pressure (Mousavi & Grosskopf, 2016a; Tung, Shih, & Hu, 2009). A study by Gustavsson (2010) revealed the creation of vortices due to door opening (Gustavsson N., 2010a).

Frequent door openings were related to the interruption, potentially reversing differential pressure leading to an increased contamination rate (E. S. Mousavi & Grosskopf, 2016). Mousavi et al. (2016) had shown that operating the isolation room door could transport 5% of the isolation chamber air to a cleaner environment. This numerical simulation study also showed that the speed of door operation is inversely proportional to exchange volume across the opening (E. S. Mousavi & Grosskopf, 2016). Existing research suggests the frequency of door opening during a surgical intervention, depending on the type of procedure (Lynch et al., 2009; E. S. Mousavi et al., 2018), can range from 37 to 40 (Adams et al., 2011), peaking during pre-incision phase (Lynch et al., 2009) for obtaining supplies, paperwork, shift change, and communication (Lynch et al., 2009). Birgand et al. (2019) studied 34 orthopedic and 25 cardiac procedures to conclude that the median frequency of door opening was 14.8 per hour in orthopedic procedures and 23.4 per hour for cardiac procedures (Birgand et al., 2015). Some studies have concluded door motion to be a plausible mechanism for mass transfer through volumetric air exchange (Ahmed et al., 1993; Balocco, C.; Petrone, G.; Cammarata, 2012; Hitchings, 1994; Kiel & Wilson, 1989; Smith et al., 2013).

Lee and colleagues (2016) measured interzonal volume exchange due to door opening using tracer gas and Computational Fluid Dynamics (CFD) to assert that in isothermal conditions, there is not much difference in air exchange volume due to opening a swing door and a sliding door (Lee et al., 2016). The results of the study by Kalliomaki et al. (2016) indicated a reduced impact of sliding doors on the airflow pattern compared to the swinging door (Kalliomäki et al., 2016). A study in an operating room (OR) demonstrated that the airflow across the door while closing a swing door was different from opening the door, indicating a difference in flow pattern between the two types of door movements (B. Zhou et al., 2018b). The generation of vortices at the door tip in swinging motion and propagation of those vortices through the flow field in the room was indicated by Eames et al. (2009) in their experiment involving measurements of dye

concentrations in a mock-up room (Eames et al., 2009). This study's findings also showed a significant airflow structure moving along the wall, implying the existence of a separate, near-wall secondary flow field. Mathijssen et al. (2016) showed that opening mixing ventilation OR door can increase the odds of microbial contamination ≥ 20 CFU/m by 5% (Mathijssen et al., 2016). For a laminar flow OR, door opening was associated with the increased CFU count outside of the laminar flow zone (Perez et al., 2018; Smith et al., 2013). In an experimental study in office rooms and laboratories, it was found that with a more extended period of keeping the door ajar, the swept volume is close to being equal to that of exchange volume (Hathway et al., 2015). The incoming traffic movement to a chamber followed by a door opening has a higher impact on the door movement generated flow field, as demonstrated through an experimental study by Villafruela et al. (2016) (Villafruela et al., 2016). Lin et al. (2007) demonstrated that the opening of doors affects the pressurization scheme. It can also change the thermal boundary condition of indoor space, aiding in the generation of lateral airflow movement, specifically found to affect displacement ventilation (Z. Lin et al., 2007). Using 3-dimensional velocity measurements near the door, Papakonstantis and colleagues (2018) demonstrated the movement of flow vectors while opening and closing the door. They explained the advection of the flow vortex along the wall during the opening (Papakonstantis et al., 2018). In a two-dimensional numerical simulation study of a door opening, Bhattacharya et al. (2020) showed that the door opening and closing movement profoundly impacts the velocity profiles and the direction of streamlines (Bhattacharya, Arup; Mousavi, 2020). As demonstrated through that study, the region close to the door tip was associated with the highest velocity magnitude during the door motion. It was also discussed that the flow field recorded a higher speed during the closing motion compared to the opening.

Barring a few, most of the published studies focused on studying door opening to assess volumetric exchange across the door to understand the contaminant transfer. Some of them provided the results combining the effects of the door opening and inbound/outbound traffics.

Despite studying the door movement through different quantitative and simulation approaches (e.g., numerical simulation, tracer gas method, etc.), there is a shortage of work that analyzed the door movement induced flow patterns as a longitudinal study in the spatial context.

Movement of Occupants

By the early 1980s, scientists found shreds of evidence of the interaction between the flow fields and personnel movement. The indoor traffic of occupants moving on foot having an impact on the spread of particles was predicted by (Leclair et al., 1980). Several studies examined the change in flow velocity due to the movements of objects in a variety of settings (Bjorn, E.; Mattsson, M.; Sandberg, M.; Nielson, 1997; Mattsson, M.; Sandberg, 1996; Nielsen, 1999). Most of these earlier studies employed surrogate methods of measurements (e.g., tracer gas method, scaled experiments, etc.). More robust experimental designs, along with the significant reductions in computing time for simulation, were achieved through the advancement of digital technologies. As mentioned earlier, the numerical simulation of an isolation room by Shih et al. (2007) showed the effects and distribution of flow fields under the influence of human movement and door operation (Shih et al., 2007). Poussou et al. (2010) demonstrated the distribution of contaminants in an airliner cabin resulting from the interaction of the human movement generated wakes and the existing flow fields (Poussou et al., 2010). Luo et al. (2018) conducted computational fluid dynamics (CFD) simulations, validated by scaled experiments to show the downward flow of contaminants before getting dispersed horizontally near floor level that follows a moving human body (Luo et al., 2018). The author also pointed out that the rate of dispersion was related to the movement speed. Mazumdar et al. (2010) replicated a hospital inpatient ward through a simulation study and established that the contaminants are moved through the wakes behind moving objects (e.g., people, equipment, etc.) (Mazumdar et al., 2010). Similarly, the numerical simulation study of a laminar airflow orthopedic surgery room by Brohus et al. (2006) established that the flow profiles, both local (in close vicinity of the moving body) and overall (for the whole

room), are severely impacted by movements of the healthcare workers. Periodic movements after near-constant intervals were behind the origin of complex turbulent flow inside the room, reducing the efficiency of the ventilation system (Brohus et al., 2006).

In settings apart from healthcare facilities, there are numerous studies that examined the aerodynamics of airflow patterns and contaminant transport under the influence of indoor movements (Han et al., 2015). The movement of occupants generates wakes that follow the movement, and those wakes disrupt the normal flow properties, leading to contaminant dispersion (Wu & Gao, 2014). Scaled experiments of indoor airflow were conducted using water-filled 3-D models to study the effects of external perturbations, as Rouaud and team (2004) conceived that full-scale experiments were not feasible (O. Rouaud et al., 2004). Cheng and Lin (2016) found the “blockage effect” that restricts the air from flowing without hindrances, as they substituted the human subject by using manikins to investigate how a moving human body interacted under stratum ventilation (Cheng & Lin, 2016). Matsumoto and Ohba (2004) found the movement speed and direction - parallel and perpendicular to the inlet air- to significantly impact the efficiency of ventilation and distribution of temperatures while evaluating the displacement ventilation effectiveness under moving objects (Matsumoto & Ohba, 2004). Choi et al. (2012) examined the dispersal of particles due to occupant movement from a contaminated room to a clean one, connected by a vestibule using large-eddy simulations. Their findings indicated that motion-induced wakes were behind the cross-contamination by particles from one compartment to another (Choi & Edwards, 2012). Han et al. (2015) mathematically modeled the in-flight spread of airborne infectious disease through likelihood analysis, using an Eulerian-Lagrangian approach (Han et al., 2015). The results corroborated previous findings of human movement disturbing air distribution and provided insight that enhanced air mixing was evident that aided the transfer of particles along the movement direction. Tao et al. (2017) suggested that the change in momentum of the airflow that follows walking motion helps distribute the particles. They demonstrated the

lingering effects of walk that continues to influence the flow fields even after movement is ceased (Tao et al., 2017). Saidi et al. (2011) investigated the movements of the contaminant source and demonstrated the relation between the source motion of contaminant spread (Saidi et al., 2011). They suggested controlling the spread by moving the source in the dominant direction of airflow. A realistic CFD simulation of a healthcare worker's movement involving swinging arms and legs by Hang et al. (2014) in an isolation room showed a complex air mixing, that generated wakes up to 6 m long and diminished after 30-60 seconds after the termination of movement (Hang et al., 2014). This discussion provides an holistic overview of the impacts that indoor human movements have on the flow properties of a ventilated space.

A large proportion of the existing studies aimed to scrutinize instantaneous and local flow profiles near the moving bodies. At the same time, there is an evident shortage of experimental results that examine actual human walk. Only a handful of research has captured the sporadic nature of occupant movements, specifically, how the effects change depending on different existing conditions and various walking exercises.

From the review, it was clear that field experiments in ventilated enclosures where the airflow parameters can be altered involving the realistic door and human movements are necessary to obtain valuable insights into the interaction. However, the time commitment to conduct experiments involving a wide range of initial conditions is enormous, in addition to the limited availability of such spaces. A numerical simulation is an essential tool in this context, as initial numerical models can be validated using the data from experiments. Those validated models can be expanded to simulate a large number of probable scenarios. As studies suggested, room geometry plays a pivotal role in the principal flow direction. It is possible to numerically model rooms with varied geometry when the abundance of chambers with different physical designs to conduct experiments is doubtful.

Event-Based Modeling:

Event-based simulations are used widely to optimize combustion engine performance in signal processing and in building energy simulation fields. The studies relevant to building HVAC performance optimization have discussed the mathematical models. The key ideas behind HVAC energy simulation models lie in optimizing Markov systems (X. R. Cao, 2005). Q. Jia (2011) published a technical report to argue that finite stage event-based optimization with discrete state spaces can be assumed as a “partially observable Markov decision process” so that approximate solutions of the Markov decision process can be used (Q.-S. Jia, 2011). These findings were corroborated by (F. Cao & Cao, 2011). Sun et al. (2013) explained the event-based optimization related to energy optimization in HVAC uses in buildings. They proposed a novel method in the Lagrangian relaxation framework to make decisions at specific discrete-time events instead of continuously computing the solutions (B. Sun et al., 2013). The results of this study demonstrated a significant reduction in computational time and energy usage. Sun et al. used the same Lagrangian relaxation framework in a separate paper. They cited the challenges related to time-dependent uncertainties and then augmented the state variables to patch the time-dependent variables with them, making the optimal solution dynamic by defining time-based events (B. Sun et al., 2015). In another similar research, Wu et al. (2016) used event-based methods to optimize multi-room HVAC systems’ energy performance. These authors agree with the reduction in computation time and effort by illustrating a smaller event-space size than state-space. The approximate solutions focused on local events resulted in better energy-saving performance than traditional threshold-based controls. Jia et al. (2018) used similar methods to demonstrate the event-based approach as a tradeoff between computational efficiency and control accuracy (Q. S. Jia et al., 2018). Several other studies have utilized these methodologies to find optimized control systems with reduced computational effort (Soyguder & Alli, 2009; Xia et al., 2014). In recent years, modal decomposition techniques of physical flow phenomena have been popular, which are procedures to identify and extract physically important flow characteristics that are

sufficient to describe the flow (Holmes et al., 2012; Taira et al., 2017). Extraction of the important features has been demonstrated to be possible using mathematical modeling, even under external perturbations (Brunton, S. L.; Kutz, 2019; Kutz et al., 2016; Rowley & Dawson, 2017). Hence, it is possible to use flow characteristics to describe and model complex flow phenomena.

These articles brought forward two crucial points – i) the ability to discretize continuous transient phenomena in events and ii) applying approximate solutions to model events in order to employ learning methods to predict outcomes. For this proposed study, optimization is not considered; instead, discrete event-based models are to be prepared for estimating flow properties.

Theoretical Framework:

The theoretical framework to explain this study's problems and support the investigation methods is Driving Force-Pressure-State-Exposure-Effect-Action (DPSEEA). This framework is constructed by connecting the indoor environment, occupant needs, and behavior to conditions supporting health (Hasselaar, 2006). The last segment of this framework's construct is translated into the evaluation of air quality for the proposed research. The derivation of this framework drew concepts from systems theory, communications theory, and environmental risk assessment theory (Hasselaar, 2006). A top-down approach is utilized that determines the effect on health conditions from hazard conditions. The author explained both the indoor space and the occupants as the system, while the connection between the systems is explained as environmental influences, which leads to the system theory and framework of systems control used in business management. When this approach is translated to the problem at hand in this proposal, the steady-state flow conditions are regarded as systems while the human walk and door movements are influences that need understanding. As Hasselaar (2006) pointed out, the evaluation methods are indirect that require indicators, and the indicator selection is an essential design element; the same concept applies to emphasize the identification of factors in evaluating perturbation effects.

The DPSEEA has been developed over many years for health-risk assessment in buildings. The OECD (Organization for Economic Cooperation and Development in Developed countries) contributed the first component: a simple pressure-state-response sequence as a framework for novel methods of environment reporting. The driving force and the effects were added to extend the scope that completed DPSEEA (Figure 3). The driving force (D) is the component representing risk conditions, generating pressure (P) on the environment by means of pollution. Responding to the pressure, the environment's state (S) changes, resulting in a particular concentration of pollutants. The concentration is translated to exposure (E) for the occupants, which is assumed to cause the (health) effects (E) (Hasselaar, 2006). Actions (A) can be taken to eliminate the effects (Corvalán et al., 1999). The dose-effect and condition perceptions are related to thermal comfort, which is not the focus of this study.

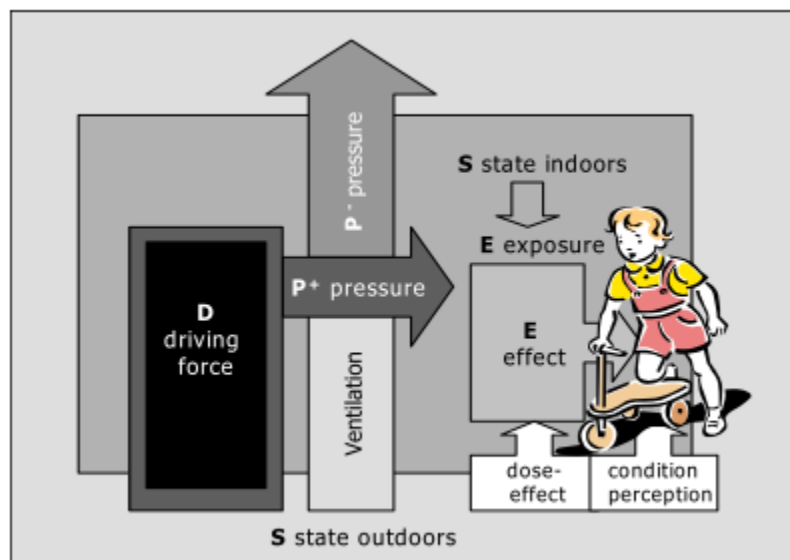


Figure 3: DPSEEA Framework (Hasselaar, 2006)

When this framework is applied to the proposal, the steady-state airflow's driving forces are the ventilation system, and the pressure differential dictates the directional airflow. The interaction of

the flow fields with the moving door and human beings are the components exerting pressure that results in unwanted exposure of the passive contaminants that have adverse impacts on clean spaces. The actions include understanding the flow phenomena and identifying specific factors. These factors are used to model the changes in the flow fields.

Conclusion:

The comprehensive literature review explored the basics of clean spaces, the diffusion of airborne contamination in cleanrooms, and concentration measurements and highlighted the issues related to reducing contamination dispersion. The literature review map (Figure 1) describes the processes employed for this review, containing publications focused on clean and sterile environments. These publications include standards, handbooks, application guides, peer-reviewed journal articles, conference proceedings, and book chapters.

To summarize the studies based on the ventilation of clean spaces, the classification of clean spaces according to the number of particles permissible in the room was discussed, along with the measurement procedures of contamination concentration. The principal methods of airborne contamination control were also discussed, and the prevalent processes (e.g., differential pressure, directional airflow, supply air velocity, optimization of air supply, and exhaust locations) were summarized in Figure 2. The discussions about the most common occupant-induced interventions on steady-state flow fields, namely, human movements and door openings, have revealed the transfer mechanisms by volumetric mass exchange across the door boundary or transport of contaminants in the wakes of a moving person. These mechanisms have been studied in fair detail to examine the quantification of contaminant transport and the relation of contaminant spread with the flow properties in ventilated critical built environments.

The general theme of studies examining the human movement on indoor airflow was found to be concentrating on the analyses of the intricate flow phenomena near the moving body, a large proportion of which was on the subject of thermal buoyancy flows from the heat emitted from the

body. There has been a dearth of experimental studies emulating the walking movement inside a controlled indoor environment and connecting the flow properties like velocity to the dispersion patterns of passive impurities. Similarly, the effects of the door opening on air exchange between the controlled environment chamber have been the principal focus of most of the literature available. Even though some studies, both experimental and numerical simulation, have examined the movement of vortices generated from door operation and their interaction with the steady-state flow, there have not been many manuscripts describing the combining effects of a door opening consequent human movements. Additionally, real-world experimental data related to these disturbances are rare to gain meaningful comprehensions in indoor conditions (like in critical environments) under different ventilation regimes.

Having said that, the reviewed literature has limitations; there is no denying the fact that the ventilation requirement in cleanrooms and operating rooms and the contamination control methods provide crucial insights. The discussion leading to these conclusions revealed that dissecting the flow properties is essential to understanding the dispersion patterns. The discussions revolved around disturbances introduced to the flow fields through interactions with indoor movements on the overview of the factors. Studying the variables that comprise flow properties (e.g., flow velocity) was also identified as crucial to understand, quantify, and model the alterations. A specific set of research summaries was also examined to understand the event-based modeling approach that focuses on events at discrete times. The idea of predicting flow properties using different learning frameworks was identified as another gap that this study aims to contribute.

The exploration of previous publications has also provided a direction for the research method and design. It is established that to study the flow properties in a real-world environment, lab-based experiments are invaluable. The quality of data obtained through experiments has provided researchers with quality data to assess the problem under study. Reduced control over the

selection of spaces and ventilation system's properties, coupled with enormous time commitments to conduct experiments, has hindered widespread use of the method. Instead, researchers have negotiated the problem and obtained comparable results to that of experiments using simulation. Many scientists have used the simulation approach as the opportunity to employ various controls is broad. In addition to that, the recent increase in computing power has reduced the time requirements and increased solution accuracy.

In synopsis, the review of literature has guided to:

- Establish occupant movement and door openings as the two most common external perturbations to study
- Identify velocity as the dominant indicator that describes flow properties
- Provide guidance for possible research methods to answer the questions posed
- Provide a framework to design the research
- Use numerical simulation to complement the experimental approach and generate more data

The answer to the research questions elaborated in Chapter 1: Introduction is expected to inform the researchers to design efficient and optimized HVAC systems in clean spaces that mitigate the contaminant spread from user interaction while paving the direction for sustainability via using less energy.

Chapter 3

Research Design

General Research Strategy:

This study aimed to explore indoor air movements introduced by external disturbances such as human movements and understand how to flow velocities can be used to describe and model the effects of those movements. The research questions derived from the literature review determined that this study was exploratory, which investigated the flow properties, velocity as its indicator, and their correlation and modeled them to estimate anticipated outcomes. Finally, this research described indoor airflow under various ventilation levels and their interactions with moving objects. The research approaches are discussed in this chapter. Figure 4 provides an overview of the broad research design.

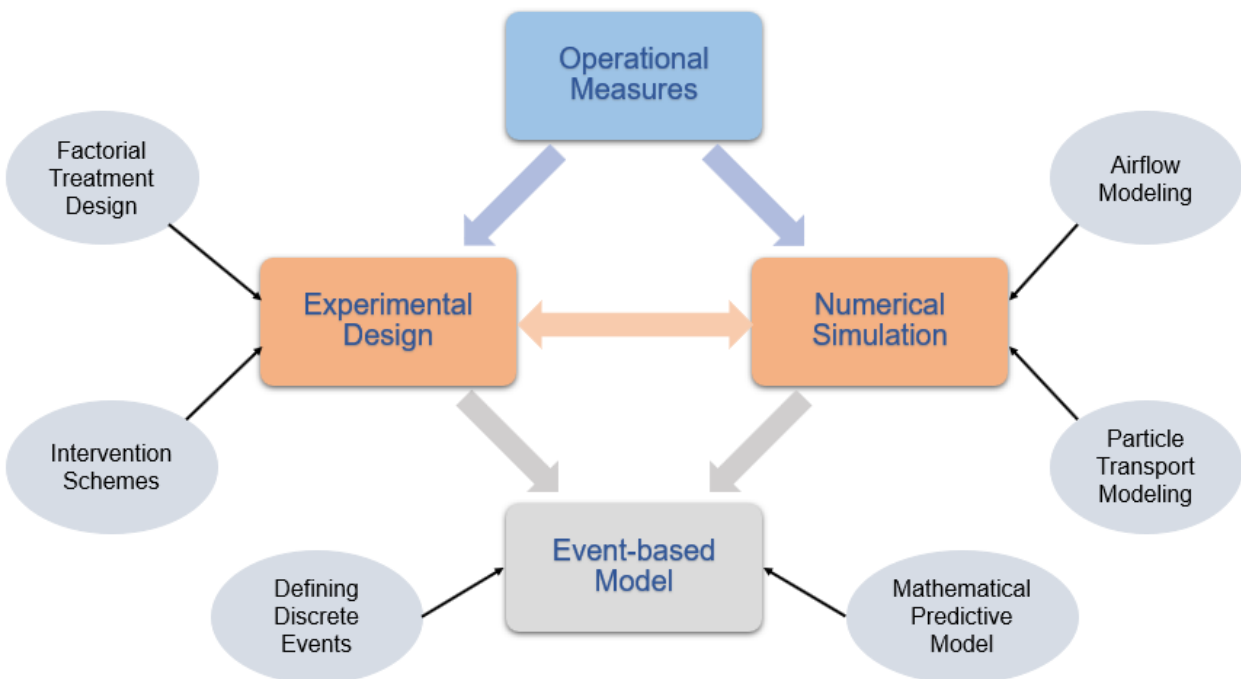


Figure 4: Research Design Map

The specific questions derived at the end of the previous section elucidated this research's purpose. To study the effects of disturbances on airflow, we postulated that the changes can be measured and quantified. These changes were measured by the spatial and temporal trends of flow velocity. This understanding of the flow phenomena is hypothesized to explain the interactions and identify the correlation between the variables for modeling.

Operational Measures:

The ventilation system comprises several factors like room geometry, ventilation system configuration, pressurization scheme, type of external disturbances introduced, frequency of disorders, etc. Considering the vast array of affecting factors, this study's objective was to identify the factors that successfully characterize the airflow when some elements are kept constant. To provide an overview, it is proposed to measure the changes in the velocity of existing steady-state flow fields in a positively pressurized, turbulent flow mixing room (keeping the room and ventilation system type constant) when opening and closing a swing door, followed by pedestrian movements of the occupants (the occupant induced perturbations).

The units of analysis in this study were the indoor airflow fields and their dispersion patterns under specific disturbances. The characteristics, i.e., the variables, of these units of analysis was the flow velocity, which was used to derive other flow attributes such as kinetic energy and turbulence intensity. The systematic relationship between the operational concepts, dimensions, variables, and measures is depicted in Figure 5.

In this relationship, the contaminant concentration spreads relative to the location of sources. Whether the contaminants originated outside or inside the space of interest, their migration pattern depends on it. As explained earlier, the presence of differential pressure and directional airflow govern the flow of passive pathogens. Disruptions are introduced by the movement characteristics of the door and occupants that generate secondary flow regions different from the preexisting initial conditions. The characteristics of a flow region are characterized by the change

in flow velocity introduced by the perturbations. Thus, these variables formed internal relations to break down the contaminant migration pattern.

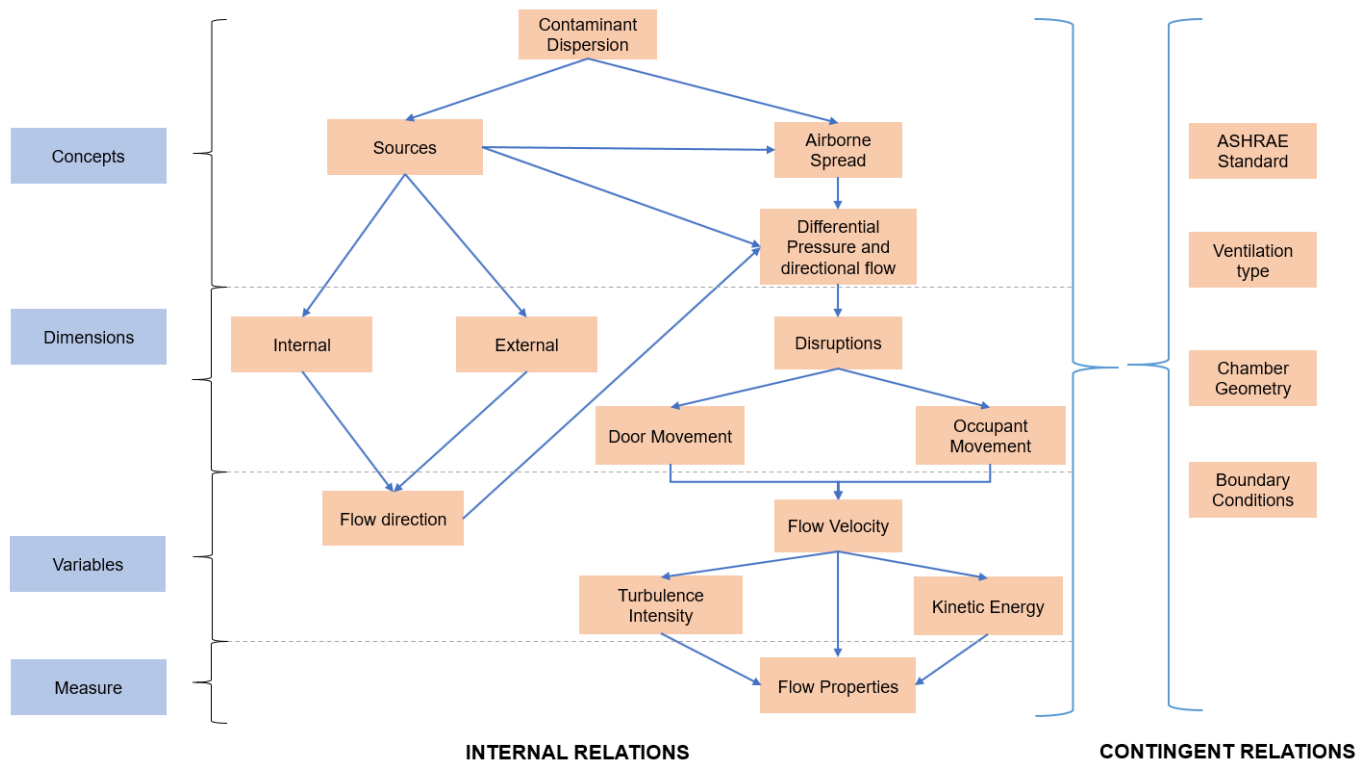


Figure 5: Systematic Relations

On the other hand, the flow system also depends on the design parameters established by design standards (e.g., ASHRAE standards) as well as the system configuration, chamber geometry, and boundary conditions of the flow regime. The airborne contamination control is contingent upon these variables but not necessary to explain in specific cases. The flow characteristics will change if the design considerations are changed, but the standards are often built on rigorous research efforts and do not change frequently. Measuring the flow velocity through experiments and simulations, a discrete event can be described when the relation between the changes in flow velocity due to occupant movement with the initial condition and movement speed is comprehensively established. To extend the event outcomes for estimating flow velocities in a

different chamber using predictive models, the initial condition and the movement speed are to be revised according to the applicable requirements to conduct experiments in that chamber.

The idea of airborne contamination spread is conceptualized by understanding the flow properties, and in turn, flow property is defined by the characteristics that can describe the flow. For this research, velocity had been identified as the measurable flow property. For the event-based modeling part of this study, the goal was to identify the changes in flow characteristics at specific points in space and time resulting from disruptions under different initial conditions and predict the flow characteristics in separate points in time, space, and under different initial conditions. The primary mode of measurement was through conducting experiments.

Let us have a closer look at the concept of flow velocity, described as the distance traveled by an infinitesimal quantity of air in a unit of time. Or mathematically, it can be expressed as, $v = \frac{ds}{dt}$, where v is the velocity, and ds is the distance traveled in time dt . In a cartesian coordinate system, the velocity as a quantity can be divided into three components such that $|v| = \sqrt{v_x^2 + v_y^2 + v_z^2}$, where $|v|$ represents the magnitude of velocity, v_x is the component in the x-direction, v_y is the component in the y-direction, and v_z is the component in the z-direction. The velocity components of airflow and the magnitude were measured using sensors during experiments.

The data obtained for velocity was spatially and temporally correlated in terms of turbulence intensity (TI) and kinetic energy (KE). Both TI and KE can be calculated numerically from the measured velocity. It is not the intention to measure either the TI or the KE through the experiments; instead, these descriptors of flow properties can be used to understand the flow better from the obtained results.

If the chamber space is considered as a congregation of discrete flow regions with equidistant points, turbulent fluctuation of velocity is given as,

$$v'_i = v_i - \bar{v} \quad \text{Equation 1}$$

where v'_i is the turbulent fluctuation at point i , v_i is the velocity at that point and \bar{v} is the mean velocity. From this, the turbulence intensity (I) is defined in Equation 2, which quantifies the ratio of the spatial velocity at a specific point over the mean velocity of the entire field.

$$I = \frac{v'}{\bar{v}} \quad \text{Equation 2}$$

On the other hand, kinetic energy at any specific location is defined in Equation 3.

$$K = \int mv \, dv = \frac{1}{2} mv^2 \quad \text{Equation 3}$$

where m is the mass of an infinitesimal quantity of air that is present at each location, and v is the velocity.

If the mass m is considered to be constant at each point in space, kinetic energy at that location is proportional to the sum of velocity components squared.

$$K \propto v^2 = v_x^2 + v_y^2 + v_z^2 \quad \text{Equation 4}$$

Both these variables, turbulent intensity and kinetic energy, are also temporally correlated. As the velocity value is changed at each time step, these quantities also take unique values at each time step. Thus, as the velocity measurements are obtained at each timestep, these flow properties can also be computed simultaneously. Furthermore, having enough information about flow characteristics to compare different initial conditions and to understand the alterations in the flow behavior is possible in accordance with the changed conditions.

Experiment Design:

The research questions and the systematic relationships described in the operational measures indicated that measurements of a flow velocity as the variable can be done using an experimental design. The experiments aimed to determine and quantify the velocity changes in the existing

flow field under a steady state when occupants introduced perturbations, controlling for factors directly affecting the flow properties (e.g., room design, ventilation system type, etc.). Before the introduction of disruptions, the initial conditions dictated the flow velocity and had significant impacts on the flow. For example, the amount of inlet air being supplied and exhausted determined the net differential pressure, which governed the directional airflow.

Treatment and application:

As the influence of external disturbances on the existing flow properties was the principal focus of the study, different initial conditions (i.e., the existing flow conditions from the ventilation system) of the steady-state flow fields were considered as treatments. Elaborating on this point, let us assume we wanted to estimate the net effect of a person's walk from outside the chamber under investigation to inside, preceded by opening and closing a swing door. The control to employ here was without any presence of HVAC supplied flow, i.e., no inlet or exfiltration of air. Measuring the change in velocities resulting from the person opening and closing the door, entering the room, and walking inside using different velocity measuring instruments enabled us to measure the effects of that series of interruptions. The door's opening motion created turbulent vortices which were carried through the wakes of a walking person, and further turbulence was introduced through the vortices from the closing door motion. Measurement of the distance inside the chamber up to which the vortices will penetrate was also obtained by placing the velocity sensors strategically inside the chamber. Then, in the same room, without altering the locations of the inlet and exhausts, different quantities of air inlet and exhaust were introduced as different levels of treatments, altering the initial conditions. This way, it was ensured that different levels of pressure differentials were governing the directional airflow. The exact sequence of the introduced perturbations (i.e., a person walks from outside the room to inside opening a closing a door) was repeated, measuring the flow velocity under this renewed initial condition. Comparing the measured velocity data between the control case (when HVAC is not working) and treatment

cases (under different levels of supply and exhaust airflow) helped to explain and quantify the differences introduced in the flow field by the specific events of human interaction, under several levels of treatment. These measurements were essential to comprehend the effects of human interaction on the flow fields inside a ventilated critical space.

As the changes in flow patterns under the occupant-induced disturbances were understood from the velocity measurements, the migration patterns of particles were understood from the experimental measurements of contaminant concentration. The steady-state concentration of pollutants inside the room under different treatments and the changes in the concentration due to the introduced perturbations were measured using particle counters. Particles of different sizes were generated inside and outside the experiment facility (i.e., internal and external sources) by aerosolizing an oil-based substance (Bis-2-ethylhexyl sebacate, CAS: 122-62-3, Density @ 25°C = 0.914 g/mL). The concentration of particles of different sizes was measured under different flow regimes, and their migration patterns were deduced following their dispersion by occupant-introduced perturbations. These measurements were to understand the changes in the migration pattern of the pollutants when human interactions are introduced under separate flow regimes.

In a sense, the setting was a factorial experiment design, as the treatments were administered at different levels. The randomization was not a concern here since measurements of the changes were carried out in the control group first before introducing the treatments and then measuring the effects of the treatments subsequently in the same indoor environment. Both control and treatments were applied to the same chamber for a specific test setup. This way, the pretest and post-test measurement samples were equivalent, if not wholly identical, considering minor changes in the chamber characteristics during treatments are being administered.

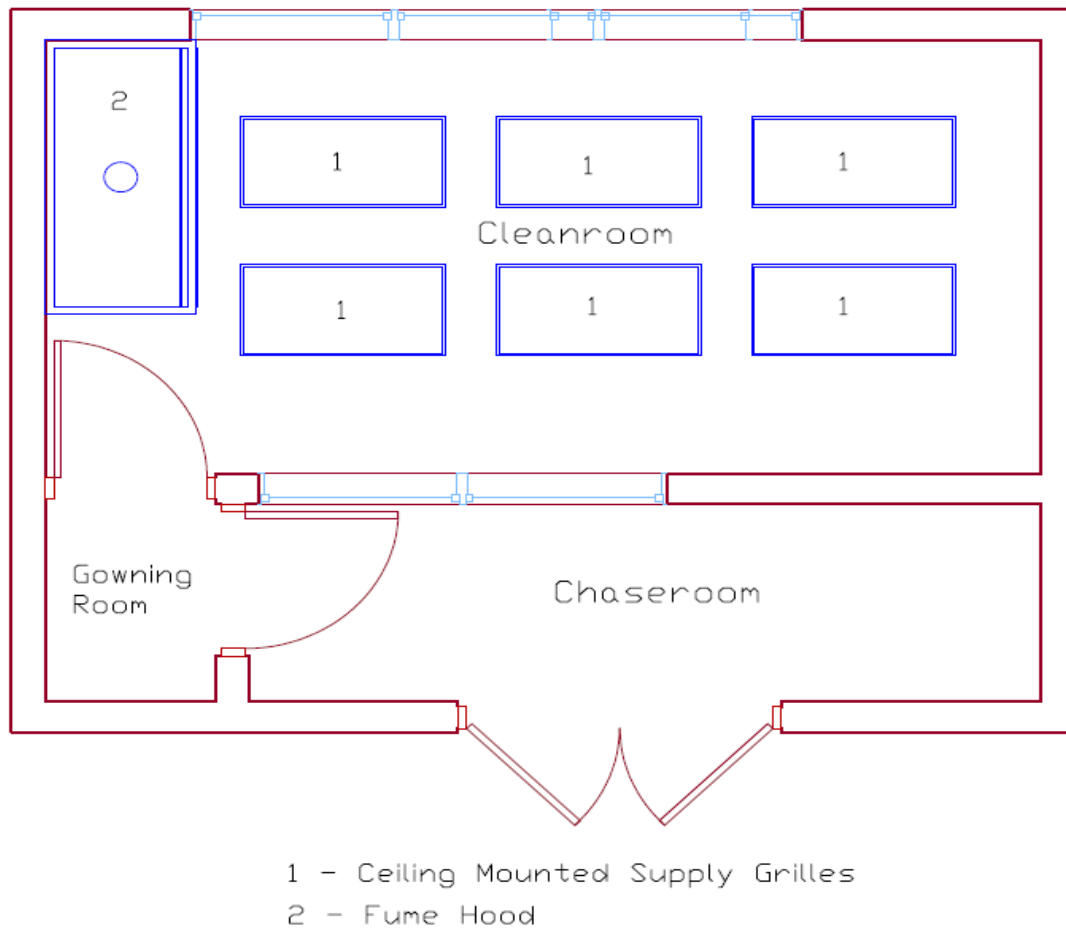


Figure 6: Plan view of Cleanroom at Clemson University

Experiment Facilities:

The experiments were conducted in two different chambers – a cleanroom in Clemson University's Environmental Research Lab and the Controlled Environment Chamber at the Centre for Built Environment at the University of California, Berkeley. The cleanroom at Clemson university is a biosafety cleanroom with a vented fume hood. The dimension of that room is 5.94 m × 2.89 m × 3.05 m (L x W x H), and it is separated from a gowning room of size 1.52 m × 1.12 m × 3.05 m by a single hinged doorway. This door has a 0.30 m × 0.60 m fenestration louver to allow for pressure release when the door is closed. This cleanroom is separated from the rest of the research laboratory by a chaseroom – a framed enclosure space (Figure 6). This cleanroom

provides a unique opportunity to collect data in an actual cleanroom. The controlled environment chamber at UC Berkeley is a research facility with capabilities to have air supply at various flow rates from the wall-mounted grille, from ceiling-mounted diffusers, or from raised floor supply grilles. The chamber was 5.48 m × 5.44 m × 2.5 m, with a door of 1.98 m × 0.98 m at one corner (Figure 7).

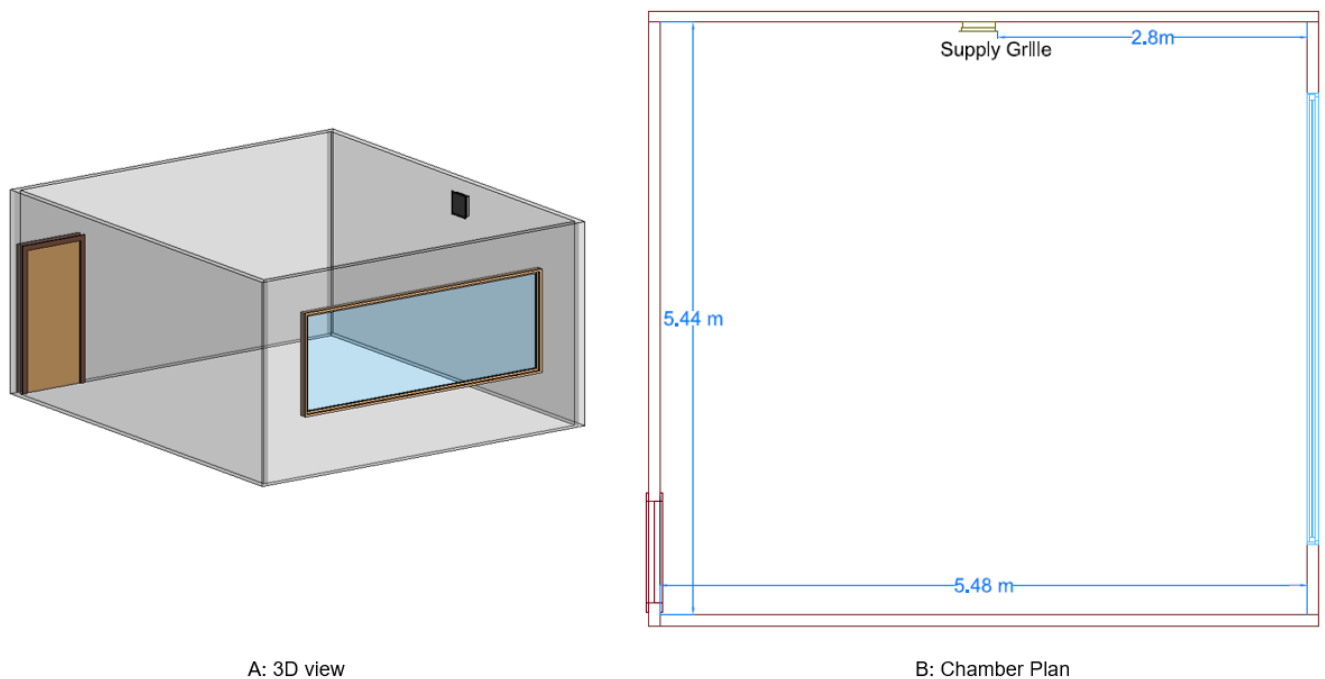


Figure 7: Schematic of Controlled Environment Chamber at UC Berkeley

Both of these spaces had the capabilities to alter the initial conditions as different levels of treatments in terms of flow rate and pressurization schemes. Hence, the controlled environment chamber at CBE, UC Berkeley, was emulated as a critical built environment such as a positively pressurized operating room from the flow perspective, despite not being as clean as a typical OR.

Instruments:

1. Velocity measurement:

- a. Omnidirectional Sensors: The AirDistSys 5000 manufactured by Sensor Electronic, Poland, was used to record the velocity magnitudes. These sensors consisted of a transducer, a converter, and a transmitter. SensoAnemo5100LSF is a transducer with omnidirectional (spherical) sensor with a diameter of 2mm, measurement speed range of 0.05 to 5 m/s, ± 0.02 m/s or $\pm 1.5\%$ of reading accuracy of measurement, directional sensitivity error for $v > 2$ m/s of $\pm 2.5\%$ the actual value. AirDistSys 5000 logs one data point every two seconds. Designed for low-speed measurement in indoor environments, has a wide range of frequency responses and high sensitivity. The transducer measures instantaneous mean airspeed and standard deviation of airspeed. The probes in all the sensors are connected to SensoDACon series 5400 converter, which allows the conversion of a digital signal with Sensoanemo transducer to the analog signal of velocity as output which is recorded in the computer through a wireless connection using SensoBee transmitter and receiver. For more details, please see the operator's manual, available online at http://www.sensor-electronic.pl/pdf/MAN_AirDistSys5000.pdf.
- b. Ultrasound Sensors: The ultrasound sensing system, able to log 4 data points of 3-dimensional air velocity components per second, is developed indigenously at the Center for the Built Environment at the University of California, Berkeley. At the heart of this lightweight and portable sensor, there is a CH-101 ultrasonic transceiver, utilizing new microelectromechanical systems technology for ultrasonic range finding. A tetrahedral arrangement of four such transceivers, minimum required number to capture 3-D flow, was used that provided enhanced measurement redundancy. These transceivers communicate with the outside world through a carrier board—a four-layer printed circuit board. The firmware used to control the microprocessor, which can be optimized for each application at

run-time, also enables shielding errors generated by the wakes from anemometer support struts. The anemometer has a resolution and starting threshold of 0.01 m/s, an absolute airspeed error of 0.05 m/s at a given orientation with minimal filtering, 3.1 ° angle and 0.11 m/s velocity errors over 360 ° azimuthal rotation, and 3.5 ° angle and 0.07 m/s velocity errors over 135 ° vertical declination. For more details, please refer to (Arens et al., 2020; Ghahramani et al., 2019). A schematic of these sensors is in Figure 8.

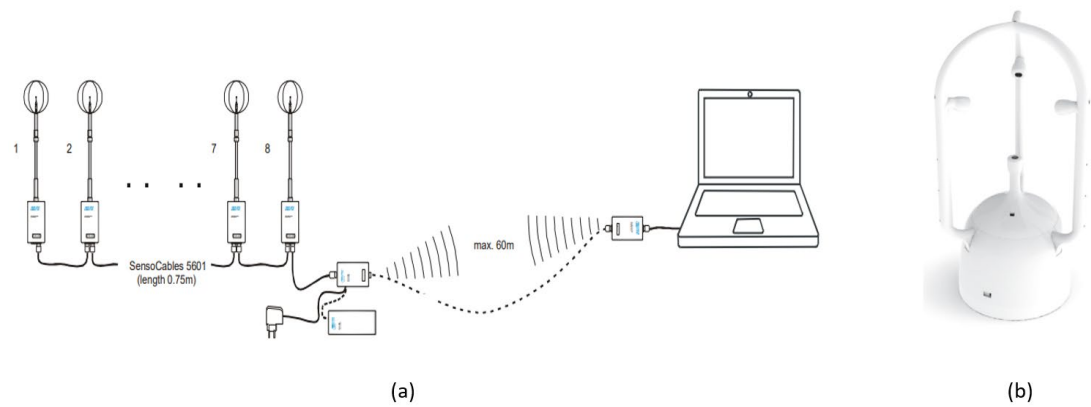


Figure 8: Velocity Measurement Devices: (a) Omnidirectional (b) Ultrasound

2. Flow Measurement: An ALNOR EB-731 (TSI Incorporated, MN, USA) passive capture hood (610 mm x 610 mm) was used to measure the inlet/outlet flow rates. The capture hood is connected to a digital micro-anemometer that records airflow data in one-second intervals. The details of this instrument are available online at https://tsi.com/getmedia/643561c1-4d2a-43b1-a557-88b549a9da80/EBT730-731_Owners_Mnl_6005725_US?ext=.pdf.
3. Particle Concentration Measurement: Extech VPC300 six-channel handheld particle counters (PCs) with isokinetic probes were used to measure the concentrations of particles. The PCs were calibrated by the vendor prior to use and had a 5% coincidence loss at 2×10^6 particles per ft³, per the manufacturer catalog. The PCs sample air at a

rate of 0.1 ft³/min, controlled by an internal pump, and counted the number of particles of different sizes (0.3, 0.5, 1, 2.5, 5, and 10 μm) every six seconds. For more details, please refer to the manual available online at http://www.extech.com/products/resources/VPC300_UM-en.pdf.

4. Pressure differential measurement: The differential pressure between the chamber of interest (where the experiments are carried out) and the outside was measured by a portable pressure monitoring device which logs the pressure differential at 0.5 s intervals. This device has an operating range of -25Pa (-0.1") to +25Pa (+0.1"). For more details, please refer to the manufacturer's website <https://www.abatement.com/ca/ppm3-s.html>.

In this preceding discussion, a general overview of the experiment facilities and measuring instruments is provided. The specific test setups, including the arrangement of sensors for optimized data collection for all the conducted experiments, are discussed in the following chapters that address and discuss the research questions.

Numerical Simulation:

In the context of this study, experiments were useful but had limited applications. Apart from access to a wide range of chambers, experiments are time and cost-intensive. Additionally, the ability to apply treatment levels beyond a small number is also restricted as the facilities are made available to conduct experiments for a restricted duration. Computational Fluid Dynamics is a very efficient and economical simulation method to investigate different aspects of indoor environment design. Acceptable comparisons were reported between CFD simulation results and results obtained from experiments in the literature.

General Mathematical Model:

The space in which the flow field is going to be simulated is modeled as geometry, and then requisite boundary conditions are applied to the geometry in order to define the initial conditions. The fluid flow patterns are determined by solving the continuity equation (Equation 5), the

conservation of momentum (Equation 6), and energy (Equation 7) equations employing proper boundary conditions.

Equation 5

$$\frac{\delta \rho}{\delta t} + \frac{\delta}{\delta x_i} (\rho u_i) = 0$$

where ρ – density of the fluid, u_i – velocity vector component (in x-, y-, and z-direction), t represents time, and x_i – Cartesian coordinate in three-dimensional space.

Equation 6

$$\frac{\delta}{\delta t} (\rho u_i) + \frac{\delta}{\delta x_j} (\rho u_i u_j) = - \frac{\delta p}{\delta x_i} + \frac{\delta}{\delta x_j} \left[\mu \left(\frac{\delta u_i}{\delta x_j} + \frac{\delta u_j}{\delta x_i} \right) \right] + \rho g_i$$

where p – pressure, μ – kinematic viscosity, and g_i – gravitational acceleration acting on the fluid elements in x, y, and z-direction.

Equation 7

$$\frac{\delta}{\delta t} (\rho H) + \frac{\delta}{\delta x_i} (\rho u_i H) = \frac{\delta}{\delta x_i} \left[\frac{K}{c_p} \frac{\delta H}{\delta x_i} \right] + S_H$$

where H – enthalpy, K – thermal conductivity of fluid element, c_p – specific heat and S – a source term. These equations are discussed in further detail by (Loomans, 1998).

The above equations are used to model viscous flows (Sekhar & Willem, 2004). The Reynold Averaged Navier-Stokes method (RANS) is then applied to model turbulent flows, averaging the flow equations over a much larger time scale than the turbulent motion. Out of many turbulence models developed by RANS, the two-equation *RNG* $k - \varepsilon$ model is recommended for airflow in enclosed spaces (BE Launder, 1972; Q. Chen, 1995). The k , and ε in this model denotes the

turbulent kinetic energy and turbulent kinetic energy dissipation rate, calculated at the inlet and outlet using the following equations:

Equation 8

$$k = \frac{3}{2} (u_{avg} I)^2$$

where u_{avg} – mean flow velocity and I – turbulence intensity.

Equation 9

$$\varepsilon = C_{\mu}^{\frac{3}{4}} \left(k^{\frac{3}{2}} I \right)$$

where C_{μ} –is a constant of value 0.09 for indoor airflow. Please refer to (Tung et al., 2009) for elaborate details.

The energy equation (Equation 7) is solved when there is a heat source and temperature gradients are present in the airflow. For the purpose of this study, the temperature was not considered as a variable, and hence, isothermal conditions were assumed. Solving these equations using numerical simulation software ANSYS Fluent also provided another advantage – visualization of the velocity vectors. The package provided powerful graphics and animations that better understand flow patterns, which was not a possibility in experiments.

Chapter 4

Factors Affecting Airflow and Particle Dispersion in a Clean Space Under Occupant Movements¹

To study the influences of occupant introduced perturbations, specifically door opening and indoor walking movements, and how the effects are related to the other airflow governing factors such as particle size, the direction of occupant movements, and pressure differential, a series of experiments were conducted in the cleanroom at Clemson University. The experiments were aimed at characterizing the particle dispersion patterns when the origin of the particles was outside the cleanroom. The opportunity to conduct experiments in an actual cleanroom was during Summer 2018, when the cleanroom went under a major renovation to add a vented fume hood while maintaining positive pressure in the room with an air supply through HEPA filters. After the significant renovation activities and before the room was returned for occupancy, the team conducted several experiments, which provided a short window of 6 days to run the tests. This experimental facility's dimension and geometry details are provided in the 'Experiment Facilities' subsection of the 'Research Design' section in Chapter 3.

Methods:

Test Procedure

Figure 9 shows the 3D geometry of the experiment setup, where two particle counters, the biological safety cabinet, the fume hood inside the cleanroom, and a part of the chase room are visible. The chase room is a framed enclosed space between the gowning room (also known as the anteroom) and the rest of the research laboratory. The gowning room was separated from

¹ The contents of this chapter are reproduced from (Bhattacharya, Metcalf, et al., 2020) with the permission from the co-authors and the publisher.

the chase room by a single hinged door (outer door) and was connected to the cleanroom via another door (inner door).

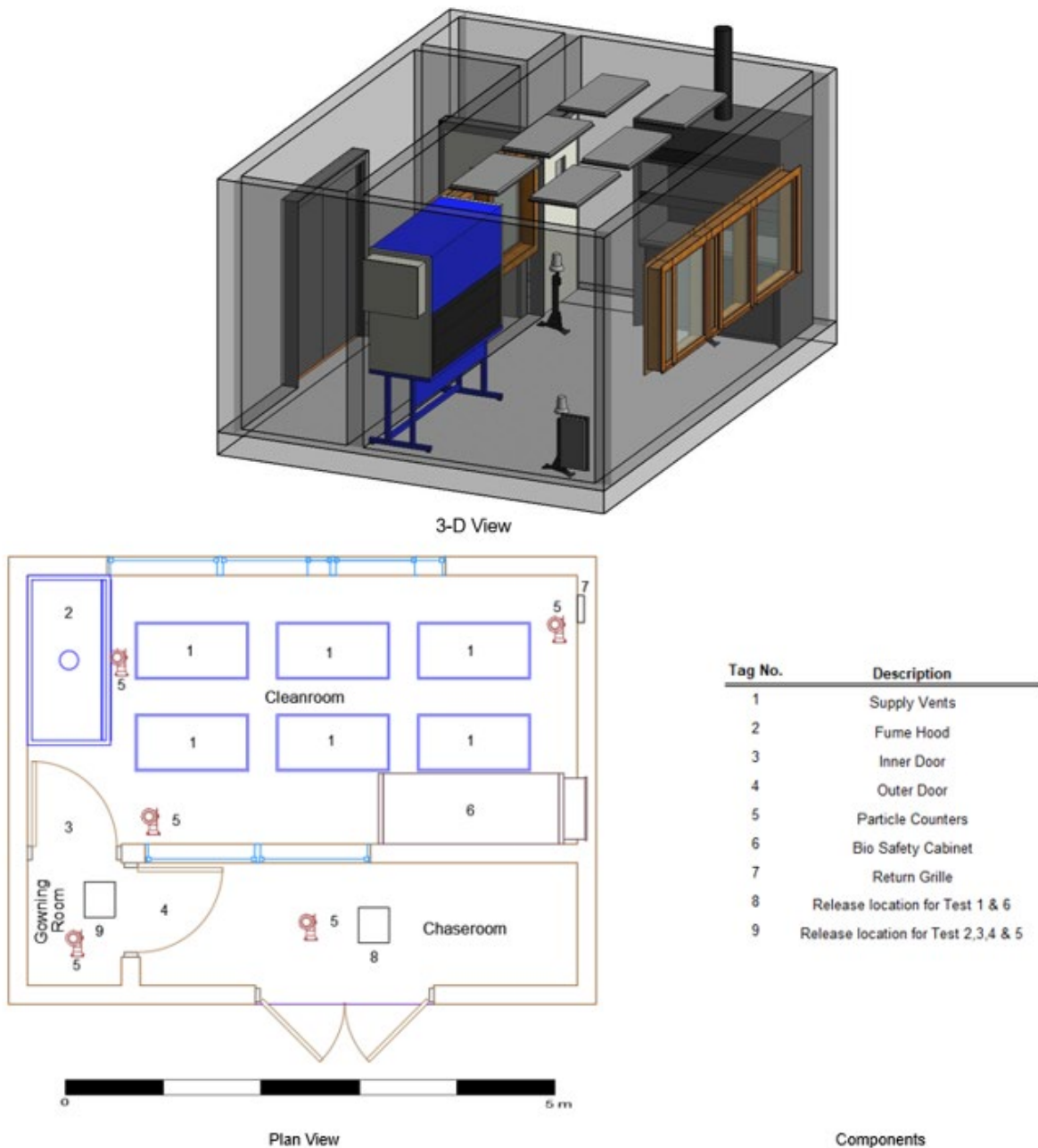


Figure 9: Layout of the cleanroom and experimental setup.

To study the effect of traffic, a person started moving from the chase room, opening the outer door to enter the gowning room and eventually into the cleanroom through the inner door. This process was then reversed, and the person returned to the chase room. Altogether, these activities form one ‘traffic cycle.’ Experimental runs consisted of three consecutive cycles. Prior to the first cycle, background concentrations of particles were measured for one minute. In the second minute, an oil-based substance (Bis-2-ethylhexyl sebacate, CAS: 122-62-3, Density @ 25°C = 0.914 g/mL) was aerosolized in the chase room (tests 1 and 6) or in the gowning room (tests 2, 3, 4, and 5) using a pharmaceutical nebulizer (Rescoe Medical Portable Travel Nebulizer System, model – NEB-PORT). The instrument nebulized particles at a rate of 0.2 ml per minute at an average flow rate of 6 liters per minute and at an average operating pressure of 0.6 bar, per the manufacturer’s specification. The plan view in Figure 9 depicts different compartments, particle release locations, the doors, and the particle counters – which are also labeled in the components table in figure 9.

Table 4: Gravitational Settling Time of Particles with Different Sizes

Particle Size	Gravitational settling time (min.)
0.3 μm	3188.31
0.5 μm	1339.38
1 μm	382.76
2.5 μm	66.99
5 μm	17.29
10 μm	4.39

The gravitational setting times for these particles were predicted using the Stokes’ law (Hinds, 1999), and the settling times for different particle sizes of interest were listed in Table 4. The

results indicate that the settling times of particles, when released 0.74 m above the floor, could be as long as 3188 minutes for small particles (Table 4). Given that the sampling time, from the beginning of background concentration measurement till the end of each traffic cycle, was 5 minutes, it is observed from Table 4 that for all sizes except 10 μm , the generated particles likely remain suspended for the duration of the entire experiment. In addition, the Stokes number for all size particles in this study was less than $\sim 10^{-3}$, indicating that these particles were able to adopt the fluid velocity very quickly and follow the air patterns in the rooms. The length scale used to calculate Stoke's number was the maximum distance a particle could have traveled from the origin at the chase room to particle counter 5 inside the cleanroom. For details procedure of this calculation, please refer to (Hinds, 1999).

The activities from the start of every experiment for the first cycle, their duration and the events based on different activities are tabulated in Table 5. Particle generation lasted until the end of the third cycle. The generation rate was not a fully controlled variable as it was varied by many confounding variables (pump flow rate, leakage, etc.). However, independent particle measurements showed two different generation rates when the pump was operated on high-mode (high-generation) or on low-mode (low-generation). The door opening, closing, and waiting times before moving to the next compartment were kept constant for all experiments. Two people timed the procedure to ensure compliance with the test procedure noted in Table 5. It has been shown that the door opening/holding time is linearly related to the volume of air exchange (Hathway et al., 2015; Hayden et al., 1998; Kalliomäki et al., 2016; Kiel & Wilson, 1989; E. S. Mousavi & Grosskopf, 2016; Tang et al., 2005). Hence, the door opening/closing time was kept constant at 5s.

Experiments were divided into six categories based on the location of release, generation rate, and pressure differential across the inner door. Different experiments, as designated as tests,

along with the particle generation location (chaseroom or gowning room), rate of generation (high or low), and level of differential pressure (high or low), are listed in Table 6. The level of high- and low-pressure differences and the procedure to achieve such pressure differences are explained later.

Table 5: Test Procedure - background, injection, and cycle 1

Start Time (in Min.)	Finish Time (in Min.)	Activity	Events	Traffic
0.00	1.00	Collection of Background Data		
1.00	9.00	Injection of particles (continues until the end of the experiment)		
3:00	3:05	Opening outer door and entry from chase room to gowning room	Event 1	Forward
3:05	3:30	Wait inside the gowning room		
3:30	3:35	Opening of the inner door and entry from gowning room to Cleanroom	Event 2	Forward
3:35	4:00	Wait inside Cleanroom		
4:00	4:05	Opening the inner door and exit from Cleanroom to gowning room	Event 3	Reverse
4:05	4:30	Waiting inside the gowning room		
4:30	4:35	Opening the outer door and exiting from gowning room to chase the room	Event 4	Reverse
4:35	5:00	Wait inside the chase room		

Tests 4 and 5 were conducted under the same conditions (high pressure, high generation rate) to reinforce the findings, and the results for these tests were combined. An OMNI-Guard III differential pressure recorder was used to measure the pressure difference (PD) across the outer door. The pressure recorder had a differential pressure range of +/- 62.5 Pascals with an accuracy

of +/- 1% of reading, per the manufacturer specification. The two inlets with 3/16" OD barbed hose connectors were connected to the hose, and one of the hoses was placed in the cleanroom while the other was placed in the gowning room. Measurements were done before the experiments and once again after the test was finished. The data showed a constant pressure difference of 0.01 inches of water gauge (in. w.g.) (2.5 Pa) from the gowning room to the chase room for all the tests. Across the inner door, a PPM3-S (Abatement Technology) pressure monitoring device recorded pressure differentials every 0.5 seconds throughout the test. This functionality was particularly important to evaluate the changes in pressure difference when the cleanroom door was operated.

Table 6: Experimental Setups

Test	Release point	Generation rate	Differential pressure level
Test 1	Chase Room	Low	Low
Test 2	Gowning Room	Low	Low
Test 3	Gowning Room	Low	High
Test 4	Gowning Room	High	High
Test 5	Gowning Room	High	High
Test 6	Chase Room	High	High

In order to study particle dispersal to the rooms, data were organized with respect to the time of collection and the test procedure. Next, the data were segmented into a series of predefined events. Events were defined as the activity of opening a door, entering (exiting) to (from) one room to another (~5s), and waiting for 25s at the destination (Table 4). Traffic was also divided

into two categories: forward and reverse. The forward traffic is defined as going towards the cleanroom, and the reverse traffic is used as coming back to the chase room from the cleanroom. Given the nature of cleanroom pressurization, the forward traffic was always against the airflow direction.

Measurements

The particle concentrations were measured using the Extech VPC300 six channel handheld particle counters (PCs). The PCs sampled air at a rate of 0.1 ft³/min, controlled by an internal pump, and counted the number of particles of different sizes every six seconds (with a standard deviation of 0.9) during the experiments. Using the software provided with the VPC300 particle counters, tabular results for every particle counter with timestamps for every data point were generated.

The cleanroom had a major air supply line installed in the ceiling. Air left the room through three outlets, one return grille, a vented fume hood, and the fenestration in the inner door. An ALNOR EB-731 (TSI Incorporated, MN, USA) passive capture hood was used to measure the inlet/outlet flow rates in each room outlet. Air velocities were recorded every two seconds at each grid location for three minutes. For the fume hood, the face velocity tests were performed by dividing the opening of the hood into 15 equal-area grids of approximately 0.3 square feet at the design sash height (18") and measuring the velocity at the center of each grid. Using Equation 10, the mean grid velocity was calculated for the opening to determine the overall average face velocity:

$$Q = \frac{(\sum_{i=1}^{15} V_i)}{n} \times A \quad \text{Equation 10}$$

Where Q is the overall flow rate at the fume hood and V_i is the face velocity at each grid, n is the number of grids (15), and A is the area of the sash (5 SF). For additional details about the instruments used, please refer to the subsection 'Instruments' in the 'Experiment Design' section of Chapter 3.

The amount of supply air through the inlet, the exhaust through different outlets, the Net Flow rate, and the air changes per hour are tabulated in Table 7 for the two scenarios of low – and high–pressure differentials. The unbalanced inlet/outlet flow rates ($\Delta Q = 189$ CFM) resulted in pressure differentials (ΔP) of 1.0 Pa between the cleanroom and the gowning room, measured by an Abatement PPM3-S portable pressure monitoring device in 0.5s intervals for the duration of the tests. The 1.0 Pa pressure differential is designated as the ‘Low’ level in Table 6. Later, for a different set of experiments, the return grille (Figure 9) was covered by an air shield such that no air could return through that exhaust vent. Hence, the ΔQ (529 CFM) produced much higher ΔP ’s (4.0 Pa) than in the previous scenario. These findings are consistent with the theoretical bases where the change in ΔP is proportional to ΔQ -squared (ASHRAE, 2011). This scenario is designated as the ‘High’ differential pressure level in Table 6.

Table 7: Airflow inside the cleanroom

Inlet	Outlets			Net Airflow	Air Changes per Hour
Ceiling	Return Grille	Fume Hood	Fenestration		
1284 CFM	340 CFM	500 CFM	255 CFM	189 CFM	42

The temperature was also measured to observe any buoyancy-driven impact on the airflow during each test. Table 8 shows the mean temperature at the sampling location and the corresponding standard deviation. It can be seen that the variation in temperature was within 1 °C, which had little buoyancy impact on the flow.

Table 8: Mean temperature (°C) at the sampling location and the corresponding standard deviation

	Test 1		Test 2		Test 3		Test 4		Test 5	
	Mean	St. Dev.	Mean	St. Dev.	Mean	St. Dev.	Mean	St. Dev.	Mean	St. Dev.
Chaseroom	14.01	0.28	14.70	0.12	14.05	0.11	14.20	0.03	14.30	0.06
Gowning room	15.02	0.09	15.30	0.20	15.11	0.15	15.20	0.11	15.30	0.11
CR-Door	14.20	0.09	14.60	0.20	14.45	0.08	14.60	0.07	14.69	0.06
CR3- Return	14.05	0.07	15.01	0.09	14.39	0.09	14.50	0.05	14.58	0.06

Statistical Analysis

As the data shows that the fluctuation of particle concentration within an event does not have a significant trend, the movement of particles was analyzed by the change in exposure for different compartments (i.e., cleanroom, gowning room, and chase room) during experiments. As the cleanroom was not entirely devoid of particles at the time of the tests, the background concentration (C_{BG}) in any compartment during data collection was calculated using Equation 11.

$$C_{BG} = \frac{\sum_{t=0}^1 C_t}{n_{BG}} \quad \text{Equation 11}$$

Where C_t is the concentration at the time of sampling, t is the sampling time in minutes and n_{BG} is the number of data points observed in the first minute prior to the start of particle injection. C_{BG} was different for each experiment and was calculated separately for each size bin. To avoid the effects of dissimilar background concentrations, C_{BG} was deducted from each data point. For concentrations smaller than C_{BG} , the negative value was not considered and instead was replaced

by zero. The normalized data for particle sizes from 0.3 μm to 10 μm from each PC were grouped according to the events. As each event was observed 3 times, 3 groups of data were obtained from each PC per event. The average concentration for every particle size was determined using Equation 12.

$$C_e = \frac{\sum_{t_i}^{t_f} C_t}{n_e} \quad \text{Equation 12}$$

where C_e is the average concentration for an event, t_i is starting time of that event, t_f is the finish time of that event, C_t is the concentration at the time of sampling, and n_e is the number of data points in that event. The exposure, or the number of particles in one cubic foot of air for the duration of the event, was then calculated using Equation 13. Note that the duration of each event (δt) was 30 s.

$$E = \int_0^{30} C_t dt \quad \text{Equation 13}$$

Next, event-specific exposures (E) were compared between different compartments. The particle migration from room A to room B for an event was characterized as a ratio of the exposure in the two rooms. Hence,

$$\varepsilon_{A,B} = \frac{E(A)}{E(B)} \quad \text{Equation 14}$$

As, Exposure E embodies the concentration of particles in the compartments during any event, the ratio, $\varepsilon_{A,B}$ denotes the ratio of exposure in Compartment A to that of Compartment B. This ratio depicts the percentage difference in particle concentration – the number of particles that were present in Room B and escaped into Room A during various events. For example, the percentage of particles migrated to the gowning room (GR) from the chase room (CH) was calculated as $\varepsilon_{GR,CH} = \frac{E(GR)}{E(CH)}$. During the same event, particle migration from the gowning room to the cleanroom (CR) was calculated as $\varepsilon_{CR,GR} = \frac{E(CR)}{E(GR)}$.

Findings:

Cleanroom Pressurization and Door Opening

Particle movements from outside compartments into the cleanroom were influenced by different variables such as door opening, traffic flow, pressure differential, and particle size. The data collected during different experimental setups and event-specific cross-contamination of the cleanroom were analyzed. Because the cleanroom had undergone major renovation prior to the tests, it was not completely dust-free. Before aerosolization, an average number concentration of 74 particles per ft³ at 0.5 μm means diameter was observed, which is equivalent to an ISO 5 cleanroom. At the onset of aerosolization, an abrupt increase of particles was observed near the release location. This change manifested itself in other spaces (e.g., the cleanroom) as spikes in the concentration when the door was operated.

The pressure differential across the cleanroom door was continuously monitored throughout the experiments. The average ΔP for tests 3 through 6 was 4.2 Pa ($\sigma = 1.02$). Results of the ANOVA test showed that ΔP remained consistently similar (p-value= 0.503) with the same behavior for these tests. However, ΔP was significantly lower for Tests 1 and 2 with an average of 0.93 Pa ($\sigma = 0.29$). Regardless of the amount, pressure differentials rapidly decrease at the onset of every door opening (Figure 10 and Figure 11). Results showed that even for high ΔP , as depicted in Figure 10, a door opening can significantly lower the difference in positive pressure. The door opening resulted in a drop of pressure from nearly 4.5 Pa to a minimum of approximately 0.5 Pa in less than 2.5 seconds. After closing the door, the time required to recover the average differential pressure of 4.2 Pa was around 4 seconds.

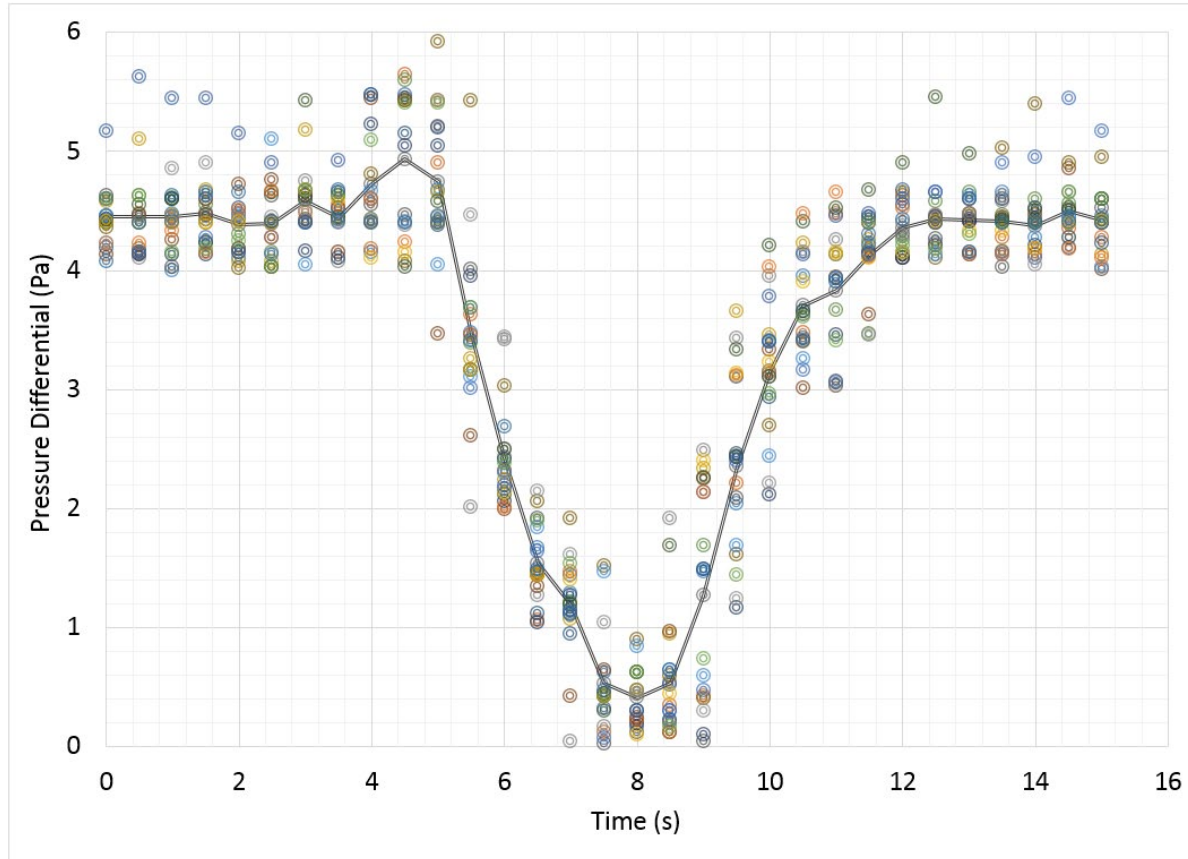


Figure 10: Pressure differential across the cleanroom door during 5-second door openings for the high-pressure experiments. The door was opened at time =5 s and closed at time = 10 s. The different colored markers indicate each individual event during the experiments.

Figure 11 shows that opening the door was able to eliminate and even reverse the positive pressure across the door for a low initial pressure difference. The differential pressure for this scenario dropped to an average of -0.2 Pa in almost 10 seconds, which is a more gradual decrease than that of higher differential pressure. Also, with low ΔP , the time required to restore the stable pressure difference followed by a door opening was almost 30s which was significantly slower recovery compared to a door opening with higher ΔP . These results conform to the finding from previous studies (Hathway et al., 2015; Kalliomäki et al., 2016; E. S. Mousavi et al., 2018; Tang et al., 2005) that door opening can terminate the isolation condition.

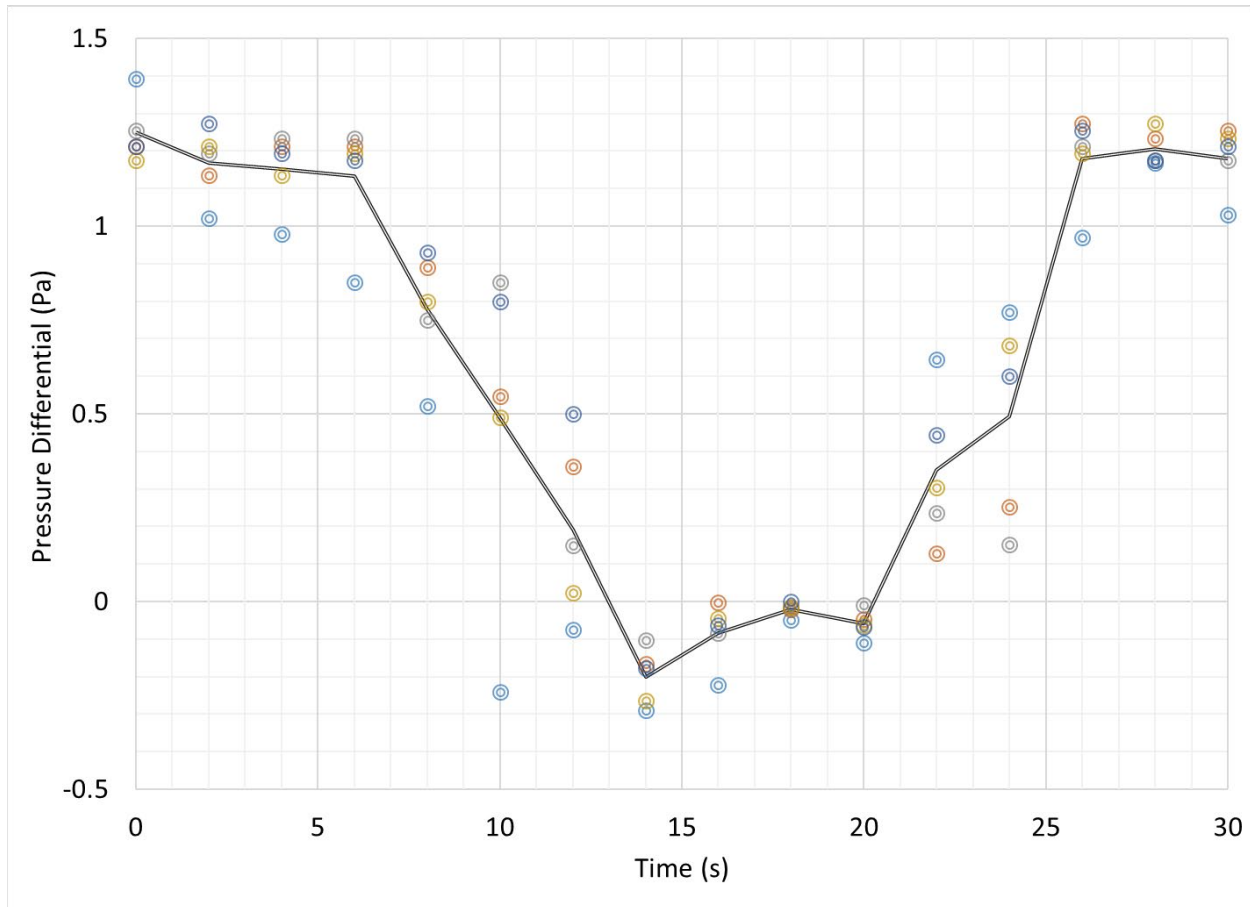


Figure 11: Pressure differential across the cleanroom door under 'low ΔP .' The door was opened at time = 5 s. and closed at time = 10 s. The different colored markers indicate each individual event during the experiments.

Exposure vs. Pressurization and particle size

The exposure to particles of different sizes in different compartments for separate events when contaminants were released in the CH are listed in Table 9, and corresponding data is listed in Table 10 when the release location was the GR. The data presented in Table 9 depicts two different test cases – one with low number of particles released along with lower ΔP (test 1) and another with higher particle generation coupled with higher ΔP . Number of $0.3\mu\text{m}$ particles generated in test 6 was approximately 6 times than that of test 1.

Table 9: Exposures at different compartments from particle release in CH

Event	Location	Test 1(low generation-low PD)						Test 6 (high generation-high PD)					
		0.3µm	0.5µm	1µm	2.5µm	5µm	10µm	0.3µm	0.5µm	1µm	2.5µm	5µm	10µm
Event 1	E_{CH}	9805	1692	1013	117	12	0	53391	45108	16755	5161	469	148
	E_{GR}	45	13	2	0	0	0	510	198	46	8	2	1
	E_{CR}	2	0	0	0	0	0	11	4	0	0	0	0
Event 2	E_{CH}	10390	5269	1184	107	12	0	64319	56377	20222	5702	660	195
	E_{GR}	206	76	9	0	0	0	203	71	17	3	0	0
	E_{CR}	1	0	0	0	0	0	20	6	1	0	0	0
Event 3	E_{CH}	13120	7232	1800	271	15	0	50047	42740	14417	3719	548	166
	E_{GR}	201	68	9	0	0	0	505	191	44	7	2	1
	E_{CR}	18	9	1	0	0	0	11	3	0	0	0	0
Event 4	E_{CH}	9918	4808	1005	83	0	0	52957	41759	12399	2769	520	164
	E_{GR}	65	13	0	0	0	0	842	320	71	12	2	1
	E_{CR}	4	3	0	0	0	0	19	5	0	0	0	0

Consequently, as fewer particles were present for experiment 1, the exposures in compartments other than CH, the generation location, were less than it was for test 6, and even with lower differential pressure, the exposure of even smaller particles in the cleanroom was low. In contrast,

for test 6, even with a much higher number of particles generated, the higher-pressure difference was able to contain particle migration to CR effectively, even though the exposure in CR was slightly higher for 0.3 and 0.5 μm particles compared to test 1. In both these tests, almost none of the particles of size $\geq 1.0 \mu\text{m}$ were recorded in the cleanroom. These results concluded that when the source of contamination was not adjacent to the space with intended cleanliness, restricting the amount of contamination generated or applying high differential pressure when particle generation was high proved to be efficient in maintaining the cleanliness.

Table 10 depicts the tests with three test cases, as follows. Test 2 with low generation-low ΔP , test 3 with low generation-high ΔP , and Tests 4 & 5 with high generation-high ΔP . As both tests 4 and 5 had the same release location, a similar rate of generation, and similar pressure difference, the exposures in the GR and CR for these two tests are averaged and presented in Table 10.

As for these tests, the location of particle release was the GR, higher exposures in the CR were observed in general, in contrast to the data presented in Table 9. With low- ΔP , even when the number of particles was not so high (test 2), considerable exposure was recorded in the CR for particle sizes upto 2.5 μm . For test 3, the number of particles generated was comparably lower than the other two tests and had a higher ΔP ; hence, exposure recorded in the cleanroom, even for smaller particles, was not that significant. It was interesting to see that for tests 4 & 5 when there was a large number of particles present in GR, no exposures were recorded for particles of size $\geq 1 \mu\text{m}$. Even for smaller particles, given that E_{CR} was comparable in value with that of test 2, when compared to E_{GR} for the same tests, it could be noticed that not many particles present in GR could travel to CR. When pressurization was increased, $\epsilon_{CR, GR}$ was decreased. Even with the low generation, a significant proportion of particles inside the GR migrated to the CR under the smaller differential pressure (Test 1 and 2) as $\epsilon_{CR, GR}$ ratio is high for small particles. This finding was consistent for all the events, irrespective of generation location. The event-wise ratios of exposures to different particle size bins over different experiments are tabulated in Table

10. The larger ΔP was able to contain the contamination source outside CR more effectively. These results demonstrate that the closer the source of contamination, the higher the probability of cross-contamination, which is in line with findings by (Bolashikov et al., 2012). It could also be concluded that when the source of contamination was fairly close to the Cleanroom door, the application of higher differential pressure prevented cross-contamination more effectively, substantiating the results from the study by (Adams et al., 2011). The data in Table 9 also confirms, as does the data in Table 10, that smaller particles are more prone to contamination by means of cross-contamination. Irrespective of the generation rate and pressure differential, almost no particles $\geq 2.5 \mu\text{m}$ migrated inside CR. When the source of contamination was in CH, the exposure of particles greater than $1.0 \mu\text{m}$ inside CR was zero, unlike the tests where the source was in GR, where definite exposures of particles $>1.0 \mu\text{m}$ were evident in the CR. Larger particles have lower mobility, and higher pressurization was effective even when a great number of large particles were generated.

It is noteworthy that during Event 1 and Event 4, when the inner door was not operated, even with higher differential pressure, particles of sizes $\leq 0.5 \mu\text{m}$ found their way into the cleanroom in the case of particle release in CH. Particles of a mean diameter of $1.0 \mu\text{m}$ were found inside the CR when the contamination source was in the GR. Particles are often assumed to move in the same manner as the airflow (Zhao & Wu, 2005). However, even in the presence of directional airflow, probably due to reasons attributable to Brownian diffusion of highly mobile particles with small diameters through the gaps in fenestration louvers and gaps around the door frame, some particles leaked inside CR. As seen from Table 9 and Table 10, the exposures of particles were notably high for particle sizes up to $0.5 \mu\text{m}$ and these numbers are confusing when particle trajectories are opposite to the airflow direction. As every experiment was repeated three times and the obtained data were averaged in terms of different events, it was observed that for the first run, there was a negligible number of particles inside CR during event 1. But during events 2 and 3, particles were transported by the door opening and the movement of the person to and from

the CR. Some of the particles were removed by means of the directional airflow, but a few of the smaller particles remained inside CR, especially those which were able to travel to the farthest corner of CR. During the 2nd and 3rd runs of the experiment, this phenomenon cascaded, and the particle counters measured the newly introduced particles along with those already remaining from the previous run for events 1 and 4. It was impossible to measure background concentration in the CR for every run of the same experiment, and hence the data for the 2nd and 3rd run data could not be normalized.

Table 10: Exposures at different compartments from particle release in GR

Event	Location	Test 2 (low generation-low PD)						Test 3 (low generation-high PD)						Test 4 & 5 - merged (high generation-high PD)					
		0.3 μm	0.5 μm	1.0 μm	2.5 μm	5 μm	10 μm	0.3 μm	0.5 μm	1.0 μm	2.5 μm	5 μm	10 μm	0.3 μm	0.5 μm	1.0 μm	2.5 μm	5 μm	10 μm
Event 1	E_{GR}	955	378	94	19	4	1	248	102	27	6	2	0	35047	14920	4517	845	210	56
	E_{CR}	40	32	11	4	0	0	11	5	1	0	0	0	37	18	3	0	0	0
Event 2	E_{GR}	788	315	71	16	4	1	283	119	35	8	2	1	34238	14588	4394	831	195	52
	E_{CR}	172	79	15	3	1	0	2	0	0	0	0	0	54	23	3	1	0	0
Event 3	E_{GR}	1140	442	104	21	6	2	227	93	27	7	2	0	31360	13249	3851	681	167	47
	E_{CR}	84	39	7	1	0	0	5	2	1	0	0	0	34	10	2	0	0	0
Event 4	E_{GR}	1248	501	120	24	6	2	260	103	31	7	2	1	31204	13179	3916	730	185	51
	E_{CR}	19	16	3	1	0	0	1	1	0	0	0	0	34	12	2	0	0	0

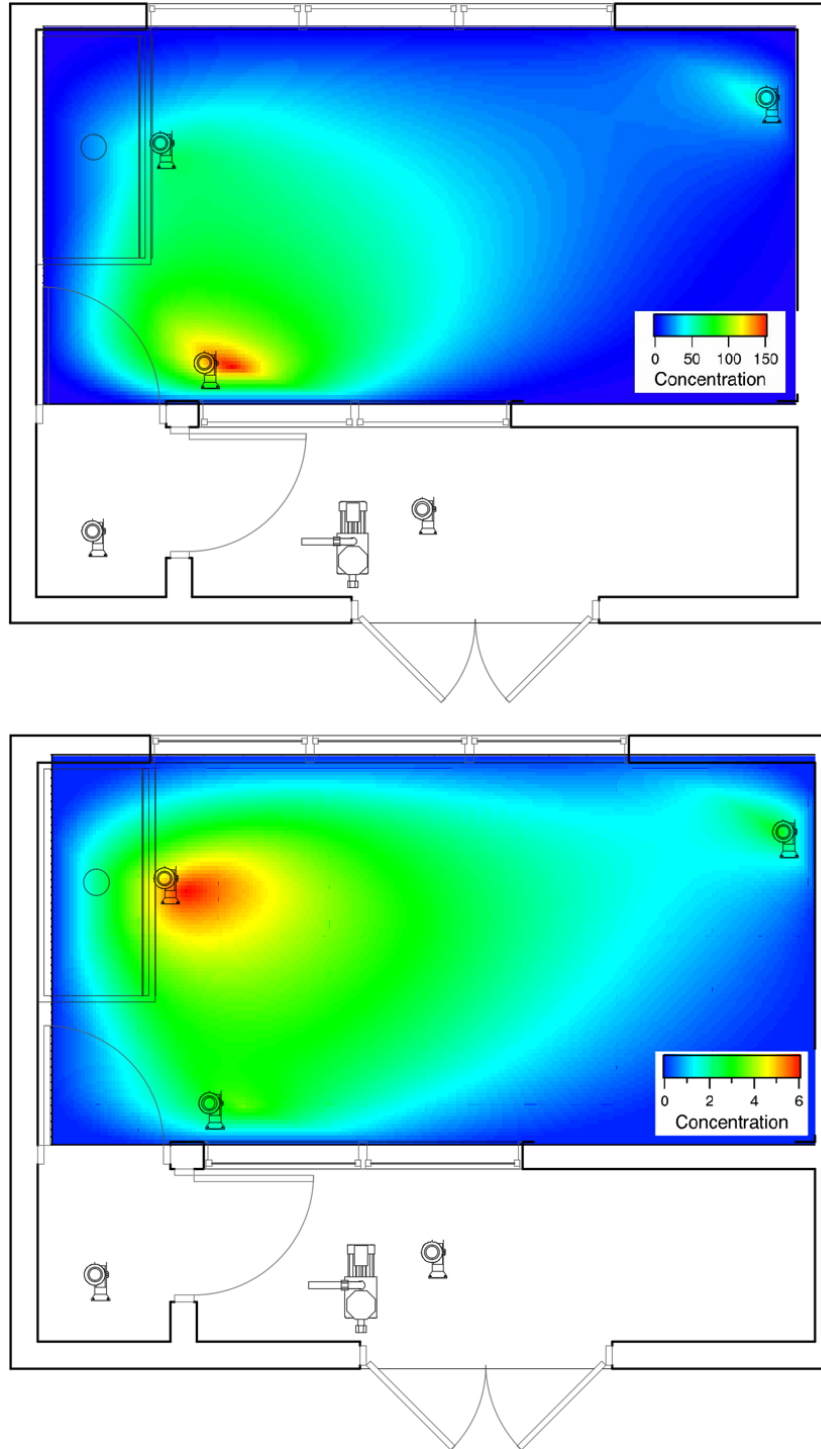


Figure 12: Concentration heat map inside the CR for low ΔP (top figure) and high ΔP (bottom figure) for 0.3 μm particle measurements. Note the difference in colorbar concentration scale between the two images

Figure 12 shows a heat map of 0.3 μm particle distribution inside the CR when released in the GR for both high and low differential pressure conditions. It is evident from this figure that with high ΔP , the concentration of particles was near the door, whereas with lower ΔP , particles were able to move further inside the cleanroom. Also, the particles were spread around the CR with lower- ΔP in contrast to congregated particle presence when ΔP was higher.

The particle concentration heatmaps (Figure 12) were produced using the data obtained from the particle counters placed inside the cleanroom, and it was assumed that the concentration at the walls was zero. The concentrations at all the other places were interpolated, and hence the lower right corner shows a low concentration of particles, which might be unrealistic.

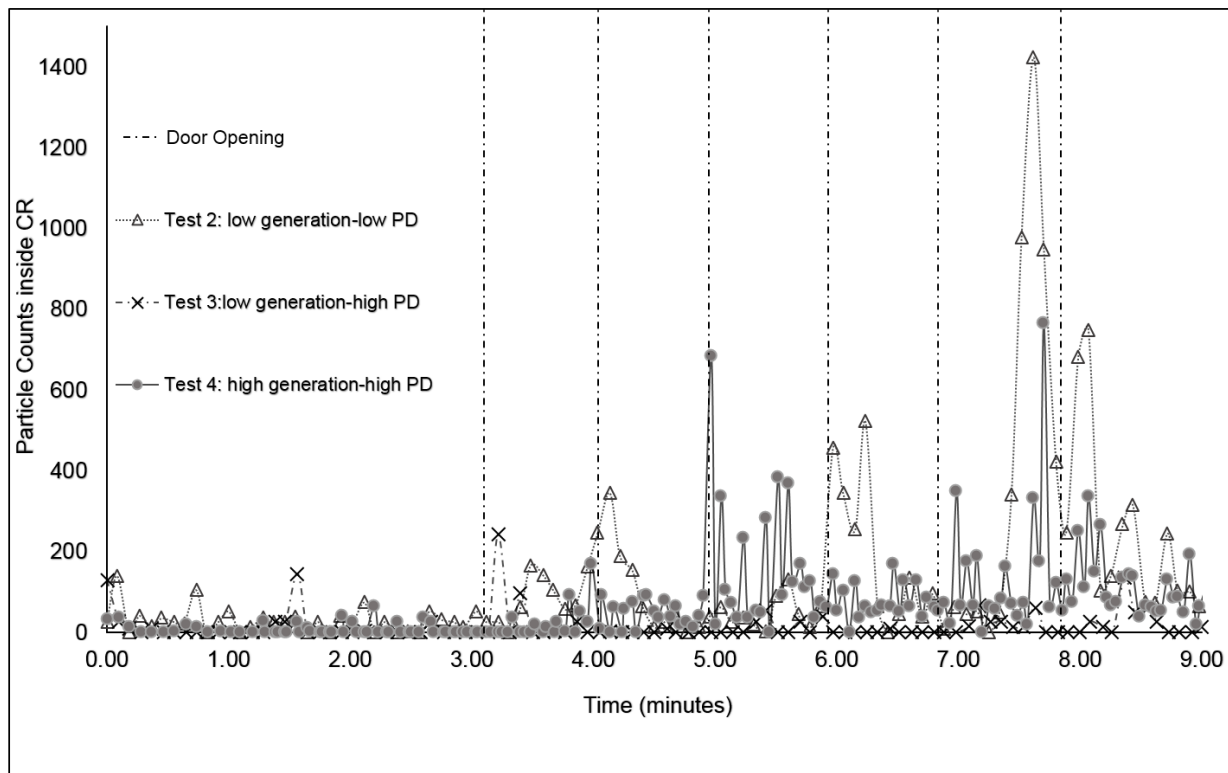


Figure 13: Particle Counts inside CR with Respect to Cleanroom Door Opening

Door opening and traffic flow

In all tests, 0.3 μm particles were observed inside the CR shortly after door openings. In Figure 13, the number of 0.3 μm particles inside the CR against the time in minutes from the start to end of experiments for three different test scenarios (test 2: low generation-low ΔP , test 3: low generation-high ΔP , and test 4: high generation-high ΔP) are plotted; notice the spikes in particle counts occurring after each dashed line, which indicate a door opening). The spikes in the particle count occurred at each door opening when traffic movement was both forward and reverse.

It was noticed that for tests 2 and 3 and except for the first cycle, the door opening followed by the forward traffic resulted in more particles inside the CR compared to the door opening followed by reverse traffic (Figure 13). For test 4 (i.e., the high generation rate experiment), fluctuations were more prominent and sharper, and the door opening with the forward traffic saw a steeper peak. Each time the door was opened, there were higher concentrations inside CR than in the previous cycle as particles accumulated in the GR due to continuous particle generation. Interesting to note that the peaks associated with test 2 took longer to tail off, whereas those associated with test 4 were quick and frequent. The opening of the door disturbed the differential pressure, barring the directional airflow. As stated earlier, these disruptions due to door opening are recovered quickly when ΔP is higher. The opening of the door and moving traffic caused turbulence and created vortices that carried the particles inside the CR.

Figure 14 displays the fraction of exposures in the CR as compared to the GR for all particle size bins measured by the PCs in low and high differential pressure settings for both forward and reverse directions of traffic movement. The results clearly show that exposures measured inside the CR for forwarding traffic are enhanced relative to reverse traffic for all particle sizes and irrespective of differential pressure between the rooms. For example, in test 2, the $\epsilon_{CR, GR}$ in Event 2 was 25.7% for 0.5 μm , compared to 8.9% in Event 3, meaning that the forward traffic clearly introduced more particles into the CR than the reverse traffic event. Similar trends were observed

analyzing test 4, although the percentages are significantly smaller due to the overall effect of higher differential pressure preventing as much particle introduction to the CR (Figure 14). Higher ΔP could positively affect the leakage (i.e., closed doors) and the mixing processes (i.e., door openings and traffic passage). However, its effects on the latter were less substantial.

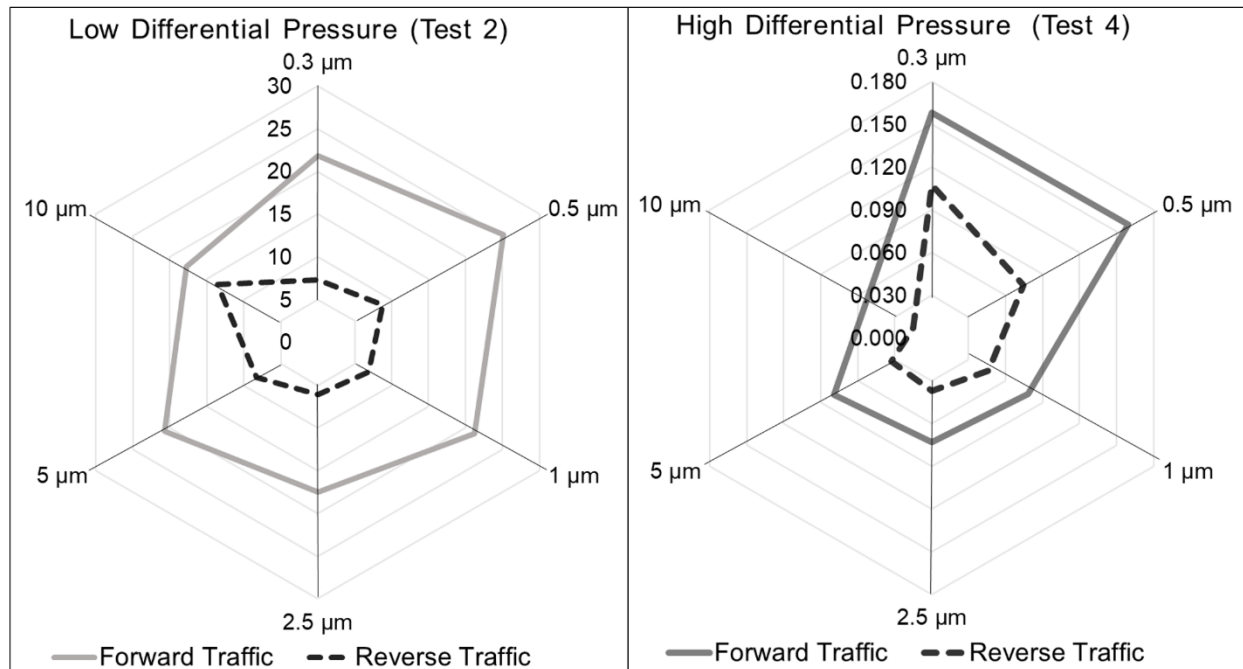


Figure 14: Exposure in CR with respect to the traffic movement direction. Particles were released in GR

The vortices resulting from the turbulence created due to the pressure difference disruption follow the direction of moving traffic and effectively altered the directional airflow towards the cleanroom. As explained, for low differential pressure, this effect lasts longer, carrying more particles into the CR, while for a higher-pressure difference, the recovery time is quick. Thus, Test 2 results in Figure 14 show enhancements more uniform with particle size, whereas enhancements for smaller particles are more pronounced than for larger particles in Test 4. These findings give credence to the findings in studies by (Mears et al., 2015) and (E. S. Mousavi & Grosskopf, 2016). Under the low generation scheme and when the origin of particles was in the chase room, very

few particles could escape into the GR. Hence, there were not enough particles that could migrate into the CR. This could be the reason why the effect of the forward traffic was not clear for tests 1 and 3.

Limitations:

This paper, as a case study, focused on specific experiment setups with predetermined human movements, which can widely vary in actual cases. But the finding on the effect of positive pressurization, door opening, and occupant movement may provide the track to build on for further research about the true effect of random human walks and their effect on cross-contamination.

This study was conducted in a university research facility cleanroom, which may not represent the industrial cleanroom in terms of size and geometry. The duration of door opening and waiting inside a compartment was constant in this study. In a production environment, the operation of the door may not be fixed. Also, the effects of the consequent opening of the door with a shorter waiting time might have a different impact on the cross-contamination, which was not considered for this study.

As stated in the method section, the cleanroom was available in a short window of time. Thus, the team was able to conduct the experiments with limited repetition. Though the results of the multiple runs were consistent, the outcome of this paper would have been much stronger with a larger set of data. For instance, this study has only studied two levels of differential pressure difference. With larger sets of data, a clearer influence of pressurization could have been studied. Nevertheless, this paper can serve as the starting point for more rigorous and holistic future research.

Conclusion:

In this study, in a particular case of cleanroom contamination, the movement of particles originating outside the cleanroom and their migration patterns into the cleanroom were observed relative to the differential pressure, door opening, traffic flow, and particle size. This study

indicates that even with no source of contamination inside the cleanroom, the room can be contaminated by a worker operating the door and moving in and out of the room. Three main aspects of this work were influential in airflow inside the cleanroom, as described below.

The behavior of particles is rightly dependent on their size. Fine particles are highly mobile and can leak into the cleanroom, even in the presence of a ΔP and with the door closed. Conversely, large particles are removed (or settled) much easier and providing a large pressure differential guarantees a full containment. However, it must be noted that the majority of practical problems in the cleanroom emanate from the contamination of submicron-sized particles (Xu, 2007b), and our study confirmed that submicron-sized particles are most difficult to avoid. Hence, to prevent cross-contamination in a cleanroom, the focus should be on containing smaller particles, for which the sole application of higher-differential pressure may not be effective.

The results suggest that higher differential pressure was more effective in containing the cross-contamination of the cleanroom. Spillage of particles into the cleanroom is significantly lower for a sufficiently high ΔP . Moreover, higher pressure differentials tend to recover swiftly after a door opening, minimizing the duration of mass transfer. However, a high ΔP results in more air mixing when the door is operated. As a case study, this paper does not recommend a minimum pressure difference since only two ΔP s were tested. Federal Standard 209, Airborne Particulate Cleanliness Classes in Cleanrooms and Clean Zones, recommended a 12.5 Pa ΔP for semiconductor cleanrooms (W. Sun et al., 2013). However, more recent studies done by Sun et al. (2013), Hendiger et al. (2016), and Mousavi et al. (2016) suggested that a thorough investigation of the magnitude of positive pressure in cleanrooms is needed to determine optimal pressurization in order to ensure efficient cleanliness according to the process required in the cleanroom as a future research direction.

It was noted that the door movement and the inward direction of moving traffic (movement opposite to the direction of airflow) contributed to more particle migration than the outbound traffic from the cleanroom. It can be suggested using precautions while going inside a cleanroom, for

example, going through a decontamination process, can prove to be effective in minimizing particle transportation, although not tested in this study. While this is a great subject for future research, some European countries (France and England) implement an adaptive design where very high pressure is applied when the inner door is opened and remains for the duration of the door opening. Once the door is closed, the system returns to its normal set point. Innovative approaches such as this example shall be further studied and implemented.

Chapter 5

Effects of Indoor Human Movements on Indoor Airflow Patterns²

The literature review section and Chapter 4 elucidated how occupant movements significantly affect steady-state indoor airflow patterns. In the context of contaminant dispersion, the human walking motions carry the pollutants in the wakes that follow the walking direction. A series of experiments were conducted to study the impacts of walking movements on the airflow patterns in a controlled environment. The data collection process was designed to understand the three-dimensional dispersion of velocity profiles. The experiments were conducted under three different flow conditions and for two different walking schemes in the Controlled Environment Chamber at the Center for Built Environment, UC Berkeley. Several tests were conducted over a span of two months in Summer 2019 for three rates of supply air (one control, two treatments). Please refer to subsection 'Experiment Facilities' in the 'Research Design' section of Chapter 3 for the detailed dimension of the Controlled Environment Chamber, where the experiments discussed in this chapter were conducted.

Methods:

Test Procedure

For the experiments, the air was supplied to the chamber from the wall-mounted diffuser 0.3 m below the ceiling (Figure 15). Excess air was exfiltrated from the chamber through the gap when the air was supplied to the chamber, creating a positive pressure differential in the chamber with respect to the hallway outside.

In order to study the effects of the walking movement of a person on the temporal and spatial characteristics of indoor airflow, a series of walking experiments were conducted in the chamber.

² The contents of this chapter are reproduced from (Bhattacharya, Pantelic, et al., 2020) with permissions from the co-authors and the publisher.

To eliminate the randomness associated with walking, a 3.04 m long and 0.3 m wide track was defined, and sensors were placed at each side along the track to measure air velocity. The walk's starting point was 1.1m from the wall across the supply grille and 2.25 m from the wall with the hinged door (Figure 15 B). The measurement units were mounted on tripods and were placed in six rows along imaginary lines perpendicular to the walking track, each located at a distance of 0.61 m from the adjacent row, as shown in Figure 15 B. The first row was co-linear with the start of the track with a pair of sensors on each side of the track, and row 6 was located at 3.05m (10 ft) apart from the first row, colinear with the end of the track and had sensors arranged exactly like that of row 1. The intersection of the vertical and horizontal dimension lines delineated the name of the sensor. For example, sensor L4 is located at the intersection of 'L' and 'Row 4'. The walking track was drawn in such a way that the sensing stations on the right side of the track were directly exposed to the inlet airflow from the supply grille, as evident from Figure 15 B and C. Furthermore, the adjustable fins of the supply grille were oriented at 60° angle with the vertical plane (Figure 15 D) in order to direct the airflow towards the sensing stations.

Walking Exercise and Initial Conditions

The experiments were conducted under different initial conditions regarding the inlet airflow from the supply diffuser. Depending on the amount of air supplied to the chamber, three separate flow regimes were described below.

a) Still air – during this scenario, the initial steady-state condition inside the experiment chamber was quiescent as the fan and the AHU responsible for air supply to the chamber were not operating, and the supply diffuser was shut off.

b) 70% fan – for the second type of flow regime, the supply fan, and the AHU were throttled to operate at 70% of full capacity. The supply grille configuration was as described in Figure 15 D. After the steady state condition was reached inside the chamber, the manometer reading indicated a positive pressure differential of 22.4 Pa between the room and outside.

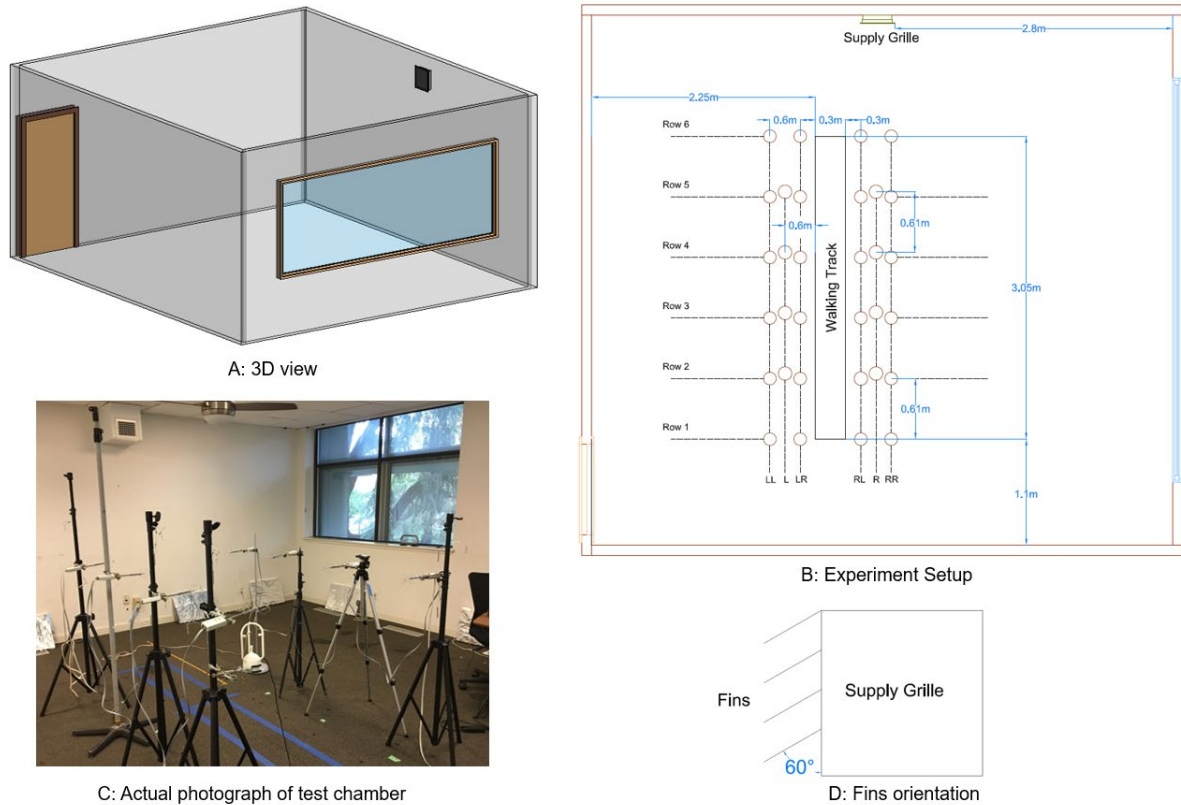


Figure 15: Chamber Geometry and Experimental Design

c) 100% fan – for this inlet condition, the supply fan and AHU operated at full capacity and the orientation of the supply grille was the same as in case b. With 190 cfm (90 L/s)(Bauman, Fred; Arens, Edward A; Tanabe, S; Zhang, H; Baharlo, 1995) air inlet during this flow setting, the positive differential pressure between the chamber and outside was measured to be 37.3 Pa at steady state.

Two walking scenarios were defined. For walking once, the person began the walking movement from the start point and covered the track distance (3.04m) up to 3 seconds before coming to a standstill (walking speed = 1.02m/s). During this movement, the movement direction of the individual walking was towards the supply grille – designated as the forward movement. During walking twice and similar to walking once, the person walked in the forward direction facing the inlet for three seconds until the entire track distance was covered, stopped walking and remained

stationary at the end of the track for 1 second, and moved backward for 3 seconds to reach the start point and stop walking. The walking exercises in these experiments were realistic, where the arms and legs were swinging naturally. But the airflow data due to swinging motion through the gaps around the arm and feet were not collected, and the walking exercise was considered to be simplified. As the human walk had inherent randomness, the walking durations were recorded using a handheld stopwatch. The durations for all the experiments were recorded and averaged, which are provided in Table 11, with the standard deviations presented in parenthesis. For these two walking exercises under the above-described flow regimes, different test case scenarios were defined, and multiple repetitions were performed for each of them to increase the number of observations at each location and ascertain the statistical consistency of the collected data (Table 11).

Table 11: Experiment conditions

	Inlet Flow	Walking Exercise	Average walking time	Data Logging Duration	No. of trials
Test 1	Still	Once	3.18 s ($\sigma=0.27$)	60 s	33
Test 2	70%	Once	3.2 s ($\sigma=0.13$)	60 s	33
Test 3	100%	Once	3.09 s ($\sigma=0.17$)	60 s	33
Test 4	Still	Twice	7.18 s ($\sigma=0.23$)	60 s	33
Test 5	70%	Twice	7.01 s ($\sigma=0.18$)	60 s	33
Test 6	100%	Twice	7.07 s ($\sigma=0.14$)	60 s	33

Data Collection

As described in subsection 'Instruments' in the 'Research Design' section of Chapter 3, both the omnidirectional and ultrasound sensors were placed along the walking track, as shown in Figure 15.

Table 12: Comparison between the measurements by ultrasound vs. omnidirectional sensors

Sensor	Sensor type	non-zero entries [s]	Peak velocity [m/s]	Lag [s]	Average Velocity [m/s]- (σ)
R2	Omnidirectional	---	0.048	1s	0.039 (0.028)
	Ultrasound	5s	0.132	<1s	0.037 (0.009)
L2	Omnidirectional	---	0.057	1s	0.043 (0.021)
	Ultrasound	---	0.087	<1s	0.029 (0.024)
R3	Omnidirectional	16s	0.079	1s	0.037 (0.022)
	Ultrasound	7s	0.103	2s	0.035 (0.025)
L3	Omnidirectional	16s	0.099	2s	0.048 (0.026)
	Ultrasound	10s	0.110	2s	0.041 (0.029)
R4	Omnidirectional	16s	0.151	3s	0.059 (0.025)
	Ultrasound	10s	0.132	3s	0.042 (0.029)
L4	Omnidirectional	16s	0.168	3s	0.065 (0.050)
	Ultrasound	13s	0.214	3s	0.058 (0.049)
R5	Omnidirectional	15s	0.160	4s	0.062 (0.029)
	Ultrasound	11s	0.104	5s	0.049 (0.028)
L5	Omnidirectional	15s	0.194	4s	0.066 (0.060)
	Ultrasound	15s	0.174	5s	0.068 (0.056)

Data from the two sensing techniques were mostly consistent with two major differences: 1) the ultrasound sensors measured four data points per second, which resulted in capturing fluctuations in the flow. 2) The omnidirectional sensors tend to show speeds over the background for a longer period of time, whereas the ultrasound sensors' reading dropped to (near) zero faster. As far as detecting a lag in data logging, the two techniques performed rather similarly, as shown in Table 12. The difference could mainly lie in the roots of different measurement techniques adopted by the sensors. The Omnidirectional sensors measure, via a hot wire, the average speed of air in two-second intervals in a small spherical control volume ($r = 25\text{mm}$). The low resolution of data sensing led to larger magnitudes during a longer time span. However, this technique does not account for temporal fluctuations in airspeed. In a sense, the magnitudes reported by the omnidirectional sensors are the volume-averaged readings by the sensor during the two-second interval. During the same interval, the ultrasound sensors produced 8 data points (4 per second). Nonetheless, the time-average speed of air measured by the two sensing techniques is reasonably consistent. These data points manifested the true fluctuations of air velocity in three dimensions. Later in the paper, we discuss why these fluctuations play an important role in characterizing the true effect of human walk on airflow patterns. In summary, the ultrasound measurement technique led to two novel outcomes, (i) sub-second resolution in data measurements and (ii) indoor air velocity as a vector (3-D) quantity.

Statistical Analysis

The time-averaged outputs of the omnidirectional sensing system for every test case were collected for 60 seconds which generated 30 data points for every 33 replications. In order to obtain a transient velocity profile, all 30 data points collected over the repeated experiments were averaged for all the sensing stations. The results indicated consistency in the collected data at each point in time for every measuring station. To assess the consistency of measurements, all the spatial-temporal data points were combined in one array (\mathbf{V}). The Relative Standard Errors

(RSE) were defined as the data standard error (SE) of \mathbf{V} its average. Since the RSEs were normalized by average velocity, presenting the data in percentage (Table 13). RSE was largest for quiescent air, perhaps due to the low average value of data points.

Table 13: Consistency of Data Measurements by Omnidirectional sensors for all Test Repetitions

Experiment	Average RSE
Test 1	13.67%
Test 2	6.90%
Test 3	5.68%
Test 4	19.37%
Test 5	6.92%
Test 6	5.75%

Findings:

Indoor airflow characteristics were influenced by the induced flow resulting from the walking movements of a person. The data collected during different experimental setups were analyzed, and the results are presented specifically to the test case scenarios. As stated in the methodology section, air velocities were measured by two different sensors. In this section, measurements for both sensors will be discussed, and the outcomes will be compared. Specifically, the ultrasound sensor-enabled measuring air velocity vectors. To our knowledge, this is the first report of three-dimensional velocity measurements of human-induced indoor airflow.

Walking Once- Still Air:

During experiment setup 1, the initial condition prior to the start of the movement, the indoor air was quiescent. The data showed that with no other motion than the unidirectional human walk

(along the x-axis), there were changes in the air velocity in three dimensions (Table 14). Figure 3 shows the change in velocity magnitude (airspeed) with respect to time.

Table 14: Three-dimensional velocities, lag, and range of non-zero data recorded by the ultrasound sensor

Sensor	Background velocities [m/s]	Maximum Velocity [m/s] (time it occurred [s])			
		V	V _x	V _y	V _z
R2	0.0231	0.132 (10.0)	0.119 (11.0)	0.052 (11.0)	0.047 (19.6)
L2	0.0450	0.118 (15.0)	0.051 (10.6)	0.095 (15.0)	0.081 (11.3)
R3	0.0385	0.103 (14.0)	0.057 (12.6)	0.0511 (14.0)	0.057 (20.0)
L3	0.0177	0.089 (14.3)	0.085 (14.3)	0.070 (14.67)	0.026 (16.0)
R4	0.0297	0.113 (13.6)	0.053 (13.6)	0.095 (13.6)	0.043(17.0)
L4	0.0269	0.215 (13)	0.167 (13.0)	0.175 (10.6)	0.081 (13.0)
R5	0.0270	0.115 (15.0)	0.098 (15.0)	0.081 (14.0)	0.039 (14.6)
L5	0.0200	0.180 (15.6)	0.084 (21.3)	0.174 (15.6)	0.081 (17.0)

The change in velocity was sensed immediately by the onset of walking in sampling stations R2 and L2. After about two seconds velocities at sampling stations, R3 and L3 began to rise. One second later, sensors L4 and R4 showed speeds above zero, and finally, after about five seconds, the Row 5 sensors (R5 and L5) sensed the effect of walking on the airflow. Considering three seconds of walking duration, the sensors started recording the surge in velocity after the moving body was past them, resulting in the lag between the time the human passed the sensor and the time changes in airflow were recorded. Further, the increase in velocity magnitude over the background values sustained up to 15 seconds. The ultrasound sensors recorded non-zero

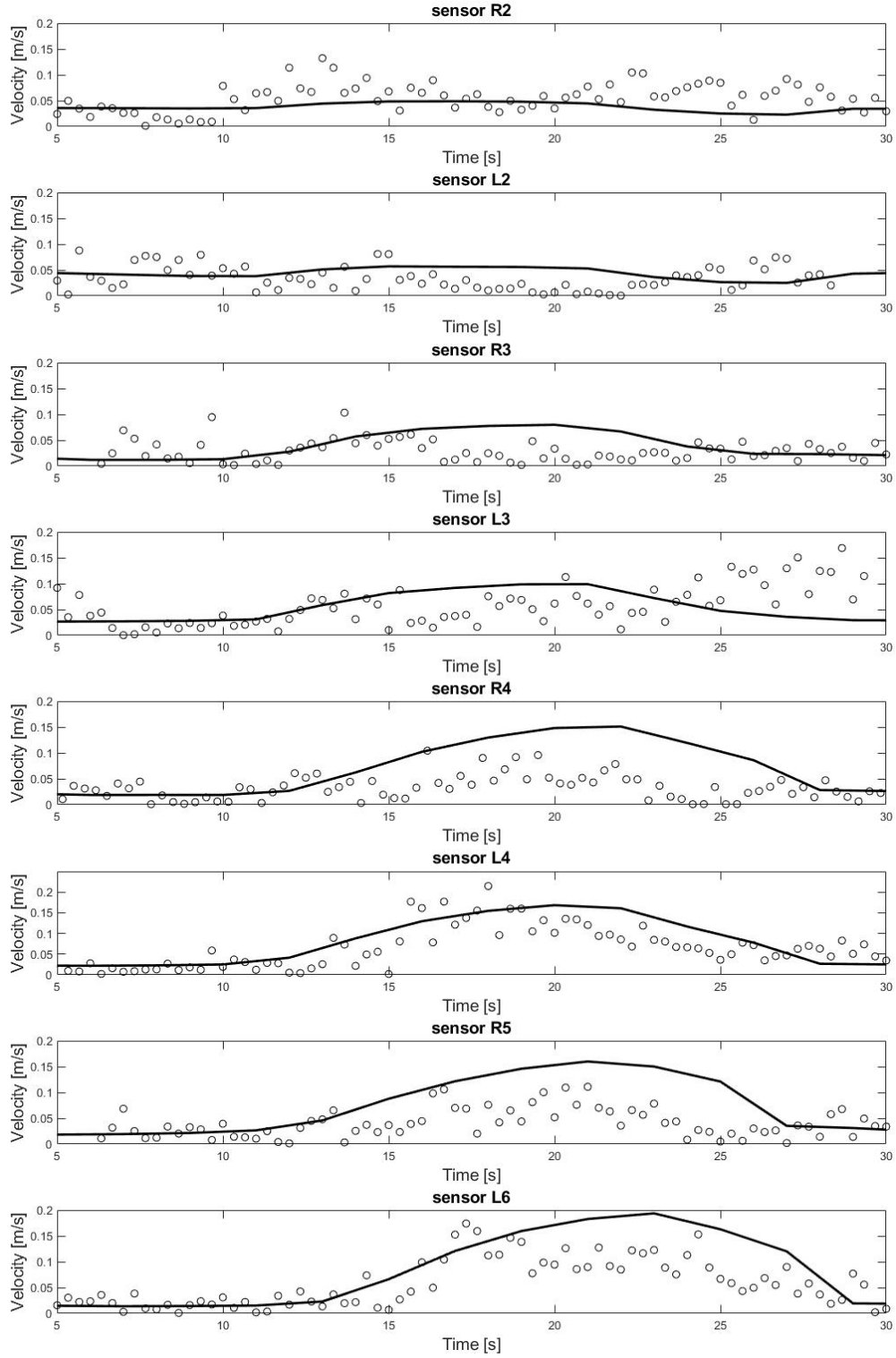


Figure 16: Air Speed due to walking once in still air by omnidirectional (—) and ultrasound (°)

magnitudes up to about 10 seconds after the walk ended (Figure 16). Both cases reveal that the effect of human walking on the flow is not negligible.

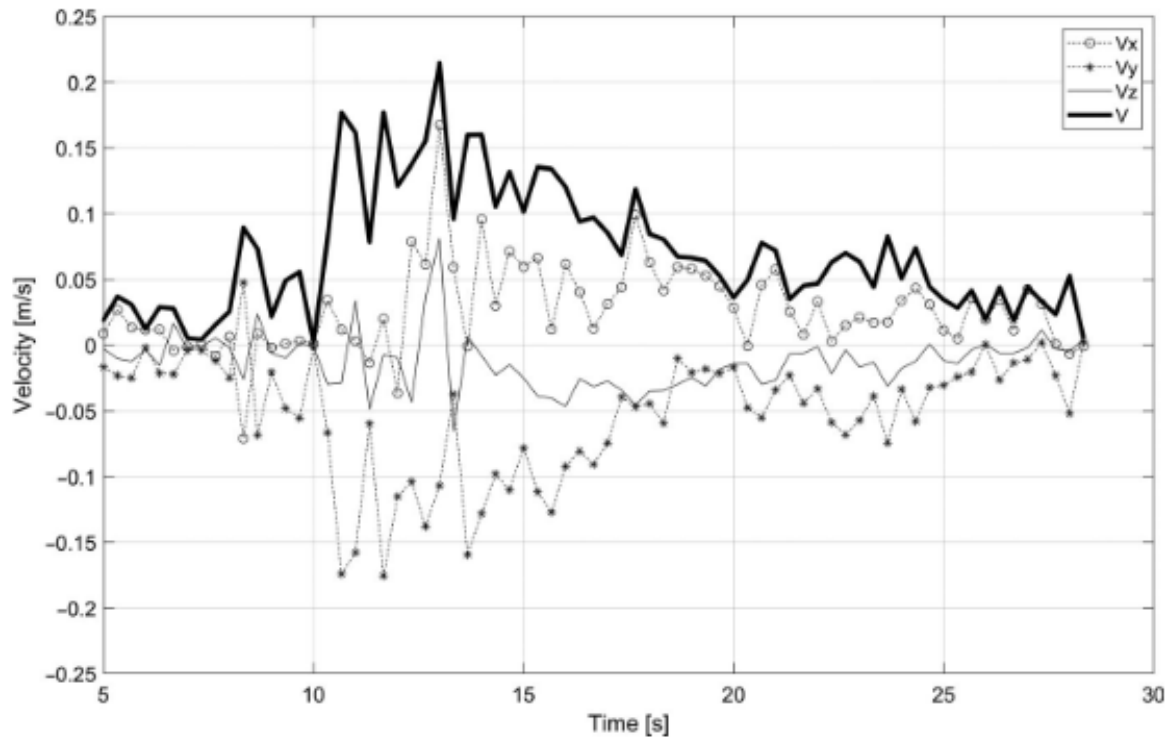


Figure 17: Patterns of air speed for Sensor L3 and the Cartesian components of air velocity

As the movement proceeded, the sensors along the track recorded a higher magnitude of velocity than those which were placed before them. For example, sensors R3 and L3 recorded a higher magnitude of maximum velocity than R2 and L2, and sensors R4 and L4 had a higher magnitude of air velocities recorded than the rest. For the first pair of sensors, the air was quiescent before the walk started. As the moving body moved by the sensors, its momentum was transferred to the air, increasing the velocity of air over the background. For the following sensors, the air around was not quiescent anymore and already had some velocities, which, when interacted with the moving body, had contributed to the higher magnitudes of velocity. Although the moving body

made a unidirectional walk along the length of the track (x-axis), the velocity components perpendicular to the track (y-axis) and normal to the plane of the track (z-axis) were recorded (Figure 17).

Results illustrated that none of these components were insignificant. In fact, velocities along the y-axis were in the same order as those along the main direction, indicating that the moving body pushes the air forward and to the sides. The vertical component of velocity (V_z) was not as large as the horizontal component. Nevertheless, the maximum value of V_z was of the same order of magnitude as V_x , and in most cases, the maximum value for V_z did not occur at the same time as the other components were maximum. It must also be noted that all the maximum values of velocity in all three dimensions were between 2 to 10 times larger than the background airspeed. This information, brought by the ultrasound sensing technique, is critical in characterizing indoor airflow patterns. For example, the oscillating behavior of V_z is known to be responsible for the resuspension of dust and a large particle when they settle on the floor.

Air Distribution Perpendicular to Walking Direction:

The dispersion of human movement induced airflow fields, perpendicular to the direction of movement, was found to be concentrated near the walking track, and velocity dropped quickly with increasing distance from the walking track. Even with the varied location of the sensors, i.e., data for different rows at different times exhibited similar trends, with some variations in the magnitude. Figure 18 illustrates the trends in the flow field along the width of the test chamber (perpendicular to the walking track) at four different times, measured by omnidirectional sensors located in Row 4, for walking once (bottom graph) and walking twice (top graph). To put this in context, airspeed measurements were normalized by the background speed (V_{BG}), that is, the average speed of air at each station before the walk began. The dark hatch on the horizontal plane shows (symbolically) the walking track. For walking twice, the velocity magnitude inside the walking track was nearly ~6 times V_{BG} , and that of walking once was nearly three times V_{BG} . These

normalized velocities rapidly approached 1.0 (i.e., V_{BG}) for sampling points farther from the walking track. Data showed that the effect of human walking on airflow patterns was only limited to a 1m range [1.85m-2.85m], 0.5m from each side from the center of the walking track. However, within the 1.0m range, velocities over the background were sustained for nearly 15 seconds after the walk ended.

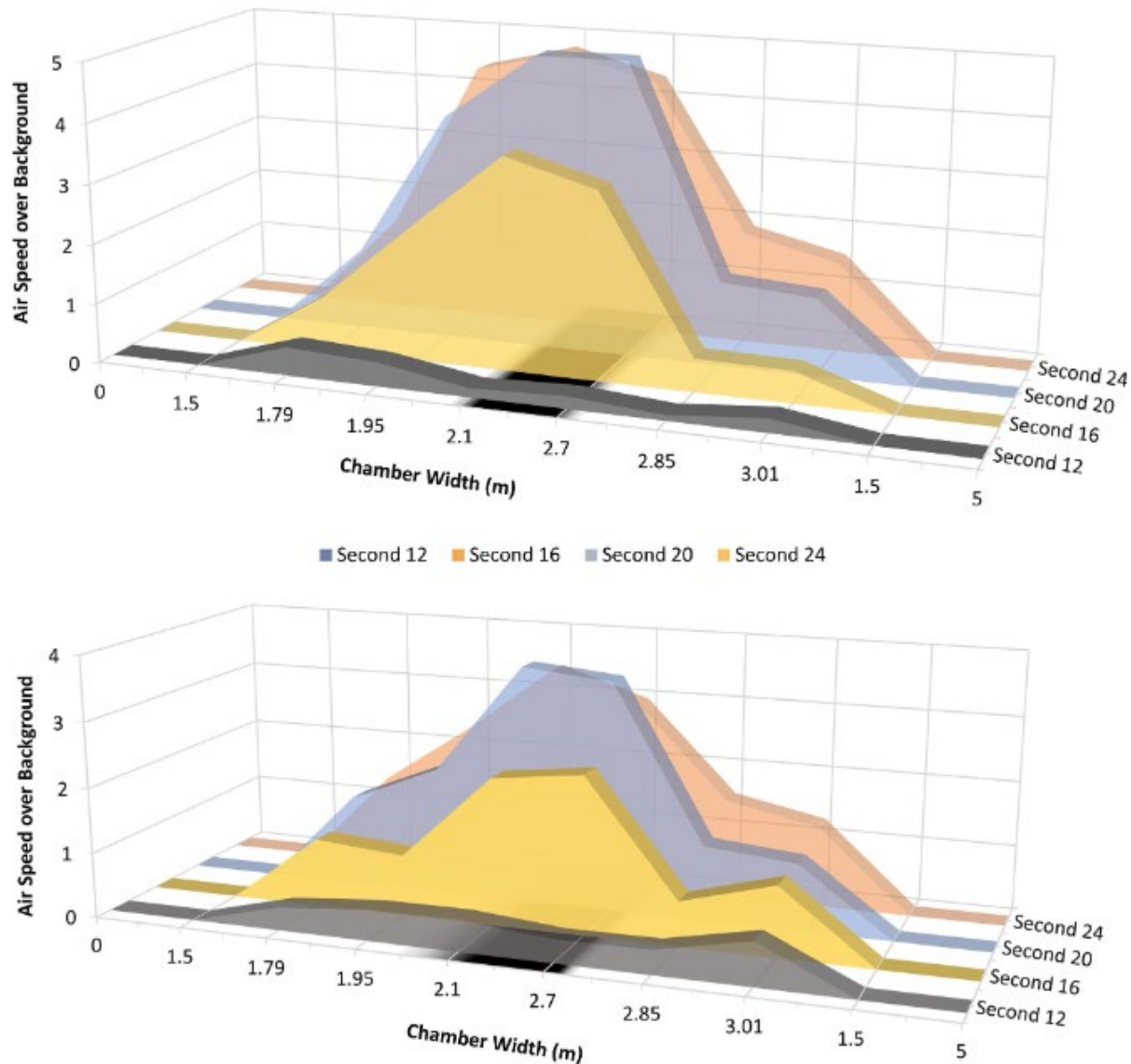


Figure 18: Effect of Human Walking on the Airflow Perpendicular to Walking Direction for Walking Once (bottom) and Walking Twice (Top)

Walking Twice-Still air

Even though the movement was present for a longer duration than walking once, the properties associated with characteristics of air movement displayed analogous trends, albeit with higher magnitudes during walking twice. It is demonstrated from Figure 19 that, similar to Test 1, all the sensors recorded the beginning of airspeed increase from second 12 apart from sensors R5 and L5, which recorded the beginning of the surge from second 14. The results from walking twice were more interesting as Sensor R4 recorded the highest speed among all the sensors, which was 0.26 m/s ($\sim 6 \times V_{BG}$), followed by sensor R5, which recorded 0.24 m/s ($\sim 5 \times V_{BG}$), both at the second 19. Note that V_{BG} is different for different sampling stations, as it is the time-average velocity of air before the walking began. In the walking twice scenario, the middle sensors recorded high velocities as they virtually experienced the full human walk twice. During the forward movement, the moving body carried the air wakes until the endpoint and at this point, the airstream had a motion in the direction of the first walk. While moving backward, the initial air was moving in a different direction, and the movement of the human walk had interacted with the moving air. As a result, one should expect to observe a less significant increase in V_x between tests 1 and 4 as the walking direction is inverted. Along the Y-axis, however, since walking in both directions led to pushing air to the sides of the walking track, a significant increase in V_y was observed. Worthy to note, the sign of velocity changed for the sensors placed on different sides of the moving body. Table 15 demonstrates the average velocities. On average, the x- and z-components of velocity did not change for the two cases, while the y-component doubled for walking twice.

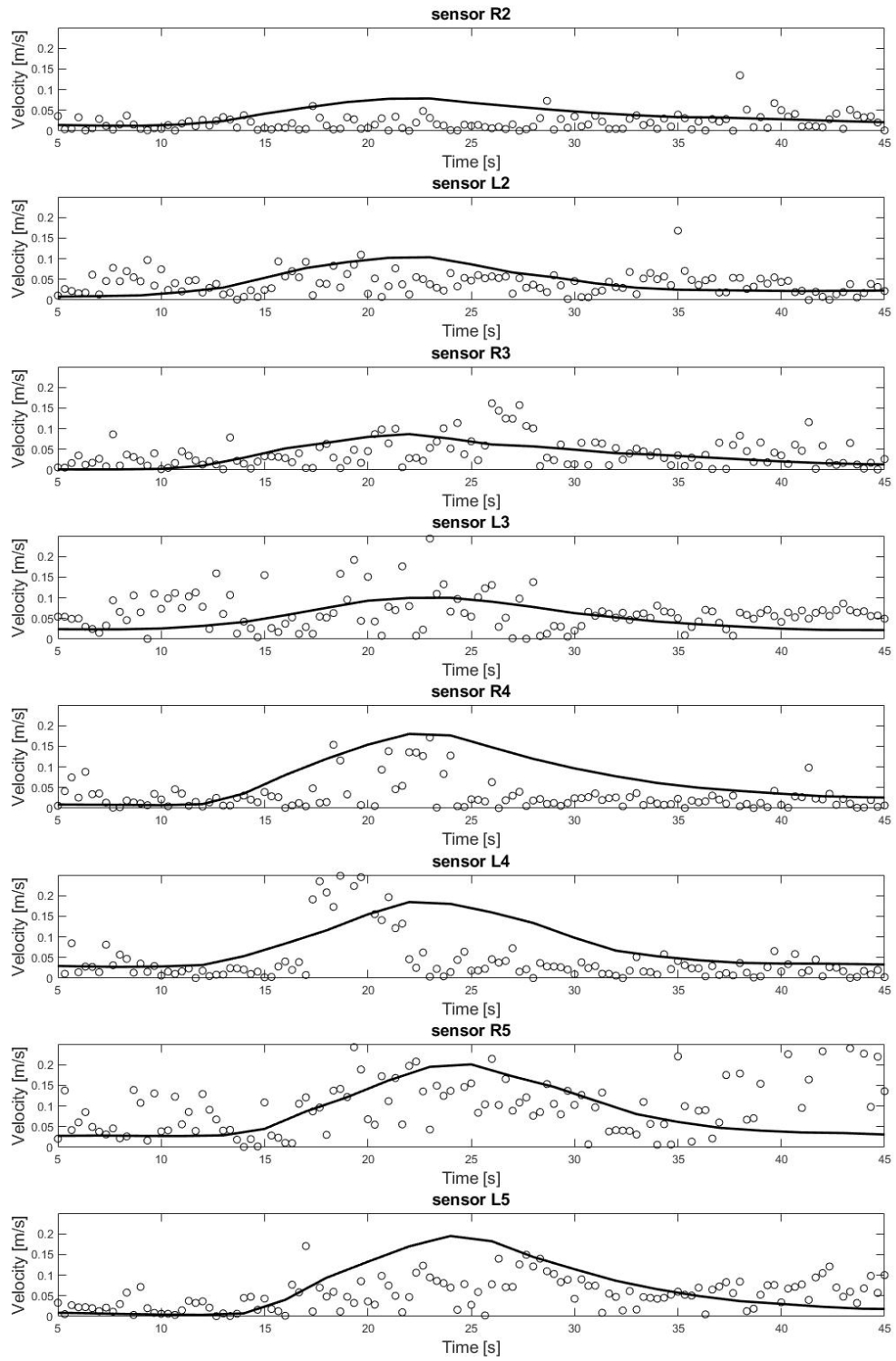


Figure 19: Airspeed due to walking twice in still air by omnidirectional (—) and ultrasound (°)

Table 15 : Comparison between Time-Averaged Velocity Components of Walking Once and Twice

Sensor	Walking Once			Walking Twice			Velocity Proportions		
	$\frac{\sum_{t=10}^{20} V_x}{N}$	$\frac{\sum_{t=10}^{20} V_y}{N}$	$\frac{\sum_{t=10}^{20} V_z}{N}$	$\frac{\sum_{t=10}^{20} V_x}{N}$	$\frac{\sum_{t=10}^{20} V_y}{N}$	$\frac{\sum_{t=10}^{20} V_z}{N}$	X-axis	Y-axis	Z-axis
Column	A	B	C	D	E	F	(D/A)	(E/B)	(F/D)
R2	0.054	-0.023	-0.018	0.032	-0.036	0.015	0.59	1.57	0.83
L2	0.010	0.017	0.006	0.017	0.096	0.020	1.69	5.72	3.12
R3	0.004	-0.004	-0.003	0.006	-0.009	0.002	1.65	2.00	0.52
L3	0.034	0.024	-0.010	0.018	0.050	-0.016	0.53	2.10	1.60
R4	0.013	-0.036	-0.002	0.021	-0.021	-0.002	1.61	0.59	0.91
L4	0.044	0.083	-0.020	0.014	0.017	-0.014	0.32	0.20	0.71
R5	0.038	-0.019	0.008	0.048	-0.050	-0.010	1.25	2.67	1.21
L5	0.023	0.013	-0.005	-0.006	0.070	-0.002	0.26	5.40	0.42

The effect of Initial conditions

In the experimental setup, the airstream was directed in such a way that the sensors on the right side of the walking track (R's) were directly influenced by the inlet air, whereas the sensors on the left side of the track (L's) were free from such direct influence. Obviously, the sensors to which the supply airstream was directed recorded higher magnitudes of velocity. The sensors away from direct exposure to the supply air stream recorded velocity due to walk, and the magnitudes are comparable to that of walking in still air. Figure 20 shows one example of such observation for sensor L4. Especially for walking once, velocity magnitudes are comparable and show very similar behavior. However, since air has an initial velocity prior to the walk, the initial measurements ($t < 10$ s) are appreciably higher compared to the still air. Generally, the cases with non-zero initial velocities depicted higher fluctuations, indicating a higher potential for turbulence. Nonetheless, the effect of walking was well captured by the sensors (Figure 20). Conversely, those sensors

directly exposed to the supply air showed different behaviors with respect to the initial conditions (Figure 21). Most notably, the effect of body movement seemed to be dissolved in the current flow of air. There are minor indications of the walk but not as conspicuous as in the other cases.

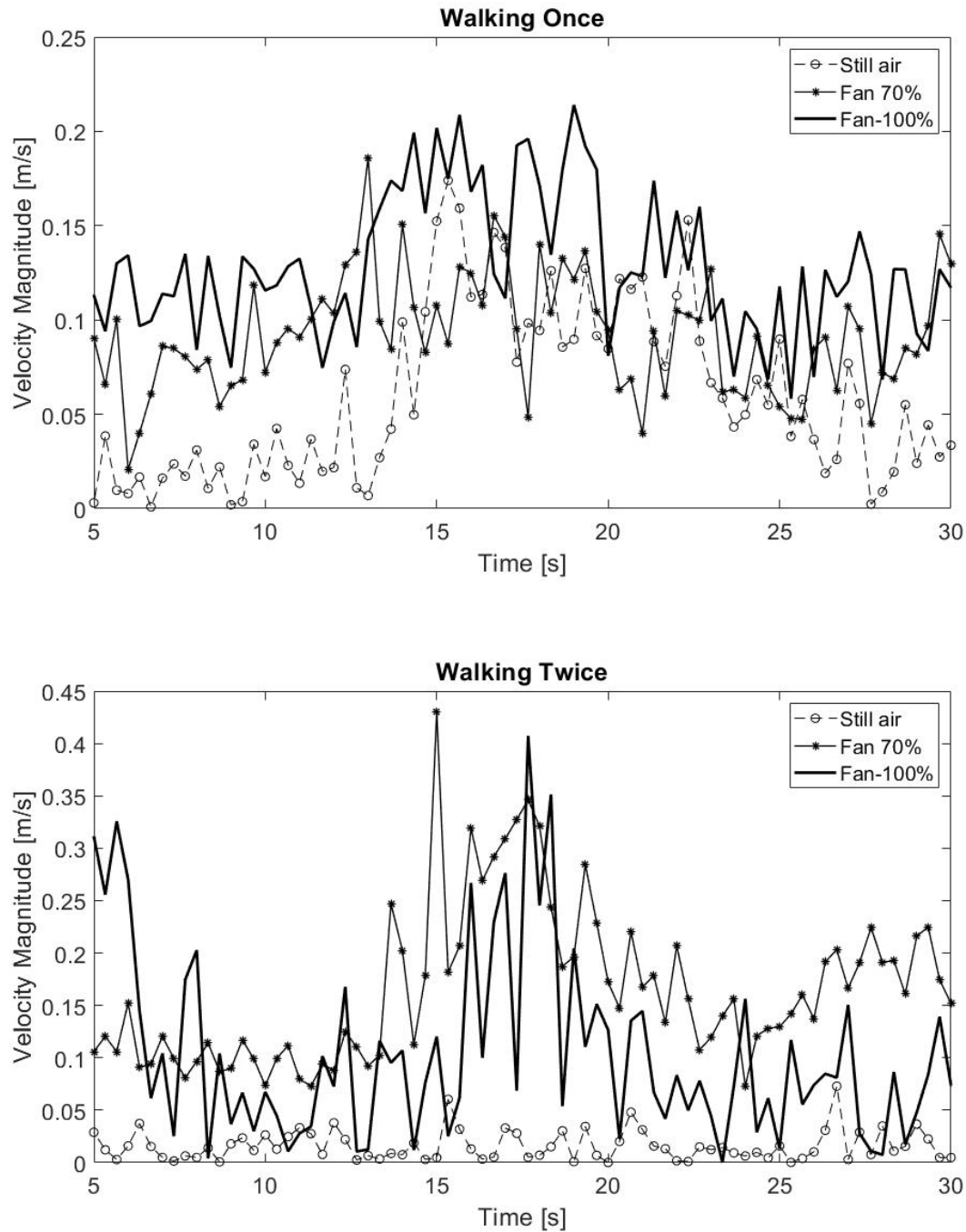


Figure 20: Velocity Magnitudes in Sensor L4 for Three Initial Conditions and Two Walking Schemes

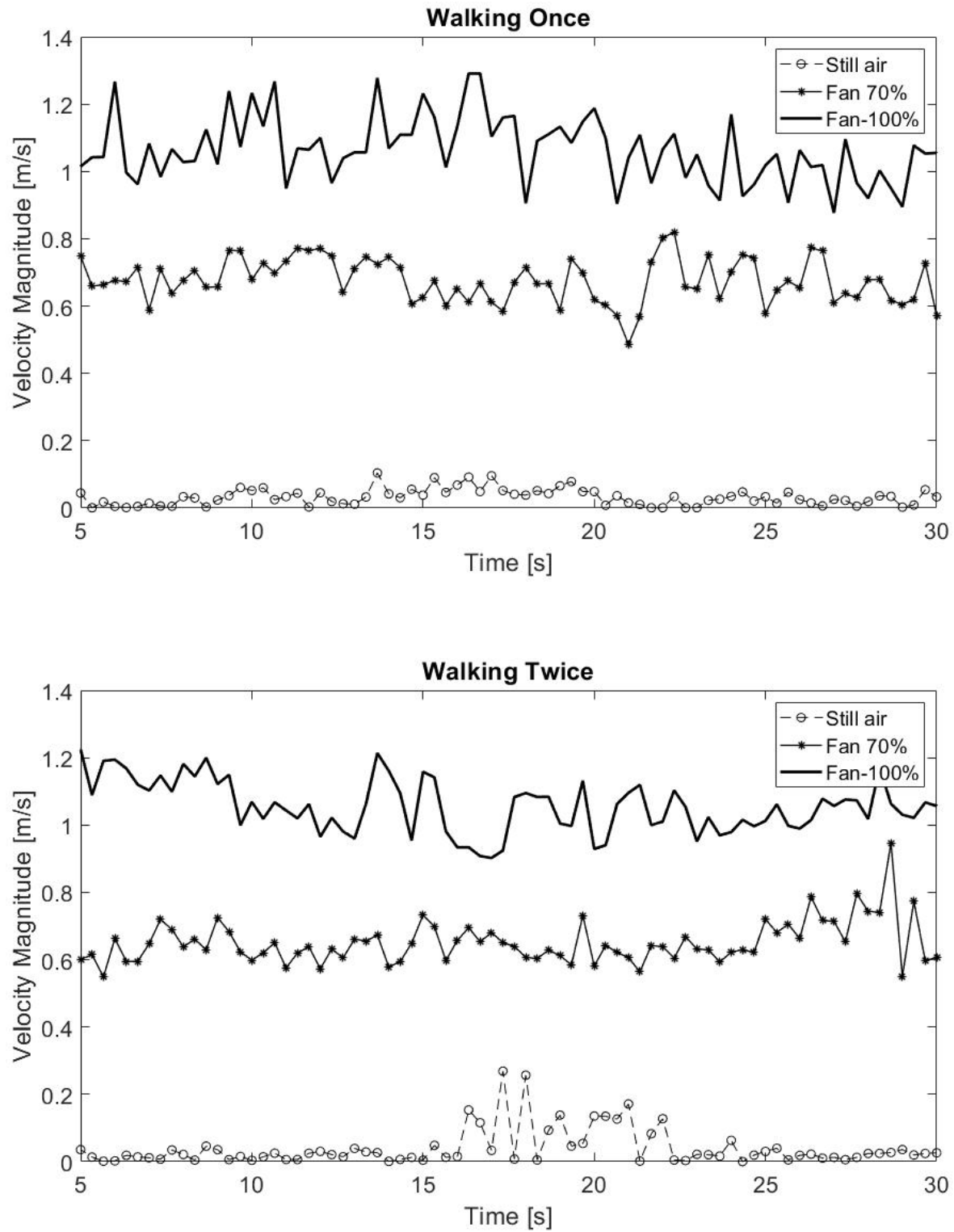


Figure 21: Velocity Magnitudes in Sensor R4 for Three Initial Conditions and Two Walking Schemes

For each sensor location, the kinetic energy of air is proportional to the sum of Cartesian velocity components, raised to the second power (Eq.15). Further, one can define the time-average initial kinetic energy (K_0) and the time-average walk kinetic energy (K_w) in the following manner:

$$K = \int mv \cdot dv = \frac{1}{2}mv^2 \propto v_x^2 + v_y^2 + v_z^2 \quad \text{Equation 15}$$

$$K_0 = \frac{\int_0^{t=10s} v_x^2 + v_y^2 + v_z^2}{(10 - 0)} \quad \text{Equation 16}$$

$$K_w = \frac{\int_{10}^{t=20s} v_x^2 + v_y^2 + v_z^2}{(20 - 10)} \quad \text{Equation 17}$$

Table 16: Kinetic Energy of Human Walking vs. Initial Condition

Initial condition	Still Air		70% Fan		100% Fan	
Walking status	Walking	Walking	Walking	Walking	Walking	Walking
	Once	Twice	Once	Twice	Once	Twice
K_0	0.012	0.015	1.197	1.123	2.689	2.658
K_w	0.044	0.068	1.255	1.218	2.837	2.888
$\Delta K = K_w - K_0$	0.032	0.053	0.057	0.095	0.148	0.229
ΔK (twice)/ ΔK (once)	1.682		1.651		1.549	

These embodiments of kinetic energy can help to compare the sheer effect of walking on the airflow. Table 16 shows the sum of K_0 and K_w recorded in every sensor and for all the experiment settings. Admittedly, the initial kinetic energy of air considerably rises with the increase in the supply rate. Interestingly, however, the walking period consistently had higher kinetic energy relative to the background energy (Figure 22). Moreover, the increase ratio in the kinetic energy of air between the two walking cases was between 1.5 to 1.6 times. This is consistent with our

observations on the components of air velocity. As stated earlier, since the walks are in the opposite directions, some of the kinetic energy from the moving body would be used to invert the direction of air. That's why walking twice did not precisely double the kinetic energy of air.

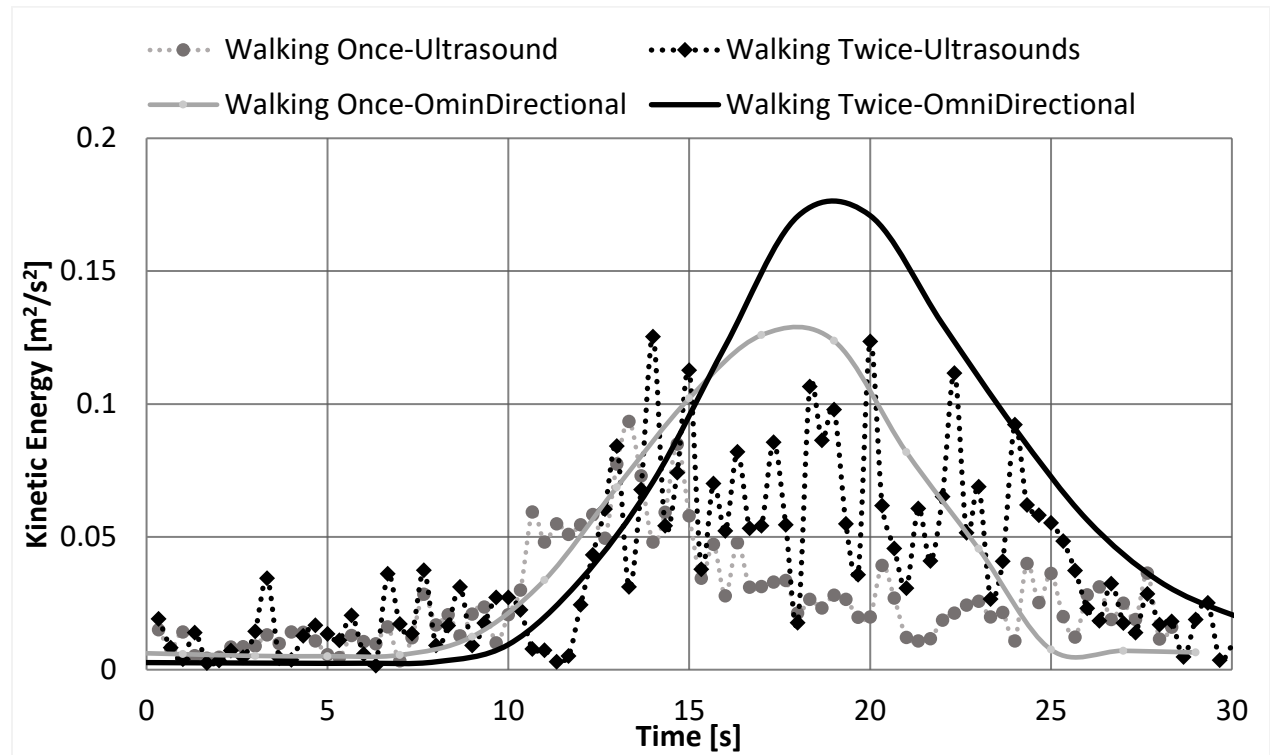


Figure 22: Total Kinetic Energy of Still Air for Two Walking Schemes and Two Measurement Techniques; Sum Over All Sensor Locations

Limitations:

This study aims to characterize the effect of human movement on airflow patterns by high-resolution and three-dimensional measurements of air velocity in a controlled chamber. As stated in the introduction, researchers have made various attempts on this issue, from a qualitative approach (Mattsson, M.; Sandberg, 1996) to computer simulations (C. Chen et al., 2016; Luo et al., 2018) and scaled experiments (O. Rouaud et al., 2004) to surrogate (i.e., particles or tracer gas) measurements (Mazumdar et al., 2010). However, this work is unique in measuring air velocities for real human walks. This is, in part, due to employing a state-of-the-art ultrasound

indoor air velocity sensor. This technology has put the research team in a unique position to measure the velocity field under different initial conditions, for different walking schemes, and using two different measurement sensors. Each test was repeated at least 24 times to assure the repeatability and consistency of the experimental outcomes. Access to a limited number of sensors resulted in measurements in the one-foot vicinity of the walking track. Another limitation of this study was that due to a large number of tests and limited time in the chamber, we could only define a walking twice test of opposite walking directions. Also, the ultrasound sensors had not been commercialized at the time of the experiments, and one could see unreasonable large data logs ($>2.0\text{m/s}$) due to mixing signals. The research team analyzed the data and omitted the datapoints that were larger than three standard deviations away the mean. These data points occurred on very few occasions. For instance, a one-minute test with 710 data logs had approximately 15 such data points.

Conclusions:

This study indicated that a walking motion with an average speed of 1.02 m/s can have sustained impacts on the magnitude of air velocity as the movement progresses in time. The walking movements generated wakes and carried the wakes with the moving body, which was evident from the airflow distribution across the whole region when no predominant inlet airflow was present (i.e., still air). Even with inlet airflow, the movement of the individual was able to alter the airflow properties noticeably. As the walk progressed, the wakes carried behind the moving body interacted with the existing flow field, generating turbulence, resulting in increased airflow velocities. Higher values of velocity magnitude were observed up to 1m away from the moving body and were sustained up to 15 seconds after the end of walking. The change in the flow field was realized with a short lag behind the moving object. The first sensors recorded higher airspeeds nearly immediately after the walk commenced. But the last row of sensors had almost 2s lag to realize the human walk. These experiments were controlled under limited and

constrained conditions where almost every aspect, starting from walking direction, speed to the airflow speed, and directions, was controlled, which would oversimplify the generalization and applicability in a real-world indoor environment. Having said that, meeting the assumed conditions, this study can substantiate the fact that a detectable flow of airstream can sustain up to 10 s in the direction of the walk after the moving body has passed by. Additionally, the walking-induced wake flows will mostly be contained within 1m perpendicular to the principal walking direction when the walking speed is not altered significantly. These findings can serve as recommendations for designing a sterile environment that is sensitive to airborne particle transport over a short distance.

Another significant observation was the behavior of the velocity components due to walking. A dominant unidirectional move along the x-axis resulted in significant y- and z-velocity components. The z-component is responsible for the resuspension of settled particulate matters. Furthermore, opposite walking directions reduce the velocity magnitudes along the walking track while increasing the velocity normal to the walking track (e.g., pushing air to the side). Nonetheless, it seemed that the alterations resulting from the moving body are similar to different walking motions, which allows the predictability of flow field changes due to the human walk. This is an interesting direction to carry forward this research. It is notable that even though the walk performed during tests was a realistic human walk, the restricted experimental setup and lack of pertinent instruments limited our ability to gather and analyze data associated with the swinging arm and leg motions. Instead, the walking exercises were considered to be simplified where the walking motion is equivalent to the sliding motion of a rigid body.

This study investigated the kinetic energy of the air as it related to human walking. The results consistently showed a rise (ΔK) over the background kinetic energy due to the human walk. ΔK was larger when the air inlet performed at full capacity, perhaps due to higher-amplitude velocity fluctuations over the mean (i.e., turbulence). When ΔK for walking once and walking twice was

compared, the increase seemed to be independent of the initial condition. This observation motivates the idea of predicting airflow patterns due to multiple walks from a known walking case. From this study, a strong flow field from high-velocity supply air was able to contain the effects of movement to a very small area; in other words, the effects of walking movement on the flow properties were more prominent in the absence of a dominant air supply. Additionally, it was also demonstrated that the further down the direction of the walk, the more apparent the change in airspeed.

Chapter 6

Effects of Door Opening on Indoor Airflow Patterns³

As explained in the literature review and studied experiments described in Chapter 4, the impacts of the door opening and closing on the predominant indoor airflow patterns are significant. The turbulent vortices created by the door opening aid in the air mixing through volumetric exchange on both sides of the door. This mixing results in the unwanted distribution of contaminants to the clean spaces from relatively less clean surroundings. Hence, to control all the unwanted dispersion of airborne pathogens resulting from the door opening, it is crucial to understand how door opening affects the airflow, given that door openings are common in indoor settings. A series of experiments were conducted to comprehend and quantify the changes in steady-state airflow patterns when a swing door is opened and closed in a positively pressurized room. Several tests were conducted over the summer of 2019 in the Controlled Environment Chamber at the Center for Built Environment, UC Berkeley. Three different initial conditions, i.e., three supply air rates (one control, two treatments) for two door opening schemes, were tested. For details about the dimensions of the experimental facility, please refer to Chapter 3, section ‘Research Design,’ and subsection ‘Experiment Facilities.’

Methods:

Test Procedure

As discussed in Chapter 5, a similar experiment arrangement was used apart from the use of the walking track and sensor placement schemes. The 0.3m x 0.3m wall-mounted diffuser 0.3 m beneath the ceiling was used for our experiments due to the ease of flow variation through user

³ The contents of this chapter is reproduced with permission from the co-authors and the publishers from (Bhattacharya et al., 2021) and an unpublished manuscript by Bhattacharya et al. (2022), submitted to Building Simulation

control (Figure 23). The supply flow rate created a positive pressure in the room, and the excess air left the room through the gaps around the door frame.

A series of tests were conducted to observe the patterns and characteristics of indoor airflow and quantify the volumetric air exchange emerging from the consequent door opening and closing motions. To capture the flow characteristics of an indoor space with the dimensions 5.48m x 5.44m x 2.5m, at least 16 pairs of omnidirectional sensors would suffice to cover the whole space. Instead, we had 4 pairs. With the limited availability of air velocity measuring instruments, the experiments were conducted in stages. Therefore, a set of sensing instruments were deployed to obtain near-boundary data at the proximity of the door movement periphery (Figure 23b) 63.5 mm away from the door tip. There were 3 locations housing the measuring instrument for 8 rounds of tests. The sensing station P1 was closest to the door tip when fully closed, and when fully opened, the closest station was P3, with P2 exactly in the middle. At locations P1 and P2, three sensors were mounted at equal distances to each other, covering a third of the door height, with the bottom one being 0.66 m above the floor level. Only the bottom two sensors were mounted at location P3, owing to the limited number of available sensors.

Another set of 8 omnidirectional sensors was arranged in 4 imaginary rows, designated as R1 to R4, going inside the chamber in a radial direction (Figure 23 C) at two elevation levels. The row R1 was parallel to the closed door, and the sensors were at a distance of 0.1m from the wall, whereas the row R4 was perpendicular to the closed door, with rows R2 and R3 making 30 degrees and 60-degree angles with R1, respectively. The measuring instruments were mounted on tripods along each row in four locations, identified using sensor ids 1 through 4. The first sensing system was the closest to the door tip at a distance of 0.1m, and the subsequent instruments were allocated 1.0m farther from each other.

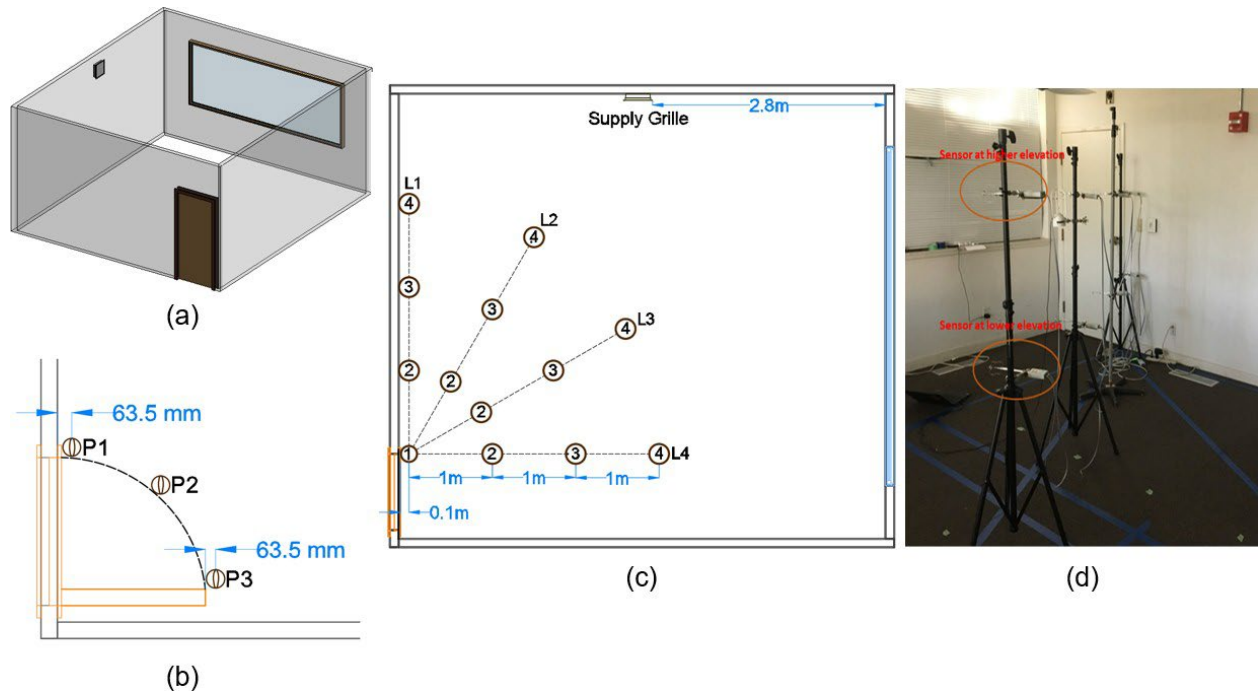


Figure 23: (a) Chamber geometry – 3D (b) Peripheral Configuration of Sensors (c) Radial Configuration of Sensors (d) Actual Photograph from Test Chamber

Moreover, the measuring instruments at the lower elevation were 0.66 m above the floor level, which was a third of the total door height. The higher-level sensors were placed at another 0.66 m from those at the lower elevation, covering two-thirds of the door height from the ground. The denotation of sensors was such that they were identified based on their elevation and location on a row. For example, the second sensor at the lower level (L) of row 3 is identified as RL32, or the third sensor at the upper elevation (U) of the first row will be identified as RU13.

Door-opening Exercises and Initial Conditions

Different sets of experiments were defined for two different door movements and three initial conditions, provided by the amount of air inlet from the diffuser. The experiments were conducted in sets for each experimental setup due to the limited accessibility of multiple sensors simultaneously, as expressed in the Experiment Setup section. The two

movements of the swing door that opened into the chamber are defined as follows:

1. Opening and closing the door once in a way that the door opens in the first second of every trial that takes two seconds to complete and stays open for a second before the closing movement completes by another two seconds, a total opening cycle of 5 seconds. This represents a typical door opening by a healthcare professional.
2. Opening and closing the door twice with the first cycle finished by second 5, then the door is kept shut for two seconds before replicating the first cycle, i.e., opening through two seconds, keeping ajar for one second, and closing for two seconds.

Each trial of experiments was run for 60 seconds during both of these settings, while each test was repeated 60 times to ensure statistical consistency. For every set of experiments, the door opening was initiated at the first second, and it was closed at the end of ~ 5 s (for opening once) or ~ 12 s (for opening twice). The sensors started recording air velocity from the start of the door opening at second 1 and continued for a minute. The door was again opened at the first second of the next minute, and these repetitions continued for 60 minutes. With the absence of any automatic door controlling device, the opening and closing and the timekeeping were done manually. Owing to this reason, the time required for the first cycle to complete was not exactly 5 seconds, and for double operation, not 12 seconds. The associated deviations for all 60 repetitions of each test based on door operation and initial conditions are tabulated in Table 17. Three different flow regimes were identified according to the volumetric airflow through the diffuser, which is described below.

- Still air – With the absence of airflow, as the fan and the AHU responsible for air supply to the chamber, were not operating, the initial steady state condition inside the experiment chamber under this scenario was quiescent, and the supply diffuser was shut off.
- 70% fan – The supply fan and the AHU were throttled to operate at 70% of the

full capacity. With the exfiltration through the gaps around the door frame, the manometer reading indicated a positive pressure differential of 22.4 Pa between the room and outside at steady state condition was reached inside the chamber.

- 100% fan – During this flow regime, the supply fan, and AHU operated at full capacity. With 190cfm (90 L/s) (Bauman, Fred; Arens, Edward A; Tanabe, S; Zhang, H; Baharlo, 1995) air inlet, the steady-state reading of the positive differential pressure between the chamber and outside was measured to be 37.3 Pa.

Table 17: Experiment Conditions

	Inlet Airflow	Door Opening Exercise	Average Door Operation Time (s)	Data Logging Duration	No. of Repetitions
Test 1	Still	Once	5.38 ($\sigma = 0.21$)	60 s	60
Test 2	Still	Twice	12.33 ($\sigma = 1.14$)	60 s	60
Test 3	70% Air	Once	5.52 ($\sigma = 0.82$)	60 s	60
Test 4	70% Air	Twice	12.49 ($\sigma = 0.24$)	60 s	60
Test 5	100% Air	Once	5.42 ($\sigma = 0.39$)	60 s	60
Test 6	100% Air	Twice	12.48 ($\sigma = 0.19$)	60 s	60

Data Collection

The omnidirectional sensors that measured the velocity magnitude and the ultrasound velocity sensors that measured the components of velocity along with the three cartesian coordinates were used to measure the velocity of air during the steady-state and during the events of the door opening and closing. Please refer to the ‘Instruments’ subsection under the ‘Research Design’ section in Chapter 3 for details of these sensors.

Statistical Consistency of Sampling

the sensing instruments recorded time-averaged values of velocity magnitudes for 60

seconds in each experiment, which was repeated 60 times. Those data points were averaged to obtain temporal trends and transient velocity profiles. The collected data demonstrated consistency at each point in time. The consistency was assessed by the relative standard error (RSE), defined as the percentage of data standard error over the mean velocity. Depicted in Figure 24, the solid lines portray the mean velocity for each set of experiments, and the surrounding shaded region displays the standard error bounds. Notably, the maximum distance between the bounds is associated with the time of the door movement cycle, probably due to the stochastic patterns in the turbulent flow.

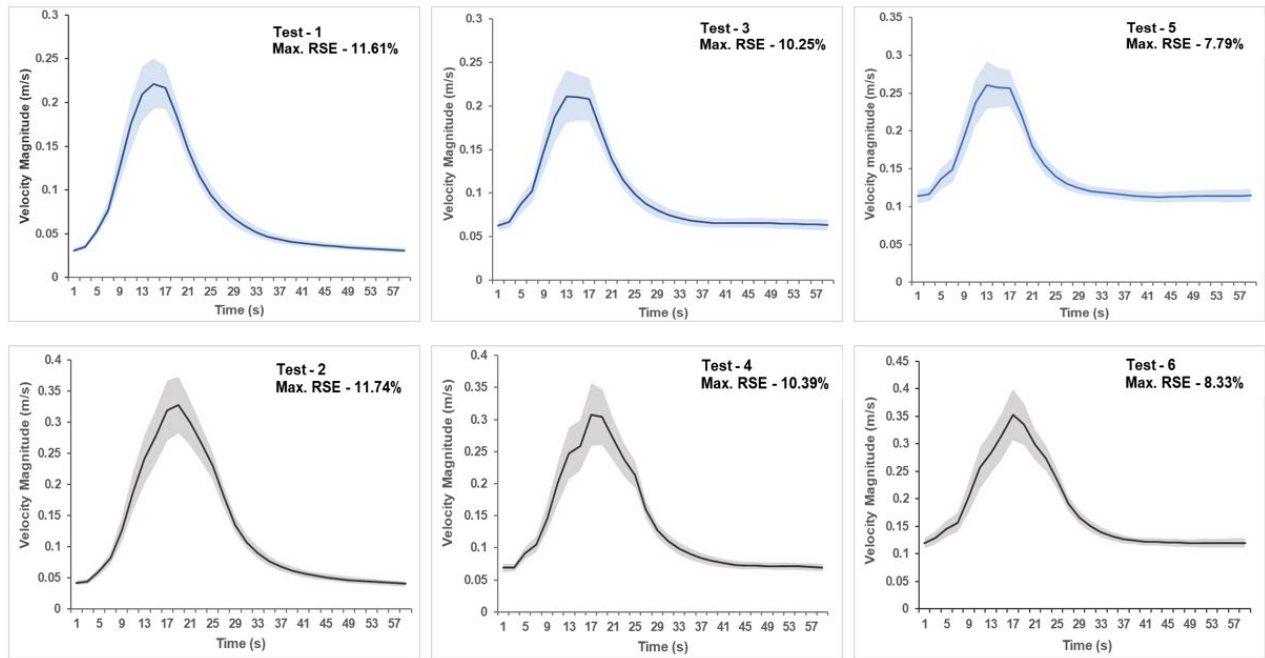


Figure 24: Data Consistency

Findings:

The results of the conducted experiments are discussed in parts:

- a) The distribution of flow patterns inside the chamber, as obtained from the sensors placed in rows L1 through L4
- b) The mass transport calculations when the room is under positive pressure, i.e., for the two levels of treatments – 70% airflow and 100% airflow.
- c) The flow patterns near the door opening periphery, as obtained from the sensors placed along the door opening periphery, namely, sensors in locations P1 through P3.

Flow patterns from door openings inside the chamber

The velocity magnitude data obtained for 60 seconds at every location during different experiment setups were analyzed to understand the alterations in indoor airflow characteristics influenced by the door movement. These findings are discussed in this section according to the measuring system locations.

Door Opening Once – Still Air

As explained in the method section, the door was opened at the first second of the tests. There was considerable delay after which an increase in the flow velocity was measured, meaning all the sensors recorded values of changing velocity after the airflow had already begun passed them. The increase in air velocity was logged quicker at sensor location 1 for all four rows (L11, L21, L31, and L41) at both elevations than sensors located further from the door. The observations are further broken down according to the elevations where the sensors were mounted.

Lower Elevation Sensors:

The temporal characteristics of a flow velocity as captured by sensors at the lower level displayed location-specific trends according to the arrangement in the imaginary rows

(Figure 23). As can be seen from Figure 25 in the first row, LL11 was the first sensing station recording an increase at second 3, as it was the closest to the tip of the door. LL12 recorded the first instance of airspeed increase at second 5, whereas L13 and L14 started to log higher velocity values from second 11. The first and second sensing stations recorded the same highest magnitude of airspeed of 0.51 m/s at 15 seconds and 19 seconds, respectively. It is also apparent that the drop after attaining the highest velocity was steeper for sensors LL11 and LL12, whereas for LL13 and LL14, the changes in the velocity magnitudes were smoother. The sensors located farther from the door, i.e., LL13 and LL14, recorded velocity greater than 0.1 m/s until almost 50 seconds, when velocity magnitude dropped to near zero by second 40 for LL11 and LL12. These findings suggest the temporal propagation of velocity fields.

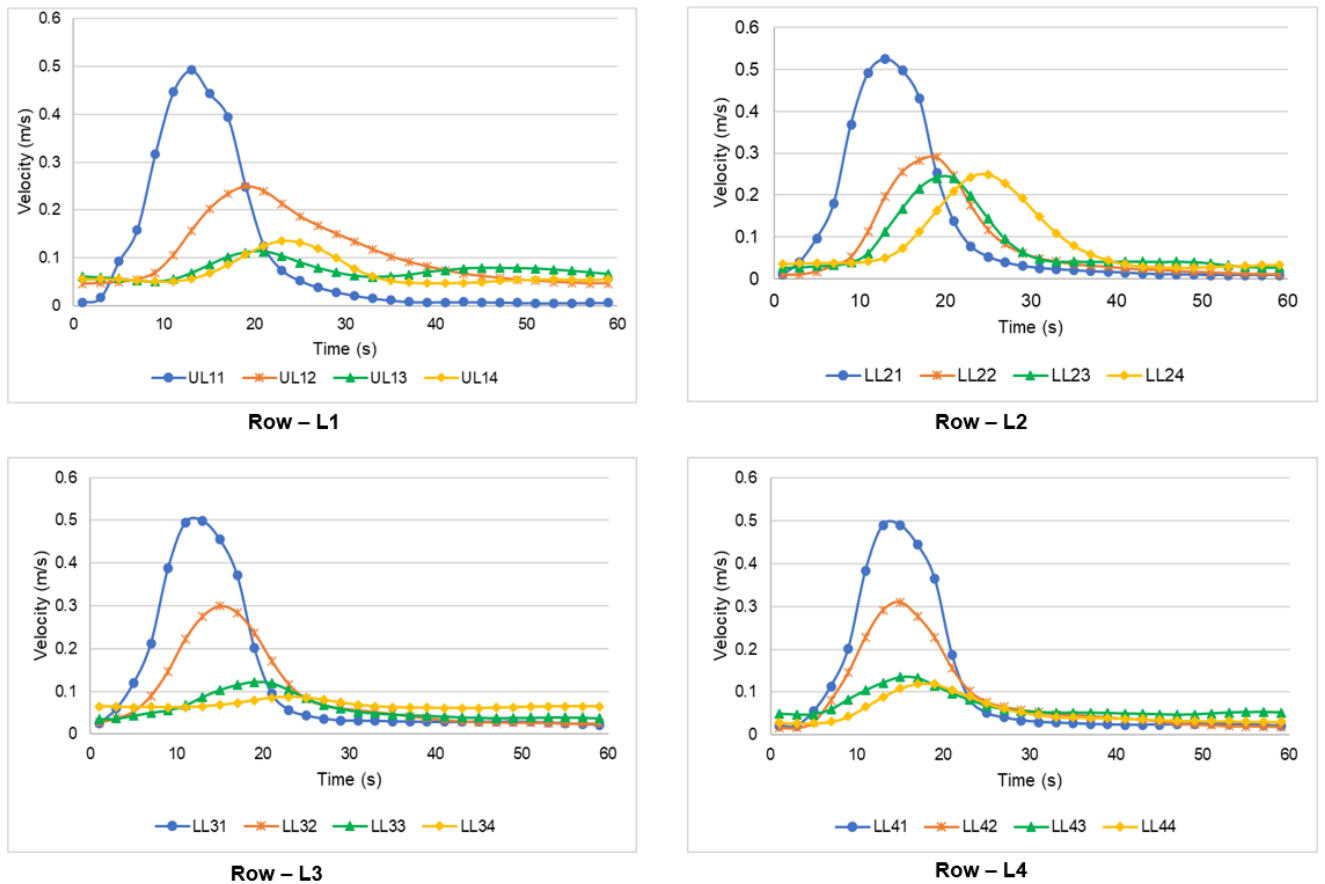


Figure 25: Temporal velocity trends for lower elevation sensors - door-opening once

At row L2, a significant change was observed – the highest recorded velocity at LL22 (0.29 m/s) was nearly 45% of the max value recorded at LL21. In this row, LL23 and LL24 had mostly similar velocity magnitude values compared to LL13 and LL14, respectively.

In the next row, L3, the first and second sensors recorded similar peak velocity as in row L2 (0.51 m/s and 0.29 m/s, respectively). Whereas LL31 logged the highest velocity at the time equivalent to that of LL11 and LL21, the sensor LL32 reached the maximum velocity quicker than that of the second sensors at rows L1 and L2. A similar trend was observed for the sensing station LL33, which had the highest velocity of 0.12 m/s at second 19. The farthest sensor, LL34, did not record much change in terms of air velocity from the door motion, but a small change in velocity magnitude is apparent around 23 seconds. The next set of sensor locations had some unique observations - the sensing stations in row L4 recorded the change of velocity at a similar time frame, unlike previous rows, which have distinguishable lag corresponding to the increasing distance of sensors from the door. LL41 and LL42 logged slightly reduced highest speed as compared to L2 and L3, but at the same time – second 15, which is 4s quicker for LL42 than the highest recorded velocity by LL12. Likewise, LL43 and LL44 also peaked at least 5s and 6s earlier than the sensors at the same locations for the other three rows.

Higher elevation Sensors:

With the initial condition of quiescent air inside the chamber, Figure 26 displays the temporal changes in the velocity profile for the sensors at the higher elevations. The sensing stations located closest to the door, i.e., UL11, UL21, UL31, and UL41, had logged the changes in air velocity with minimum lags, and they had recorded peak velocity in the order of ~ 0.49 m/s. Apart from these sensors at location 1 for all four rows, the sensors at locations 2, 3, and 4 in all the rows recorded the surge in velocity after sometime (i.e., with a comprehensible lag), which could be correlated to the distance of these sensors from the

door. The measuring units closest to the door and the following ones (sensors at locations 1 and 2) recorded an identifiable change in speed at all four rows of measurement stations, whereas sensors 3 and 4 recorded airspeeds more than 0.1 m/s only at row L1. The time of the highest observed velocity at row L4 was quicker than at row L1.

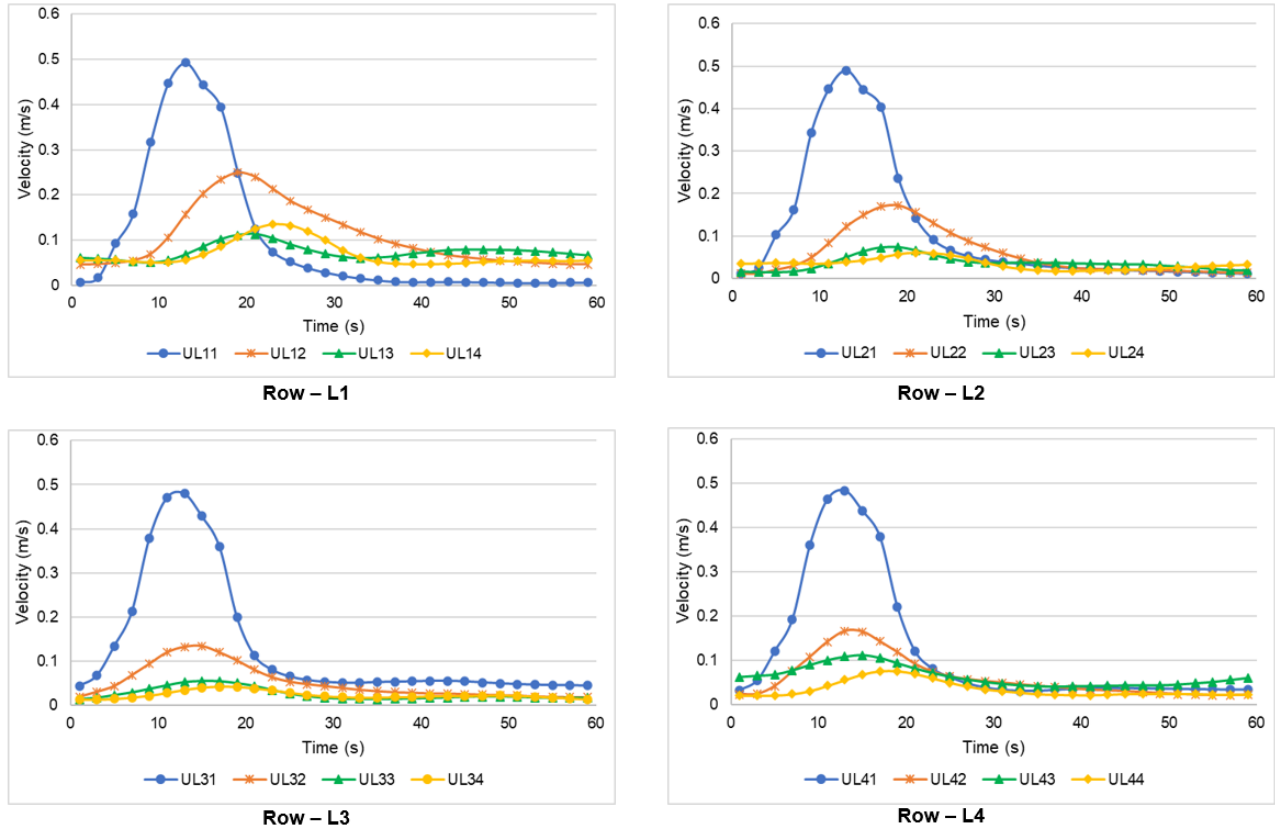


Figure 26: Temporal velocity trends for higher elevation sensors - door-opening once

Another noteworthy observation was that peak velocity magnitudes were recorded two seconds earlier in all the rows compared to the sensors at the lower elevation. Table 18, which compares the velocity profiles at the two different altitudes of sensor mounting, describes that only the values recorded by the sensors close to the door tip (location 1) were comparable between two different elevations. In contrast, other sensors (i.e., sensors at

locations 2, 3, and 4) at the higher elevation registered almost half of what the lower elevation sensors had recorded.

Door Opening Twice – Still Air

The observed temporal trends for air movement characteristics corresponding to opening the door twice with still air were comparable to that of opening the door once with quiescent conditions inside the test chamber, albeit door opening twice resulted in higher velocity magnitudes and a greater area under the curve of velocity plotted against time. It was found that the omnidirectional sensing systems used for the experiments did not record any drop in velocity magnitude at any position due to the 2 s recesstime between the two consecutive door opening activities. Even though both sets of door operations are completed close to second 12, and presumably the wakes carried by moving air hovered past the sensors sometimes close to that, a lag of at least 5 s was observed. Assuming the highest velocity was obtained from consecutive door openings, the earliest recorded maximum velocity magnitude was at the first sensors located the closest to the door at the corresponding time of second 17.

Lower Elevation Sensors:

As already witnessed during door opening once, the measuring units at the beginning of the rows (i.e., at location 1), being at the closest proximity to the door, recorded the highest magnitude of the airflow speed, which was 0.79 m/s for L1 and 0.76 for the other three rows - L2, L3, and L4. The measuring units located at the second spot in terms of greater distance from the door tip, i.e., LL12, LL22, LL32, and LL42, also captured substantial changes in air movement.

Table 18: The maximum velocity associated with the sensing stations and the time it occurred

Sensors at low elevation				Sensors at high elevation			
Sensor ID	Range of non-zero entries (s)	lag(s)	Maximum Velocity [Time it occurred] (s)	Sensor ID	Range of non-zero entries (s)	lag(s)	Maximum Velocity [Time it occurred] (s)
LL11	26	2	0.51 [15]	UL11	22	2	0.49 [13]
LL12	34	6	0.51 [19]	UL12	34	6	0.25 [19]
LL13	35	8	0.23 [21]	UL13	20	10	0.11 [21]
LL14	40	10	0.25 [23]	UL14	23	12	0.13 [23]
LL21	26	<1	0.53 [13]	UL21	26	<1	0.49 [13]
LL22	28	6	0.29 [19]	UL22	33	2	0.17 [19]
LL23	26	8	0.24 [19]	UL23	20	6	0.07 [19]
LL24	30	10	0.25 [25]	UL24	20	10	0.06 [21]
LL31	24	<1	0.5 [13]	UL31	24	<1	0.48 [13]
LL32	26	2	0.29 [15]	UL32	22	2	0.13 [15]
LL33	28	2	0.12 [19]	UL33	24	2	0.05 [15]
LL34	19	11	0.087 [23]	UL34	20	6	0.04 [17]
LL41	22	2	0.49 [13]	UL41	26	<1	0.48 [13]
LL42	30	2	0.31 [15]	UL42	26	2	0.17 [13]
LL43	24	4	0.14 [15]	UL43	24	4	0.11 [15]
LL44	26	6	0.12 [17]	UL44	22	6	0.08 [17]

For row L2, sensors at positions 3 and 4 also recorded significant changes in the temporal velocity profile. In rows L3 and L4, sensors at those positions did not record notable changes in the velocity magnitude. For row L1, the difference between the maximum speed readings at LL11 (0.79 m/s) was 25% higher than that of LL12. This was unlike door opening once, where recorded airspeed was equal for these sensors. Analogous to the readings of bottom layer sensors in door opening once, the time difference between sensors attaining the highest magnitude of velocity reduced from row L1 to L4, meaning the sensors at L4 logged the highest velocity in time quicker than at L3, and so on. In row L1, and more vividly observed in L2 (Figure 27), the sensors logged the highest velocity in a sequence when the closest sensors were the earliest to record the peak velocity and the farthest units to be the last, i.e., as a function of distance, providing additional evidence of a temporal pattern in the propagation of the velocity fields through the indoor airfield.

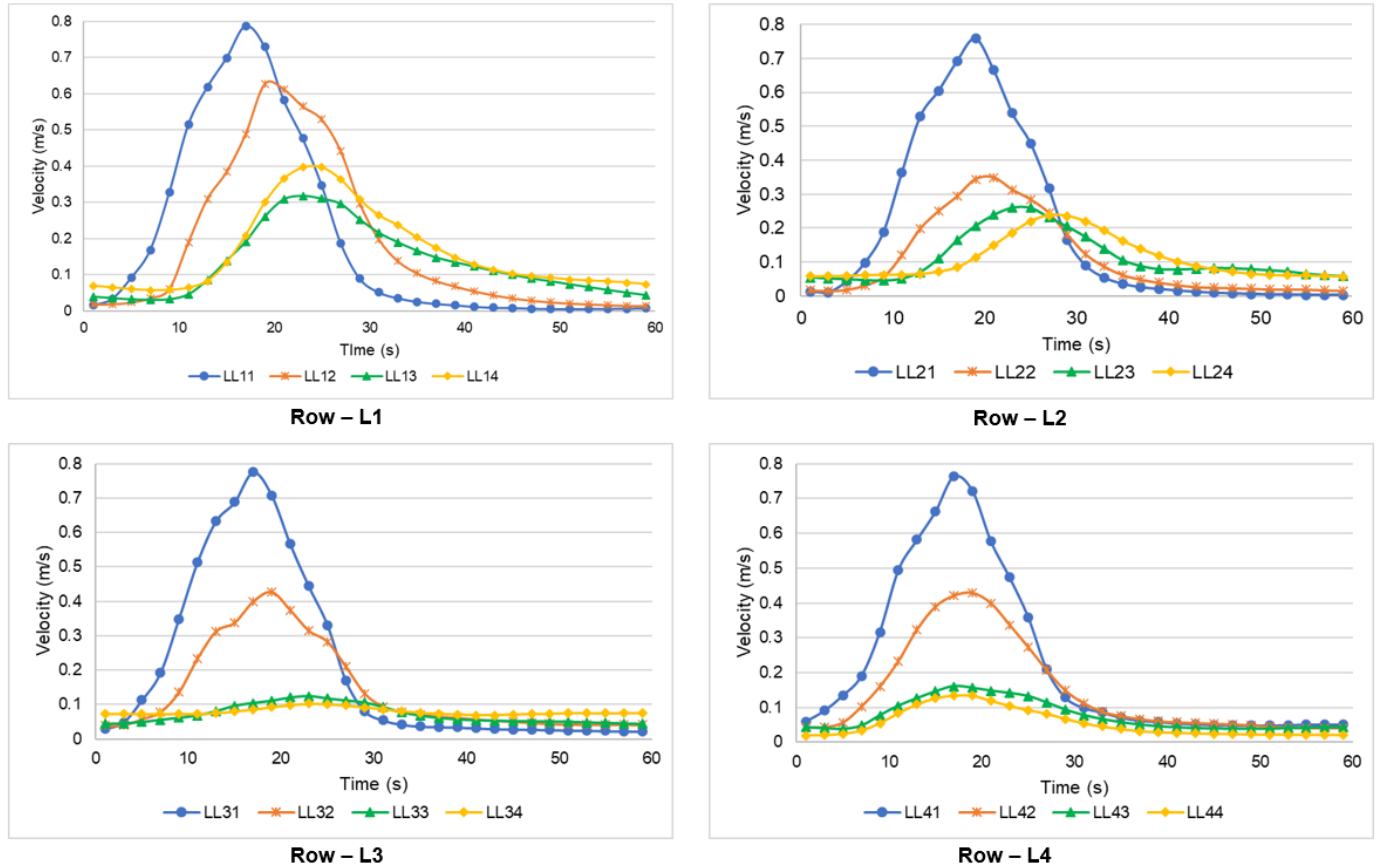


Figure 27: Temporal velocity trends at lower elevation sensors - door-opening twice

Higher Elevation Sensors:

Analogous to the results for test 1 (door opening once - no air supply), when the trends in the changes in velocity were comparable between the two altitudes of sensors with different magnitudes, the data from test 4 (door opening twice - no air supply) also showed that the change in velocity magnitudes at the upper elevation was commensurable with that of the lower elevation units, with decreased velocity magnitude.

As mentioned earlier, the instantaneous increase was logged by the sensors closest to the door, and the lag between when the wakes crossed the sensors and when the increased velocity was recorded was higher for sensors located further along the row, which can be presumed to be a function of distance from the door. An interesting fact, as observed from

Figure 28, is that similar to the units at the lower level, the peak velocity recorded at row L4 was concurrent at all four sensing stations.

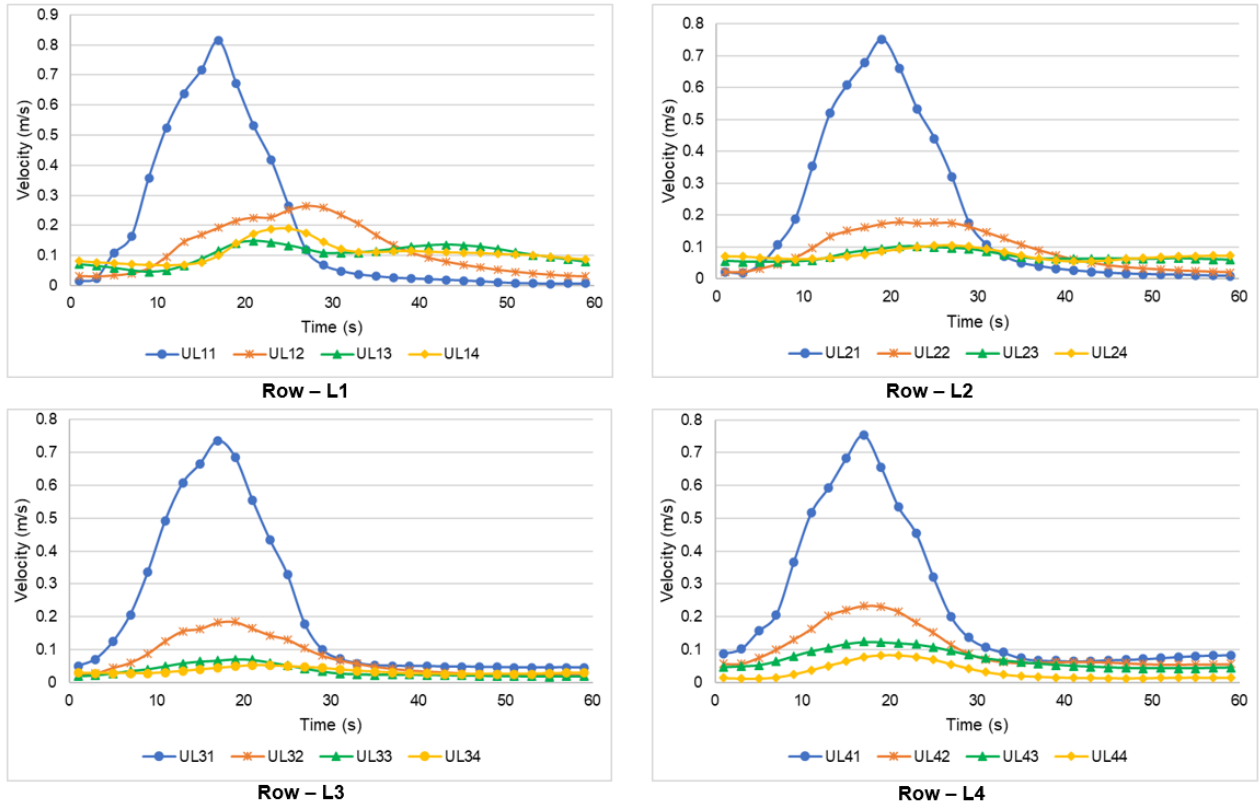


Figure 28: Temporal velocity trends at upper elevation sensors - door-opening twice

To compare the air velocity values originating from door opening once and twice, the time-averaged velocity magnitude (\bar{v}) at each location is shown in Table 19. Since, for most of the experiment scenarios, there was no significant change in velocities after 40s, the time-averaged calculation was done using equation 18.

$$\bar{v} = \frac{\sum_{t=1}^{40} V}{N} \quad \text{Equation 18}$$

Here v is the velocity magnitude, recorded at each timestep at an interval of 2 s, and N is the total no. of data points from second 1 to 40. As expected, the largest differences in the velocity profile from opening the door once and twice were corresponding to the sensors closest to the door tip, nearly a maximum of 1.5 times at the lower elevation and more than

2 times at the higher elevation, while the least proportions corresponding to the farthest sensors.

Table 19: Change in velocity proportion from opening once to twice at all sensor locations

Sensor ID	Door Opening Once	Door Opening Twice	Velocity Proportions	Sensor ID	Door Opening Once	Door Opening Twice	Velocity Proportions
Column	A	B	B/A	Column	A	B	B/A
LL11	0.1504	0.1962	1.3	UL11	0.1431	0.268	1.87
LL12	0.1824	0.1821	1	UL12	0.1318	0.1518	1.15
LL13	0.1258	0.1342	1.07	UL13	0.0739	0.1012	1.37
LL14	0.1426	0.1629	1.14	UL14	0.0753	0.1137	1.51
LL21	0.1597	0.1911	1.2	UL21	0.1547	0.2731	1.77
LL22	0.1029	0.1103	1.07	UL22	0.0766	0.1125	1.47
LL23	0.0932	0.1122	1.2	UL23	0.0404	0.0744	1.84
LL24	0.1063	0.1088	1.02	UL24	0.0376	0.0769	2.05
LL31	0.1556	0.2033	1.31	UL31	0.1645	0.2808	1.71
LL32	0.116	0.1401	1.21	UL32	0.0634	0.0929	1.47
LL33	0.0683	0.0715	1.05	UL33	0.0282	0.0404	1.43
LL34	0.0694	0.0789	1.14	UL34	0.0238	0.0364	1.53
LL41	0.1495	0.2218	1.48	UL41	0.1563	0.2971	1.9
LL42	0.112	0.1485	1.33	UL42	0.0753	0.1242	1.65
LL43	0.0745	0.0758	1.02	UL43	0.0695	0.0832	1.2
LL44	0.0613	0.0546	0.89	UL44	0.0395	0.0397	1.01

The steady-state condition before operating the door was quiescent air, and the door movement was the only physical movement present in the test chamber. There were changes in the air velocity with no other motion than the swinging door movement, clearly attributable to door movements. It is observed in the previous figures that the first sensors in every row recorded a higher magnitude of air velocity that resulted from the door opening and closing compared to the sensors located farther into the room. According to the sensing station arrangement scheme, sensors in row L1 were along the wall parallel to the closed door. When the door started to open, the moving door provided a thrust that got the air moving, and the subsequent movement transferred the momentum to the air, generating wakes in the air over the background. The recorded movements of the airflow wakes were mostly associated with the leading door tip, with other weaker wakes following. When the door was completely open and remained ajar for a second, the wakes started to dissipate further into the chamber, but then the closing movement

started, providing another motion to generate vortices in the already moving air. During the closing movement, the flow field had residual velocities moving along the direction of the opening movement. The closing operation forced the air to move in a contrasting direction, generating turbulent vortices and raising the magnitude of air velocity in the flow field.

The frequency of the sensing system, which recorded one data point every two seconds, was not responsive enough to record and reflect all the fluctuations of the air velocity. From what can be observed in the previous figures (Figure 25 to Figure 27), the location-specific fluctuations in the flow velocity represent the cumulative flow field resulting from the cyclic door motion – consisting of opening and closing. In row L1, the velocity magnitudes recorded through sensors located further from the door were higher than in the other rows as the wakes propagated further in the presence of the stationary wall. In the proximity to the wall with higher velocity gradients present, the flow field was unable to dissipate; instead, the boundary acted as a surface that aided in the wakes' translation along its length. Also, after the door was closed, there was no other movement to alter the flow of moving air, and it continued to propagate. One can see that maximum velocity magnitude and the time of logging by the sensors were functions of distance from the door. It is also noteworthy that in row L4, the temporal distribution of maximum airspeed was almost concurrent for all the sensors. At the end of the door opening, the air was moving forward along that row, but the sudden movement for the closing of the door got the air moving again, in altering directions, drawing the air streams back towards the sensors; hence all of them peaked with negligible intervals between them.

The sensing stations at the lower elevation were found to have logged higher velocity magnitude than that of the higher-level ones. This phenomenon was attributable to the increased interaction between the moving air and the floor – which could be presumed as a stationary wall with the zero-slip condition. The presence of a boundary (the floor) restricted the quick dissipation of flow fields, aided by the resurfacing of settled particles during the closing motion raised turbulence

which affected the flow plane captured by the sensors at lower elevation. The absence of any such boundary near the sensors at the higher elevation was an additional testament that the presence of a boundary has a profound impact on the indoor flow fields.

A higher magnitude of velocity was recorded for operating the door twice compared to a single opening and closing of the door. Understandably, the residual movements in the air inside the test chamber from the opening and closing of the door for the first time were the initial condition for the second cycle of door operation. Physical movements in the presence of an existing airflow resulted in increased turbulence and faster-moving vortices, which were captured at higher speeds in Figure 27 and Figure 28.

Mass Transport Calculation

The placement of sensors brought about the opportunity to calculate air mixture at the door due to door opening for various pressurization scenarios. The ultrasound sensors placed immediately around the opening radius of the door were used to measure the three-dimensional velocity components of air around the door. The results of velocity measurements by the ultrasound sensors were reported in the global Cartesian coordinates shown in Figure 29. Conversion of these values to a cylindrical coordinate was convenient in order to measure the mass flow of air through the radius of the opening.

Formally, the rate of mass transfer on the door swing surface, denoted by \dot{m} , is $\dot{m} = \frac{dm}{dt}$.

Assuming a constant density of air in ambient temperature, we have,

$$\dot{m} = \frac{dm}{dt} = \rho \frac{dV}{dt} = \rho \frac{ds dr dz}{dt} \quad \text{Equation 19}$$

It must be noted that the tangential (ds) and vertical (dz) differential elements do not change with time where the change of the radial term (dr) with time is (\vec{v}_r) . Therefore,

Equation 19 will take the following form.

$$\dot{m} = \oint \rho v_r ds dz \quad \text{Equation 20}$$

Knowing that $ds = R d\theta$, where R is the radius of the door, one can write \vec{v}_r based on its \vec{v}_x and \vec{v}_y components, which is what was measured by the ultrasound sensors (Figure 30). Thus, Equation 20 will turn to:

$$\dot{m} = \oint [\rho R (v_x \cos \theta + v_y \sin \theta)] d\theta dz \quad \text{Equation 21}$$

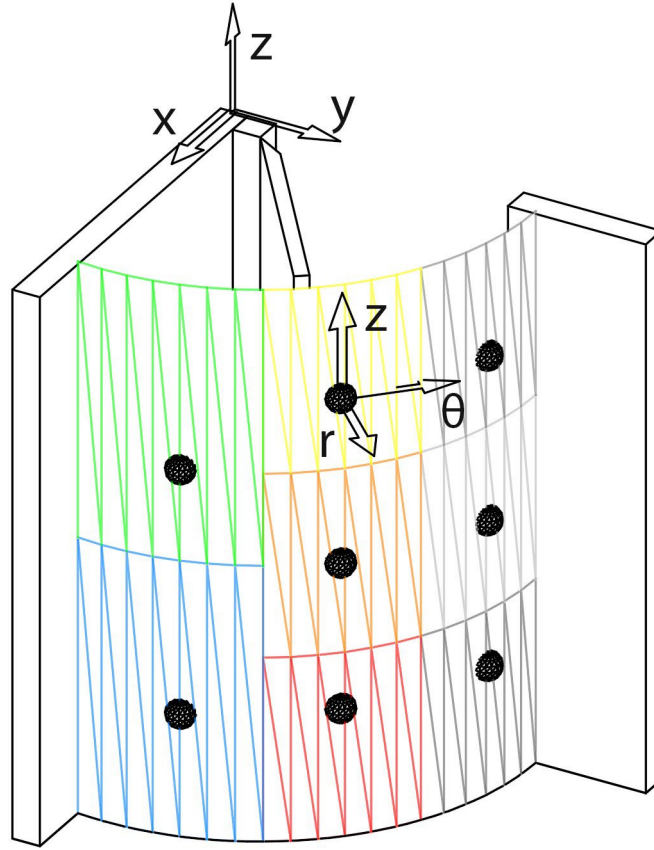


Figure 29: Placement of Sensors and Coordinate Definitions

Ideally, the radial component of velocity (v_r) varies as a function of θ and z , and the integral in Equation 21 can be numerically calculated to find the rate of mass transfer through the surface S . In our test setting, however, we only had measurements of air

velocity in eight fixed points. Thus, to solve Equation 21, we assumed that velocities measured by each sensor embodied the region around it, as demonstrated by Figure 7.

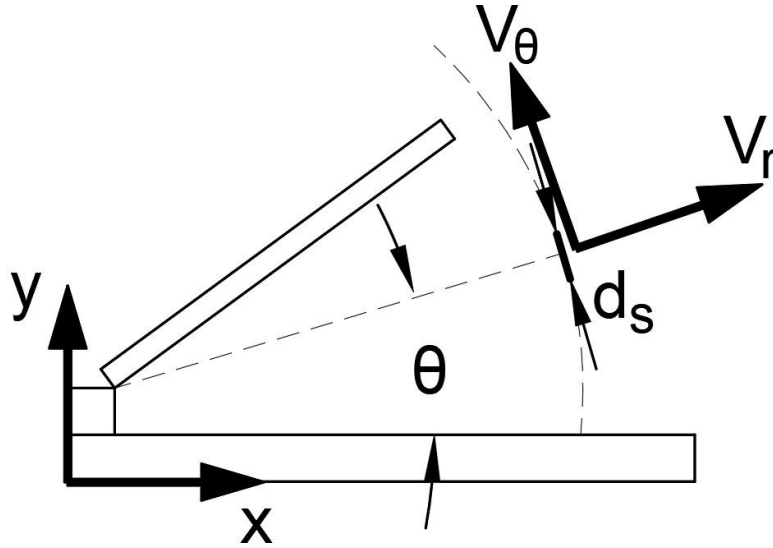


Figure 30: Cartesian and Cylindrical Coordinates Conversion

The ultrasound sensors collected 6 data points per second, that is, 12 data points from a fully closed to a fully open status, a total of 30 data points for a full door opening cycle (i.e., 5 seconds). To match this, \mathbf{S} was discretized into 12 vertical sections, each covering three different measurements from the vertically aligned sensors (Figure 29). Further, the opening degree of the door (θ) is also a function of time, and it dictates the angular width of \mathbf{S} , i.e., the space that is exposed to the outside. Algorithm 1 was used to calculate \dot{m} . Note that both T_i and v_r are functions of time, and v_r for each piece was embodied by the sensor measurements within its region. One can also take the integral of \dot{m} with respect to time to obtain the amount of air mixture across the door. Based on the coordinate convention and consistent with the positive direction of v_r , negative mass flow means air leaving the room, and positive mass flow means air entering the room.

In the absence of pressure differentials across the door, air mixing took place both ways. Initially, air entered the room following the inward door swing ($< 1.0s$). Immediately after, the room air made up for the temporary vacuum created by the large boundary movement by

leaving the room and creating vortexes at the tip of the door (~ 1.5 s). Then air from the outside began to entrain into the room until the closing cycle started (~ 3.5 s). Then the closing door pushed air out of the room ($\sim 3.5 - 5.0$ s) (Figure 31). Air velocities inside the room approached background values nearly 10s after the door was completely shut.

Algorithm 1 Grid-based Monte Carlo Approach

Let S be discretized into n equal vertical pieces of $\langle s_1, \dots, s_n \rangle$

Let a full door opening cycle takes $N = 30$ timesteps (i.e., 5 s)

for $t = 1, 2, 3, \dots, N$ **do**

Define $T_{1 \times n}$ vector (initially zero) to determine the exposure of each piece to the outside

if $t < 12$ **then**

$T(1:t) = 1$: opening cycle

else if $t < 18$ **then**

$T(1:\text{end}) = 1$ 😊 hold – open cycle)

else

$T(1:t - 18) = 1$: closing cycle

end if

end for

$\dot{m} = \sum_{i=1}^n T_i \cdot v_r$

This intermittent pattern of mass flow rate was observed in all three cases, namely when the door was opened once and both laps of opening twice. Slight differences in air velocities right before door opening started (i.e., slightly different initial conditions) resulted in respective variations in the data, yet the overall pattern indicated that the effect of the door opening could prevail over these small differences in the flow. Furthermore, the absence of pressure differential facilitated the mixing of air in both ways, though the total air exchange was nearly zero. These patterns changed dramatically by introducing positive pressure as the inward patterns followed by the door opening (2 – 3.5s) were suppressed by the positive pressure. In the presence of positive pressure, the 'balanced-mixing' across the door was changed to a 'directional pathway' from inside to room outward (i.e., negative mass flow rate values).

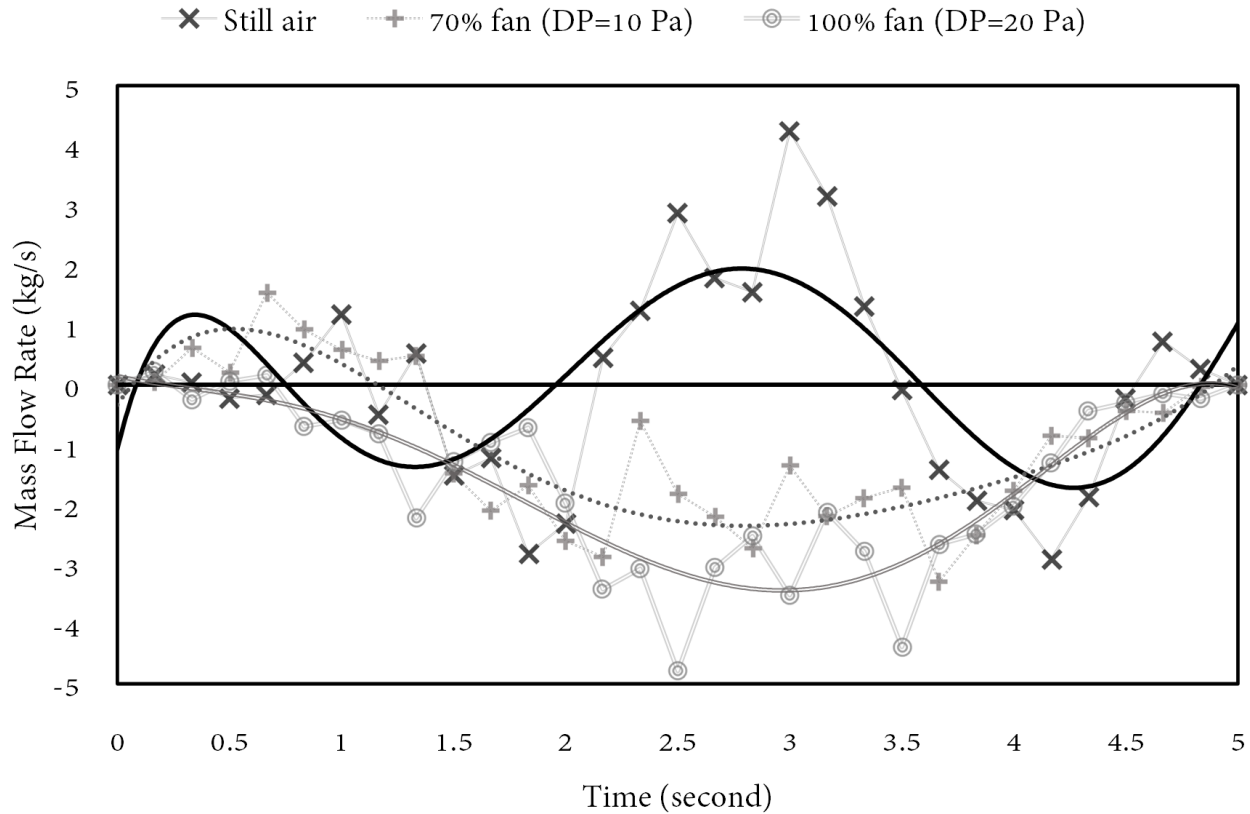


Figure 31: Mass flow rates in kg/s during door opening for various test conditions

Areas under the curves shown in Figure 30 indicate the total transport of mass (kg) across the door (Table 20). To put this in context, for $\Delta P = 37\text{Pa}$, nearly 8.5kg of air leaves room per door opening, which is equivalent to 7.5m³ of air when divided by the density of air ($\rho = 1.125\text{kg/m}^3$). Literature shows that, on average, the operating room door is operated once every three minutes (E. S. Mousavi et al., 2018). Therefore, during one hour of an average surgery, $20 \times 7.5 = 150\text{m}^3$ of air can leave the operating room. This is twice the test chamber volume, meaning that nearly 2 ACH of air escapes the operating room and enters the adjacent corridor only due to door openings. This number is equal to the ventilation rate required for patient corridors by Standards (ASHRAE Standard 170, 2013). If contaminated by the SARS-COVID-2 virus, this air can potentially spread into the adjacent corridors and jeopardize the safety of the medical personnel in the hallway.

Table 20: Total amount of air exchange (kg) across the door for different pressure differentials and door openings

Door opening Case	Still Air ($\Delta P = 0$ Pa)			70% fan ($\Delta P = 22$ Pa)			100% fan ($\Delta P = 37$ Pa)		
	entering air	exiting air	net	entering air	exiting air	net	entering air	exiting air	net
Opening once	3.38	-2.82	0.56	2.5	-7.53	-5.03	0.00	-7.58	-7.58
Opening Twice-First Lap	4.41	-3.88	0.53	0.63	-6.40	-5.77	0.09	-8.85	-8.76
Opening Twice-Second Lap	4.09	-4.93	-0.84	0.12	-4.70	-4.58	0.94	-8.81	-7.87

Transient flow patterns from door openings near the door opening periphery

The temporal patterns of air movement at the sensing stations near the door swing periphery were analyzed using the cartesian velocity components obtained from the ultrasound sensors. As discussed previously, these sensors reported 6 data points of velocity components per second at every location.

Door opening once

During Test 1, when the existing initial condition was quiescent air, and there was no other movement than the door movement, changes in three-dimensional air velocities were recorded. The transient pattern is depicted in Figure 27. At the onset of door opening motion, the sensing station at P1 recorded an increase in airspeed with a 1-s lag. The highest magnitude was recorded at 2.1 s, as the air with a high magnitude of velocity followed the moving door. The sensing station at P2 began logging an increase in airspeed from second 3.5, reaching max during the opening at second 4.5 and again peaked during closing at second 5.3. It is noteworthy that the magnitude was higher during closing

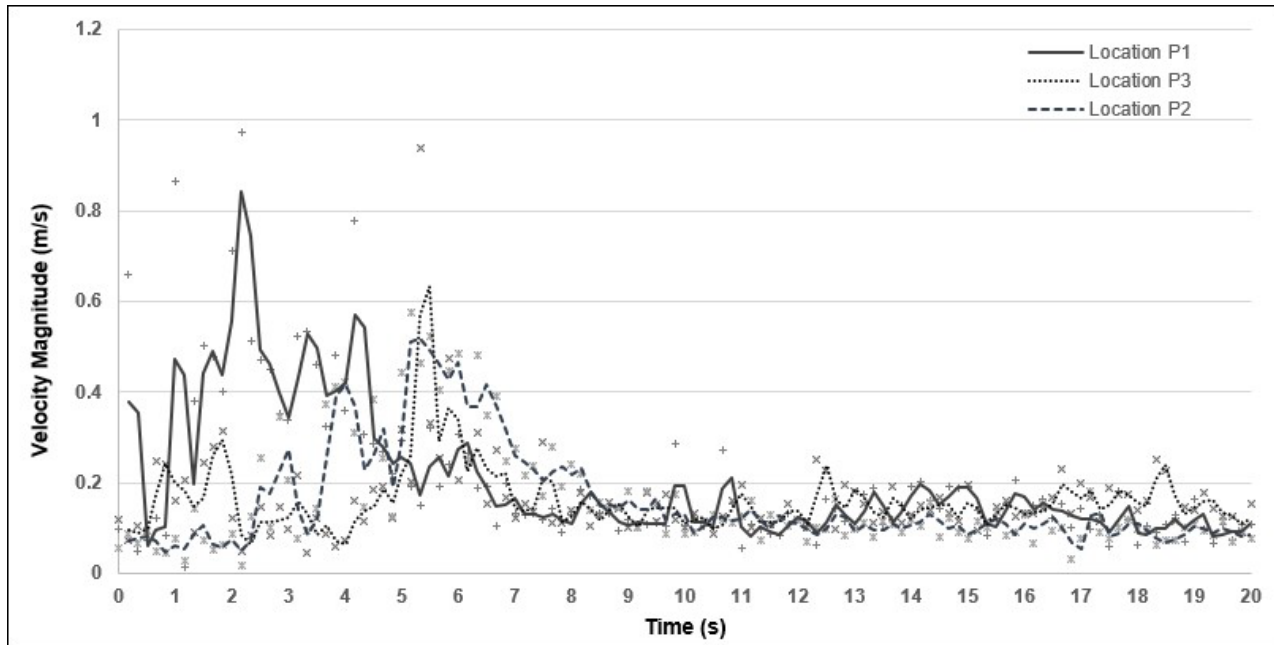


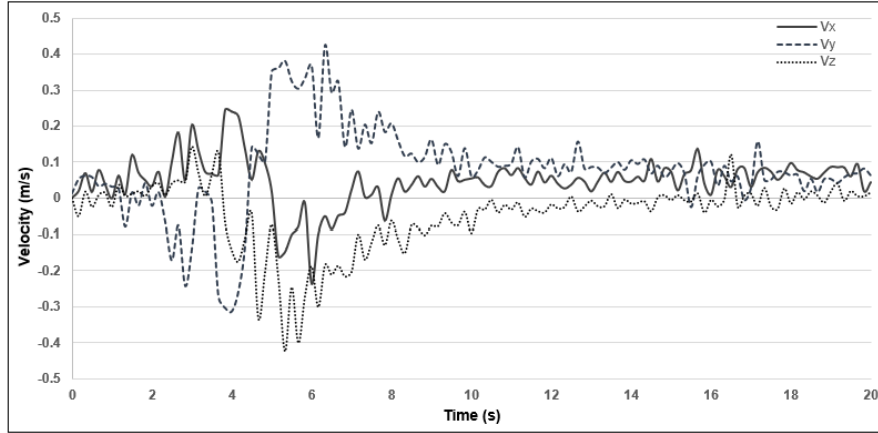
Figure 32: Transient Pattern of Airspeed from Door Opening Once (Test 1)

compared to opening motion. During the opening movement, the initial condition is still air. But while closing, the air in the chamber had a presupposed motion resulting from the door opening. Closing the door created a motion, reversing the direction of the previous one, probably affecting the change in velocity. At location P3, there is an initial surge, probably due to the impetus exerted by the door opening that carried the previously stagnant air quickly to the wall. During closing, the moving door extracts the air inside the chamber, and the wakes following the closing door were recorded at location P3, which showed a peak quickly after the closing motion was complete. Figure 32 demonstrates these changes in velocity magnitude plotted against time. Even though the magnitude of air had significant patterns that correspond to the door opening and closing duration, the velocity components obtained from the ultrasound sensors facilitated elaborated analysis of door movement. At the beginning of the door opening, the moving door was pushing the still air inside the chamber, which was recorded as a surge in velocity in the positive x-direction (as shown in Figure 29), and for a small duration, a negative y-component (normal to the door opening

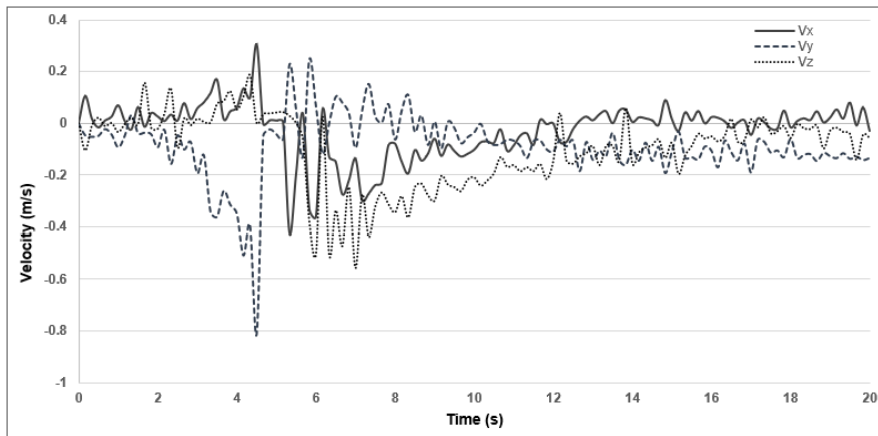
direction at $t = 0$ s) of the velocity was detected in location P1.

As the door continued to open, airwaves were carried with the door, and the y-component of velocity was recorded as negative at point 2, as at this point, the principal direction of air movement was opposite to the defined y-axis. Moreover, the x-components of velocity were flowing towards the interior of the chamber, i.e., the positive x-axis. At location P3, when the door was completely open, the generated wakes were being carried by the swinging door. The y-component of the velocity was found to be in the negative direction. As the door started closing, this component became positive. At the end of the door opening, the moving air came across and moved along the wall perpendicular to the closed door, and a surge of velocity in the positive x-direction was recorded. While closing, the door dragged the moving air back with the wakes generated, principally in the direction of the negative x-axis and positive y-axis, as recorded in measuring units located at both P3 and P2. This change in the direction of the x-component and y-component while opening and closing are distinctly identifiable in Figure 11. These elevations in velocity components were prevalent until the second 15. After the door was fully closed, all components of velocity became stable and near zero, as the air near the door became motionless while the flow field approached steady state given the absence of any further disturbance.

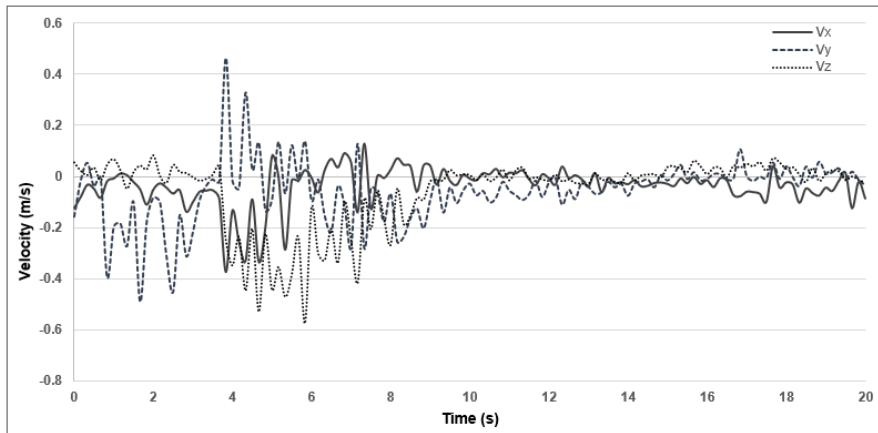
During Tests 3 and 5, air was being supplied in the room, creating a positive pressure inside the chamber. With the supply fans operating, as soon as the door opened, air started moving outside, captured as an increase in negative x-velocity at location P1. But the movement of the door, opening against a large differential pressure, displaced a large amount of air, which was captured by the increase in velocity components in the positive y direction at this point in space. The existing air inside the chamber was being pushed during the opening movement, being recorded as positive in the x-direction and negative y-component at the middle of the door movement curve. With continued opening motion of the



(a)



(b)



(c)

Figure 33: Cartesian components of velocity at location P2 for (a) Test 1, (b) Test 3, and (c) Test 5

door, there was more space for the positive pressure to push the air out of the chamber, resulting in the increase in negative x-component of the air velocity. Analogous to the test cases with still air, at the end of the opening motion, the wakes generated were pushed inside

the chamber, surging the positive x-component and negative y-component at the end of opening cycle, at location P3. But due to the positive pressure, coupled with the closing movement of the door, the prevalent air movement due to the opening motion was reversed quickly. Even though, the results obtained with fan operating at 70% and in full capacity were similar, higher quantities of supply air (i.e., higher pressure differentials), resulted in comparatively less significant changes in the flow fields inside the chamber due to the door movement. Lower magnitudes of velocity were observed, and the x-component of velocity was consistently negative, implying almost no air entering the room under this condition (Figure 33).

Door opening twice

The experiments consisted of two consecutive opening and closing cycles; the first cycle of the door opening and closing, was analogous to those of the experiments involving single door opening and closing. For the test with no ventilation (Test 2), the sensor at location P1 recorded the increase in velocity instantaneously, peaking at close to 3 seconds for the first time opening. Instruments at location P2 also recorded the surge for opening and then a higher magnitude during closing at around 3.5 s and 5.3 s, respectively, for the first round of door operation. But, during the second cycle of door opening closing, the speed recorded was higher compared to the first cycle, owing to reasons attributable to the interaction of the repeated motion with the residual movement from the first cycle. Figure 34 shows the immediate rise in air velocity, recorded by the measuring device in location P1, followed by P2 and P3. The closing motion that followed the door opening and then another set of consecutive opening and closing for the second cycle stirred the stagnant air resulting in higher velocities. The surge in velocity magnitude for the second time door operation was apparent visible for both Tests 4 and 6, as depicted in Figure 34 for Test 4. Interestingly, significant changes in velocity magnitude were recorded up to 10 seconds for Test 2 and 15 seconds for Test 4 and 6 after the door movement was stopped.

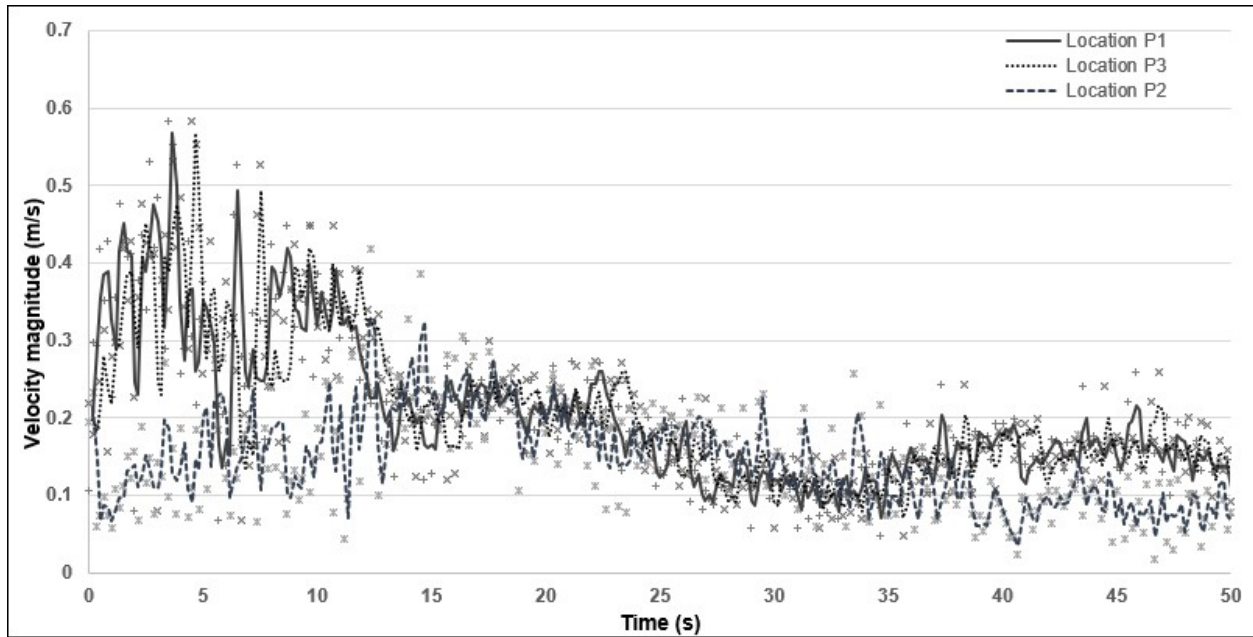


Figure 34: Transient pattern of Air Speed from Door Opening and Closing Twice (Test 4)

The 3-dimensional velocity component data, obtained using the ultrasound sensors, revealed more details regarding changes in the airflow pattern when the swing door is operated consecutively. The data demonstrated similar behavior of airflow patterns during the second cycle of door operation when compared to the first cycle, with different magnitude.

Spatial Distribution of velocity wakes inside the test chamber

The data obtained from the peripheral ultrasound sensors indicated the behavior of the flow fields near the movement zone. The radial arrangement of the omnidirectional sensors provided the data to analyze the spatial distribution of the wakes inside the chamber. The dissipation of velocity fields showed the impact of the door movement could last long after the door movement ceased.

Figure 35 compared the velocity fields in the test chamber for standalone and consecutive door opening exercises with the supply fan on working mode. For Test 3, at the initial periods of the door opening, the isometric lines with higher velocity fields are concentrated in the movement zone and spread through the space with time. Two seconds after the door closure for Test 3,

areas with significant velocity magnitude (> 0.1 m/s) were found up to 2 m from the tip of the door into the chamber. By 10 seconds after door closure, this field with velocities > 1 m/s penetrated 4.5 m inside the chamber. During Test 5, when the supply fan was operating at full capacity, the interaction between the external movement generated wakes and the high-velocity supply air resulted in a rise in the airspeed, more than in all the previous tests. Nearly everywhere in the chamber recorded velocity magnitudes greater than 1 m/s after 14 seconds of door closure, at which time the maximum airspeed recorded was 0.5 m/s. At second 23, 4 m inside the chamber, a maximum airspeed of 0.25 m/s was present. Starting from second 29, the fields started to shrink, and by second 39, the maximum speed reduced to 0.14 m/s.

When the test set involved the movement of the door twice, for Tests 4 and 6, the magnitude of the velocity fields was found to be slightly increased compared to Tests 3 and 5, respectively. Data obtained during Test 4 showed that the wakes with a velocity up to 0.12 m/s were present nearly 4 m inside the chamber. Even after 23 seconds since the first door opening began, > 1 m/s magnitude of velocity was measured at a distance of 4.75 m from the door. Notably, by second 23, higher velocity magnitudes, more than 3 times that of Test 3, were concentrated near the exhaust location.

During Test 6, by second 19, the maximum velocity magnitude inside the chamber was 0.6 m/s, owing to potential turbulence during consecutive door movements. From second 29, the supplied airflow started to push the wakes towards the exit, but velocity magnitudes were present deep inside the chamber even at second 35.

It should be noted that the heatmaps presented in Figure 35 were created considering zero slip conditions at the walls. The known location and magnitudes of velocity, obtained from the radially arranged omnidirectional sensors, were interpolated to find the velocity values in the chamber that was discretized in a grid of size 110×109 , where a square grid dimension was 5 cm.

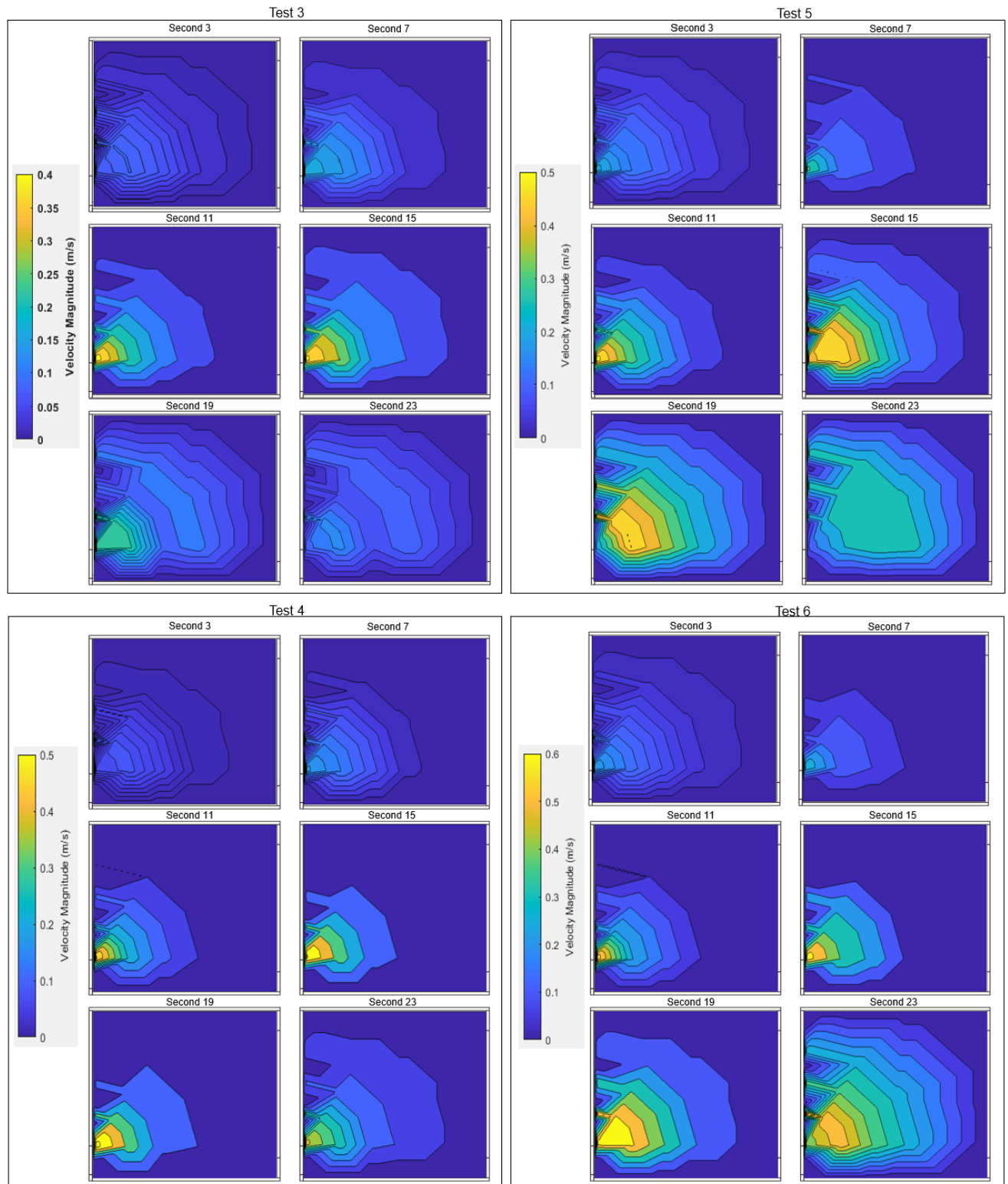


Figure 35: Spatial Distribution of Velocity Fields

Kinetic Energy

The movement of the door imparted the kinetic energy into the moving air, which is proportional to the velocity, raised to the second power (Equation 22). Additionally, the time-averaged kinetic energy of door opening (K_{do}) and background kinetic energy (K_{bg}) are defined as follows:

$$K = \int mv \cdot dv \quad \text{Equation 22}$$

$$K_{do} = \frac{\int_{t=3s}^{23} v^2}{(23 - 3)} \quad \text{Equation 23}$$

$$K_{bg} = \frac{\int_{t=40s}^{60} v^2}{(60 - 40)} \quad \text{Equation 24}$$

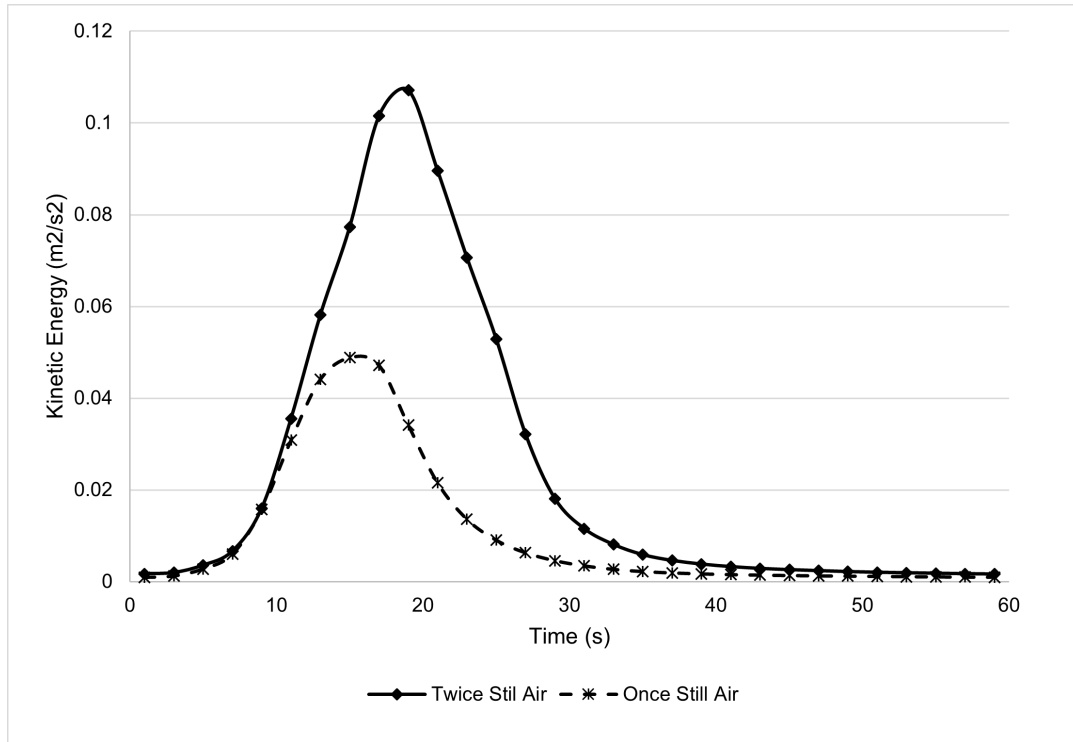


Figure 36: Total Kinetic Energy of Still Air for two door opening schemes; sum over all sensor locations

As negligible changes in the air velocity were recorded by any of the sensing stations after the

second 40, the duration from 40 s to 60 s indicated the background kinetic energy (i.e., - the kinetic energy of the air without the impacts of the door movement), which in turn helps to demonstrate the change in kinetic energy due to the door movement. The kinetic energy at the onset of the door opening initiation was comparable for both the test scenarios, but admittedly, door opening twice was associated with a higher kinetic energy transfer involved for a longer duration (Figure 36). The ratio of kinetic energy between the two-door opening scenarios was close to 2 for the three different initial conditions, as shown in Table 21. For zero initial condition (i.e., - no fan operating) and 70% air, the kinetic energy for door opening is > 2 times that of the steady-state condition without any interference in terms of door operation. But, with the maximum air supply (i.e., the 100% fan), a part of the energy is spent to overcome the heavy resistance provided by the air mass inside the test chamber when opening the door, taking the proportion below 2.

Table 21: Time-averages Kinetic Energy for two door opening schemes

Initial Condition	Still Air		70% Fan		100% Fan	
	Opening Once	Opening Twice	Opening Once	Opening Twice	Opening Once	Opening Twice
K_{do}	0.0242	0.0516	0.0249	0.0483	0.0411	0.0682
K_{bg}	0.0012	0.0022	0.0042	0.0052	0.0129	0.0145
$\Delta K = (K_{do} - K_{bg})$	0.0230	0.0494	0.0206	0.0431	0.0281	0.0537
$\frac{\Delta K_{Twice}}{\Delta K_{Once}}$	2.15		2.09		1.91	

Limitations and Conclusions:

This study was conducted to examine the impacts of the door opening in a positively pressurized chamber, which can be hypothesized as an operating room where a COVID patient is to be receiving a surgical intervention. Air mixing across a swing door and the resultant alterations in velocity field inside the chamber have been studied. Several previous studies have investigated the volumetric exchange between spaces separated by a door, ensuring differential pressures at the two compartments from the numerical simulation approach (Lee et al., 2016; E. S. Mousavi & Grosskopf, 2016) and experimental approach (Gustavsson N., 2010b; Kalliomäki et al., 2016). Although some existing studies have looked into the changes in the velocity field due to door opening (Eames et al., 2009; Z. Lin et al., 2007; Papakonstantis et al., 2018; B. Zhou et al., 2018b), the changes in the properties of existing flow field due to perturbation induced through the door opening and closing motions, and the resultant mixing of supposedly contaminated air containing virulent strains from the patient, with the supplied air inside the chamber, are holistically analyzed in this work. These set of experiments had investigated the flow characteristics at steady-state and under the occupant-introduced disturbances by means of a door opening, aiming for a broader understanding, in part by measuring flow characteristics at different heights of the chamber. The experimental study was conducted in a sealed chamber with the capabilities of fresh air inlet at rates that generated sufficient positive pressure required for such a space. Access to a limited number of sensing instruments led to measurements in one-foot vicinity inside the chamber. This sensor placement scheme was thought out in such a way to capture a wider area inside the chamber, while still capturing plenty of data at the door movement periphery. The sensor placement was done intuitively, and no statistical design of experiments were conducted due to time and accessibility constraints. As the experiment chamber was controlled and maintained by the host institution, the research team had no control of the air distribution arrangements. Hence, even if it was understood that a single wall-mounted grille was not practical, the experiments had to be conducted with air supply from the wall mounted grille.

Experiments were repeated 60 times to ensure the consistency and repeatability of the outcomes. Due to a large number of tests and the restricted availability of the test facility, only two scenarios of the door opening and closing cycles could be defined. At the time of these experiments, the ultrasound sensors were not commercialized, and hence very few (17 out of 900 data points) unreasonable data logs were recorded (>2.5 m/s), and velocity values greater than three standard deviations of the overall mean values were discarded during data analysis.

This study indicated that the transient change in the velocity field from the door opening and closing was location specific – the points closest to the door tip responded to the changes quicker than those located farther, e.g., point 1 of the radial arrangements recorded changes quicker than point 4. Different points (P1, P2, and P3) in the vicinity of the door swinging radius were also found to respond according to the door's position while opening or closing. Emulating the opening and closing movement twice resulted in a further increase in the flow velocity. During opening the door for the first time, disturbances are introduced to the quiescent air inside the chamber. While closing, more disturbances are introduced to an existing velocity field, which results in increased velocity components. For Tests 3 and 5, i.e., one-cycle of the door opening under ventilated condition, lower velocity magnitudes were observed compared to Test 1. The existing airflow suppressed the effect of the door opening on the indoor flow fields. The second cycle of door movement interacted with the flow field under an existing motion exerted by the first cycle of door operation. Hence higher magnitude velocity components were recorded during Tests 2, 4, and 6, as compared to Tests 1, 3, and 5.

The spatial distribution had provided insights about unwanted air mixing due to secondary velocity fields originating from door movement. The increase in air velocity inside the chamber was due to the wakes carried by the moving door in the background air. These wakes dissipate through the chamber, and as they penetrate further into the chamber, the velocity field continues to decrease due to the lost momentum during transfer between air molecules. But with the supply

fan working, the interaction between the primary flow field due to inlet air and the secondary flow fields was higher and reached very far inside the chamber. Results from door opening twice indicated that with an increased number of door operations, the secondary fields were stronger, and the increased interaction resulted in deeper penetration of wakes inside the chamber. These results suggested that even with a high quantity of supplied airflow, the door operation can disrupt the predominant flow pattern. The perturbation is capable of sustaining long after the door was closed, carrying high-velocity air deep into the chamber. In a positively pressurized operating room with a contagious patient, this kind of air mixing is undesirable as the directional airflow from positive pressure differential is aimed to carry the contaminated air out of the facility.

A large proportion of this work aimed to quantify the air escape from the positively pressurized operating room due to door opening to gain insights about risks of air potentially contaminated with SARS-COVID-2 getting out, putting the health of healthcare providers at risk. This study found that with an inlet airflow rate of 190 cfm (90 L/s), 7.5 m³ of air can leave every time the swing door is operated. This translates to almost 2 ACH of air escaping during a typical surgical procedure, carrying contagions to the adjacent spaces. Future research would focus on utilizing the results of this study to imitate real-time operating procedures involving sporadic door opening for further validation. Optimization of positive pressurization and exhaust locations for such sensitive procedures involving pathogens such as SARS-COV-2 is also one of the main future research directions.

Chapter 7

Event-Based Approach for Modeling Airflow Patterns⁴

The previous two chapters described and quantified the effects of occupant introduced disturbances in a controlled and mechanically ventilated indoor environment. It was observed that the changes in flow patterns from the transient events like occupant movement or door opening in the controlled environment setting seem to follow a trend that can be mathematically modeled. It can be noted that the numerical simulation approach has been the dominant method of modeling indoor airflow but often oversimplifies the transient phases due to extremely large computational intensity, leading to unrealistic scenarios. As a result, the ventilation system designers often work with steady-state models to determine the air distribution and ventilation efficiency leading to overdesign of the system. To counter that limitation, a novel approach, called the ‘Event-Based Modeling’ (EBM), is discussed in this chapter to simulate airflow patterns for realistic human-environment interactions. The sporadic door opening, and walking movements are considered discrete events, and the flow patterns are accurately approximated using EBM. The EBM method is formulated and evaluated in this chapter and validated using the data obtained through the door opening experiments described in Chapter 6, more data obtained through numerical simulations.

Core Idea:

EBM proposes that repetitive human-environment interactions (e.g., walking) could be modeled once and be used multiple times. This approach can eliminate parallel modeling of the same phenomena. It must be noted that EBM does not require the events to be sequential. They can be simultaneous and/or have overlaps. The core idea of EBM is that every interaction between a subject and its surroundings can be broken down into a series of events. Consider a simple

⁴ Contents of this chapter are taken from (E. Mousavi & Bhattacharya, 2022) with permission from the co-author and the publisher.

scenario of an office with a person standing 2 m away from the door. Then this person decides to move toward the door and leave the room. By focusing on what drives the fluid flow in this scenario, two major causes are identified: 1) steady events: those that are constant in time, such as a constant air volume ventilation system or a ceiling fan running with a constant angular velocity; and 2) transient events: those that change with time. Modeling of the first group is less expensive and has been extensively utilized. EBM specifically targets the latter category. In the above example, two main transient events are identified: walking and door opening. The EBM approach develops walking and door opening models separately. The walking model simulates the movement of the human body in quiescent air. The model is run until air velocities approach zero. Experiments show that for a 2 m walk at ~ 1 m/s speed, the velocity field reaches ± 0.03 m/s everywhere in about 20 s, as seen in the 'Findings' section of Chapter 5. While a steady model describes airflow before the person decides to move, the 20s walking model can be superposed on the steady model to describe airflow. The same logic will be followed for door opening. Suppose that one intends to model the airflow in a room for 1 h, including the transient effect of the door opening. Previous efforts show that numerically simulating this work can take weeks, if not months, to complete due to small timesteps. For instance, Carneiro et al. reported that modeling one door operation (14s) took about 168 h (Carneiro et al., 2017). In response, EBM proposes that instead of developing a transient model for the full duration of interest, transient events (i.e., door opening and human walking) can be modeled separately, and the results are stored. Developing models for each event is computationally intensive and could take a long time to converge. However, these models will be run once and used multiple times. Calling out a stored result is much less expensive than running the model each time. The EBM approach uses the existing model for an event and superposes the stored results to the current field. The true challenge of EBM then becomes how to methodically define superposition in this case. The superposition can simply become an addition for an inviscid flow where the Navier-Stokes

equation simplifies to a linear partial differential equation (PDE). However, for more complex, realistic flow fields, one has to rigorously define superposition.

EBM Definition of Superposition using Dynamic Modal Decomposition

Let's consider a simple transient event that is quite frequent in the indoor environment: door operation. Also, it is assumed that the door operates every time with the same angular velocity and the same opening-closure cycle, and other boundary conditions. As stated in the previous section, EBM proposes that this event can be revived from a set of known cases with available solutions. Numerically speaking, any subsequent repetitions of the door opening in a constant boundary conditions environment (i.e., the same room) would be identical to previous events, with a different initial condition. The velocity field due to a new event (E_i) is denoted by $\vec{U}_i(\vec{x}, t)$ with an initial condition of IC_i . Note that IC_i is known as it is equivalent to the latest state of the system before the event E_i occurs. EBM assumes that the velocity field due to a new case can be approximated by a function $f_i(\vec{U}^*(\vec{x}, t), IC_i)$, where \vec{U}^* is a glossary of solutions to the same event under different initial conditions. The true contribution of EBM relies on proposing a method to approximate f_i . Without loss of generality, the N-S equation can be written in 2-D where \vec{u} and \vec{v} are the x- and y-direction velocity magnitudes.

$$\rho \frac{\partial \vec{u}}{\partial t} + \frac{\vec{u}(\partial \vec{u})}{\partial x} + \frac{\vec{v}(\partial \vec{u})}{\partial y} = \mu \left(\frac{\partial^2 \vec{u}}{\partial x^2} + \frac{\partial^2 \vec{u}}{\partial y^2} \right)$$

Equation 25

$$\rho \frac{\partial \vec{v}}{\partial t} + \frac{\vec{u}(\partial \vec{v})}{\partial x} + \frac{\vec{v}(\partial \vec{v})}{\partial y} = \mu \left(\frac{\partial^2 \vec{v}}{\partial x^2} + \frac{\partial^2 \vec{v}}{\partial y^2} \right)$$

Using a standard numerical approach (e.g., the explicit central difference), it can be shown that spatial velocities for a particular timestep can be written as a linear combination of spatial velocity magnitudes from the previous timestep. In that sense, the problem is Markovian, i.e., the current state of the system is sufficient to stimulate its future. Hence, the matrix \mathbf{X}^* is defined by each $\vec{U}^*(\vec{x}, t)$ where rows of \mathbf{X}^* represent velocity magnitudes at n discrete spatial point, and columns

provide data for m time step. For one known case of $\vec{U}_0(\vec{x}, t)$ we will have:

$$\mathbf{X}_0 = [\vec{U}_0(\vec{x}, t_0), \vec{U}_0(\vec{x}, t_1), \dots, \vec{U}_0(\vec{x}, t_m)] \in \mathbb{R}^{n \times m} \quad \text{Equation 26}$$

Solely for simplicity, let us replace the notation $\vec{U}_0(\vec{x}, t)$ with u^i . In this construct, an identifier can be defined to linearly approximate u^{i+1} from u^i .

$$(u^{i+1})_{1 \times n} = (u^i)_{1 \times n} \times \alpha_{n \times n}^i \quad \text{Equation 27}$$

$$\alpha^i = (u^i)^{p-1} \times u^{i+1} \quad \text{Equation 28}$$

Note that in Equation 28, the p_{-1} is the pseudo-inverse operator. With this approach, a time-variable $\alpha (\in \mathbb{R}^{n \times n \times m-1})$ can be found for each known case that would make possible the prediction at each timestep based on the previous timestep. Let's assume that a total of K previous cases with known solutions are available, i.e., \mathbf{X}_1 to \mathbf{X}_K . Hence, α can be calculated and stored for each case. To predict a new case (i.e., \mathbf{X}_{new}), one only needs to approximate the α_{new} and use that to predict velocity magnitudes beyond the initial condition. Several approaches could be perceived to reconstruct α_{new} from a set of known α 's. We propose three approaches, test each approach via a theoretical framework and experimental observations.

1. Weighted Average of Known Cases

Perhaps the very first approach to reconstruct anew is the estimate it as some weighted average of $\alpha_1 \dots \alpha_K$.

$$\alpha_{new} = \sum_{i=1}^K \alpha_i \zeta_i \quad \text{Equation 29}$$

Where ζ_i 's are linear coefficients that demonstrate the contribution of each case to α_{new} . One way to estimate ζ_i is by projecting the initial condition of the new case IC_{new} on those of the existing

cases. Therefore,

$$IC_{new} = \sum_{i=1}^K IC_i \zeta_i \quad \text{Equation 30}$$

Note that in practice, Equation 30 is converted to a minimization problem where ζ_i is estimated to minimize the difference between the left and right hands side of Equation 30. To avoid unreasonably large ζ values, a constraint could be added to force the sum of these coefficient equal to unity.

$$\begin{aligned} \min & \left(IC_{new} - \sum_{i=1}^K [IC_i \zeta_i] \right) \\ \text{s.t.} & \sum_{i=1}^K \zeta_i = 1 \end{aligned} \quad \text{Equation 31}$$

Theoretically, this approach assumes that the α and the initial condition (IC) of the system covary linearly. This approach has been referred to as WAC throughout the manuscript from this point on. However, Equation 28 shows that α is calculated from the pseudo-inverse of IC; therefore, the linearity assumption is under serious question. The findings from the experimental results presented later in this chapter substantiate this theoretical conflict.

2. Closest Case Approach

One special case for the WAC approach is when the number of known cases (i.e., K) is equal to the number of spatial points (n), in which case, Equation 30 will become a determined algebraic system and ζ has an exact solution. However, this approach is essentially data-fitting, where spatial values of the IC_{new} are fitted by linear combinations of a known case. Therefore, the solution for ζ will become sensitive to the IC of the known cases, and outlier cases can produce

great 'noise' to the prediction. A reasonable variation of the WAC is only using a subset of the known cases closest to the new case. In this approach, IC_{new} will be first compared to the existing cases, and a predetermined number of the close cases will be chosen to predict α_{new} . This approach can have a greater theoretical promise. Suppose that there are an infinite number of known cases. Then there will exist a known case that is identical to the new case. Then using Equation 28, one can find the exact velocity magnitudes. Similarly, the closest case approach, which is referred to as CS, can be reduced to choosing the closest known case for prediction. Algorithm 2 depicts the mechanics of this approach.

Algorithm 2: EBM's Closest Case Approach

Let $\langle X_1, \dots, X_K \rangle$ be the K known cases

Let IC_{new} be the initial condition of the new case and $\langle IC_1, \dots, IC_K \rangle$ be the initial conditions of the known cases

for $q = 1, 2, \dots, K$ **do**

$d_q = \text{norm}(IC_{new} - IC_q)$

end for

$Q = \text{Index}(\min(d))$ Determine the closest case

$\alpha_{new} \approx \alpha_Q$

for $i = 1, 2, \dots, m$ **do**

$u_{new}^i = u_{new}^{i-1} \times \alpha_{new}^i$ Note: $u^{i-1} = IC_{new}$ for $i = 1$

end for

3. Dynamic Closest Case Approach

As alluded to earlier, the CS approach returns the exact solution as the number of known cases approaches infinity. Yet, in the absence of a sufficient number of known cases, one perceived improvement is to dynamically search for the 'closest case' at each timestep. That is, Algorithm 2 will be used to estimate the velocity magnitudes (u) only for the second timestep. In this approach, we aim to find, independently, the closest case at every timestep, meaning that at each iteration, α_{new} could come from a different case. This could potentially result in a smaller error. This approach is referred to as DCS from hereinafter.

Validation Approach:

To check the accuracy of the velocity field estimated by EBM, the predicted velocity field a new case (U_{new}) is compared to a test case (U_{test}). Next, the absolute error (e) was defined as the absolute value of the difference between the predicted velocity and the measured velocity at each of the n locations at every timestep.

$$e = |U_{new} - U_{test}| \in R^{n \times m} \quad \text{Equation 32}$$

To normalize the error and make it a dimensionless index, Relative Error (ε) is calculated by dividing the absolute error (e) by the measured velocity matrix U_{test} . As both $e \in R^{n \times m}$ and $U_{test} \in R^{n \times m}$; mathematically, ε can be defined by:

$$\varepsilon = \frac{e}{U_{test}} \in R^{n \times m} \quad \text{Equation 33}$$

While studying e and ε made the most granular level of analysis, in some instances within this chapter, only the mean spatial (i.e., row average) or temporal (i.e., column average) errors were offered. Moreover, all the individual error data ($n \times m$) were visualized using statistical histograms. In this particular case, we used the algebraic value of ($u_{new} - u_{test}$) instead of the absolute value.

Assessment of EBM Using the Experimental data:

To analyze and validate the EBM method using the three approaches explained above, the data obtained through the door opening experiments, as described in Chapter 6, were used. The two door opening movements were conducted at each of the three flow rates (no air supply, 70% air and 100% air), repeated 30 times, and data was collected for 60 s for each repetition. Next, the EBM approximation of the new cases was compared against the experimental findings to study the error of each EBM approximation approach (i.e., WAC, CS, and DCS).

The EBM was a data-driven approach to predictive modeling, where the collected data was used to train the algorithms and use them to predict new cases. To compute the new case and compare it with the test case to determine the accuracy of the method, the data collected through the experiments are divided into training and testing sets. As explained in the method section, the WAC approach to EBM is sensitive to the data used to approximate the α_{new} , as including every set of data introduces noise to the calculation, since in this approach, every set of data in the training set contributes to the α_{new} in terms of the weight. Moreover, as the WAC approach compares the initial condition of the test case and the training data, it would not be able to capture the difference in velocity magnitudes at later timesteps and would skew the approximation. For example, the velocity field obtained from door opening twice would be different from the velocity field obtained from the door opening once and computing a new case of the door opening once from a dataset that includes both doors opening once and twice data would result in a poor estimate when using the WAC approach. Hence, for the calculation of weighted averages, the obtained data were sorted into four distinct sets for the four specific events - door opening once, door opening twice, walking once, and walking twice, such that the dataset would only contain the specific event-related information. Each of these four datasets had 90 sets of velocity fields, 30 for each of the three inlet airflow rates. Each of these 90 velocity matrices was divided into training and testing sets, where 80% of the data (72 out of 90) was randomly selected for training, and the remaining 18 sets of the data were kept for testing the approximation.

As the other two methods, the CS approach and the DCS approach, compare the new case to the training set and find the closest velocity vector in the training set, the data only needed to be sorted for the type of event, i.e., separate databases were created for door opening that had both door opening once and twice data, and for walking which also contained both walking once and walking twice data. 180 sets of data were available for both types of interventions. In each case, 80% of the data were randomly chosen to form the training dataset, and the testing

dataset comprised the remaining 20% of the total data. This way, the known cases used for the approximation are a subset of the training set, whereas the u_{test} used to check the accuracy of the approximated new case is a subset of the testing set. The algorithms were coded in MATLAB 19.1 (academic version) in a 16-node Windows computer (each node having two Intel Xenon @3.50 GHz processors) with a shared 128 GB memory. The training data embodied the K existing cases and were used to estimate a new case from the test set.

Weighted Average Approach

As explained, the approximation using the weighted average approach was made separately for four different events, namely, door opening once, door opening twice, walking once, and walking twice. For each of these events, ζ_i 's were computed by solving the minimization problem offered in Equation 31. These ζ_i 's were then used to approximate α_{new} using Equation 31. Using the Initial Condition and this α_{new} , the new case is predicted and compared to a specific case from the test database. The spatially averaged absolute error (\bar{E}), defined as the average of the absolute error e over the n spatial points, when approximating a new case of door opening once and another new case for door opening twice are shown in Figure 37.

It is evident that approximating the velocity fields using this approach results in a maximum of 22% and 32% error for door opening once and twice events, respectively. The highest errors are associated with the locations in the proximity of boundaries, i.e., walls and the moving edge of the door. Temporally, the higher errors are correlated to the door movement time. As the sensors recorded velocity values with some lags, Figure 37 shows an increasing trend in error until ~ 17 seconds. This graph also demonstrates that computing for the door opening twice events results in a higher error compared to approximating for door opening once event. This could probably be attributed to the increased complexity of the velocity field resulting from subsequent door movements compared to opening and closing the door once. The distribution of spatially averaged errors when approximating new cases for both door opening once and twice shows that the error

distribution is a left-skewed, non-parametric distribution. Perhaps the small size of training samples, as well as computing the α_{new} as a linear combination of known α 's when known α 's are computed using pseudo-inverse, are contributing to the large errors.

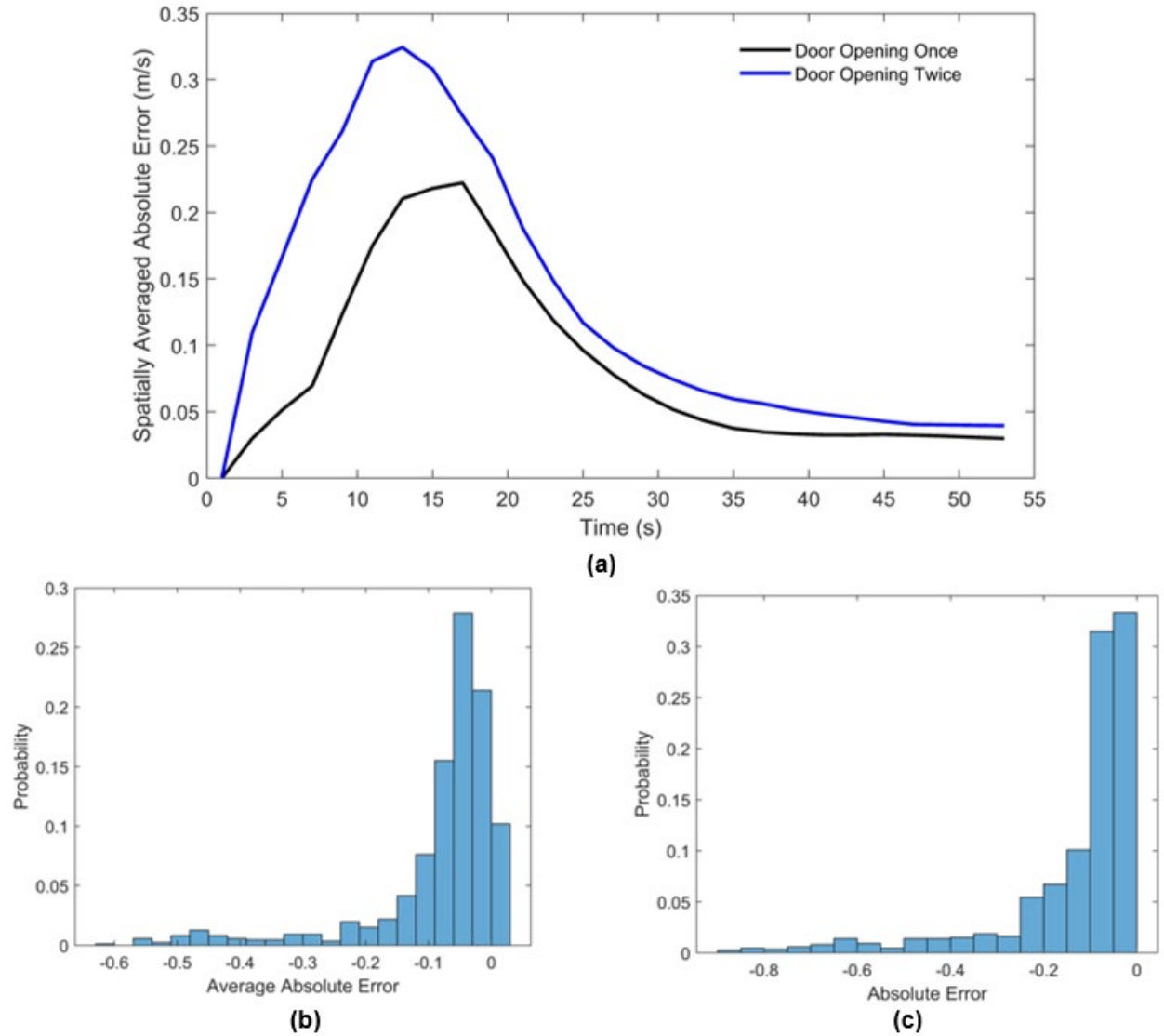


Figure 37: Error from Door Opening Events - Weighted Average Approach: [a] Comparison of Temporal Trend - Door Opening Once and Twice, [b] Error Distribution - Door Opening Once, and [c] Error Distribution - Door Opening Twice

Closest Case Approach

For this approach, the norm of $(IC_{new} - IC_K)$ was minimized, where K was the number of known cases from the training set, and these cases were sorted based on the ascending value of the norm, the closest case is the one for which the $norm(IC_{new} - IC_K)$ was the smallest. The velocity field for the new case was approximated as described in Algorithm 2. The Absolute Error (e) for Door Opening experiments at every location for all timesteps is plotted against time in Figure 38.

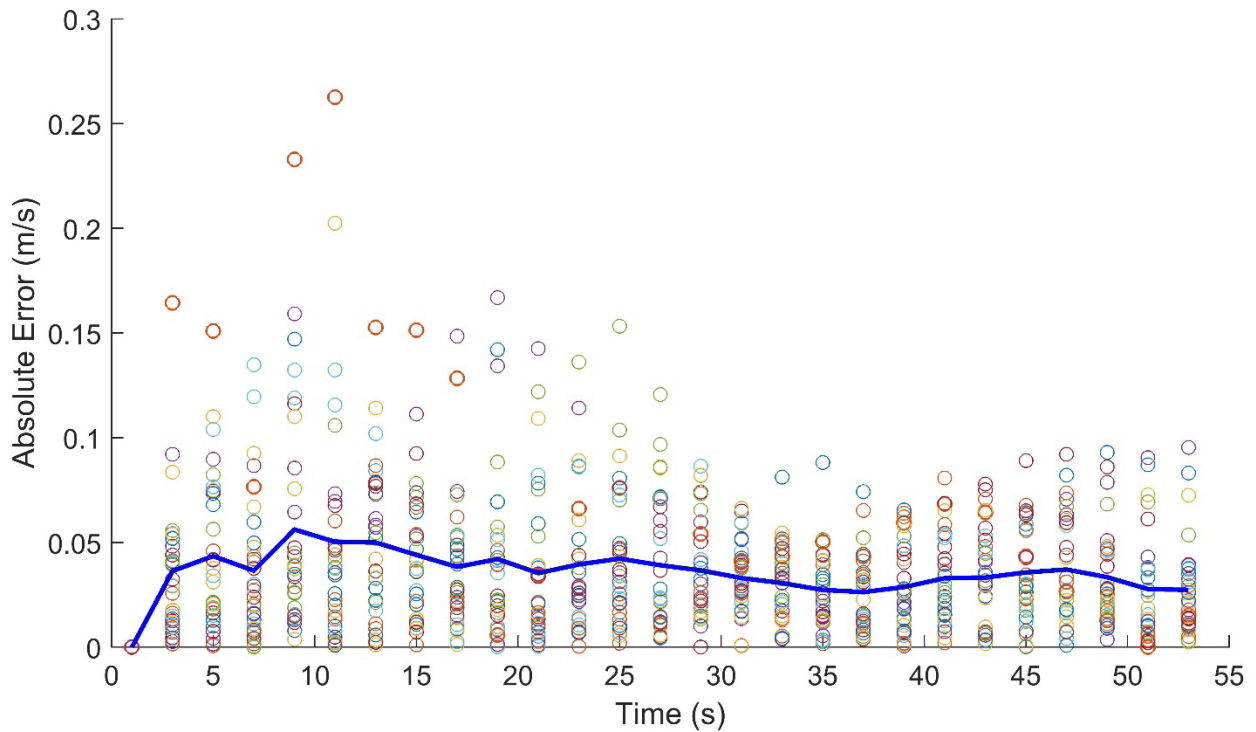


Figure 38: CS approach - temporal trend of absolute error: The pointers show absolute error at all locations at every timestep; the line shows spatially averaged absolute error.

From Figure 38, it can be observed that even though for most of the locations, the absolute errors are <0.1 m/s, there are some locations where the errors are higher, specifically until the second 30. These locations were found to be either in the proximity of the door's moving edge or locations close to the wall. Airflow at these locations had turbulent interactions, as the air moving close to

the wall, i.e., a stationary boundary, the velocity wakes could not disperse, and hence contributed to the increased error.

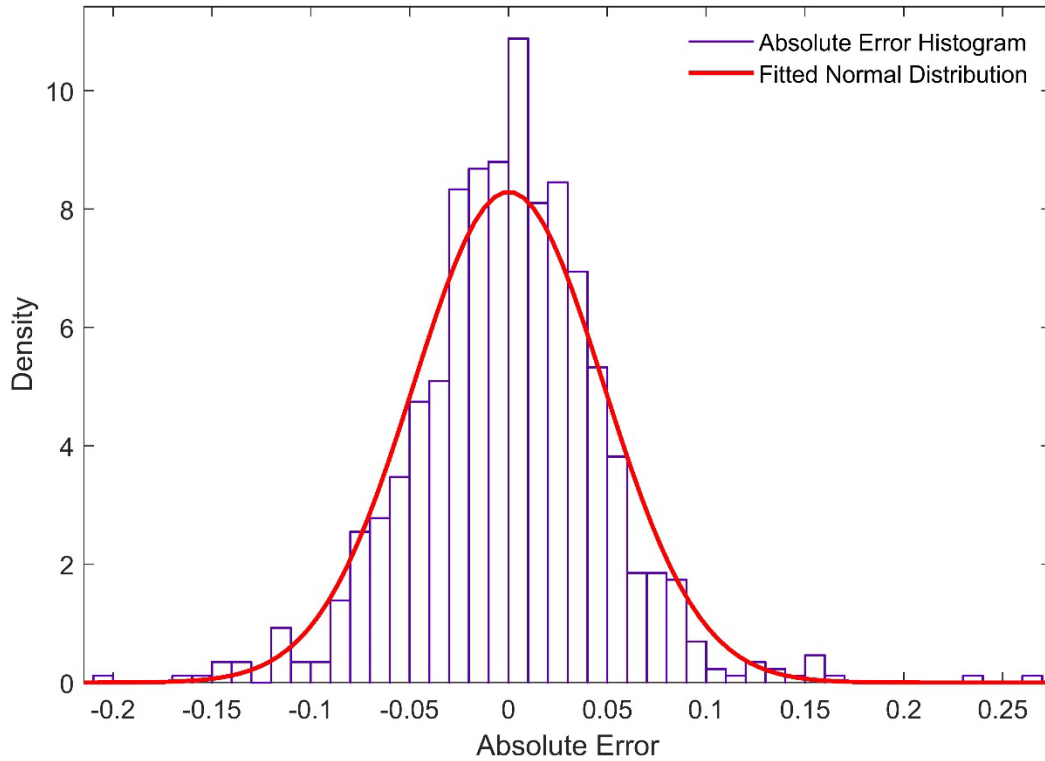


Figure 39: Distribution of error - CS approach

The distribution of error, visualized in Figure 39, demonstrates it to be a unimodal and symmetric distribution with some outliers in the tails. Fitting a normal distribution to the data, it was observed that the estimated mean of the distribution was very close to zero (0.000105036) (standard error = 0.0016), with an estimated standard deviation of 0.0481215 (standard error = 0.0011.)

Next, instead of calculating α from a single case (whose IC is the closest to the IC of the case that is being predicted), one can use several close cases to approximate α , and in turn, approximate the velocity field for the new case.

In this case, α is calculated for each of these selected closed cases, and $\bar{\alpha}$ is calculated by averaging α 's over the number of selected cases, as given in the equation, where N is the number of close cases selected.

$$\bar{\alpha} = \frac{\sum_{i=1}^N \alpha_i}{N} \quad \text{Equation 34}$$

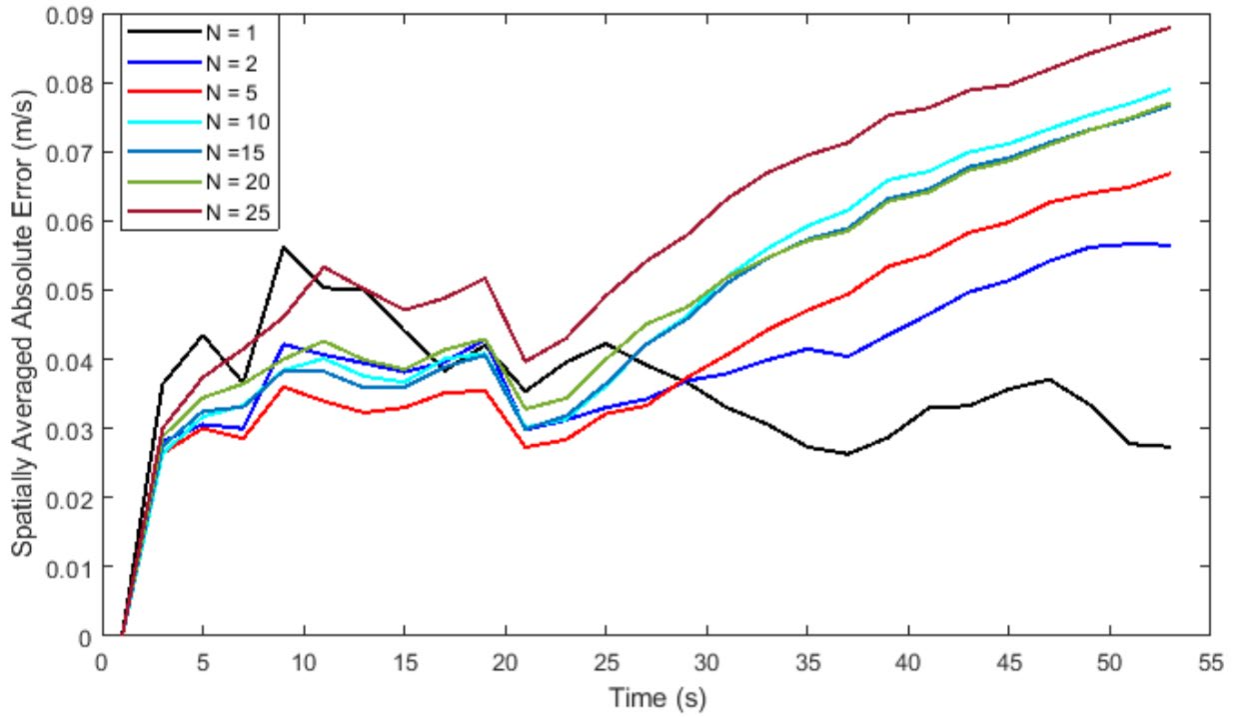


Figure 40: Effect of Number of Close Cases Selected to Approximate α on Average Absolute Error - CS Approach.

Figure 40 shows the spatially averaged absolute errors for several different values of N. This demonstrates that the area under the spatially averaged absolute error curve or overall error was minimum when $N = 1$, i.e., the new case is approximated based on the single case whose initial condition was the most similar to the predicted case. For a few initial timesteps, selecting more than one close case may have produced a smaller error, but that trend was temporally not consistent - when $N > 1$, the absolute error tends to increase quickly after 20 s. In other words,

approximating a new case using only the closest case resulted in less error. Theoretically, this makes sense as adding training points that are farther from the test case can create noise in the approximation algorithm.

Dynamic Closest Approach

For this approach, at the first timestep, the norm of $(IC_{new} - IC_K)$ was minimized, where K was the number of known cases from the training dataset, and these cases were sorted based on the ascending value of the norm. For the closest case, i.e., for which the $norm(IC_{new} - IC_K)$ was the smallest, α was calculated using Equation 28, stored, and used to approximate the velocity vector at the second timestep of the new case (using Algorithm 2). This procedure is done at every timestep n , using the velocity vector at timestep $n - 1$ as the initial condition. As stated earlier, reconstructing α at every timestep can potentially improve the accuracy of the approximation, contingent on the training dataset richness. It turned out that our experimental dataset was not rich enough to accommodate such improvements. That is, the closest case solely based on the initial condition remained the closest case throughout the simulation period (i.e., converging to the Closest Case approach). However, to capture whether this dynamic approach produced any improvements, we changed the number of closest cases to $N = 2$. It can be seen from Figure 41 that the dynamic closest case results in a better approximation of the new case. If the overall spatially averaged error (\bar{E}_{ov}) is described as the area under the curve, then it can be expressed as in Equation 35.

$$\bar{E}_{ov} = \int \bar{E} \, dt \quad \text{Equation 35}$$

where \bar{E} is spatially averaged absolute error at each timestep.

The overall error (\bar{E}_{ov}) for the DCS approach is 14% less than the \bar{E}_{ov} computed using the CS approach. It is also evident from the fact that the \bar{E}_{ov} of the CS approach starts increasing from second 20, whereas the \bar{E}_{ov} of the DCS approach starts to blow up from second 33. Within second

30 to second 53, the \bar{E}_{ov} resulted from the DCS is 36% less than that of \bar{E}_{ov} calculated from the CS, on average. These observations indicate that using the DCS approach approximated the new case more accurately. The transition from the transient event to the steady state was also faster than the CS approach.

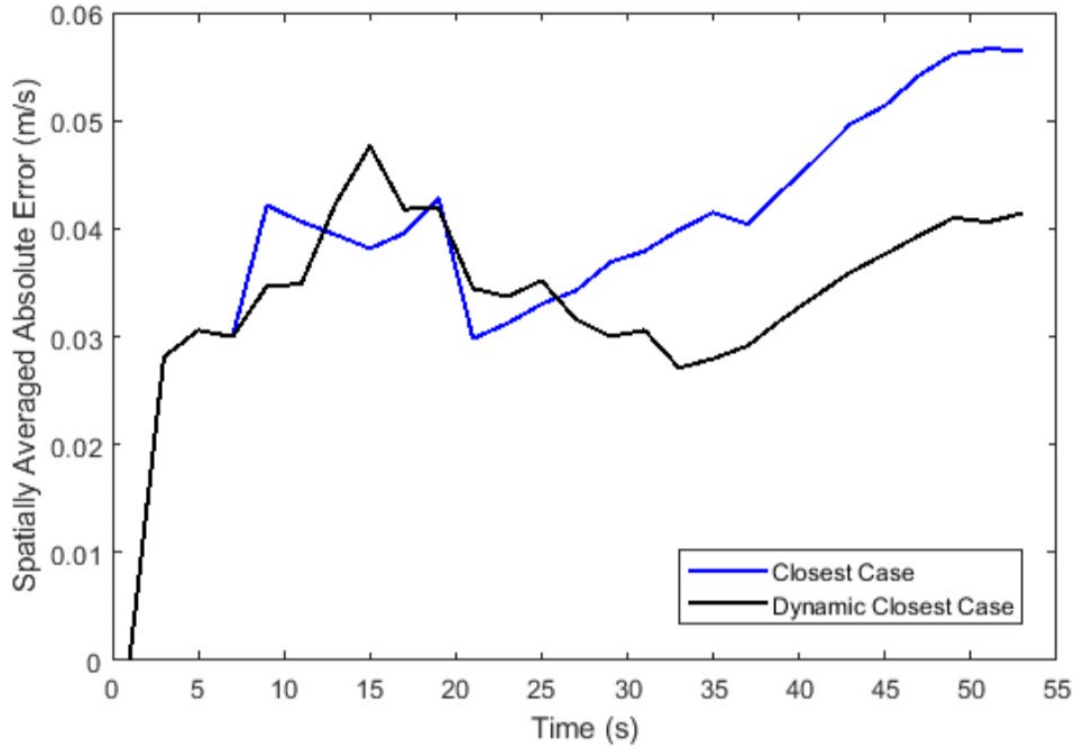


Figure 41: Comparison of DCS approach and CS approach for approximating a new case using two close cases ($N = 2$) from the training dataset.

Comparison of Velocity Fields

To further assess the accuracy of approximation using the DCS approach, 2D velocity fields from both experimentally obtained data and EBM approximated data for the door opening event were visualized in terms of filled contour plots, shown in Figure 42. These contour plots were obtained using the locations of the radially arranged sensors and assuming zero slip conditions at all the boundaries, e.g., walls. Furthermore, as the velocity values were available at the sensor locations only, the velocity values were interpolated throughout the testing facility. The area of the test chamber was discretized in grids of 110×109 , where the dimension of each square grid was 5

cm × 5 cm. It can be noted that these visualizations of the velocity fields are at one instance, specifically at timestep 10. From this comparison, it can be noted that using the DCS approach, EBM produces an accurate approximation of the velocity fields, with notable deviations at the proximity to the walls and the door movement periphery.

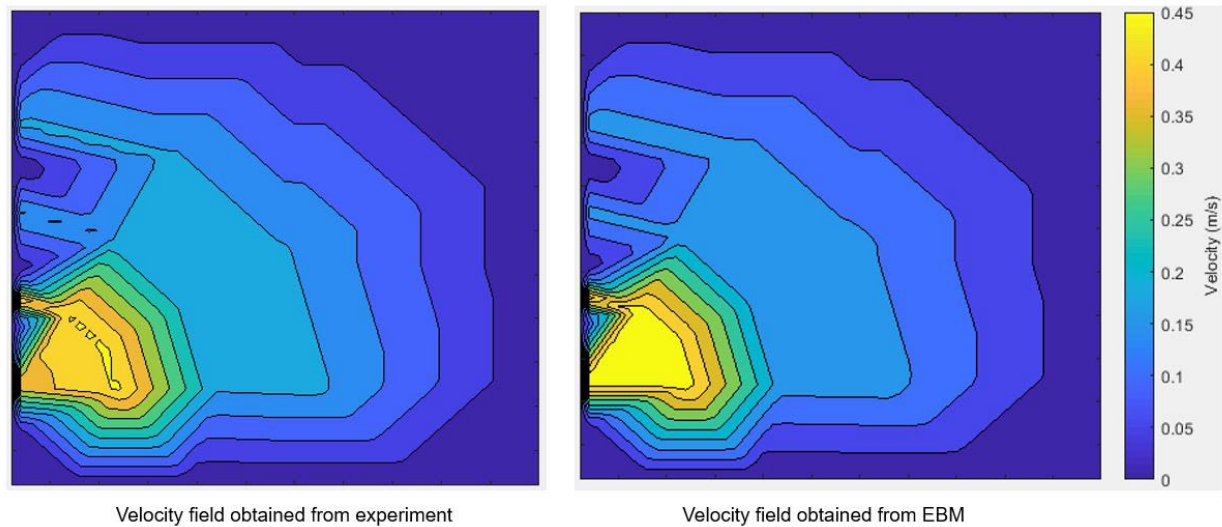


Figure 42: Comparison of Spatial Velocity Fields Obtained from Experiment and Approximated using DCS Approach.

Assessment of EBM Using Numerical Simulation Data:

The EBM method was tested for human walks, as simplistic human walks along a straight walking track were modeled in Ansys Fluent 2020, R1. The geometry of the modeled chamber was identical to the controlled environment chamber at UC Berkeley, where actual experiments were conducted. These 2-D models were developed to generate air velocity data from multiple simultaneous walks and test the prediction accuracy of EBM.

Model Geometry and Discretization

DesignModeler, the built-in drafting software in Ansys, was used to draw the geometry that was used to examine the effects of a translation movement in indoor airflow fields. The domain of this simulation was identical to the controlled environment chamber at UC Berkeley. As the human

walk was simulated by moving a circular surface body of diameter 0.3m along the track, this arrangement provided the opportunity to create CFD models of the walking experiments in 2-D. The simulation model is shown in Figure 43.

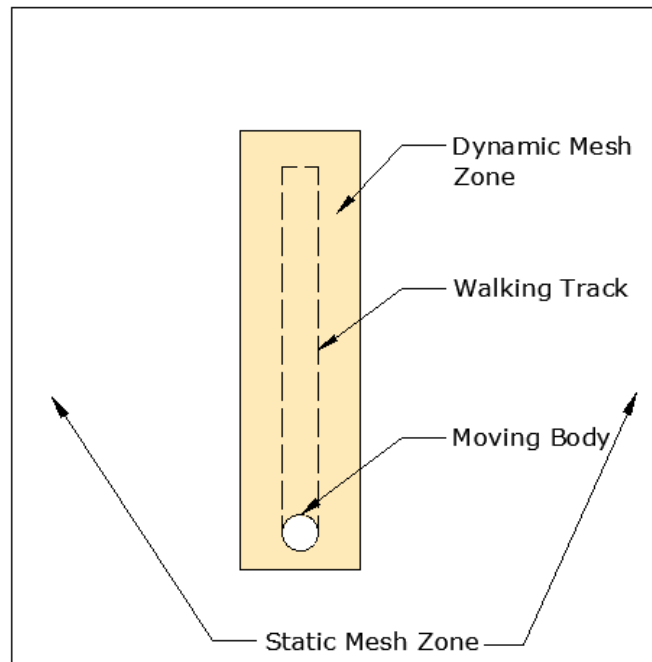


Figure 43: Simulation Geometry

The CFD simulation domain was discretized using uniform, unstructured meshing scheme and triangular meshing element in Ansys Meshing. Mesh refinement process was conducted to ensure the grid independence of surface-averaged velocity. To simulate the walking movement, the entire domain was divided into two parts, the dynamic mesh zone (a 3.65 m x 1m area at a distance of 1.9 m from the west wall and 0.8 m from the south wall) and the static mesh zone, to reduce the computational time (Figure 43).



Figure 44: Mesh Configuration

The size of each element in the static zone was 0.1 m, and the size of the elements in the dynamic zone was 0.03 m. The total no. elements in the dynamic zone were 8257, whereas 7540 elements constituted the static zone. To facilitate better interconnection at the dynamic and static zone interface, the mesh was refined along with the interface. The mesh configuration is displayed in Figure 44. The Smoothing and Remeshing schemes were used as dynamic mesh update methods. The smoothing method adjusts the mesh of an area by moving or deforming boundaries, but the number of nodes and connections does not change. In the spring-based smoothing method, the edges between the two mesh nodes are known as a mesh of interconnected springs and adjust the node displacement during mesh movement.

The remeshing method is used where the boundary displacement is large compared to the size of the local cells, which causes the cell quality to deteriorate, resulting in a negative cell volume. The remeshing method tackles this by compressing cells that disrupt the skewness value or

critical size limit and locally remeshing the meshed cells or surfaces at each timestep to maintain the required mesh quality. The simulations were assumed to be isothermal, and no heat sources were considered as the data collected from the experiments showed that the fluctuation in temperature was negligible during the entire duration of the experiments. The walls in the room and the wall of the moving body were considered to be rigid boundaries with the no-slip condition, i.e., the x- and y-components of the velocity were zero.

Table 22: Transient Movements

Movement	Direction	Start time (s)	End time (s)	Pause before next movement (s)
1	Forward	0.00	3.00	1.00
2	Reverse	4.00	7.00	1.00
3	Forward	8.00	11.00	0.50
4	Reverse	11.50	14.50	0.50
5	Forward	15.00	18.00	2.00
6	Reverse	20.00	23.00	-

Transient Movements

The simulation of the walking movement was done using a user-defined profile in Ansys Fluent. As mentioned, the CFD models were developed to simulate multiple walks along the walking track in both directions. For simplicity and computational feasibility, the moving body covered the track distance six times during the simulation, where the distance was covered in 3 seconds at a speed of 1.02 m/s, identical to the walking speed in the experiments. Between every forward (moving south to north in Figure 43) and backward movement (moving north to south in Figure 43), the movement paused for some duration. Table 22 describes the movements of the circular surface element. A start time of 4.00 s indicates that the specific movement began 4 seconds after the

simulation started. This way, the pause before the subsequent movement provided a chance to obtain a different initial condition for each cycle of forward-reverse movements.

Initial Conditions

As mentioned earlier, the CFD simulations were carried out to obtain airflow velocities from occupant movements under different initial conditions. Three specific initial conditions were used in the study. An area of 0.6m x 0.6m in the dynamic mesh zone, at a distance of 2.7 m from the center of the circular surface body was defined (the area marked in red in Figure 45) where an initial flow velocity was given as an initialization parameter.

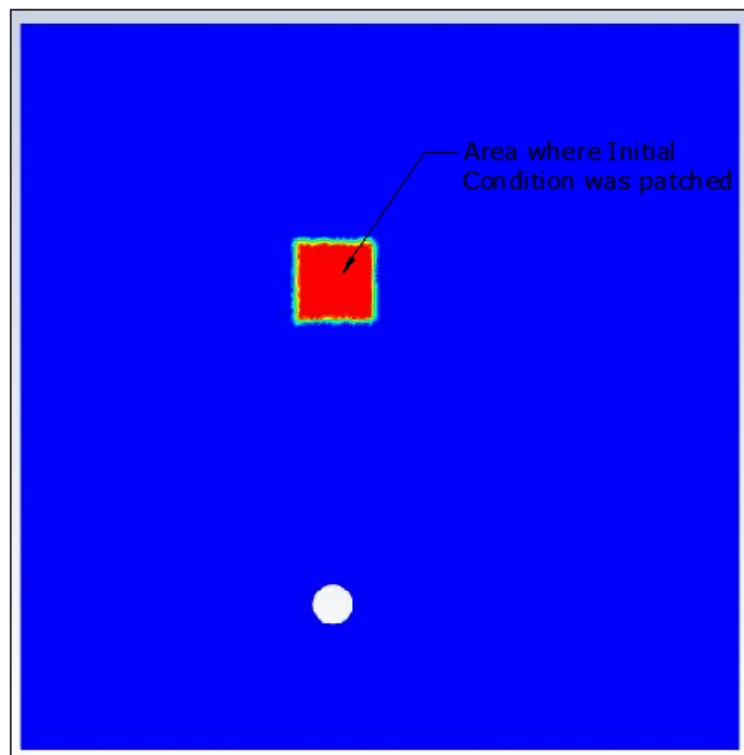


Figure 45: Initial Condition for the CFD Simulations

During the first simulation, the entire chamber was initialized using a zero velocity of air, i.e., the air in the chamber was quiescent. For the second simulation, the area marked red in Figure 45 had a velocity of 1m/s in the positive x-direction, and quiescent air was the initial condition

everywhere else. For the third simulation, the model was initialized using a 1 m/s velocity in the negative x-direction in the marked area and quiescent air elsewhere. This way, for all three simulations, the first forward walk had a separate initial condition. As there was no air inlet to maintain a constant initial velocity, it encountered a different initial condition before the movement began by the time the first reverse movement started. Similarly, all subsequent movements had different initial conditions, and those initial conditions differed according to the prescribed initial velocity. This way, a rich database was obtained that contained velocity values from a wide range of initial conditions for movements in both directions.

Solver Details

Out of many Reynold Averaged Navier-Stokes method (RANS), the two-equation RNG k- ϵ model with standard wall functions was used to model turbulence since it has been shown to produce good results for indoor airflow simulations. The pressure-implicit with the splitting of operators (PISO) algorithm was employed for the pressure velocity coupling since the PISO algorithm has been proved to be better suited for transient problems with unstructured mesh and relatively large timestep size than the SIMPLE and SIMPLER algorithms. The second-order upwind scheme was used for spatial discretization, and the transient formulation was done through the second-order implicit scheme. The pressure-based transient solver was used during the movement, with a timestep size of 0.008s. The convergence criteria were set as to when the normalized residuals of the continuity, two velocity components, k and ϵ were less than 10^{-4} . The simulations were computed in a 16-node Windows computer (each node having two Intel Xenon @ 3.50 GHz processors) with a shared 128 GB memory.

Training and Testing Sets for EBM

The three simulations included three forward and three reverse movements, and at the end of the last movement, the simulations continued till a steady state condition was established in the chamber. The run the EBM algorithm, the data for one such walk (out of the six) from one of the

simulation cases (i.e., zero initial condition, the initial condition of 1m/s in the positive x-axis, and initial condition of 1m/s in the negative x-axis) was left as the testing data, and everything else consisted of the training set. That is, the data for one walking event of three seconds out of 18 such events in total were selected at random as a testing set, and the rest 17 events made up the training set. Once a CFD solver solves the problem over the discretized region, a solution is obtained at every node. Now, given that after meshing, the nodes generated for each model were located at different coordinates, the obtained results were also available at discrete points for all the models. Additionally, as the simulations were done using dynamic meshing, the location of nodes where calculations were done at one time changed for the next time. In order to be able to compare the models, the properties had to be available at common locations in all the regions. This was achieved by interpolation - the simulation results spread over discrete points were distributed evenly in grids that were sized in coherence with the size of the modeled chamber. The resultant data was interpolated to 1568 equidistant nodes. As the transient motion timestep size was 0.008s, each of the training set and the test set consisted of 375 timesteps, i.e., the resultant matrix for the training set was $1568 \times 375 \times 17$, and the resultant test set matrix was of size 1568×375 , where the first dimension was spatial points, the second dimension was timesteps, and the third dimension being the no. of walking events in the dataset.

Findings from using the simulation data in the EBM algorithm

To evaluate the performance of the EBM method using the data from the CFD models, the EBM model on experimental door opening data showed that the DCS approach had resulted in the lowest error compared to the other two approaches (WAC and CS). Hence, the following section will discuss the results of employing the EBM model on the CFD data using the DCS approach only.

As explained earlier, the metric absolute error was used to compare the approximated velocity field using EBM and the test set data. Figure 46 shows the temporal trend of spatially averaged

absolute error with respect to the timesteps when the first forward movement, i.e., movement 1 in Table 22 under the initial condition of zero velocity, was selected as the test case. As can be seen from the figure, the error spiked in the initial three timesteps to a maximum of 0.022 m/s at timestep 3, and then remained below 0.02 m/s for the entire duration of the movement.

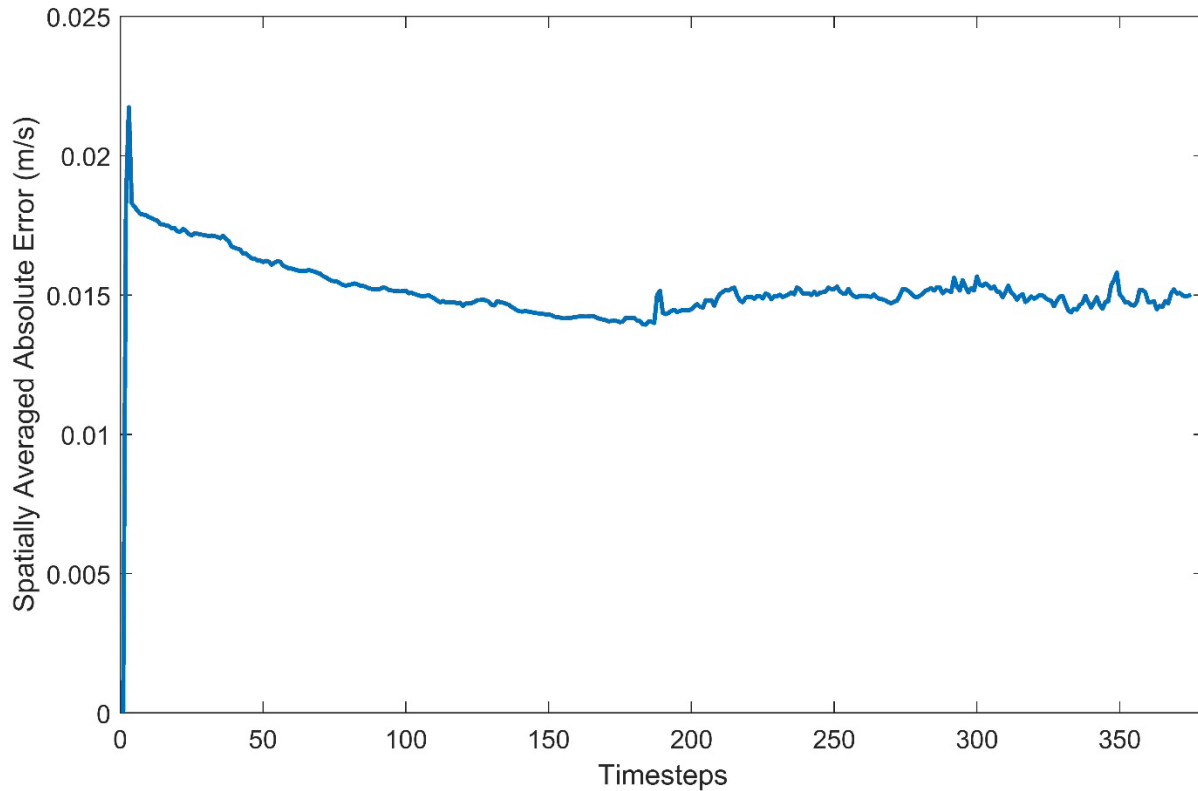


Figure 46: Temporal Trend of Average Absolute Error for the Simulated Walking Events

The distribution of the absolute error, shown in Figure 47, depicts that the error was normally distributed across all spatial locations and timesteps. When a normal distribution was fitted to the error data, the estimated average was very close to zero (0.0001 , with standard error 1.06×10^{-5}), and the standard deviation was 0.008 (standard error 7.47×10^{-6}), indicating a unimodal distribution of the error, centered at zero, with few outliers in the tails.

The flow fields of the test set obtained from EBM, and CFD simulation were plotted for the timesteps for visual comparison to confirm a good approximation using EBM. Figure 48 shows

one such comparison at timestep 301, which corresponds to 2.4 s after the movement began. It is evident that the velocity field obtained from EBM was a fair approximation of the actual velocity field. It is apparent that the areas with the highest velocity values are surrounding the moving body.

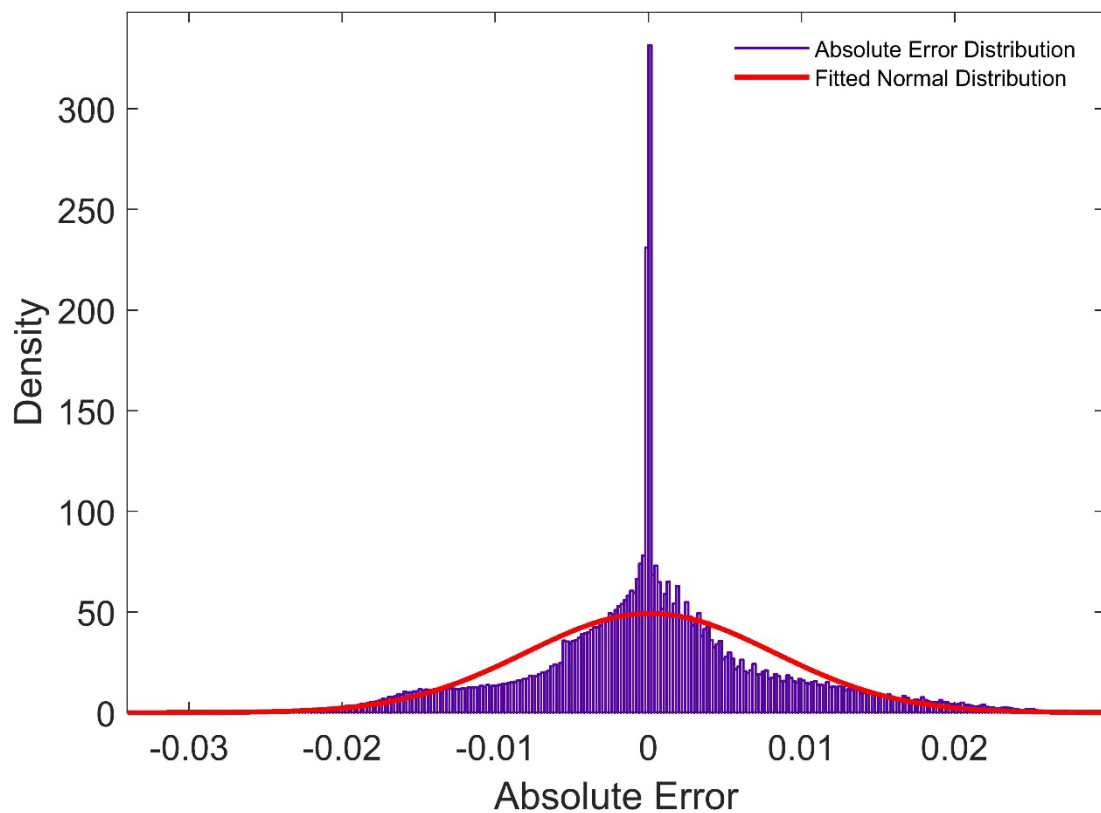


Figure 47: Distribution of Absolute Error for Simulated Walking Event

Conclusion:

This chapter discussed a novel methodology called event-based modeling (EBM) to approximate airflow velocities for human-environment interactions such as door opening and walking movements. This study used real-time experimental data collected at a controlled environment chamber and 2-D CFD simulation data to characterize airflow characteristics under occupant movements in a steady-state flow. Data for the changes in flow velocity was collected at several spatial locations for the duration of the start of the intervention until the effects of transient

occupant interventions diminished and steady-state conditions were restored. The results presented in this study considered constant boundary conditions.

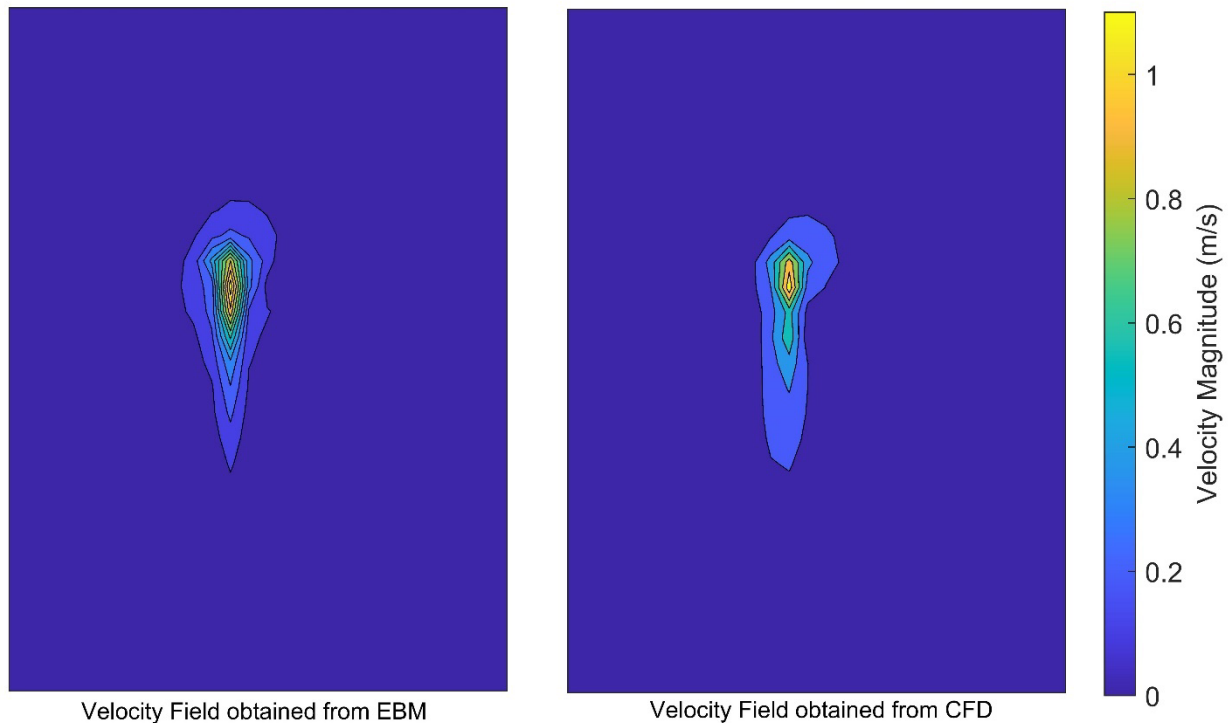


Figure 48: Comparison of Velocity Fields from CFD Simulation and EBM

The principal idea behind this study was that the current ventilation system design paradigm does not consider the transient events like occupant introduced perturbations while determining the ventilation requirements and parameters, primarily because studying transient events are difficult either by experiments or by numerical simulations. In response, the EBM method presented in this paper can approximate the flow properties under transient events using a data-driven model. Suppose a database of flow properties, either from experimental studies or fluid dynamic simulations, can be amassed. In that case, EBM can predict the resultant flow characteristics in

those environments for separate initial conditions without having to run another set of experiments or a set of simulations.

Using the measured airflow velocity at every timestep from repeated experiments, the EBM method was proposed to calculate identifiers (α 's) that connect the velocity profile at one timestep (m) to the next ($m + 1$). In this paper, three methods, namely, weighted average approach (WAC), closest case (CS), and dynamic closest case (DCS), to approximate a new velocity field with a new initial condition were presented.

Among those three, the WAC method, which determines the contribution of every velocity field of the known cases in the EBM database to calculate the new case in terms of weights, was found to be the least accurate approximation accuracy as measured using the index error (e). When an event of the consecutive door opening was approximated using this method, the spatially averaged error was more than 30%, with a skewed distribution of the error. One reason behind such poor estimates was that the WAC method linearly combined the weighted information from the database, which was questionable since the identifier α 's were calculated using a pseudo-inverse operator.

The second method introduced in this paper, the CS method, improved approximation as measured by reduced error. This method compared the initial condition of the new case to the database and used the one having the closest initial condition to approximate the entire velocity field of the new case. The error was normally distributed, and when spatially averaged for any approximated door opening event, it was below 6% for the duration of the event. Instead of selecting the case closest to the new case, the authors also investigated the impacts of utilizing the information from several close cases and found out that the best approximation was obtained when the single closest case was used for approximation. The third approach, namely the DCS approach, resulted in the best approximation of the velocity field with a new initial condition. This method compared the velocity vectors of the new case with the known cases at every timestep,

rather than comparing only the initial condition as in the CS approach, and calculated the velocity field at the next timestep. Interestingly, it was found that when DCS used the single closest case, the single closest case did not change over timesteps - essentially converging the calculation to the CS approach. The limited availability of velocity fields in the database might have been the reason attributable to this. But when the information from several close cases was used to approximate the new case, the close cases at every timestep changed, and the DCS method resulted in better prediction accuracy, as evident from the low spatially averaged error. Lastly, it is critical to successfully approximate a transient event to converge to the steady-state condition. This feature was clearly observed in experimental data that the velocity magnitudes converge to the steady-state values approximately in 30 s. The DCS approach satisfied this feature as the absolute errors diminished with time.

Limitations, future outlook, and applications:

The experimental method of data collection posed several constraints for this study, specifically because of the restricted access to the test chamber and the availability of adequate sensing devices. The test chamber was available for a limited time; hence the velocity values could be collected for three initial conditions, i.e., the supply air rates. Additionally, the availability of eight sets of omnidirectional velocity sensors at a time led to conducting experiments in sets. Despite these constraints in the experimental procedure, at least 30 sets of data were collected for each experiment setup. Even then, to maximize the velocity information over a large spatial area, the sensors were arranged in a sparse way inside the chamber, leaving a significant area of the room where data collection was not possible.

The limited number of spatial locations where data could be collected led to a comparably smaller dataset. The fact that the dynamic closest case approach converged to the closest case approach, i.e., the closest case did not change from one time step to another, could be attributed to the unavailability of enough data in the training set that represent the velocity field in that

timestep, so the algorithm brought back to the initial closest case for every timestep. Thus, to efficiently implement the EBM model, it is crucial to have a database containing information on a substantial number of cases. Scientists studying the indoor airflow patterns originating from occupant-environment interaction will be able to contribute to building the database. The 2-D CFD simulation data somehow alleviated this limitation and proved that access to a larger database over many spatial locations results in a better approximation performance.

With significant improvements in the database, this EBM method can be very useful to determine the airflow velocity under a transient discrete event like occupant movement. When the airflow velocity is approximated using this data-driven technique, using the Lagrangian framework of particle flow can be solved rather easily, considering it to be an ordinary differential equation at that point as the air velocity values are available. This way, the dispersion of airborne particles can be approximated under occupant-induced disturbances in a steady-state flow environment, which promises significant improvement in occupant-centric adaptable ventilation system design, which can reduce energy use and control contamination dispersion.

One of the major applications of EBM is in the design, operation, and maintenance of healthcare facilities. Airflow distributions and air-conditioning systems of hospitals are designed to control the spread of infectious agents. Standards specify general requirements about ventilation rate, filtration, and the location of air inlets and outlets, to remove, dilute and capture contamination from the space. However, these general design schemes are highly susceptible to temporal perturbations such as the movement of occupants and door openings (E. Mousavi et al., 2019). EBM can be applied to such circumstances and incorporate these movements into the design and operation of the healthcare ventilation systems.

Chapter 8

An application and future outlook of EBM

The EBM method to approximate the airflow patterns from human-built environment interactions, evaluated in the previous chapter, can be applied to simulate the random occupant movements in an indoor environment rather than numerically simulating it. EBM is a data-driven study where we have used the data collected through experiments and numerical simulations to develop an algorithm that approximates the relationship between the velocity values at timestep m and the velocity at timestep $m + 1$. This is similar to numerically simulating a fluid flow. Instead of solving the conservation equations at every step, the collected data was used to match the closest velocity values at timestep m from the database and determine the flow characteristics in the next timestep. As an example of how computationally efficient EBM is compared to the CFD simulation, the walking experiments using two-dimensional CFD models were modeled. The models that used two equations k - ϵ RANS method to model turbulence with a second-order implicit time-stepping took nearly 14 hours to converge on a 16-node Windows computer (each node having two Intel Xenon @ 3.50 GHz processors) used in parallel with a shared 128 GB memory. In comparison, when the EBM model was run on the same data on a 4-node Windows computer with Intel Core i5-7200U CPU @ 2.50GHz with 8 GB memory, it took around 5 mins to get the predicted velocity fields, which is equivalent to a little more than 1 minute in the computer where the simulations were run. Before the EBM code was executed, it took nearly 20 mins to read the data using a MATLAB script.

Methods:

Numerical simulation model

A 2-D CFD model of a random human walk was developed in Ansys Fluent, version 2020 R1, using an academic license from Clemson University. This model was used to emulate multiple human walks in straight lines. The following sections describe the CFD model.

Table 23: Multiple Walking Scheme

Location	Walking Scheme	Time since start	Waiting time
A	Beginning of the first walk	0 s	-
B	End of the first walk	3 s	1 s
	Beginning of the second walk	4s	
C	End of the second walk	7s	1.5 s
	Beginning of the third walk	8.5 s	
D	End of the third walk	11.5 s	0 s
	Beginning of the fourth walk	11.5 s	
E	End of the fourth walk	14.5 s	-

The in-built drafting software in Ansys Fluent, the DesignModeler, was used to build the 2-D geometry where a 9m x 9m indoor chamber. A circular surface body that emulated the 2-D version of an occupant was placed 2.5m from the left wall and 1.1m from the south wall, as shown in Figure 49. Four translation motion in a straight line covering 3.1 m was imparted on the circular surface body, and the locations of the beginning and end of each walk are shown in terms of points A through E in Figure 49. The distance of the walking track for each of these four walks

was identical to the walking track distance of the walking experiments in the Controlled Environment Chamber at UC Berkeley, as described in Chapter 5, and equal to the walking track distance to the CFD walking models discussed in Chapter 7. Each of these walks was for a duration of 3s. At the end of each walk, there was a brief waiting duration before the next walk started, as shown in Table 23.

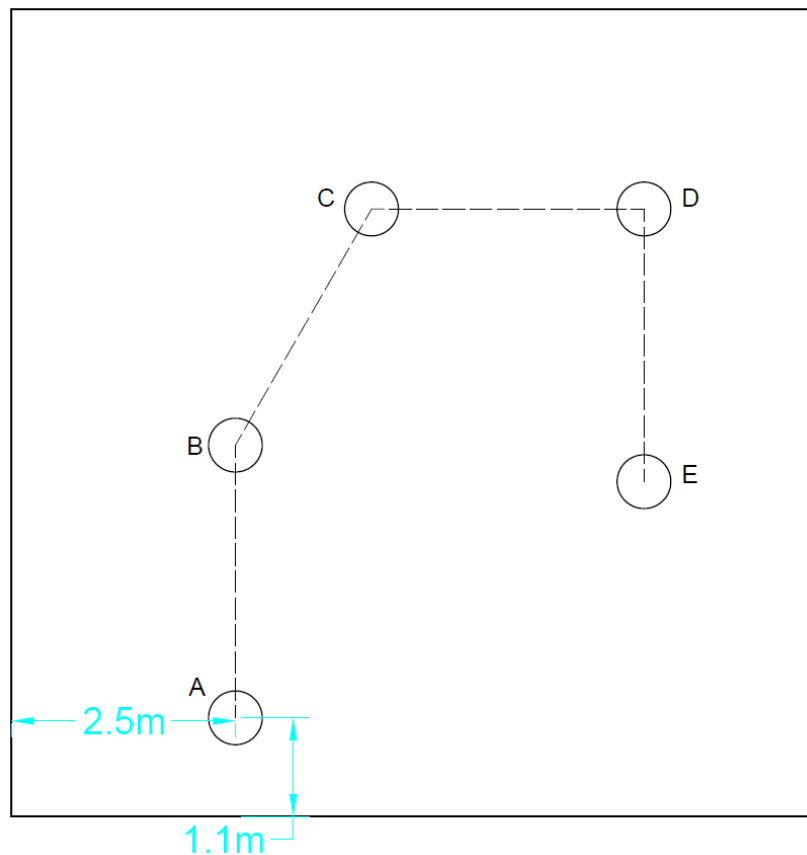


Figure 49: Multiple Walk Geometry

The solution domain was discretized using the in-built meshing software in Ansys Fluent. The triangular meshing scheme was used, which resulted in 68046 elements. The Smoothing scheme, which adjusts the mesh of an area by moving or deforming boundaries, but the number of nodes and connections does not change, along with the Remeshing method, which tackles the

deterioration of cell quality at the boundary by compressing cells that disrupt the skewness value or critical size limit and locally remeshing the meshed cells or surfaces at each timestep to maintain the required mesh quality, was used as the dynamic mesh update method. No heat source or sink was considered to maintain parity with the experimental findings, which showed that the change in temperature throughout all the experiments was negligible. No-slip conditions were assumed at the walls, essentially considering zero values of velocity components at rigid boundaries.

At the beginning of the walks, a quiescent air was considered the initial condition. The initial condition changed at every timestep with the turbulence generated from the walking movement. That way, without the presence of a mechanical air inlet-exhaust system to maintain a constant initial velocity profile, every walk started with a different initial condition, and the numerical simulation computed the resultant velocity field at the end of all four walks. The two-equation RNG k- ϵ model with standard wall functions was used to model turbulence as it performs better when used to model indoor airflow. Similar to the CFD walking models described in the subsection 'Assessment of EBM Using Numerical Simulation Data' in Chapter 7, the pressure-implicit with the splitting of operators (PISO) algorithm was employed for the pressure velocity coupling, which has shown to perform better with unstructured mesh compared to the popular SIMPLE and SIMPLER algorithms. Spatial discretization was done using a second-order upwind scheme, while the second-order implicit scheme was used for transient formulation. A timestep size of 0.008s was found to be appropriate for the pressure-based transient solver, which computed the solution with convergence criteria set as to when the normalized residuals of the continuity, two velocity components, k, and ϵ were less than 10^{-4} . The simulations were computed in a 16-node Windows computer (each node having two Intel Xenon @ 3.50 GHz processors) with a shared 128 GB memory.

Employing the EBM algorithm:

The training sets:

The 2-D walking models discussed in Chapter 7 that simulated six forward-reverse movements under three initial conditions (Table 22 of Chapter 7) were used to develop the training sets to be used for EBM. The experimental results and the simulation results showed that an area of 4 m (perpendicular to the walking direction) X 4.4 m (parallel to the walking dimension) covers most of the changes in the velocity profile from the beginning to the end of the walking event – as shown in Figure 50. The dimension of this area along the y-axis consists of a) 0.7 m from the center of the circular surface body at the starting point of the forward movement in the negative y-direction, b) the length of the walking track, and c) 0.7 m from the center of the circular surface body in the positive y-direction from the endpoint of the forward movement.

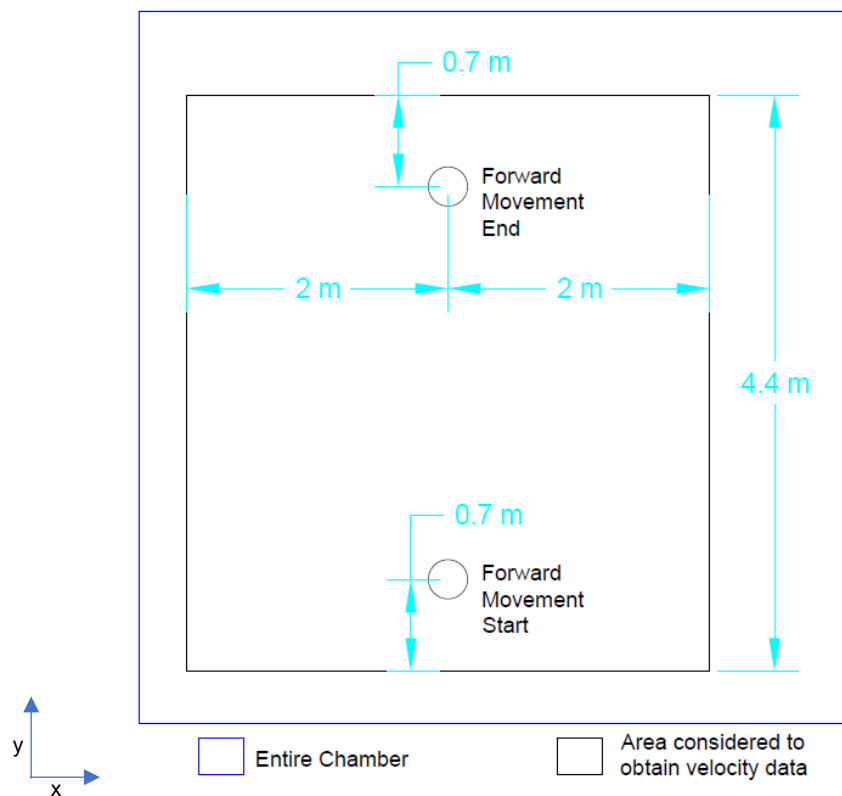


Figure 50: The Area Considered to Obtain Velocity Data for the Training Set

The 4m along the x-axis covers 2 m from the center of the circular surface body in the negative x-direction and another 2 m from the center of the moving body in the positive x-direction. As this (4 x 4.4) m² rectangular area contained a dynamic mesh region (please refer to Chapter 7, section Assessment of EBM Using Numerical Simulation Data, subsection 'Model Geometry and Discretization'), the velocity values were obtained at different nodes at every timestep, so to obtain values at defined points, the entire domain was discretized in 1cm X 1cm grids that resulted in 1845 points with velocity values at each of them, and the velocity values were stored in a matrix where the spatial information was stored in the rows, and the temporal information was stored in the columns. The total time for all six translation motions was 23 seconds, and to build the training sets, 24 seconds of the simulation data was used. Given that three different initial conditions were used for the simulations, the final training set was a matrix of size 1845 x 3000 x 3.

Using EBM to predict the velocities in the multiple walk scenario:

The idea here is to use the training sets and the EBM algorithm to predict the velocity values in the multiple walk scenario and evaluate the results by comparing them with the velocity values obtained through multiple walk CFD simulation. As the training set was built for an area of 4 x 4.4 m² encompassing the walking track for one walk, the multiple walks were also broken down into four subspaces with the area of 4x4.4 m², as shown in Figure 51.

Each of these subspaces was considered separately and compared with the training set to find the velocity vector that is closest to the velocity vector within the training set at every timestep, and the Dynamic Closest Case (DCS) approach of the EBM algorithm was used to predict the α , which was then used to compute the velocity vector at the next time step (m+1), using the velocity vector at that timestep (m). The computation using the EBM was initiated based on the velocity vector at timestep 1 for the entire domain. Based on the time and location of the moving surface, the subspace to consider for prediction was determined. It must be noted here that after the first of the four walks (i.e., walking motion from point A to point B), when the next subspace was

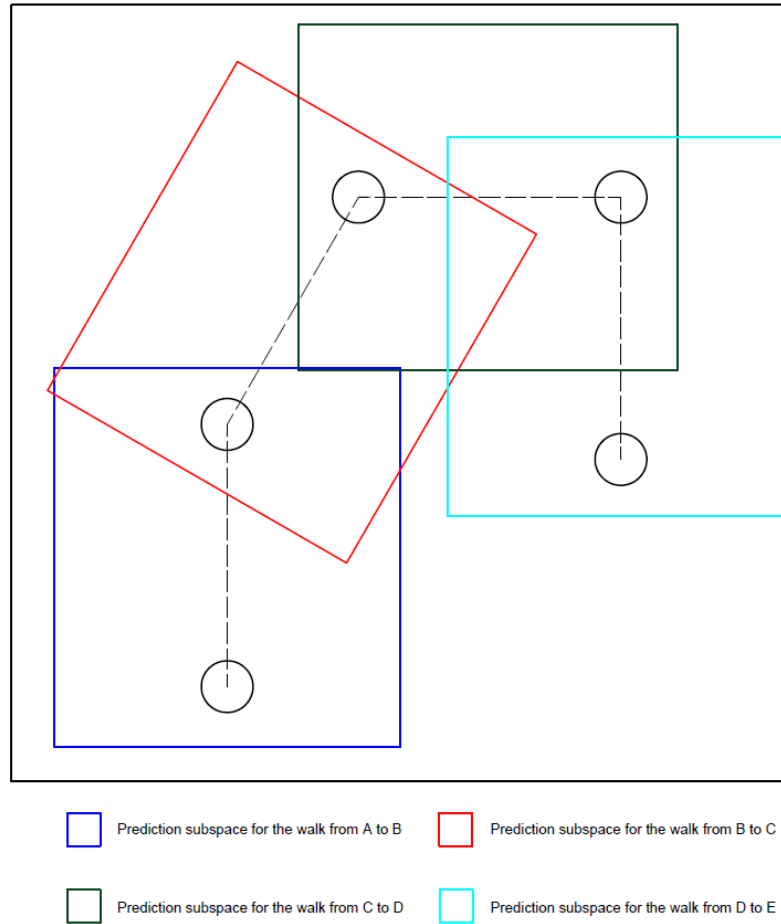


Figure 51: Defining Prediction Subspace for the Multiple Walk Scenario

considered, the velocity values continued to change in the previous subspaces. For example, when approximating the velocity values in the subspace for the third walk (i.e., from point C to point D), it was still required that the EBM algorithm continues calculating the changes in velocities for the previous two subspaces. The timestep sizes were determined from the beginning of a walk to the beginning of the next walk. The velocity field for the entire 9m X 9m domain was updated at every timestep. If a particular node was inside the subspaces, the velocity value was updated according to the approximated velocity values as calculated by the EBM algorithm. It is also important to note that some points within the prediction subspace were outside the domain boundary for the last walk, i.e., the movement from point D to point E. When updating the velocity

profile, it should be noted that if a point is beyond the entire domain or on the boundary, the velocity value must be considered zero at that point. Algorithm 3 summarizes this process of computing the velocity profile for multiple walks using the EBM method. The subspace IDs were sorted in an ascending order to ensure that the velocity vectors were updated for the latest timestep, which was important for nodes that were in the overlapping region between the subspaces.

Algorithm 3: Employing EBM to predict velocity profile for multiple walks

Let $\langle X_1, X_2, \dots, X_K \rangle$ be the training sets

Let V_i be the velocity vectors at all the nodes of the entire domain at timestep i

if $t \geq 0$ and ≤ 4

 subspaceID = 1 (for the walk from Point A to B)

elseif $t \geq 4$ and ≤ 8.5

 subspaceID = 2 (for the walk from point B to C)

elseif $t \geq 8.5$ and ≤ 11.5

 subspaceID = 3 (for the walk from point C to D)

else $t \geq 11.5$ and ≤ 14.5

 subspaceID = 4 (for the walk from point D to E)

end if

for subspaceID = 1:m **do**

 Determine the coordinates of the four corners of the subspace

 Interpolate the velocity values from the entire domain V to subspace1 at timestep 1

 % Use EBM to approximate velocity values every node of subspace1

 Let IC_{m_i} be the velocity vector at all nodes inside subspace m at timestep i

 Let IC_{XK_j} be the velocity vectors of the training database timestep j (1:3000)

for $i = 1:T$ **do**

 % $T = (\text{duration of beginning of a walk to the beginning of the next walk})/\text{timestep size}$

for $j = 1:3000$ **do**

for $k = 1:K$ **do**

$d_K = \text{norm}(IC_{1_i} - IC_{XK_j})$

end for

$Q = \text{Index}(\min(d))$ % Determine the closest case at every timestep

end for

$\alpha_{\text{new}} = \alpha Q$

$u_{\text{new}}^i = u_{\text{new}}^{i-1} \times \alpha_{\text{new}}^i$

if subspaceID = 1

 Check the coordinates of the entire domain

if coordinates of the domain is within the subspace

 update with u_{new}^i

else

 keep the velocity value from the first timestep

end if

if subspaceID > 1

 Check the coordinates of the entire domain

if the coordinates are \geq largest x – and y – coordinate value

 use $u_{\text{new}}^i = 0$

else if the coordinates match with the coordinates of the subspaces

$[S] = \text{index}(\max(\text{subspaceID}))$ % sorting based on ascending values

 update the nodes in the subspace with subspaceID(1:S)

 with u_{new}^i computed for that subspace

else

 update the nodes with V_i

end if

end if

end for

end for

Evaluating the prediction:

The absolute error (e), which is the absolute value of the difference between the velocity magnitude calculated using both approaches, was calculated to compare the velocity fields obtained using the EBM and the CFD model. Figure 52 shows the evolution of spatially averaged absolute error over the timesteps. It may be noted that there is a spike in error at timestep 500, which can be attributed to the movement at a 60-degree angle with the x-axis that started from timestep 500. As the movement was at an angle, the subspace selection for the walk from point B to C involved turning the coordinate system. However, the average absolute error did not exceed 0.025 m/s.

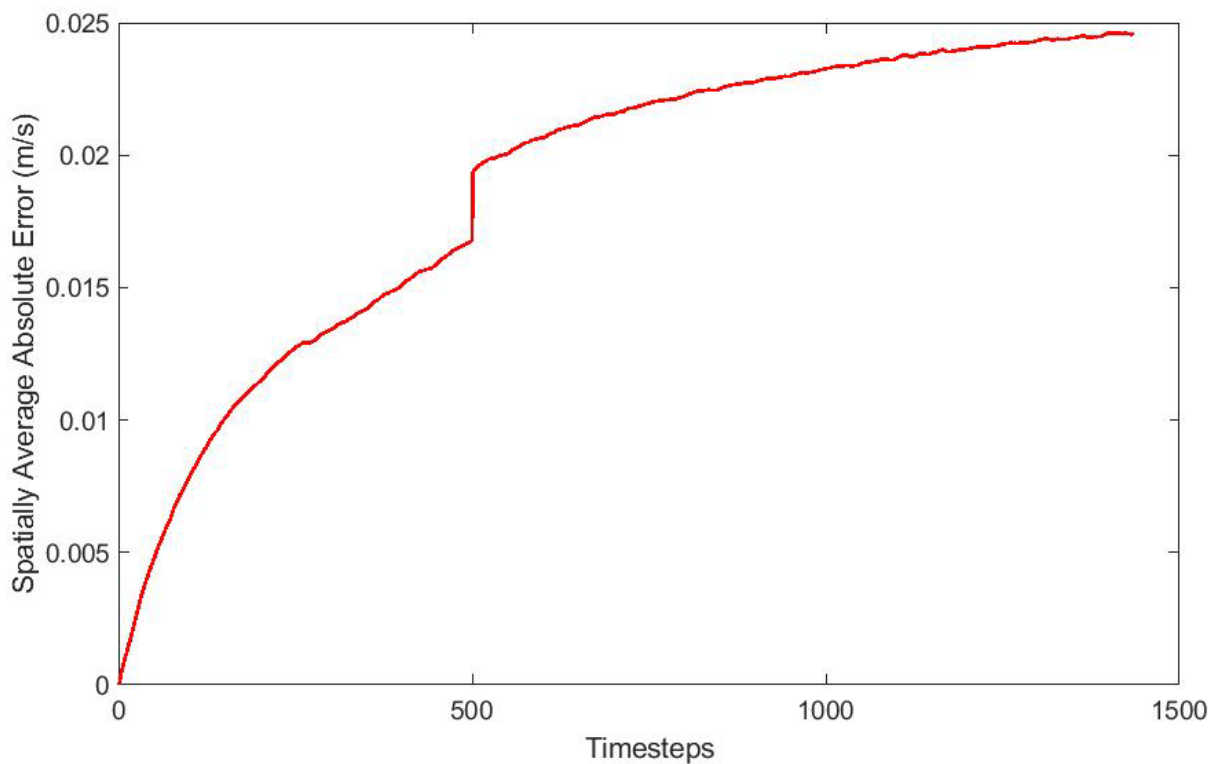


Figure 52: Spatially Averaged Absolute Error

The absolute error distribution was visualized using statistical histograms, where the algebraic value of the error was used instead of the absolute value, as shown in Figure 53. It was found

that the distribution was normal and unimodal, with a few outliers in the left tail. The histogram of temporally averaged error depicts that the EBM approach undercalculates the values, as there were more negative errors than there were positives. When a normal distribution was fitted to the distribution, the estimated mean was found to be -0.016 with a stand error of 0.3×10^{-4} , and the standard deviation was 0.03 with a standard error of 2×10^{-4} . This finding that the estimated mean is close to zero confirms that the EBM approach's approximation is reasonable to predict the airflow patterns for multiple consecutive transient events when the boundary condition is constant.

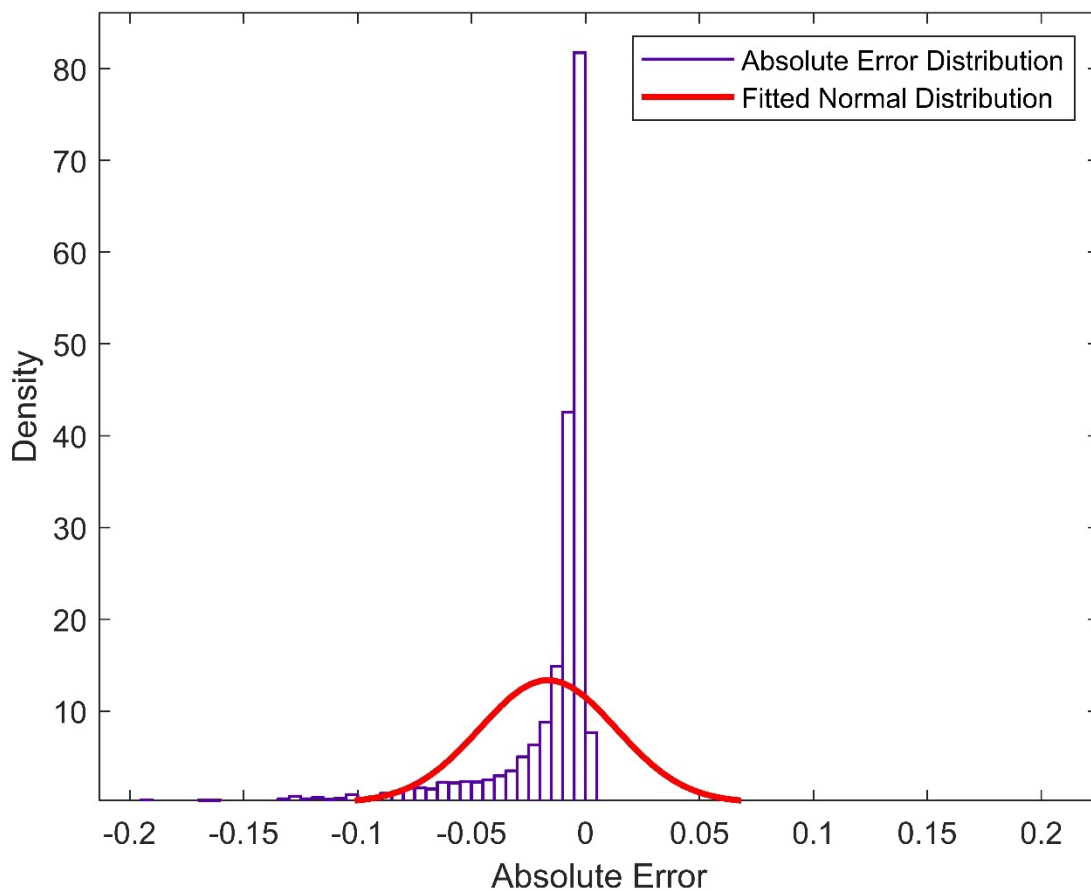


Figure 53: Distribution of Temporally Averaged Error

Apart from the accuracy aspect of the simulation, it is also important to discuss the reduction in computational intensity. Computationally simulating compressible flow problems using implicit

time-stepping means forming and solving a sparse linear system for every time step, for which direct matrix inversion is required, resulting in the computational complexity of N^3 , N being the number of nodes where solutions are computed. In practice, iterative processes are used to reduce the intensity (Computational Time Complexity of Solvers (Big O), 2019). In comparison, when EBM is used, the computational complexity is reduced further. To illustrate this, when the computational complexity of the simulating multiple walks (discussed in this chapter) using CFD and EBM was compared, the time taken to obtain the flow fields was reduced by nearly 40%, indicating the EBM method is efficient.

Extending the EBM approach to approximate airborne particle movement:

Although it is out of scope for this research to formulate and evaluate the particle movement approximation using the outcomes of an EBM model, this section provides an overview of how EBM models can be extended in simplifying complex mathematical approaches to determine airborne particle dispersion. The particle transport models are discussed here to introduce a potential application of the EBM.

Particle Transport model:

Particle transport models can be integrated into the simulations to gather useful insight into how the principal airstream carries the passive contaminants and how the occupant-induced perturbations disperse the contaminants separately. There are two principal methods of modeling particle transport, namely the Eulerian and Lagrangian methods.

Eulerian Method:

This method is used for small and passive particles, having small relaxation time (the time required to adjust to a new condition). In this method, a continuum assumption is used for the particles phase, which follows the scalar transport equation (Equation 36)

$$\frac{\delta \rho C}{\delta t} + \nabla \cdot [(u_i + v_{s_i}) \rho C] = \nabla \cdot (\Gamma \Delta C) + S_c \quad \text{Equation 36}$$

where t - time, C - particle concentration; ρ - the air density; u_i - the averaged air velocity components for the RANS models in three-dimensional space, Γ - the effective diffusivity for a particle; v_{s_i} - the particle settling velocity in the three-dimensional space, to be modeled accounting for gravitational settling, and S_c - a source term. ∇ is an operator given by Equation 37.

$$\nabla = \begin{bmatrix} \frac{\delta}{\delta x} \\ \frac{\delta}{\delta y} \\ \frac{\delta}{\delta z} \end{bmatrix} \quad \text{Equation 37}$$

Suppose the Eulerian method of particle flow modeling is used, and the air velocity is predicted by EBM. In that case, it decouples the partial differential equation, making it easier to solve, even if it does not transform into an ordinary differential equation.

Lagrangian Method:

Unlike the Eulerian method, this method does not consider particles as a continuum; instead, the motion of many individual particles is calculated to obtain their trajectories. That is why the Eulerian method directly accounts for the physical phenomena of the particles. This method, however, is established for environments in which the second species' concentration is sufficiently large to create a continuum. Alternatively, the Lagrangian method treats contaminants as solid, non-deformable entities whose motion is determined by their forces. For an enclosed environment, the diffusion equation by the Lagrangian method is given in Equation 38.

$$\frac{du_{p_i}}{dt} = F_D(u_i - u_{p_i}) + \frac{g_i(\rho_p - \rho)}{\rho_p} + F_i \quad \text{Equation 38}$$

where, u_{p_i} and u_i - particle and air velocities, respectively, in three-dimensional space; ρ_p and ρ - particle and air densities, respectively; g_i is the gravitational force with i denoting the components in three principal directions; F_i is additional forces such as Brownian force acting in three-dimensional space; and F_D is the drag coefficient. Here u_i is the actual velocity of the airflow, given by the RANS flow model as given in Equation 39.

$$u_i = \bar{u} + u'_i \quad \text{Equation 39}$$

Where mean velocity \bar{u} is obtained from the airflow model, and the fluctuating component u'_i is calculated using a Discrete Random Walk (DRW) model. For $k - \varepsilon$ RANS models, DRW is given by Equation 40.

$$u'_i = \zeta_i \sqrt{\frac{(2)k}{3}} \quad \text{Equation 40}$$

where k - turbulent kinetic energy and ζ_i - a normally distributed random number. For more detailed discussions on these particle dispersion models, please refer to (M. Wang et al., 2012) and (ANSYS, 2009). These models quantify contamination concentrations and their dispersion patterns with reasonable accuracy.

As discussed earlier, the computational intensity to simulate transient events is significant, and that's why the EBM approach can be useful. When EBM is used to calculate u_i , the only unknown in Equation 38 is the particle velocity u_{p_i} , making that equation an ordinary differential equation with one unknown variable, in which case the solution can be obtained easily. Particle trajectories can be computed from the particle velocity using Equation 41.

$$\vec{u}_p = \frac{d\vec{x}_p}{dt} \quad \text{Equation 41}$$

Thus, computing the airflow patterns that originate from occupant-built environment interactions using the EBM approach can ultimately lead to modeling the airborne contamination spread as a

function of time. This way, the passive mode of pathogen transmission can be computed and ultimately used to control the ventilation system. Regulating the ventilation system based on real-time occupant movements has a great potential in informing occupant-centric and demand-controlled ventilation system design. Increasing the flow rates when a door is opened, or a human walking movement is detected and going back to a reduced airflow when a steady state has been reestablished can pave the way to energy-efficient ventilation system design.

Chapter 9

Research Validity and Limitations

Internal:

Internal validity deals with the existence and directions of causal relations between the variables (Cook, Thomas D; Campbell, 1979). The experiments designed for this study were controlled in the sense that the indoor environments eliminate unwanted events and variables. The outcome variable was associated with the independent variables, and the effects of interventions were clearly described. The absence of human subjects and recorders countered the threats of maturation and testing. Instead, the person carrying out the walking or door opening exercises in the space improved with increased involvement with multiple experiments. Applying the levels of treatments in the same chamber, the threats related to attrition and regression were not applicable. The binding definitions of the events used for data collection and analysis prevented human behavior's haphazard nature and controlled randomness associated. Although the randomness could not be avoided in full, repetition of experiments in each setting (at least 30 rounds of data collection in each setup) aided in averaging that randomness out. The threats to internal validity due to instrumentation were present as the instruments used in these experiments are velocity sensors. Nevertheless, according to the manufacturer's recommendation, proper calibration prior to the beginning of the experiments helped minimize errors with data collection. Another source to counter the threats to establish causal relationships with experiments was that the findings from simulations supported and supplemented the findings. Numerical approximation using CFD warranted the relations between variables, given the convergence criteria of the simulation models were closely monitored and controlled.

External:

The external validity is about the possible generalizations of the results across the settings and time (Cook, Thomas D; Campbell, 1979). This study examined the effects of treatments at different levels. Suppose it is observed that the disturbances are contained within 12 seconds after the first detection when the supply fan is operating at 50% and within 5 seconds when the supply fan is operating at 90% for a specific operating room. Suppose another treatment (system operating at 70% capacity) is employed, and the movement-generated wakes are suppressed within 7 seconds. The experimental results showed that increased flow of air was helpful in subsiding the effects of transient occupant interactions. Thus, it can be generalized that increasing the airflow rate helps contain the disturbances quicker for a given chamber with a similar HVAC system.

Construct:

Construct validity is associated with the measurement of the intended concept abstracted at the beginning of the research design, such that the measures represent the concept appropriately. In this study, the constructs were related to the flow properties measured using the variables that describe the characteristics of the flow. One such measured variable was velocity, and it was used to compute other properties like kinetic energy. Collecting the data over multiple experiments provided reliable measures. Also, to ensure construct validity, several numerical simulation models were run. As explained earlier, these models eliminated the randomness associated with human-induced movements and provided measures not confounded by the interventions. These models are based on physical laws (for our purpose, we will use Navier-Stokes' equation) and solve for the equations depending on the initial and boundary conditions. Additionally, proper sensor calibration was a method for consistent measurement during experiments, while minutely modeling the flow's physical properties during simulation also mitigated threats to construct

validity. It is to be emphasized again that the numerical models cannot replicate a real-life event; instead, the results are approximated, assuming the true changes in physical properties.

Reliability:

A reliable research design is one that yields consistent results with multiple measures. When considering the reliability of this study, the reliability was consistent for both experiments and simulations. Reliability was enhanced, with each experiment being repeated multiple times (at least 30 sets of data collection per experiment set). These experiments were conducted in indoor settings, where unwanted interaction with the outdoor environment was avoided. With this high level of control, the reliability of the tests was significant, and it also provided similar control administered for repetitions. For simulations, replicability lies in consistently modeling the flow phenomena using mathematical models. The numerical simulation models are sensitive to the discretization parameter, i.e., the mesh size and the convergence criteria. Consistently obtaining near-zero error values when both the experimental and CFD simulation data were used alleviated the threats to reliability.

Limitations:

This dissertation discussed investigating the spread of airborne contaminants under indoor occupant interventions. The research propounds for experiments in indoor environments complemented by mathematical approximation of results using simulations. But the research approach and the design have some limitations.

The experimental setups considered for this study are constrained and simplified. The rate of ventilation; the walking direction, distance, and speed; and the door opening scenarios were all structured to aid the research design and are not randomized. The type of HVAC systems, airflow supply and exhaust conditions, the introduced disturbances, and their characteristics were all

limited, and it was not feasible to expand their selections. Though some of these were alleviated using CFD simulations to obtain data, the simplified generalizations remained in the design.

Human occupants' behavior is stochastic, and it is very cumbersome to capture those natures through experiments when an event-based approach is used. Similarly, modeling these irregular motions is computationally intensive, even with considerable computing power. Thus, this study simplified the activities that approximate the events, even though the results had been found to be satisfactory in previous studies.

Chapter 10

Conclusion

This research study was developed to examine the indoor airflow patterns in steady states and their alterations from occupant-introduced perturbations. Through this experimental study, the effects that occupants exert on the indoor airflow patterns and consequently on airborne contamination spread were quantified and modeled to make predictions based on the given initial condition, i.e., the state of the air distribution system in a balanced and closed system. The primary focus of this study was to understand how occupants aid in the changes in the airflow patterns that result from the air supply and exhaust by the ventilation system. Additionally, this study also proposed and validated a novel methodology to use the experimental and numerical simulation data to make predictions of the transient airflow when occupants interacted with the steady-state system. The Event-Based Model (EBM) methodology was found to be acceptably accurate in predicting the changes in airflow properties. This research also paves the way to use EBM to approximate flow properties and use those properties to calculate indoor particle motions.

The experiments conducted in the cleanroom studied the migration of particles from the external source. It was observed that even without any sources of particulate contamination inside the cleanroom, a user of the cleanroom can take a significant amount of contamination from the door opening closing and getting in/out of the cleanroom. The particle size was also found to be an important determinant of airborne contamination. Submicron-sized particles, which are mostly responsible for pathogenic contamination, were found to be sneaking into the positively pressurized cleanroom even without the door being opened. Higher differential pressure resulted in better containment, as the prescribed pressure differential was reestablished quicker after a door opening had nullified the pressure differential. When the door opening was followed by an inward movement of the occupant, i.e., opposite to the principal direction of air movement due to

positive pressurization in the cleanroom, more particles migrated inside the cleanroom, compared to when the door opening was followed by the occupant getting out of the cleanroom.

The pressure differential in critical indoor spaces is generally dictated by codes, and it also depends on the space function. As it was established that occupant movements had a significant impact on the flow patterns, it was important to study how occupant interventions affect the flow properties. Thus, a set of experiments were conducted to quantify the spatiotemporal effects of walking indoors. To control for inherent randomness of occupant movements, a walking track was defined to examine how walking once and twice within that walking track impacted the flow field of the entire chamber. The experiments were conducted for one control case (no air was supplied) and two treatment cases (the air was supplied at 70% and 100% of the full capacity). It was found that walking at a normal indoor walking speed of around 1 m/s for 3 minutes left distinguishable and significant changes in the airflow properties. Depending on where the sensors were placed along the walking track, wakes with higher velocities than the initial conditions were present up to 15 seconds on average even after the walking was stopped. The effects of walking were also realized based on the locations of the sensors – the sensors, which were closest to the beginning of the walking movement, recorded a change in the velocities immediately after the walk started. Whereas the sensors at the tail end of the walking movement recorded the changes with about 2 s lag, meaning they recorded the changes in the velocity 2s after the moving body passed their location. It was also noteworthy that walking twice, i.e., covering the walking track distance twice consecutively in the alternating direction, also increased the resultant flow velocity due to the increased interaction of the walking occupant and the wakes generated from the first round of walk. It was also seen that the kinetic energy of the air was increased due to the human walk. The increase was more prominent when there was air supply in the chamber when compared to the quiescent air background scenario, which could be attributable to fluctuations in higher

velocity magnitude over mean, i.e., increased turbulence. Interestingly, the increase in kinetic energy for walking twice when compared to walking once was independent of the initial condition.

Similarly, experiments were conducted to examine the alterations in the steady state flow fields in addition to quantifying the air mixing due to the opening and closing of a swing door in a positively pressurized room. Flow velocities were measured at different heights inside the chamber. These experiments showed that the change in the air velocity was location-specific – the area closest to the door opening periphery was associated with the maximum changes in the velocity. Similar to the walking experiments, it was also found that subsequent operation of the swing door resulted in a further increase of the flow velocities when compared to operating the door once, as the remainder of the wakes generated from the first door opening interacted with the second cycle of opening and closing. Interestingly enough, higher supply rates were associated with increased velocity changes, but the changes were suppressed quickly with higher supply rates. When there was an air supply in the chamber, opening the door for 5 s resulted in 2 ACH air escaping through the door opening. Finally, to summarize, it was found that the velocity values originating from door opening once and twice exhibited similar patterns, as did the walking experiments, under all three inlet conditions. This was an interesting and significant finding as it was possible to model those changes to make predictions.

Every set of walking and the door opening experiments was repeated at least 30 times, and for every repetition, the data was collected for one minute to capture the change in velocity from the occupant interactions until the flow field went back to the initial condition. That way, a considerable quantity of data was collected for three different initial conditions for two separate interventions for walking and door opening experiments. This way, a mathematical predictive model was developed that could approximate the changes in the velocity values from occupant introduced disturbances like a door opening or walking for a different initial condition, given the boundary conditions were kept constant. The principal idea behind the model was that the current ventilation

system design paradigm relies mostly on steady state calculations, largely without considering transient events like occupant introduced perturbations, as studying those transient events are computationally extremely intensive and oftentimes not feasible to study using experimental techniques. The predictive model, EBM, which was proposed in this study, can approximate the flow properties under transient events using a data-driven model. The developed model included three methods of approximation, namely the weighted average approach, closest case approach, and dynamic closest case approach. These methods used the data from every timestep of the repeated experiments to approximate an identifier that marches on time to calculate the velocity value at the next time step, given a specific initial condition. The results showed that the dynamic closest case was the most accurate method in terms of prediction accuracy. The EBM model was applied to the door opening experiment data, where 80% of the collected dataset was used to train the model, and the rest 20%, was used to gauge the prediction accuracy. The error was defined as the difference between the predicted velocity and the experimentally measured velocity across the spatial locations over all the timesteps, and when spatially averaged, the error-index was found to be less than 0.2 m/s. A set of two-dimensional CFD models were developed for the walking experiments, where multiple walks in a defined walking track were simulated for three different initial conditions. The EBM model was also applied to that dataset, and the prediction turned out to be even better than using experimental results since simulation allowed to collect of data over a large number of spatial locations across the chamber, with the timestep being small (0.008s), resulting in a rich database to train the model.

The applicability of the EBM approach was also tested in this dissertation. The argument behind the EBM approach was that it was easier and computationally efficient to predict the effects of transient events compared to numerical simulation. A two-dimensional simulation of a person randomly walking in an indoor environment was developed in Ansys Fluent (v.21.2). The data obtained from the 2D CFD simulation of a person walking back and forth under three different

initial conditions in a straight walking track, which was developed and used to test the prediction accuracy of the EBM model (as described in Chapter 7), was used as the training set to approximate the random walks. The approximation of the velocity profile using the EBM method was found to be fairly accurate. These findings proved that EBM can be crucial to assessing the indoor airflow patterns under realistic occupant interventions. This way, the flow properties, approximated by the EBM, can be used to simplify the fundamental equations of particle flow, especially in the Lagrangian framework of reference, which can potentially lead to easier ways to track airborne particles' movements under occupant interventions. These findings ultimately lead to developing an occupant-centric ventilation system that can effectively adapt to occupant activities, reducing the chances of airborne particle dispersion and optimizing energy usage.

Annexure 1 – List of the Sources of Limitations

In this annexure, the potential sources of limitations for the pertinent chapters have been listed and the associated page numbers in parenthesis indicate the page where it has been discussed within the dissertation.

Chapter 4:

- The cleanroom used for the experiments was a bio-safety laboratory, not typically representing the industrial cleanrooms in size or geometry (page 79).
- The traffic movement was constrained to follow the same pattern, instead of the sporadic movement of an occupant (page 80).
- The door opening and closing times were kept constant, and the timekeeping was done manually. In an actual cleanroom environment, the door opening and closing times may vary according to the occupant movement (page 80).
- For all the experiments, the door between the gowning room and the chaseroom were opened and closed, the occupant waited in the gowning room before opening the door between the cleanroom and the gowning room during the forward movement. Similarly, during reverse movement, there was waiting time before the doors were opened. The impacts of subsequently opening both doors with no waiting time was not examined (page 80).
- The experiments were conducted over a short period of time due to limited availability of the cleanroom, resulting in the ability to conduct experiments for two levels of differential pressure (page 80).

Chapter 5:

- Only three levels of the inlet airflow rates could be used to conduct experiments due to limited access to the experiment chamber (page 99).
- The walking exercises were controlled to simulate two separate walking scenarios in straight line motions, and the experiments did not study stochastic human walking movements (page 99).
- The experiments did not consider the effects of the hands and legs movements during walking (page 85).
- Limited number of omnidirectional sensors were available which constrained the spatial velocity data collection across the room and the velocity data was only available in close vicinity of the walking track (page 86).
- The ultrasound sensors used to collect three-dimensional velocity data were not commercialized, and only one such sensor was used during the experiments. This sensor logged some unrealistic data that were omitted while data analysis (page 99).
- The velocity data was collected at a single horizontal plane due to limited availability of sensors (page 86).

Chapter 6:

- Limited access to the experiment chamber led to conduct experiment under three initial conditions (page 133).
- Only two scenarios of swing door opening events were studied (page 133).
- Only eight sets of sensors were available that restricted the data collection at sparse locations; sensors could only be placed one meter apart to maximize the area of data gathering inside the chamber. Access to more sensors would have provided better resolution of the spatial velocity data (page 133).

- These experiments did not study the combined effects of door opening and occupant movement through the door (page 133).

Chapter 7:

- Similar to chapters 5 and 6, the experimental data used to develop and validate the EBM algorithm was obtained from experiments had only three initial conditions, limited spatial data from sensors, and constrained occupant-introduced transient events (page 162).
- The CFD simulations were two-dimensional, limiting the comparability to practical scenarios of three-dimensional environments (page 162).

Chapter 8:

- Only two-dimensional translation movements were simulated and tested (page 170).
- Changing the movement axes and availability of simple forward-reverse walking pattern as training dataset led to increase in the error (page 172).

References:

- Adams, N. J., Johnson, D. L., & Lynch, R. A. (2011). The effect of pressure differential and care provider movement on airborne infectious isolation room containment effectiveness. *American Journal of Infection Control*, 39(2), 91–97. <https://doi.org/10.1016/j.ajic.2010.05.025>
- Ahmed, O., Mitchell, J. W., & Klein, S. A. (1993). Dynamics of laboratory pressurization. *ASHRAE Transactions*, 99(pt 2), 223–229.
- Airborne Particulate Cleanliness Classes in Clean Rooms and Clean Zones. (1992). In *Federal Standard 209E*,.
- Alhamid, M. I., Budihardjo, & Rahmat. (2018). Performance analysis of air conditioning system and airflow simulation in an operating theater. *AIP Conference Proceedings*, 1933(February). <https://doi.org/10.1063/1.5023991>
- ANSI, A. (2006). AHAM standard AC-1-2006, method for measuring performance of portable household electric room air cleaners. *Washington, DC: Association of Home Appliance Manufacturers*.
- ANSYS, F. (2009). *12.0 Documentation*. Ansys Inc.
- Arens, E., Ghahramani, A., Przybyla, R., Andersen, M., Min, S., Peffer, T., Raftery, P., Zhu, M., Luu, V., & Zhang, H. (2020). Measuring 3D indoor air velocity via an inexpensive low-power ultrasonic anemometer. *Energy and Buildings*, 211, 109805. <https://doi.org/10.1016/j.enbuild.2020.109805>
- ASHRAE. (2011). *2011 ASHRAE HANDBOOK HVAC Applications BUILDING OPERATIONS AND MANAGEMENT*.
- ASHRAE. (2019). *ASHRAE Handbook of Applications*. American Society of Heating, Refrigerating, and Air Conditioning Engineers (ASHRAE).
- ASHRAE Standard 170. (2013). *Ventilation of Health Care Facilities*. American Society of Heating, Refrigerating, and Air Conditioning Engineers (ASHRAE).
- Awbi, H. B. (2003). *Ventilation of buildings*. Taylor and Francis.
- Bai, Yan; Yao, Lingsheng; Wei, tao; Tian, Fei; Jin, Dong-Yan; Chen, Lijuan; Wang, M. (2020). Presumed Asymptomatic Carrier Transmission of COVID-19. *Journal of American Medical Association*, 323(14), 1406–1407. <https://doi.org/10.1056/NEJMoa2001316>
- Balocco, C.; Petrone, G.; Cammarata, G. (2012). Assessing the effects of sliding doors on an operating theatre climate. *Building Simulation Volume*, 5, 73–83.
- Bauman, Fred; Arens, Edward A; Tanabe, S; Zhang, H; Baharloo, A. (1995). Testing and optimizing the performance of a floor-based task conditioning system. *Energy and Buildings*, 22(3), 173–186. <https://doi.org/10.11436/mssj.15.250>
- BE Launder, D. S. (1972). *Mathematical Model of Turbulence*. London, Academic Press.
- Beggs, C. B., Kerr, K. G., Noakes, C. J., Hathway, E. A., & Sleight, P. A. (2008). The ventilation of multiple-bed hospital wards: Review and analysis. *American Journal of Infection Control*, 36(4), 250–259. <https://doi.org/10.1016/j.ajic.2007.07.012>

- Bhattacharya, Arup; Mousavi, E. (2020). The Effect of Boundary Conditions on Transient Airflow Patterns : A Numerical Investigation of Door Operation. *ASHRAE Transactions - Papers Presented at the 2020 ASHRAE Winter Conference in Orlando, Florida*.
- Bhattacharya, A., Ghahramani, A., & Mousavi, E. (2021). The effect of door opening on air-mixing in a positively pressurized room: implications for operating room air management during the COVID outbreak. *Journal of Building Engineering*, 44(May), 102900. <https://doi.org/10.1016/j.jobbe.2021.102900>
- Bhattacharya, A., Metcalf, A. R., Nafchi, A. M., & Mousavi, E. S. (2020). Particle dispersion in a cleanroom – effects of pressurization, door opening and traffic flow. *Building Research & Information*, 0(0), 1–14. <https://doi.org/10.1080/09613218.2020.1720500>
- Bhattacharya, A., Pantelic, J., Ghahramani, A., & Mousavi, E. S. (2020). Three-Dimensional Analysis of the Effect of Human Movement on Indoor Airflow Patterns. In *Indoor Air*. <https://doi.org/10.1111/ina.12735>
- Birgand, G., Toupet, G., Rukly, S., Antoniotti, G., Deschamps, M. N., Lepelletier, D., Pornet, C., Stern, J. B., Vandamme, Y. M., Van Der Mee-Marquet, N., Timsit, J. F., & Lucet, J. C. (2015). Air contamination for predicting wound contamination in clean surgery: A large multicenter study. *American Journal of Infection Control*, 43(5). <https://doi.org/10.1016/j.ajic.2015.01.026>
- Bjorn, E.; Mattsson, M.; Sandberg, M.; Nielson, V. (1997). Displacement Ventilation – Effects of Movement and Exhalation. *Proc. Of Healthy Buildings*, 163–168.
- Bolashikov, Z. D., Melikov, A. K., Kierat, W., Popiolek, Z., Brand, M., & Melikov, Arsen Krikor; Bolashikov, Zhecho Dimitrov; Kostadinov, Kamen ; Kierat, Wojciech; Popiolek, Z. (2012). Exposure of health care workers and occupants to coughed airborne pathogens in a double-bed hospital patient room with overhead mixing ventilation. *10th International Conference on Healthy Buildings*, 18(4), 602–615. <https://doi.org/10.1080/10789669.2012.682692>
- Bringmann, A., & Meuter, R. (1985). Clean Room Technology for Production Processes. In *Sulzer Technical Review: Vol. 67/2* (pp. 37–40).
- Brohus, H., Balling, K. D., & Jeppesen, D. (2006). Influence of movements on contaminant transport in an operating room. *Indoor Air*, 16(5), 356–372. <https://doi.org/10.1111/j.1600-0668.2006.00454.x>
- Brouns, C.; Waters, B. (1991). A guide to contaminant removal effectiveness. *Technical Note AIVC 28-2, Air Infiltration and Ventilation Centre, Coventry*.
- Brunton, S. L.; Kutz, J. N. (2019). *Data-driven science and engineering: Machine learning, dynamical systems, and control*. Cambridge University Press.
- Bugaj, A. H., & Przydrozny, S. (1986). New Concept in Clean Room Techniques. *Chemical Engineering Monographs*, 24, 489–496.
- Burch, G. E., & Depasquale, N. (1959). Influence of air conditioning on hospitalized patients. *Journal of the American Medical Association*, 170(2), 160–163. <https://doi.org/10.1001/jama.1959.03010020018005>
- Campbell, J. (1996). Semiconductor secondary gas panel enclosures: an overview of good ventilation design principles. In *Environmental and Occupational Risk Management -*

Compliance Engineering (Vol. 13, p. 5).

- Cao, F., & Cao, X. R. (2011). Event-based optimization for the continuous-time Markov systems. *ASCC 2011 - 8th Asian Control Conference - Final Program and Proceedings*, 932–937.
- Cao, X. R. (2005). Basic ideas for event-based optimization of markov systems. *Discrete Event Dynamic Systems: Theory and Applications*, 15(2), 169–197. <https://doi.org/10.1007/s10626-004-6211-4>
- Carneiro, R., Gaspar, P. D., & d. Silva, P. D. (2017). 3d and transient numerical modelling of door opening and closing processes and its influence on thermal performance of cold rooms. *Applied Thermal Engineering*, 113, 585–600.
- Chaddock, J. B. (1986). Ventilation and Exhaust Air Requirements for Hospitals - Part li: Odors. *ASHRAE Transactions*, 92(pt 2A), 372–395.
- Charnley, J., & Eftekhari, N. (1969). Postoperative infection in total prosthetic replacement arthroplasty of the hip-joint with special reference to the bacterial content of the air of the operating room. *British Journal of Surgery*, 56, 641–649.
- Chen, C., Lin, C. H., Wei, D., & Chen, Q. (2016). Modeling particle deposition on the surfaces around a multi-slot diffuser. *Building and Environment*, 107, 79–89. <https://doi.org/10.1016/j.buildenv.2016.07.016>
- Chen, Q. (1995). COMPARISON OF DIFFERENT k- ϵ MODELS FOR INDOOR. *Numerical Heat Transfer, Part B Fundamentals*, 28:3, 353–369. <https://doi.org/10.1080/10407799508928838>
- Cheng, Y., & Lin, Z. (2016). Experimental investigation into the interaction between the human body and room airflow and its effect on thermal comfort under stratum ventilation. *Indoor Air*, 26(2), 274–285. <https://doi.org/10.1111/ina.12208>
- Chien, L.-H. (2009). Smoke ventilation from the opening of an isolated machine room inside a clean room. *The 4th Asian Conferene on Refrigeration and Air-Conditioning*.
- Choi, J. I., & Edwards, J. R. (2012). Large-eddy simulation of human-induced contaminant transport in room compartments. *Indoor Air*, 22(1), 77–87. <https://doi.org/10.1111/j.1600-0668.2011.00741.x>
- Chung, K. C., & Hsu, S. P. (2001). Effect of ventilation pattern on room air and contaminant distribution. *Building and Environment*, 36(9), 989–998. [https://doi.org/10.1016/S0360-1323\(00\)00051-2](https://doi.org/10.1016/S0360-1323(00)00051-2)
- Ciuzas, D., Prasauskas, T., Krugly, E., Jurelionis, A., Seduikyte, L., & Martuzevicius, D. (2016). Indoor air quality management by combined ventilation and air cleaning: An experimental study. *Aerosol and Air Quality Research*, 16(10), 2550–2559. <https://doi.org/10.4209/aaqr.2015.10.0577>
- Cook, Thomas D; Campbell, D. T. (1979). *Quasi- Experimentation: Design and Analysis Issues for Field Settings*. Houghton Mifflin Company.
- Corvalán, C. F., Kjellström, T., & Smith, K. R. (1999). Health, environment and sustainable development: Identifying links and indicators to promote action. *Epidemiology*, 10(5), 656–660. <https://doi.org/10.1097/00001648-199909000-00036>

- Crane, V. . (1963). Design Techniques for Industrial Clean Rooms. *Air Conditioning, Heating, and Ventilating*, 60(12), 57–63.
- Dorgan, C. B., Dorgan, C. E., & McIntosh, I. B. D. (2002). ASHRAE Laboratory Design Guide. *ASHRAE Transactions*, 108 PART 1, 221–231.
- Eames, I., Shoaib, D., Klettner, C. A., & Taban, V. (2009). Movement of airborne contaminants in a hospital isolation room. *Journal of the Royal Society Interface*, 6(SUPPL. 6). <https://doi.org/10.1098/rsif.2009.0319.focus>
- English, T. R. (2016). A Brief History Of Health-Care Ventilation. *ASHRAE Transactions*, June.
- Eslami, J., Abbassi, A., Saidi, M. H., & Bahrami, M. (2016). Effect of supply/exhaust diffuser configurations on the contaminant distribution in ultra clean environments: Eulerian and Lagrangian approaches. *Energy and Buildings*, 127, 648–657. <https://doi.org/10.1016/j.enbuild.2016.06.028>
- Fagner, P. O. (1970). *Thermal comfort. Analysis and applications in environmental engineering*.
- Fox, D. G. (1969). A study of the application of laminar flow ventilation to operating rooms. *Public Health Monograph*, 78, 1–50.
- Friberg, B., & Friberg, S. (2005). Aerobiology in the operating room and its implications for working standards. *Proceedings of the Institution of Mechanical Engineers, Part H: Journal of Engineering in Medicine*, 219(2), 153–160. <https://doi.org/10.1243/095441105X9282>
- Fung, W. (2002). Cleanroom Design for Operating Suite. *Journal of Documentation*, 9(2), 6–11. <https://doi.org/10.1108/eb026408>
- Garner, J. S., & Hospital Infection Control Practices Advisory Committee. (1996). Guideline for isolation precautions in hospitals. *Infection Control & Hospital Epidemiology*, 17(1), 54–80. <https://doi.org/10.1017/S0195941700006123>
- GAULIN, R. P. (1963). How to keep infection out of the air. *Modern Hospital*, 100, 93–98.
- Ghahramani, A., Zhu, M., Przybyla, R., Andersen, M., Min, S., Zhang, H., Peffer, T., & Arens, E. (2019). An Inexpensive Low-Power Ultrasonic 3-Dimensional Air Velocity Sensor. *Proceedings of IEEE Sensors, 2019-Octob*, 11–14. <https://doi.org/10.1109/SENSORS43011.2019.8956901>
- Greenberg, A. (1963). Hospital air conditioning must be flexible. *Modern Hospital*, 100(3), 103–107.
- Gustafson, T. L., Lavelly, G. B., Brawner, E. R., Hutcheson, R. H., Wright, P. F., & Schaffner, W. (1982). An outbreak of airborne nosocomial varicella. *Pediatrics*, 70(4), 550–556.
- Gustavsson N. (2010a). Dispersion of small particles into operating rooms due to openings [CHALMERS UNIVERSITY OF TECHNOLOGY Göteborg,]. In *Chalmers*. <https://doi.org/D>
- Gustavsson N. (2010b). Dispersion of small particles into operating rooms due to openings [CHALMERS UNIVERSITY OF TECHNOLOGY Göteborg,]. In *Chalmers*. <https://doi.org/D>
- Hakim, I. I., Putra, N., Marda, A. P., Alvaro, M. A., & Winarta, A. (2018). Experimental study on utilization of heat pipe heat exchanger for improving efficiency of clean room air system in hospitals. *E3S Web of Conferences*, 67, 1–8. <https://doi.org/10.1051/e3sconf/20186702056>
- Han, Z. Y., Weng, W. G., Huang, Q. Y., Fu, M., Yang, J., & Luo, N. (2015). Aerodynamic

- characteristics of human movement behaviours in full-scale environment: Comparison of limbs pendulum and body motion. *Indoor and Built Environment*, 24(1), 87–100.
<https://doi.org/10.1177/1420326X13504122>
- Hang, J., Li, Y., Ching, W. H., Wei, J., Jin, R., Liu, L., & Xie, X. (2015). Potential airborne transmission between two isolation cubicles through a shared anteroom. *Building and Environment*, 89, 264–278. <https://doi.org/10.1016/j.buildenv.2015.03.004>
- Hang, J., Li, Y., & Jin, R. (2014). The influence of human walking on the flow and airborne transmission in a six-bed isolation room: Tracer gas simulation. *Building and Environment*, 77, 119–134. <https://doi.org/10.1016/j.buildenv.2014.03.029>
- Harrison, T. (2011). Report from ISO TC209 Working Group 02 Meeting 17th-18th October 2011—ISO 14698-1 and-2. *European Journal of Parenteral Sciences and Pharmaceutical Sciences*, 16(4), 127.
- Hasselaar, E. (2006). Theoretical framework of housing health performance evaluation. *HB 2006 - Healthy Buildings: Creating a Healthy Indoor Environment for People, Proceedings*, 3, 377–382.
- Hathway, A., Papakonstantis, I., Bruce-Konuah, A., & Brevis, W. (2015). Experimental and modelling investigations of air exchange and infection transfer due to hinged-door motion in office and hospital settings. *International Journal of Ventilation*, 14(2), 127–140.
- Hayden, C. S., Johnston, O. E., Hughes, R. T., & Jensen, P. A. (1998). Air volume migration from negative pressure isolation rooms during entry/exit. *Applied Occupational and Environmental Hygiene*, 13(7), 518–527. <https://doi.org/10.1080/1047322X.1998.10390100>
- Heffernan, D. S., Evans, H. L., Huston, J. M., Claridge, J. A., Blake, D. P., May, A. K., Beilman, G. S., Barie, P. S., & Kaplan, L. J. (2020). Surgical Infection Society Guidance for Operative and Peri-Operative Care of Adult Patients Infected by the Severe Acute Respiratory Syndrome Coronavirus-2 (SARS-CoV-2). *Surgical Infections*, 21(4), 301–308. <https://doi.org/10.1089/sur.2020.101>
- Henderson, Y. (1930). The hazard of explosion of anesthetics. Report of the committee on anesthesia accidents. *JAMA Network*, 94(19), 1491–1498.
- Hinds, W. C. (1999). *Aerosol Technology*. John Wiley & Sons, Inc.
- Hitchings, D. T. (1994). Laboratory Space Pressurization Control Systems. *ASHRAE Journal-American Society of Heating Refrigerating and Airconditioning Engineers*, 36(2), 36–40.
- Holmes, P., Lumley, J. L., Berkooz, G., & Rowley, C. W. (2012). *Turbulence, coherent structures, dynamical systems and symmetry*. Cambridge university press.
- Holý, O., & Matoušková, I. (2012). The importance of cleanrooms for the treatment of haemato-oncological patients. *Contemporary Oncology*, 16(3), 266–272. <https://doi.org/10.5114/wo.2012.29298>
- Hu, S. C., Wu, Y. Y., & Liu, C. J. (1996). Measurements of Air Flow Characteristics in a Full-Scale Clean Room. *Building and Environment*, 31(2), 119–128. [https://doi.org/10.1016/0360-1323\(95\)00039-9](https://doi.org/10.1016/0360-1323(95)00039-9)
- International Organisation for Standardization. (2015). *ISO 14644*.
- Jia, Q.-S. (2011). On Solving Optimal Policies for Finite-Stage Event-Based Optimization. *IEEE*

- Transactions on Automatic Control*, 56(9), 2195–2200.
<https://doi.org/10.1109/tac.2011.2152190>
- Jia, Q. S., Wu, J., Wu, Z., & Guan, X. (2018). Event-Based HVAC Control - A Complexity-Based Approach. *IEEE Transactions on Automation Science and Engineering*, 15(4), 1909–1919.
<https://doi.org/10.1109/TASE.2018.2844258>
- Josephson, A., & Gombert, M. E. (1988). Airborne Transmission of Nosocomial Varicella from Localized Zoster. *The Journal of Infectious Diseases*, 158(1), 238–241.
- Joyce, C. T., & Iliria, J. S. (1998). Gas-phase contamination control for semiconductor clean rooms. *ASHRAE Journal*, 40(8), 46–49.
- Kalliomäki, P., Saarinen, P., Tang, J. W., & Koskela, H. (2016). Airflow patterns through single hinged and sliding doors in hospital isolation rooms – Effect of ventilation, flow differential and passage. *Building and Environment*, 107, 154–168.
<https://doi.org/10.1016/j.buildenv.2016.07.009>
- Kanaan, M., Ghaddar, N., Ghali, K., & Araj, G. (2014). New airborne pathogen transport model for upper-room UVGI spaces conditioned by chilled ceiling and mixed displacement ventilation: Enhancing air quality and energy performance. *Energy Conversion and Management*, 85, 50–61. <https://doi.org/10.1016/j.enconman.2014.05.073>
- Kang, Z., Zhang, Y., Dong, J., Cheng, X., & Feng, G. (2017). The Status of Research on Clean Air Conditioning System in Hospital Operation Room. *Procedia Engineering*, 205, 4129–4134. <https://doi.org/10.1016/j.proeng.2017.10.152>
- Karimipannah, M. T. (1998). Deflection of wall-jets in ventilated enclosures described by pressure distribution. *Building and Environment*, 34(3), 329–333. [https://doi.org/10.1016/S0360-1323\(98\)00030-4](https://doi.org/10.1016/S0360-1323(98)00030-4)
- Kato, S.; Murakami, S. (1988). New ventilation efficiency scales based on spatial distribution of contaminant concentration aided by numerical simulation. *ASHRAE Transactions*, 309–330.
- Kato, S., Murakami, S., & Nagano, S. (1992). Numerical study on diffusion in a room with a locally balanced supply-exhaust airflow rate system. *ASHRAE Transactions*, 98, 218–238.
- Khalil, E. E. (2011). Indoor air quality, airborne infection control and ventilation efficiency in hospital operating rooms. *IAQ Conference*.
- Khankari, K. (2017). Air change rate analysis for a minienvironment cleanroom. *ASHRAE Journal*, 57(8), 38–46.
- Kiel, D. E., & Wilson, D. L. (1989). Combining door swing pumping with density driven flow. *ASHRAE Transactions*, 590–599.
- Kircher, K., Shi, X., Patil, S., & Zhang, K. M. (2010). Cleanroom energy efficiency strategies: Modeling and simulation. *Energy and Buildings*, 42(3), 282–289.
<https://doi.org/10.1016/j.enbuild.2009.09.004>
- Kuehn, T. H., Pui, D. Y. H., & Gratzek, J. P. (1992). Experimental and numerical results for airflow and particle transport in a microelectronics clean room. *ASHRAE Transactions*, 98(pt 1), 940–950.
- Kuehn, Thomas H. (1988). Predicting air flow patterns and particle contamination in clean

- rooms. *Journal of Aerosol Science*, 19(7), 1405–1408. [https://doi.org/10.1016/0021-8502\(88\)90185-1](https://doi.org/10.1016/0021-8502(88)90185-1)
- Kundsin, R. B., Bodman, H. A., & Rapoport, J. M. (1979). Clean room and laminar flow room microbiology in the treatment of bone marrow transplant patients. *Journal of Environmental Sciences*, 22(4), 27–29.
- Kutz, J. N., Brunton, S. L., Brunton, B. W., & Proctor, J. L. (2016). *Dynamic mode decomposition: data-driven modeling of complex systems*. Society for Industrial and Applied Mathematics.
- Laforce, E. M. (1986). Airborne Infections and Modern Building Technology. *Environment International*, 12(14), 137–146.
- Lakshmana Prabu, S., Suriyaprakash, T. N. K., Ruckmani, K., & Thirumurugan, R. (2016). GMP in Pharma Manufacturing-Description of GMP as Related to Air-Handling Units and Prevention of Contamination and Implementation of GMP Regulatory Requirements. In *Developments in Surface Contamination and Cleaning* (10th ed., Vol. 10). Elsevier Inc. <https://doi.org/10.1016/B978-0-323-43158-3.00005-8>
- Leclair, J. M., Zaia, J. A., Levin, M. J., Congdon, R. G., & Goldman, D. A. (1980). Airborne Transmission of Chickenpox in Hospital. *The New England Journal of Medicine*, 39.
- Lee, S., Park, B., & Kurabuchi, T. (2016). Numerical evaluation of influence of door opening on interzonal air exchange. *Building and Environment*, 102, 230–242. <https://doi.org/10.1016/j.buildenv.2016.03.017>
- Li, Y., Leung, G. M., Tang, J. W., Yang, X., Chao, C. Y. H. Y. H., Lin, J. Z., Lu, J. W., Nielsen, P. V., Niu, J., Qian, H., Sleight, A. C., Su, H. J. J., Sundell, J., Wong, T. W., & Yuen, P. L. (2007). Role of ventilation in airborne transmission of infectious agents in the built environment - A multidisciplinary systematic review. *Indoor Air*, 17(1), 2–18. <https://doi.org/10.1111/j.1600-0668.2006.00445.x>
- Lin, T., Hu, S. C., Chang, A., & Lin, C. Y. (2010). An innovative ventilation system for cleanrooms with high cooling loads. *ASHRAE Transactions*, 116 PART 1, 293–297.
- Lin, T., Tung, Y. C., Hu, S. C., & Lin, C. Y. (2010). Effects of the removal of 0.1 μm particles in industrial cleanrooms with a Fan Dry Coil Unit (FDCU) return system. *Aerosol and Air Quality Research*, 10(6), 571–580. <https://doi.org/10.4209/aaqr.2010.03.0014>
- Lin, Z., Chow, T. T., & Tsang, C. F. (2007). Effect of door opening on the performance of displacement ventilation in a typical office building. *Building and Environment*, 42(3), 1335–1347. <https://doi.org/10.1016/j.buildenv.2005.11.005>
- Liu, J. Y., Wu, Y. H., Cai, M., & Zhou, C. L. (2016). Point-prevalence survey of healthcare-associated infections in Beijing, China: A survey and analysis in 2014. *Journal of Hospital Infection*, 93(3), 271–279. <https://doi.org/10.1016/j.jhin.2016.03.019>
- Ljungqvist, B. (1979). Some observations of the interaction between air movements and the dispersion of pollution. In *Swedish Council for Building Research, Stockholm, Sweden: Vol. 8/112 P*.
- Ljungqvist, Bengt, & Reinmuller, B. (1996). Clean Room Design: Minimizing Contamination Through Proper Design. In *CRC Press*. CRC Press.
- Loomans, M. G. L. C. (1998). *The measurement and simulation\nof indoor air flow*. November.

- Loomans, M. G. L. C., Molenaar, P. C. A., Kort, H. S. M., & Joosten, P. H. J. (2019). Energy demand reduction in pharmaceutical cleanrooms through optimization of ventilation. *Energy and Buildings*, 202, 1–11. <https://doi.org/10.1016/j.enbuild.2019.109346>
- Luo, N., Weng, W., Xu, X., & Fu, M. (2018). Human-walking-induced wake flow – PIV experiments and CFD simulations. *Indoor and Built Environment*, 27(8), 1069–1084. <https://doi.org/10.1177/1420326X17701279>
- Lynch, R. J., Englesbe, M. J., Sturm, L., Bitar, A., Budhiraj, K., Kolla, S., Polyachenko, Y., Duck, M. G., & Campbell, D. A. (2009). Measurement of foot traffic in the operating room: Implications for infection control. *American Journal of Medical Quality*. <https://doi.org/10.1177/1062860608326419>
- Manzo, J. P. (1977). RETROFITTING HOSPITAL AIR CONDITIONING SYSTEMS. *Specifying Engineer*.
- Mathijssen, N. M. C., Hannink, G., Sturm, P. D. J., Pilot, P., Bloem, R. M., Buma, P., Petit, P. L. C., & Schreurs, B. W. (2016). The Effect of Door Openings on Numbers of Colony Forming Units in the Operating Room during Hip Revision Surgery. *Surgical Infections*, 17(5), 535–540.
- Matsumoto, H., & Ohba, Y. (2004). The Influence of a Moving Object on Air Distribution in Displacement Ventilated Rooms. *Journal of Asian Architecture and Building Engineering*, 3(1), 71–75. <https://doi.org/10.3130/jaabe.3.71>
- Mattsson, M.; Sandberg, M. (1996). Velocity Field Created by Moving Objects in Room. *Proc. Of the 5th International Conference on Air Distribution in Rooms*, 547–554.
- Maxwell, G., Yamamoto, T., & Gerbig, F. (1994). *Optimum Airflow Velocity in Cleanrooms*.
- Mazumdar, S., Yin, Y., Guity, A., Marmion, P., Gulick, B., & Chen, Q. (2010). Impact of moving objects on contaminant concentration distributions in an inpatient ward with displacement ventilation. *HVAC and R Research*, 16(5), 545–563. <https://doi.org/10.1080/10789669.2010.10390921>
- Mears, S. C., Blanding, R., & Belkoff, S. M. (2015). Door Opening Affects Operating Room Pressure During Joint Arthroplasty. *Orthopedics*, 38(11), e991–e994. <https://doi.org/10.3928/01477447-20151020-07>
- Meneguetti, M. G., Ferreira, L. R., Silva, M. F. I., da Silva, A. S., & Bellissimo-Rodrigues, F. (2013). Assessment of microbiological air quality in hemato-oncology units and its relationship with the occurrence of invasive fungal infections: An integrative review. *Revista Da Sociedade Brasileira de Medicina Tropical*, 46(4), 391–396. <https://doi.org/10.1590/0037-8682-0022-2013>
- Mittal, R., Ni, R., & Seo, J. H. (2020). The flow physics of COVID-19. *Journal of Fluid Mechanics*, 894, 1–14. <https://doi.org/10.1017/jfm.2020.330>
- Morawska, L., & Cao, J. (2020). Airborne transmission of SARS-CoV-2: The world should face the reality. *Environment International*, 139(April), 105730. <https://doi.org/10.1016/j.envint.2020.105730>
- Mousavi, E., Betz, F., & Lautz, R. (2019). Academic Research to Support Facility Guidelines Institute & ANSI/ASHRAE/ASHE Standard 170-2013. In *The American Society for Healthcare Engineering (ASHE)*. AHA Data & Insight.

- Mousavi, E., & Bhattacharya, A. (2022). Event based approach for modeling indoor airflow patterns. *Journal of Building Engineering*, 51(January), 104244. <https://doi.org/10.1016/j.jobbe.2022.104244>
- Mousavi, E. S., & Grosskopf, K. R. (2016). Airflow patterns due to door motion and pressurization in hospital isolation rooms. *Science and Technology for the Built Environment*, 22(4), 379–384. <https://doi.org/10.1080/23744731.2016.1155959>
- Mousavi, E. S., Jafarifiroozabadi, R., Bayramzadeh, S., Joseph, A., & San, D. (2018). An observational study of door motion in operating rooms. *Building and Environment*, 144(July), 502–507. <https://doi.org/10.1016/j.buildenv.2018.08.052>
- Nielsen, P. V. (1999). The importance of thermal manikins as a source and obstacle in full-scale experiments. *Proceedings of the 3rd International Meeting on Thermal Manikin Testing 3IMM, Stockholm, Sweden*.
- Noh, K. C., Lee, H. C., Park, J. II, & Oh, M. Do. (2008). Prediction and evaluation of cleanliness levels inside a mini-environment by measuring mean air-age and effective flow rate. *IEEE Transactions on Semiconductor Manufacturing*, 21(2), 297–304. <https://doi.org/10.1109/TSM.2008.2000271>
- Ogunsola, O. T., Wang, J., & Song, L. (2019). Survey of particle production rates from process activities in pharmaceutical and biological cleanrooms. *Science and Technology for the Built Environment*, 25(6), 692–704. <https://doi.org/10.1080/23744731.2019.1581501>
- Papakonstantis, I. G., Hathway, E. A., & Brevis, W. (2018). An experimental study of the flow induced by the motion of a hinged door separating two rooms. *Building and Environment*, 131(December 2017), 220–230. <https://doi.org/10.1016/j.buildenv.2017.12.026>
- Perez, P., Holloway, J., Ehrenfeld, L., Cohen, S., Cunningham, L., Miley, G. B., & Hollenbeck, B. L. (2018). Door openings in the operating room are associated with increased environmental contamination. *American Journal of Infection Control*, 46(8). <https://doi.org/10.1016/j.ajic.2018.03.005>
- Plesu, V., Bonet-Ruiz, A. E., Bonet, J., Iancu, P., Llorens, J., & Becerra, L. I. (2018). Immission assessment inside an industrial ventilated room using CFD. *Chemical Engineering Transactions*, 70(2017), 1825–1830. <https://doi.org/10.3303/CET1870305>
- Poussou, S. B., Mazumdar, S., Plesniak, M. W., Sojka, P. E., & Chen, Q. (2010). Flow and contaminant transport in an airliner cabin induced by a moving body: Model experiments and CFD predictions. *Atmospheric Environment*, 44(24), 2830–2839. <https://doi.org/10.1016/j.atmosenv.2010.04.053>
- Robertson, E. C. (1940). On the Control of Air-Borne Bacteria In Operating Rooms and Hospital Wards. *Annals of Surgery*, 111(3), 491–497.
- Rouaud, O., & Havet, M. (2005). Numerical investigation on the efficiency of transient contaminant removal from a food processing clean room using ventilation effectiveness concepts. *Journal of Food Engineering*, 68(2), 163–174. <https://doi.org/10.1016/j.jfoodeng.2004.05.029>
- Rouaud, O., Havet, M., & Sollicec, C. (2004). Influence of external perturbations on a minienvironment: Experimental investigations. *Building and Environment*, 39(7), 863–872. <https://doi.org/10.1016/j.buildenv.2004.01.008>

- Rouaud, Olivier, & Havet, M. (2002). Computation of the airflow in a pilot scale clean room using K- ϵ turbulence models. *International Journal of Refrigeration*, 25(3), 351–361. [https://doi.org/10.1016/S0140-7007\(01\)00014-7](https://doi.org/10.1016/S0140-7007(01)00014-7)
- Rowley, C. W., & Dawson, S. T. (2017). Model reduction for flow analysis and control. *Annual Review of Fluid Mechanics*, 49, 387–417.
- Rui, Z., Guangbei, T., & Jihong, L. (2008). Study on biological contaminant control strategies under different ventilation models in hospital operating room. *Building and Environment*, 43(5), 793–803. <https://doi.org/10.1016/j.buildenv.2007.01.018>
- Sadjadi, R., & Liu, B. (1991). Supply Plenum and Airflow Uniformity in Cleanrooms. *Journal of the IES*, 34(2), 56–60.
- Sadrizadeh, S., & Holmberg, S. (2015). Effect of a portable ultra-clean exponential airflow unit on the particle distribution in an operating room. *Particuology*, 18, 170–178. <https://doi.org/10.1016/j.partic.2014.06.002>
- Saidi, M. H., Sajadi, B., & Molaeimanesh, G. R. (2011). The effect of source motion on contaminant distribution in the cleanrooms. *Energy and Buildings*, 43(4), 966–970. <https://doi.org/10.1016/j.enbuild.2010.12.021>
- Sandle, T. (2011). *Cleanrooms and Air Quality – A Risk-Based Approach* (Issue December).
- Sekhar, S. C., & Willem, H. C. (2004). Impact of airflow profile on indoor air quality - a tropical study. *Building and Environment*, 39(3), 255–266. <https://doi.org/10.1016/j.buildenv.2003.09.003>
- Setti, L., Passarini, F., De Gennaro, G., Barbieri, P., Perrone, M. G., Borelli, M., Palmisani, J., Di Gilio, A., Piscitelli, P., & Miani, A. (2020). Airborne transmission route of covid-19: Why 2 meters/6 feet of inter-personal distance could not be enough. *International Journal of Environmental Research and Public Health*, 17(8). <https://doi.org/10.3390/ijerph17082932>
- Shan, K., & Wang, S. (2017). Energy efficient design and control of cleanroom environment control systems in subtropical regions – A comparative analysis and on-site validation. *Applied Energy*, 204, 582–595. <https://doi.org/10.1016/j.apenergy.2017.07.050>
- Sharan Thatiparti, D., Ghia, U., & Mead, K. R. (2017). Computational fluid dynamics study on the influence of an alternate ventilation configuration on the possible flow path of infectious cough aerosols in a mock airborne infection isolation room. *Science and Technology for the Built Environment*, 32(2), 355–366. <https://doi.org/10.1080/23744731.2016.1222212>
- Shih, Y. C., Chiu, C. C., & Wang, O. (2007). Dynamic airflow simulation within an isolation room. *Building and Environment*, 42(9), 3194–3209. <https://doi.org/10.1016/j.buildenv.2006.08.008>
- Smith, E. B., Raphael, I. J., Maltenfort, M. G., Honsawek, S., Dolan, K., & Younkins, E. A. (2013). The effect of laminar air flow and door openings on operating room contamination. *Journal of Arthroplasty*, 28(9), 1482–1485. <https://doi.org/10.1016/j.arth.2013.06.012>
- Sooter, C. (1964). Air Distribution in Clean Rooms. *Air Conditioning, Heating, and Ventilating*, 61(5), 75–78.
- Soyguder, S., & Alli, H. (2009). An expert system for the humidity and temperature control in HVAC systems using ANFIS and optimization with Fuzzy Modeling Approach. *Energy and Buildings*, 41(8), 814–822. <https://doi.org/10.1016/j.enbuild.2009.03.003>

- Suesada, K., Takemura, M., Tanahashi, T., & Kasahara, E. (2002). An Analysis of Transient Flow in a Clean Room by a Modified GSMAC Finite Element Method. *Chemical Pharmaceutical Bulletin*, 43, 2091. <http://www.mendeley.com/research/geology-volcanic-history-eruptive-style-yakedake-volcano-group-central-japan/>
- Sun, B., Luh, P. B., Jia, Q. S., & Yan, B. (2013). Event-based optimization with non-stationary uncertainties to save energy costs of HVAC systems in buildings. *IEEE International Conference on Automation Science and Engineering*, 436–441. <https://doi.org/10.1109/CoASE.2013.6654055>
- Sun, B., Luh, P. B., Jia, Q. S., & Yan, B. (2015). Event-Based Optimization Within the Lagrangian Relaxation Framework for Energy Savings in HVAC Systems. *IEEE Transactions on Automation Science and Engineering*, 12(4), 1396–1406. <https://doi.org/10.1109/TASE.2015.2455419>
- Sun, W., Flyzik, K., & Mitchell, J. (2013). Cleanroom_Pressurization_Strat.pdf. *ASHRAE Research Project RP-1344*.
- Sundell, J. (2004). On the history of indoor air quality and health. *Indoor Air, Supplement*, 14(SUPPL. 7), 51–58. <https://doi.org/10.1111/j.1600-0668.2004.00273.x>
- Suwa, Y., Park, J. C., & Kim, Y. S. (2011). Optimal airflow performance for FOUP systems in cleanrooms using SVE quantification method. *Journal of Asian Architecture and Building Engineering*, 10(1), 257–261. <https://doi.org/10.3130/jaabe.10.257>
- Tacutu, L., Nastase, I., & Catalina, T. (2016). A Critical Regard on Romanian Regulations Related to Indoor Environment Quality in Operating Rooms and a Technical Case Study. *Energy Procedia*, 85(November 2015), 511–520. <https://doi.org/10.1016/j.egypro.2015.12.237>
- Taira, K., Brunton, S. L., Dawson, S. T. M., Rowley, C. W., Colonius, T., McKeon, B. J., Schmidt, O. T., Gordeyev, S., Theofilis, V., & Ukeiley, L. S. (2017). Modal analysis of fluid flows: An overview. *AIAA Journal*, 55(12), 4013–4041. <https://doi.org/10.2514/1.J056060>
- Talty, J. T. (1998). Chapter 2. In *Industrial Hygiene Engineering (Second Edition)* (pp. 103–114).
- Tang, J. W., Eames, I., Li, Y., Taha, Y. A., Wilson, P., Bellingan, G., Ward, K. N., & Breuer, J. (2005). Door-opening motion can potentially lead to a transient breakdown in negative-pressure isolation conditions: The importance of vorticity and buoyancy airflows. *Journal of Hospital Infection*, 61(4), 283–286. <https://doi.org/10.1016/j.jhin.2005.05.017>
- Tao, Y., Inthavong, K., & Tu, J. (2017). Computational fluid dynamics study of human-induced wake and particle dispersion in indoor environment. *Indoor and Built Environment*, 26(2), 185–198. <https://doi.org/10.1177/1420326X16661025>
- The American Society of Heating and Ventilating Engineers Guide*. (1922). American Society of Heating and Ventilating Engineers.
- Tovell, Ralph M.; Friend, A. W. (1942). Control of Physical Hazards of Anesthesia. *Canadian Medical Association Journal*, 560–564. <https://doi.org/10.1097/00001888-193203000-00010>
- Tschudi, W., Benschine, K., Fok, S., & Rumsey, P. (2001). Cleanroom Energy Benchmarking In High-Tech and Biotech Industries Cleanroom. *Proceedings of the 2001 ACEEE Summer Study on Energy Efficiency in Industry*. American Council for an Energy-Efficient Economy, 1–11.

- Tung, Y. C., Shih, Y. C., & Hu, S. C. (2009). Numerical study on the dispersion of airborne contaminants from an isolation room in the case of door opening. *Applied Thermal Engineering*, 29(8–9), 1544–1551. <https://doi.org/10.1016/j.applthermaleng.2008.07.009>
- Villafriuela, J. M., San José, J. F., Castro, F., & Zarzuelo, A. (2016). Airflow patterns through a sliding door during opening and foot traffic in operating rooms. *Building and Environment*, 109, 190–198. <https://doi.org/10.1016/j.buildenv.2016.09.025>
- Vlasenko, V., Lukasheveitch, O., Rybakova, L., & Mashenko, V. (1998). Cleanroom Garments as the Complex Multilayer Structure. *Institute of Environmental Sciences and Technology Annual Technical Meeting*, 595–600.
- Vutla, S. R., Regalla, S. P., & Ramaswamy, K. (2019). A laminar fluid flow model for study of ventilation systems in micro- electromechanical systems (MEMS) clean room. *Journal of Physics: Conference Series*, 1276(1), 012057. <https://doi.org/10.1088/1742-6596/1276/1/012057>
- Wan, M. P., Chao, C. Y. H., Ng, Y. D., Sze To, G. N., & Yu, W. C. (2007). Dispersion of Expiratory Droplets in a General Hospital Ward with Ceiling Mixing Type Mechanical Ventilation System. *Aerosol Science and Technology*, 41(3), 244–258. <https://doi.org/10.1080/02786820601146985>
- Wang, H., Chen, K., & Liu, Z. (2007). Computation of airflow-driven re-entrainment of fine PM in conventionally-ventilated clean room. *IAQVEC 2007 Proceedings - 6th International Conference on Indoor Air Quality, Ventilation and Energy Conservation in Buildings: Sustainable Built Environment*, 2, 169–174.
- Wang, M., Lin, C. H., & Chen, Q. (2012). Advanced turbulence models for predicting particle transport in enclosed environments. *Building and Environment*, 47(1), 40–49. <https://doi.org/10.1016/j.buildenv.2011.05.018>
- Watt, J. (1933). The ventilation, heating and lighting of hospital wards. *Proceedings of the Royal Society of Medicine, Section of Epidemiology and State Medicine*, 1411–1426.
- Whitfield, W. J., & Whitfield, J. (1981). Brief history of laminar flow clean room systems. *Institute of Environmental Sciences*, 15–17.
- WHO. (2007). *Infection prevention and control of epidemic- and pan- demic-prone acute respiratory diseases in health care*.
- Whyte, William; Johnston, C. (1990). *British Standard 5295*.
- Whyte, W. (2010). *Cleanroom Technology: Fundamentals of Design, Testing, and Operation*. Wiley.
- Wu, Y., & Gao, N. (2014). The dynamics of the body motion induced wake flow and its effects on the contaminant dispersion. *Building and Environment*, 82, 63–74. <https://doi.org/10.1016/j.buildenv.2014.08.003>
- Xia, L., Jia, Q. S., & Cao, X. R. (2014). A tutorial on event-based optimization-a new optimization framework. *Discrete Event Dynamic Systems: Theory and Applications*, 24(2), 103–132. <https://doi.org/10.1007/s10626-013-0170-6>

- Xie, D. shuang, Xiong, W., Xiang, L. li, Fu, X. yun, Yu, Y. hua, Liu, L., Huang, S. qiong, Wang, X. hui, Gan, X. min, Xu, M., Wang, H. bo, Xiang, H., Xu, Y. hua, & Nie, S. fa. (2010). Point prevalence surveys of healthcare-associated infection in 13 hospitals in Hubei Province, China, 2007-2008. *Journal of Hospital Infection*, 76(2), 150–155.
<https://doi.org/10.1016/j.jhin.2010.04.003>
- Xu, T. (2007). Characterization of minienvironments in a clean room: Design characteristics and environmental performance. *Building and Environment*, 42(8), 2993–3000.
<https://doi.org/10.1016/j.buildenv.2006.10.020>
- Y.Venkata Bharath. (2013). Design, Installation and Commissioning Of Clean Room and HVAC Facility for Stem Cell Technologies and Regenerative Medicine. *IOSR Journal of Mechanical and Civil Engineering (IOSR-JMCE)*, 8(4), 01–12.
<http://www.iosrjournals.org/iosr-jmce/papers/vol8-issue4/A0840112.pdf?id=6655>
- Yaglou, C., Drinker, P., & Blackfan, K. (1930). Application of Air Conditioning to Premature Nurseries in Hospitals. *ASHVE Transaction*, 36(867).
https://scholar.google.com/scholar?start=0&q=air+conditioning+author:yaglou&hl=en&as_sdt=0,33#6
- Yang, C., Yang, X., & Zhao, B. (2015). The ventilation needed to control thermal plume and particle dispersion from manikins in a unidirectional ventilated protective isolation room. *Building Simulation*, 8(5), 551–565. <https://doi.org/10.1007/s12273-014-0227-6>
- Yang, L., & Eng Gan, C. (2007). Costing small cleanrooms. *Building and Environment*, 42(2), 743–751. <https://doi.org/10.1016/j.buildenv.2005.09.010>
- Zhao, B., Cao, L., Li, X., Yang, X., & Huang, D. (2004). Comparison of indoor environment of a locally concentrated cleanroom at occupied and unoccupied status by numerical method. *Journal of the IEST*, 47, 94–100. <https://doi.org/10.17764/jiet.47.1.p2366u3r2538vh17>
- Zhao, B., & Wu, J. (2005). Numerical investigation of particle diffusion in a clean room. *Indoor and Built Environment*, 14(6), 469–479. <https://doi.org/10.1177/1420326X05060190>
- Zhou, B., Ding, L., Li, F., Xue, K., Nielsen, P. V., & Xu, Y. (2018a). Influence of opening and closing process of sliding door on interface airflow characteristic in operating room. *Building and Environment*, 144. <https://doi.org/10.1016/j.buildenv.2018.08.050>
- Zhou, B., Ding, L., Li, F., Xue, K., Nielsen, P. V., & Xu, Y. (2018b). Influence of opening and closing process of sliding door on interface airflow characteristic in operating room. *Building and Environment*, 144(August), 459–473.
<https://doi.org/10.1016/j.buildenv.2018.08.050>
- Zhou, L., Sun, W., Huang, C., Li, H., Zou, Z., & Wu, C. (2017). Studies on Comparison of Particle Concentration Models for Cleanroom. *Procedia Engineering*, 205, 3308–3315.
<https://doi.org/10.1016/j.proeng.2017.10.343>